

IPPT Report on Fundamental Technological Research
2/2013

Łukasz Jankowski

DYNAMIC LOAD IDENTIFICATION FOR STRUCTURAL HEALTH MONITORING

Institute of Fundamental Technological Research
Polish Academy of Sciences

Warsaw 2013

IPPT Reports on Fundamental Technological Research
ISSN 2299-3657
ISBN 978-83-89687-74-6

Editorial Board/Kolegium Redakcyjne:

Wojciech Nasalski (Editor-in-Chief/Redaktor Naczelnny),
Paweł Dłużewski, Zbigniew Kotulski, Wiera Oliferuk,
Jerzy Rojek, Zygmunt Szymański, Yuriy Tasinkevych

Reviewer/Recenzent:

dr hab. inż. Jerzy Rojek

Received on 28 May 2012

Copyright © 2013 by IPPT PAN

Instytut Podstawowych Problemów Techniki Polskiej Akademii Nauk (IPPT PAN)
(Institute of Fundamental Technological Research Polish Academy of Sciences)
Pawińskiego 5B, PL 02-106 Warsaw, Poland

Printed by/Druk:

EXPOL, P. Rybiński J. Dąbek Sp. J., Brzeska 4, 87-800 Włocławek, Poland

Acknowledgements

It is a great pleasure to thank the people who have made this book possible. I express my deep appreciation to Prof. Jan Holnicki-Szulc, the head of the Department of Intelligent Technologies, for his continuous support, insightful help, as well as skilled and smooth management of everyday's affairs. I thank him and all other colleagues in IPPT PAN for our numerous fruitful discussions and for providing a stimulating environment in which to work and grow. In particular, I would like to thank my Ph.D. students, Mr. Grzegorz Suwała, Dr. Jilin Hou and Dr. Qingxia Zhang, for their bright ideas and hard work. I am also very indebted to the reviewer of this book, Prof. Jerzy Rojek, and to Prof. Zenon Mróz for their encouraging, constructive and insightful comments, which have greatly influenced and improved this book.

The support of Structural Funds in the Operational Programme “Innovative Economy” (IE OP) financed from the European Regional Development Fund is gratefully acknowledged – Projects PKAERO (Modern material technologies in aerospace industry, POIG.0101 .02-00-015/08), MONIT (Health monitoring and lifetime assessment of structures, POIG.0101 .02-00-013/08-00) and TEAM (Smart technologies for safety engineering – SMART & SAFE, TEAM /2008-1/4, operated within the Team Programme of the Foundation for Polish Science). It is also my duty and pleasure to express my thankfulness to the Directorate of the Institute of Fundamental Technological Research of the Polish Academy of Sciences for financial support in publishing this work.

Finally, I thank my family, especially my wife Dorota, son Frania and daughter Zosia. Without your patience and love nothing would have been possible. To you I dedicate this book.

Łukasz Jankowski

Institute of Fundamental Technological Research
Polish Academy of Sciences

Abstract

This book deals with the inverse problem of identification of dynamic loads and its applications for low frequency structural health monitoring (SHM). It collects and unifies the work performed by the author within the framework of three research projects either alone or together with the three Ph.D. students under his supervision or co-supervision¹. In particular:

- The inverse linear problem of load identification is discussed in the practically important case of limited instrumentation. Various techniques for augmenting the missing information are described together with three complementary quantitative measures of optimum sensor placement.
- A method for identification of dynamic loads in elastoplastic structures is developed, including sensitivity analysis of the response and gradient-based optimization.
- The general methodology of the virtual distortion method (VDM) is used to represent various SHM problems in terms of a load identification problem. This includes
 - A methodology for virtual isolation of substructures for the purpose of local SHM.
 - A model-free (nonparametric and based on purely experimental data) methodology for identification of structural damages, modifications and inelastic impacts.
 - A unified approach to the problem of simultaneous identification of unknown excitations and structural damages.

All presented approaches are tested and illustrated in numerical examples that use a realistic numerical noise level of at least 5% rms. Depending on laboratory constraints, experimental verification is performed in selected cases.

¹Two Ph.D. theses are defended in 2010 (Harbin Institute of Technology, Harbin, China), and one thesis is in progress (IPPT PAN, Warsaw, Poland).

Łukasz Jankowski
Instytut Podstawowych Problemów Techniki
Polskiej Akademii Nauk

Streszczenie

Książka poświęcona jest problemowi odwrotnemu identyfikacji obciążen dynamicznych i jego zastosowaniom w dziedzinie niskoczęstotliwościowego monitorowania stanu technicznego konstrukcji. W spójnej formie prezentuje ona wyniki badań przeprowadzonych przez autora samodzielnie lub wspólnie z trojgiem doktorantów pod jego kierownictwem².

- W pracy jest rozważany problem identyfikacji wymuszeń dynamicznych w ważnym wypadku niekompletnej informacji, tzn. ograniczonej liczby czujników. Zaproponowano techniki heurystycznego uzupełniania brakującej informacji oraz trzy miary optymalności rozmieszczenia czujników.
- Zaproponowana metoda identyfikacji jest rozszerzona na wypadek konstrukcji o sprężystoplastycznej charakterystyce materiałowej; opracowana jest metoda analizy wrażliwości umożliwiająca zastosowanie klasycznych, gradientowych metod optymalizacji.
- Autor wykazuje, że wykorzystując metodę dystorsji wirtualnych, szereg istotnych problemów monitorowania stanu technicznego konstrukcji można rozwiązać poprzez sprowadzenie ich do problemu identyfikacji równoważnego obciążenia dynamicznego. Dotyczy to problemów takich jak:
 - wirtualna izolacja istotnych podstruktur pozwalająca na ich lokalne monitorowanie z pominięciem wpływów pozostałej części konstrukcji;
 - bezmodelowa (nieparametryczna i czysto eksperymentalna) identyfikacja uszkodzeń i modyfikacji konstrukcji oraz uderzeń niesprężystych;
 - jednoczesna identyfikacja wymuszeń dynamicznych i uszkodzeń.

Opracowane metody przetestowano numerycznie z błędem pomiarowym symulowanym na realistycznym poziomie 5% rms. W ramach możliwości praktycznych, część metod zweryfikowano eksperymentalnie w warunkach laboratoryjnych.

²Dwie dysertacje zostały obronione w 2010 roku na Politechnice w Harbinie, Chiny (współpromotorstwo); przewód doktorski trzeciego doktoranta został otwarty w styczniu 2013 roku w Instytucie Podstawowych Problemów Techniki PAN (promotorstwo pomocnicze).

Symbols and abbreviations

The following list provides the most frequently used symbols and abbreviations:

ω	– angular frequency
t, τ	– time variables
T	– time interval length
\mathbf{a}^L	– vector of sensor responses in undamaged structure
\mathbf{a}^M	– vector of measured sensor responses in damaged structure
\mathbf{a}	– vector of modeled sensor responses in damaged structure
\mathbf{f}^0	– external excitation vector
\mathbf{f}_{test}	– testing excitation vector
φ_{ij}	– j th basis distortion vector of i th element
κ_{ij}	– j th distortion of i th element
κ_{ij}^0	– j th virtual distortion of i th element
\mathbf{p}^0	– pseudo load vector
ν^0	– vector of virtual distortions and pseudo loads
ε_i^0	– axial virtual distortion of i th truss element
β_i^0	– plastic strain of i th truss element
Ψ_i	– total plastic strain of i th truss element
Φ_i	– yield function of i th truss element
σ_i^*	– initial plastic yield stress of i th truss element
γ_i	– hardening coefficient of i th truss element
ε_i	– axial strain of i th truss element
E_i	– Young's modulus of i th element
\mathbf{M}	– mass matrix
\mathbf{K}	– stiffness matrix

$\tilde{\mathbf{K}}$	– modified stiffness matrix
$\Delta\mathbf{M}$	– modification of mass matrix
$\Delta\mathbf{K}$	– modification of stiffness matrix
$\boldsymbol{\mu}$	– vector of damage (or modification) coefficients
F	– objective function
\mathbf{H}	– displacement impulse response matrix
\mathcal{H}	– operator of convolution with \mathbf{H}
\mathbf{B}	– reduced impulse response matrix
\mathcal{B}	– operator that transforms excitations or virtual distortions into sensor responses
\mathbf{D}	– time-discretized reduced impulse response matrix
\mathcal{I}	– identity operator
\mathbf{L}^f	– load allocation matrix
$\mathbf{L}_0^a, \mathbf{L}_1^a, \mathbf{L}_2^a$	– sensor placement matrices
q_i	– experimentally applied quasi impulse excitation
\mathbf{I}_p	– indicator function
N_t	– number of time steps
N_{dof}	– number of degrees of freedom
N_e	– number of externally excited DOFs
N_r	– number of sensors
δ_{ij}	– Kronecker's delta
$\delta(t)$	– Dirac's delta
APA	– amplified piezo actuator
AVM	– adjoint variable method
CA	– combined approximations
CGLS	– conjugate gradient least squares
DDM	– direct differentiation method
DOF	– degree of freedom
ERA	– eigensystem realization algorithm
FE	– finite element
FFT	– fast Fourier transform
MAC	– modal assurance criterion
SVD	– singular value decomposition
SVE	– singular value expansion
TSVD	– truncated singular value decomposition
VDM	– virtual distortion method

Contents

1. Introduction	13
1.1 The inverse problem of load identification	13
1.2 Structural health monitoring and load identification	15
1.3 Numerical models and experimental setups	17
1.4 Scope of the work	18
2. Load identification in linear structures	23
2.1 Introduction	23
2.1.1 Overview of the problem	23
2.1.2 State-of-the-art	24
2.1.3 Aims and techniques	27
2.2 Problem formulation	29
2.2.1 Impulse response matrices	29
2.2.2 Direct problem	33
2.2.3 Inverse problem	36
2.2.4 Practical considerations	37
2.3 Overdetermined case	42
2.4 Underdetermined case	46
2.4.1 Decomposition of excitation	47
2.4.2 Single-stage identification	52
2.5 Optimum sensor placement	53
2.5.1 Criterion of conditioning	55
2.5.2 Criterion of informativity	55
2.5.3 Compound criterion	56
2.6 Numerical example	56
2.6.1 The structure	56
2.6.2 Optimum placement of sensors	57
2.6.3 Actual excitation	61
2.6.4 Identification results	61

3. Virtual distortion method	67
3.1 Introduction	68
3.1.1 Structural reanalysis	68
3.1.2 Overview of the VDM	69
3.1.3 Introductory examples	72
3.1.4 VDM and load identification	75
3.2 Distortions of a finite element	76
3.2.1 Basis distortions and equivalent element loads	76
3.2.2 Total distortions	77
3.2.3 Decomposition of global elastic forces	78
3.2.4 Equation of motion of the original structure	78
3.3 Direct problem	79
3.3.1 Structural modifications and damages	79
3.3.2 Pseudo loads and virtual distortions	80
3.3.3 Solution scheme	82
3.3.4 Time discretization	83
3.4 Inverse problem	84
3.4.1 Objective function	85
3.4.2 Sensitivity analysis	86
3.4.3 Time discretization	89
4. Model-free structural health monitoring	93
4.1 State-of-the-art and introduction	94
4.2 Time-domain formulation	96
4.2.1 The direct problem	96
4.2.2 The inverse problem	102
4.2.3 Time discretization and numerical solution	106
4.3 Frequency-domain formulation	111
4.3.1 The direct problem	112
4.3.2 The inverse problem	113
4.3.3 FFT and windowing function	114
4.4 Identification of inelastic impacts	114
4.4.1 The direct problem	115
4.4.2 The inverse problem	115
4.5 Selected experimental results	116
4.5.1 The structure	116
4.5.2 Excitations and measurements	116
4.5.3 Single nodal mass modification	118
4.5.4 Modification of two nodal masses	120

5. Virtual isolation of substructures for local health monitoring	125
5.1 Motivation	126
5.2 State-of-the-art	127
5.2.1 Static case	127
5.2.2 Dynamic case	127
5.2.3 Substructure separation methods	129
5.3 Overview of the isolation method	129
5.3.1 Two-stage monitoring	129
5.3.2 Excitations, sensors and measured responses	130
5.3.3 Stage I: substructure isolation	133
5.3.4 Stage II: local identification	134
5.3.5 Substructure isolation and load identification	135
5.4 Isolation in time domain	135
5.4.1 Isolation with other types of virtual supports	137
5.4.2 Time discretization and numerical stability	139
5.5 Isolation in frequency domain	140
5.5.1 Isolation in time domain vs. isolation in frequency domain	141
5.5.2 FFT of the time-domain responses	142
5.6 Numerical examples	142
5.6.1 2-DOF mass-spring system	143
5.6.2 6-DOF mass-spring system	144
5.7 Experimental verification	152
5.7.1 Experimental setup	152
5.7.2 Isolation and identification in time domain	157
5.7.3 Isolation and identification in frequency domain	160
6. Simultaneous identification of damages and dynamic excitations	165
6.1 State-of-the-art	166
6.2 Damage-equivalent excitations	168
6.2.1 VDM-based formulation and the direct problem	168
6.2.2 Off-line identification	171
6.2.3 Online identification	174
6.2.4 Numerical example	175
6.2.5 Experimental example	184
6.3 Parametrization of loads	190
6.3.1 Modeling of moving masses	191
6.3.2 Coupled modeling of moving masses and damages	194
6.3.3 Identification	197
6.3.4 Numerical example	200

7. Load identification in elastoplastic structures	211
7.1 Bilinear isotropic hardening plasticity	213
7.2 The direct problem	214
7.2.1 Continuous formulation	214
7.2.2 Discrete-time setting	216
7.3 The inverse problem	221
7.3.1 Objective function	222
7.3.2 First order sensitivity analysis	222
7.3.3 Approximate second order sensitivity analysis	224
7.4 Numerical example	225
7.4.1 The structure	225
7.4.2 Actual excitation and the response	225
7.4.3 Sensor placement	227
7.4.4 Identification results	227
8. Conclusions	231
8.1 Original results	231
8.2 Further research	233
A. Linear inverse problem	235
A.1 Linear operators	235
A.1.1 Boundedness, continuity and compactness	236
A.1.2 Ill-posedness, ill-conditioning and regularization	237
A.2 Infinite dimensional integral problems	239
A.2.1 Linear integral operator	240
A.2.2 Linear integral equations	241
A.2.3 Discretization	246
A.3 Finite dimensional discretized problems	249
A.3.1 Solvability and conditioning	249
A.3.2 Numerical regularization	252
Bibliography	257

1

Introduction

The book is devoted to the inverse problem of identification of dynamic loads and its applications in low frequency structural health monitoring (SHM). This chapter approaches the problem of load identification from the perspective of a general classification of inverse problems, considers its relation to the field of SHM and provides an overview of the scope of the book.

1.1 The inverse problem of load identification

Figure 1.1 depicts a general scheme of a system together with its input and output. Schematically, the relation between the input and the output can be stated as

$$\mathbf{a}^L = \mathcal{B}^0 \mathbf{f}^0, \quad (1.1)$$

where \mathcal{B}^0 is a certain operator that acts on the input \mathbf{f}^0 (excitation) to produce the output \mathbf{a}^L (response). The scheme can be used to introduce and differentiate between the three following general types of problems:

1. *Direct problem.* Known the system \mathcal{B}^0 and the input \mathbf{f}^0 , find the output \mathbf{a}^L of the system.
2. *Inverse problem I.* (system identification) Known the input \mathbf{f}^0 and the output \mathbf{a}^L , find the system \mathcal{B}^0 .
3. *Inverse problem II.* (input identification) Known the system \mathcal{B}^0 and the output \mathbf{a}^L , find the input \mathbf{f}^0 .

The superscripts “L” and “0” are used in (1.1) to maintain notational consistency with the rest of the book. Their purpose and the precise meaning of the symbols will become clear in Chapters 2 and 3.

The problem of identification of dynamic loads is an inverse problem of type II (input identification). Such a problem occurs in many applications, where excitation by unknown loads can result in significant structural response, but it is impossible or hardly possible to measure these loads directly. This includes

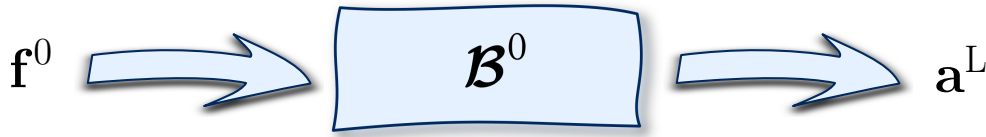


Figure 1.1. A general scheme of a system, its input and output.

excitations by moving crowd during sport events, in-flight collisions with birds, ambient environmental excitations such as due to wind or traffic, vehicular loads of a bridge, etc. In all such cases, only indirect load monitoring is possible: the excitation can be only deduced based on measured structural response and knowledge of certain characteristics of the underlying structure. At the same time, accurate knowledge of the actual dynamic loads can be important in off-line applications (black-box monitoring systems for forensic engineering, fatigue assessment or design code calibration, etc.) or even crucial in online applications (such as decision support systems or traffic control), which stimulates progress in the field. A brief review of the current research can be found in Subsection 2.1.2.

Within the context of identification of excitation loads, this book is focused on problems related to:

limited instrumentation In many practical cases, the instrumentation is insufficient to attain a unique solution, since little is known about the excitation and a general form has to be assumed. Means of augmenting the missing information are considered.

ill-conditioning Load identification is an inverse problem. In linear case, it can be formulated in the form of a Volterra integral equation with a weakly singular kernel. Therefore, it is ill-conditioned, or even ill-posed in the sense of Hadamard, which has to be taken into account in all identification procedures.

optimum sensor placement Limited instrumentation and ill-conditioning of the problem significantly decrease the amount of useful information that is contained in the measured response. In practice, the identification is thus based on incomplete information, and it becomes especially important to consider optimum placement of the available sensors.

elastoplastic structures As a rule, literature on force identification takes into account only linear structures. And when nonlinear structures are considered, they are elastic. Identification techniques need to be developed for the case of nonelastic structures.

1.2 Structural health monitoring and load identification

The primary task of SHM systems is damage detection, which is the first level of the three-level process known as damage identification:

- *Level 1.* Damage detection.
- *Level 2.* Localization of the detected damage.
- *Level 3.* Quantification of the damage.

In general, all existing methods can be divided into two groups: local and global approaches, which are respectively based on high and low frequency testing. Local monitoring methods are used for precise identification of small defects in narrow inspection zones via ultrasonic testing (for reviews and examples see [1–6]) or statistical classification techniques [7, 8]. These methods do not require global structural modeling and are outside the scope of this book. Global SHM methods are aimed at detection or identification of significant defects in a nonlocal inspection zone, which is often the whole structure. A vast number of existing approaches can be categorized with respect to various criteria. In an excellent overview [9], Friswell differentiates between model updating, modal and pattern recognition methods; others like Yan [10] single out modal, time domain and wavelet approaches. For other classifications and reviews, see, e.g., Carden and Fanning [11], Chang *et al.* [12], Worden and Dulieu-Barton [13], Kołakowski [14] or the short Section 4.1 in this book. Modal methods detect, locate and quantify damages by the changes of the related modal parameters; reviews can be found in Doebling *et al.* [15, 16] or in Uhl and Mendrok [17]. Time domain methods utilize either statistical concepts and time series models [18] or deterministic model-updating approaches [19, 20], which can be further categorized into direct and sensitivity-based methods. In the last decade, wavelet analysis has become a popular tool [21–25], and it is often used together with pattern recognition methods [26]. A part of these methods rely on the assumption that external excitations are known. Others, like some modal and time series methods, can be used without exact information about the excitation, but they are confined to special conditions like ambient excitation or free response of the monitored structure.

According to the classification introduced in Section 1.1, damage identification is the inverse problem of type I: the excitation is known or at least well characterized, the response is measured, and it is the system that is (partially) unknown and needs to be identified. Model-based approaches represent the damage in terms of a vector $\boldsymbol{\mu}$ of damage parameters, which fully defines the system $\mathcal{B}^0(\boldsymbol{\mu})$. Damage identification is then equivalent to the task of finding the

unknown vector $\boldsymbol{\mu}$, that is to the problem of solving the following counterpart to (1.1) with respect to $\boldsymbol{\mu}$:

$$\mathbf{a} = \mathcal{B}^0(\boldsymbol{\mu})\mathbf{f}^0, \quad (1.2)$$

where \mathbf{f}^0 is the known excitation and \mathbf{a} is the known response of the damaged system that is different from the response \mathbf{a}^L of the original system. Such a formulation suggests that there is a fundamental difference between the problems of damage identification (type I) and load identification (type II), and it explains why they are typically solved using approaches that are essentially different. *This book is aimed at bridging this gap.* In particular, this book demonstrates that effective load identification techniques are crucial for SHM, since many typical SHM problems can be formulated and solved in terms of load identification problems. This is possible thanks to the virtual distortion method [27, 28], which allows structural damages and material nonlinearities to be conveniently modeled using the equivalent pseudo loads (or virtual distortions, which are certain combinations of the pseudo loads). These pseudo loads are additional loads that excite the original unmodified structure at the locations of the modeled modifications [29, 30]. This is discussed in detail in Chapter 3 and illustrated in subsequent chapters. In short, the VDM expresses (1.2) in the equivalent form of

$$\begin{aligned} \mathbf{a} &= \mathcal{B}^0\mathbf{f}^0 + \mathcal{B}^{a\nu}\boldsymbol{\nu}^0 \\ &= \mathbf{a}^L + \mathcal{B}^{a\nu}\boldsymbol{\nu}^0, \end{aligned} \quad (1.3a)$$

where \mathcal{B}^0 is the original undamaged system, the vector $\boldsymbol{\nu}^0$ collects the pseudo loads and virtual distortions, and it is related to the damage parameters $\boldsymbol{\mu}$ and the response \mathbf{a} by the following implicit equation

$$\mathbf{0} = \mathbf{R}(\boldsymbol{\nu}^0, \boldsymbol{\mu}, \mathbf{a}). \quad (1.3b)$$

Equation (1.3b) is stated here in a general form, as its specific form depends on the particular system and the type of the considered damages, modifications or nonlinearities. All potential nonlinearities (material or related to damages) are modeled by (1.3a), so that \mathcal{B}^0 and $\mathcal{B}^{a\nu}$ in (1.3a) are linear, which is an important feature of the method. The VDM provides thus a framework, in which the unknowns in type I and type II inverse problems can be treated in a unified manner, and allows the same methodology of load identification to be uniformly applied across a range of seemingly loosely related SHM problems, such as identification

of structural damages and inelastic impacts, virtual isolation of substructures for the purpose of local SHM, simultaneous identification of coexistent loads and damages, etc.

Throughout this book, load identification is thus understood in a broader sense than just force identification: besides identification of the actual *external excitation forces*, it includes also identification of the *pseudo loads* that are used to model structural damages and modifications such as virtual supports, as well as identification of *parametrized excitations* such as inelastic impacts or moving masses.

1.3 Numerical models and experimental setups

This book is focused on identification of dynamic loads, and hence the excitation \mathbf{f}^0 in (1.1) and (1.3a), as well as the response \mathbf{a} and the pseudo load \mathbf{p}^0 , are initially assumed to be functions of a continuous time variable t (or sometimes the frequency ω). Such a formulation allows the load identification problem to be represented in the form of an integral equation and gives more insight into its properties. Then, for the purpose of numerical solution, the time variable is discretized, which transforms the identification problem into a large discrete linear system with a dense structured matrix.

The response and the loads are also assumed to be spatially discretized, that is \mathbf{a} , \mathbf{f}^0 and \mathbf{p}^0 are originally vector functions of time t or frequency ω . Spatial discretization corresponds well to the framework of the finite element (FE) method, which is ubiquitously used for modeling of real-world structures, since in FE models any excitation has to be distributed onto a discrete set of the degrees of freedom (DOFs). The FE modeling approach is also used throughout this book in all the numerical examples, which are all either 3D trusses or 2D frames composed of Euler–Bernoulli beams with consistent mass matrices, with the sole exception of two simple mass–spring systems in Section 5.6. Since the VDM assumes that the original undamaged structure is linear, no geometric nonlinearity is considered and the formulation is limited to the case of small displacements and rotations.

Many of the techniques proposed and discussed in this book are verified experimentally. Two stands are used for this purpose: either a 3D steel truss structure (26 nodes, 70 elements, 4 m length, mass 32 kg) constructed using a commercially available system of nodes and connecting tubes [31], see Fig. 4.1, or a vertically suspended slender aluminum cantilever beam (1.36 m length, mass 0.307 kg), see Fig. 5.13.

1.4 Scope of the work

The book is organized in eight chapters and one appendix. The current chapter is the first chapter.

Chapter 2 discusses the inverse problem of indirect identification of dynamic excitation loads in linear structures based on their measured response. This is the problem of solving (1.1) with respect to \mathbf{f}^0 , where \mathcal{B}^0 is assumed to be a linear transformation. The chapter presents a methodology focused on the case of a limited instrumentation and takes into account the inherent ill-conditioning of the problem. The subspaces of reconstructible and unreconstructible excitation components are introduced; the identification problem is unique within the former subspace, while the latter is used to construct an observationally equivalent excitation that, in a given sense, optimally approximates the actual excitation. Three complementary criteria of sensor placement optimality are discussed; they are based on either conditioning or informative content of the reconstructible subspace. The proposed techniques are verified in a numerical example of a 3D truss structure. In its earlier form, the approach has been proposed by the author in [32], see also [33–37].

Chapter 3 is devoted to the virtual distortion method, which is a method for quick structural reanalysis being developed in the Institute of Fundamental Technological Research (IPPT PAN) [27, 28]. The VDM yields the response of a modified structure by computing the effect of the modifications on its original response, without solving structural equations from scratch. In case of a localized modification, it results in a significantly shorter time of computation. Various types of modifications are treatable in a unified manner, including modifications of structural stiffness and mass, which within the context of the SHM are often used to represent the damage. The inverse problem of load identification is at the core of the VDM, since the modifications are modeled using the equivalent pseudo loads or virtual distortions, which are such combinations of pseudo loads that result in distortions of the affected structural elements, see (1.3a). Throughout the rest of the book, the method is extensively used as a convenient vehicle for formalization of various SHM-related identification problems in terms of the load identification problem. The chapter is focused on the deterministic time-domain formulation of the VDM in direct and inverse problems of dynamics. A new continuous-time notation is introduced, partly based on the work earlier presented by the author in [29, 38–40]. Compared to the original discrete-time notation, this formulation is more concise and clearly emphasizes the mathematical structure and properties of the reanalysis problem together with its relation to the inverse problem of load identification. The derivation

sets out from the equation of motion, which seems to be more straightforward than the postulate of equality of local strains and element forces. Moreover, in the inverse problem, a distinction is introduced between the cases of known and unknown types of local damages (e.g., “a breathing crack with an unknown constant reduction of stiffness in tension” vs. just “an unknown damage that affects stiffness of the element”); the latter is discussed in detail and further developed in Chapter 6.

Chapter 4 presents a part of the research on model-free SHM conducted by the author together with Grzegorz Suwała, a Ph.D. student under his supervision¹ within the framework of project TEAM. The approach aims to address the common practical problems that occur in monitoring of complex structures: model-based methods tend to provide accurate identification results, but it is difficult to update a reliable parametric model of such a structure, while pattern recognition methods are typically unable of parametric quantification of damages. The essentially nonparametric approach of the VDM to structural modeling is used here to develop a purely experimental monitoring methodology that is directly based on experimentally measured impulse response functions, see [29] and [30, 38, 41–45]. Such an approach can be advantageous in case of real-world structures, where it is often much easier to perform a number of localized measurements of impulse response functions than to update a parametric model of the global structure. Even if the developed method requires no parametric numerical model of the monitored structure, it still can be used for identification of parametrized modifications, damages or inelastic impacts; in the field of SHM, this is atypical and characteristic enough to warrant the name of a *model-free* approach. In line with the general methodology of the VDM, all structural modifications are modeled with the equivalent pseudo loads that need to be computed using load identification procedures. The approach is verified experimentally in identification of nodal mass modifications of a 3D truss structure.

Chapter 5 reports on a part of the research on local SHM performed together with Jilin Hou, a Ph.D. student² co-supervised by the author together with Prof. Jinping Ou. The presented research has been performed during a one-year stay of Mr. Hou in IPPT PAN within the framework of project MONIT and concerns the substructure isolation method, see [46–53]. The motivation behind it are the facts that global SHM of large and complex structures is

¹The doctoral proceedings of Mr. Suwała have been opened in IPPT PAN in January 2013; the author of this book is his associate supervisor.

²Thesis defended on the 3rd July 2010 in School of Civil Engineering, Harbin Institute of Technology (Harbin, China).

generally difficult and that often only small substructures are crucial and require monitoring, which suggest that there is a need for ways of applying global SHM approaches locally. The chapter offers an overview of the state-of-the-art in substructuring and introduces the concept of a virtual support, which is modeled using a pseudo load in place of its reaction force. The pseudo load is identified by solving a type II inverse problem (load identification). A series of virtual supports can be placed on the interface of a substructure to isolate it numerically from the outside influences. The method splits thus the task of local monitoring into two stages: (1) Isolation; the outside influences are numerically eliminated from the measured response of the substructure. (2) Local SHM; all methods aimed originally at global SHM can be used with the constructed response of the isolated substructure. This is in contrast to other substructuring methods that perform both stages simultaneously and require thus dedicated approaches for local identification. The proposed method is illustrated in a numerical example of a simple mass–spring system and then substantiated in an experimental study using a damaged slender cantilever beam; the robustness of the isolation with respect to unknown modifications of the outside structure is tested.

Chapter 6 describes a part of the research performed together with Qingxia Zhang, a Ph.D. student³ co-supervised by the author together with Prof. Zhong-dong Duan. The presented research has been performed during a two-year stay of Ms. Zhang in IPPT PAN within the framework of project TEAM and concerns simultaneous identification of excitations and damages, see [39, 40, 54–62]. In practice, unknown loads and damages often coexist and can be both of interest in applications such as bridge and traffic monitoring, forensic engineering, design code calibration, etc., but the available body of research in the topic is very limited; the main difficulty seems to lie in very different types of the involved unknowns and the respective inverse problems (mixed type I and type II). As a rule, two-step iteration procedures are adopted and the unknowns are updated separately, so that optimization proceeds in an alternate manner. This is a non-standard approach that requires dedicated methodologies. The chapter provides a literature review and proposes two solutions, which use the VDM to unify the variables and avoid the alternation. The first approach represents the damages in the form of the equivalent virtual distortions and identifies them together with the excitation using load identification procedures (reduction to an inverse problem of type II, see (1.3a)). The stress–strain relationships of damaged elements are then recovered and used to characterize the type and extent of the

³Thesis defended on the 22nd June 2010 in School of Civil Engineering, Harbin Institute of Technology (Harbin, China).

damage. The second approach proceeds the opposite way and parametrizes the considered moving load excitation (reduction to an inverse problem of type I, such as (1.2)). Both approaches are tested in numerical examples (using respectively a modeled 3D truss structure and a modeled 2D bridge-like three span frame structure composed of Euler–Bernoulli beams); the first approach is also verified experimentally using the same experimental stand as in Chapter 5.

Chapter 7 considers the problem of identification of excitation loads in elasto-plastic structures, which are governed by the well-defined model of the bilinear isotropic hardening plasticity [32]. Plastic yield represents the damage caused by an excessive load, and it is modeled using plastic distortions, which are imposed on the original linear structure and processed using the methodology of the VDM. The structure, although materially nonlinear, is assumed to be geometrically linear. The direct differentiation method is employed to derive analytical formulas for the gradients of the response with respect to the unknown excitations, which allows any general-purpose gradient-based optimization approach to be used for a fast identification. The identification is essentially formulated as a least-squares problem, hence its Hessian is also approximated along the lines of the Gauss–Newton approach. A numerical example of a 3D truss structure excited by a moving load is used for verification.

Chapter 8 contains conclusions, summarizes the original results considered to be important, and provides outlook and directions for further research.

Most load identification problems analyzed in this book are either inverse linear problems or, thanks to the VDM, can be represented in such a form. The Appendix provides thus an overview of the basics of linear inverse problems with the focus on the often neglected aspects that are important in load identification: posedness, conditioning and regularization techniques for finite-dimensional problems. First, the fundamental notions of a linear compact operator, problem posedness, conditioning and regularization are briefly discussed. Then, integral inverse problems are reviewed. Finally, the appendix proceeds to their numerically treatable discretized counterparts, which naturally arise in practice due to the discrete nature of the measurement process.

2

Load identification in linear structures

This chapter considers a methodology for off-line identification of transient excitation forces in linear, time-invariant and spatially discretized structures, including the time-histories and spatial characteristics of the excitation. The motivation is the need for an effective analysis technique for reconstruction of the scenario of an unknown sudden dynamic load, which could be used in black-box type systems. Moreover, as discussed later in this book, load identification is crucial in structural health monitoring, as many types of structural damages and modifications can be conveniently modeled using equivalent pseudo loads and/or virtual distortions.

2.1 Introduction

2.1.1 Overview of the problem

As illustrated in Fig. 1.1, formulation of the direct problem, as well as the inverse problem of load identification, requires three elements to be specified:

1. *The input* to the system, which are its external excitation forces. They are assumed to act in selected N_e degrees of freedom (DOFs) of the structure and are represented in the form of an N_e -element excitation vector $\mathbf{f}^0(t)$. Usually only a limited number of DOFs will be exposed to the excitation, so that $N_e \leq N_{\text{dof}}$, where N_{dof} is the total number of DOFs.
2. *The output* of the system, which is its mechanical response to the excitation $\mathbf{f}^0(t)$ as measured with a certain number N_r of linear sensors. Zero initial conditions are usually assumed, and $N_e \leq N_{\text{dof}}$. The response is represented in the form of an N_r -element response vector, which is either
 - computed in the direct problem and denoted then $\mathbf{a}(t)$, or
 - measured to be used in the inverse problem and denoted then $\mathbf{a}^M(t)$ in order to emphasize that it is actually measured.

3. *The system*, which is (a model of) the structure subjected to the external excitation $\mathbf{f}^0(t)$. Two general categories of system models are usually considered:

- *parametric* model, such as the finite element (FE) model, or a
- *nonparametric* model, which can be specified in terms of the structural impulse response matrix.

This chapter considers the nonparametric model, see Subsection 2.2.1. The parametric formulation is used only to introduce the methodology and verify its validity.

In terms of the above terminology:

The direct problem consists of computing the response $\mathbf{a}(t)$, given the excitation $\mathbf{f}^0(t)$ and a certain structural model.

The inverse problem of load identification consists of computing the excitation $\mathbf{f}^0(t)$, given the response $\mathbf{a}^M(t)$ and a certain structural model.

Figure 2.1 shows a schematic example of a structure with $N_r = 7$ strain sensors and $N_e = 8$ external excitation forces.

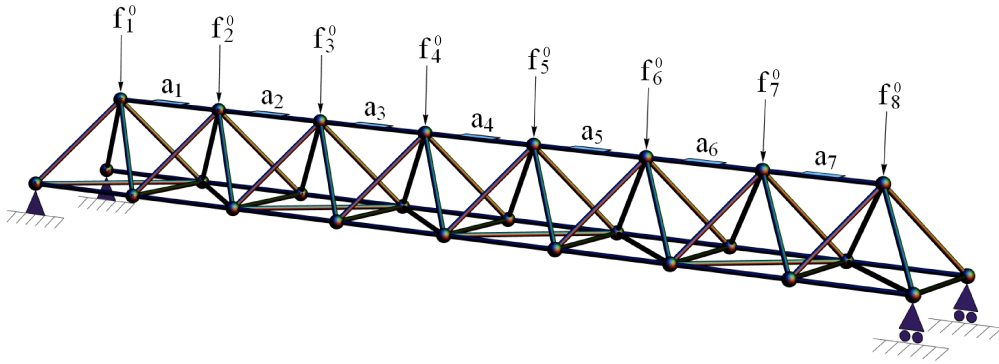


Figure 2.1. A 3D truss structure subjected to $N_e = 8$ external excitation forces and equipped with $N_r = 7$ strain sensors. The total number of degrees of freedom is $N_{\text{dof}} = 68$.

2.1.2 State-of-the-art

This subsection presents a general overview of the techniques used for identification of dynamic loads. As a general baseline work in the static case, Mróz and Garstecki [63] can be consulted, which presents a uniform formulation of the optimum static loading problem in various design and identification tasks, including an extension to nonlinear elastic structures.

There is a continuous research effort in the field of indirect identification of dynamic loads, see [64–71] and [72, Chapter 6] for detailed reviews and example applications. In general, all approaches used for identification of time-history of dynamic excitations can be categorized into two broad groups of model-based methods and computational intelligence techniques.

The majority of the approaches considered in the literature belong to the first group of *model-based* methods. These methods are aimed at identification of the time-history of the excitation. For this purpose, they use a full model of the loaded structure, which is most often specified in terms of the FE method. The identification is performed either off-line, that is based on the full recorded time-histories of the response, or online, that is based on measurement data that are successively collected in real time, without insight into future data. The *off-line* approaches reduce the identification problem to the deconvolution of the measured structural response with respect to the impulse response function, which is computed in advance or on-the-fly during identification (as in the dynamic programming approach, see [69, 73, 74]). The deconvolution is performed in time domain [32, 73, 75, 76], in frequency domain [77–80] and [81, Chapter 6], or in wavelet domain [82]. The inherent ill-conditioning of the problem is usually addressed by using the Tikhonov regularization, that is by limiting the ℓ^2 norm of the excitation, which is well-researched and numerically efficient, but might not be well-suited to typical load characteristics as it tends to distribute the identified excitation among all DOFs and time instances. For *online* identification of excitations, Kalman filter [83], observer techniques of unknown input estimation [84, 85], as well as inverse system filter [86–88] have been used. The great majority of all these methods take into account only linear systems; there are only a few papers that consider nonlinear [84, 89] or elastoplastic [32] structures, or allow for geometric nonlinearities [90].

Methods of the other group are based on *computational intelligence* techniques. As a rule, they are aimed at rough identification of only a limited number of basic characteristics of the excitation, such as its location or amplitude, which are treated as system input. The identification is based on certain numerical fingerprints (usually wavelet expansion coefficients) that are extracted from the measured response and treated as system output. The structural model used in the process of identification is no longer a full model of the structure, but rather a relationship between response fingerprints and the selected characteristics of the excitation. Such a relationship is obtained empirically and either directly stored, in the form of a fingerprint database, or encoded indirectly, usually in the form of a trained neural network. As an example, a case-based reasoning approach is used in [26, 91] with a fingerprint database for identification of the

location of an impact on an aircraft wing, while in [92] a similar technique is used to identify both impact location and magnitude. In [93], static loads acting on an aircraft wing are identified by using an artificial neural network.

Approaches of both groups usually limit the considered excitation to a single stationary point-wise force with the location known in advance, see, e.g., [94]. The location of such a force is sometimes assumed to be unknown, as in [95, 96], and determined in a second-stage nonlinear optimization, which is performed with respect to space. Several researches deal with a single point-wise load of an impact type and disregard all its characteristics (time history, magnitude, duration, etc.) besides the location [26, 97, 98].

Identification of moving loads. A relatively large body of research seems to be devoted to the special case of indirect identification of the time-history of a moving point-wise force (or a set of forces) from measured responses of bridge-like structures, see a review in [71]. The moving forces are almost always assumed to have a constant velocity and model vehicular loads; rare exceptions are [99, 100], which consider braking vehicles. Such a problem seems to be important in traffic studies, for assessment of pavements and bridges, for traffic control, design code calibration, etc. In a series of publications, Chan, Law *et al.* propose several general methods for indirect identification; the bridge is modeled either as a continuous viscous beam (in a time-domain method [101] and in a frequency-time domain method [102]) or in terms of the FE method (as an assembly of lumped masses and massless elastic beams [103], Euler–Bernoulli beam elements [104] or general FE elements [105]). These methods are summarized and compared in [106–108].

The problem of identification of a moving load is not equivalent to a deconvolution, but it still can be expressed in the form of a linear integral equation with a weakly singular kernel. As such, it is inevitably ill-conditioned [109–112], which seems to be the main factor that decreases the accuracy of the identification results. In order to improve the accuracy, several regularization techniques have been investigated and adapted for the inverse computation, including the truncated singular value decomposition (TSVD) [113] and the Tikhonov regularization, which is applied either directly [114, 115] or coupled with the dynamic programming approach [69, 116, 117]. The optimum value of the regularization parameter seems to be sensitive to the properties of the vehicle and the bridge; see [118, 119] for a discussion of this problem and for a method named the updated static component technique, which extracts the static component of the load and iteratively identifies only its dynamic component.

2.1.3 Aims and techniques

In [73], Adams and Doyle postulate several attributes that a load identification method should feature to be usable in practice. These attributes can be summarized into the three following points:

1. The method should address the inherent ill-conditioning of load identification problems.
2. From a computational cost aspect, the method should have a scalability similar to forward problems.
3. The method should allow for possibly general setups with respect to the structure, the excitations and the instrumentation.

The problem of ill-conditioning of inverse problems is well-known, widely discussed in literature and effectively handled by techniques of numerical regularization, see Subsection A.3.2. It should be however noted that the typically used regularization criteria are based on the ℓ^2 norm and tend to distribute the identified load evenly among all the DOFs and time instances, which might not be well-suited to typical load characteristics; see Subsection 2.4.1.2 for other possible criteria. The other two postulates are less generally acknowledged.

In the same paper ([73], see also Doyle [74] and Uhl [69]), Adams and Doyle propose a method that addresses their three postulates: (1) The method incorporates the Tikhonov regularization. (2) A dynamic programming approach is employed to reduce the time complexity to linear with respect to the number of the time steps, and (3) the approach of the finite element (FE) analysis is used to model the setup in a possibly general way. However, even this approach seems to have two important drawbacks:

1. However general is the approach of the FE method, a FE model (as any other physical parametric numerical model) of a real-world structure is, in fact, an additional abstraction layer between the actual structure and the identification procedure. Such a model requires a laborious stage of initial model updating, which for complex structures can be difficult and time-consuming.
2. In the case of multiple independently loaded DOFs, the method proposed in [73], as well as most other methods, use a large number of sensors in order to ensure the uniqueness of identification. Such a rich instrumentation is often not feasible in practice, and it is not in line with the postulate of the generality of the setup.

This chapter describes an approach that aims to address both of the above problems:

1. The problem of updating and a potential inadequacy of parametric numerical models is resolved by using a data-driven approach: the identification is performed based on a nonparametric model of the involved structure, which consists of a collection of impulse response functions. Such an approach is flexible, as the impulse responses can be either directly measured or generated from an updated parametric model, provided such a model is available and accurate enough. An inevitable cost is a larger-than-linear identification time with respect to the number of the time steps: the approach involves the singular value decomposition of a time-domain impulse response matrix, which might be of large dimensions. In such a case, scalability of the approach can be improved by a repetitive application in a moving time window, see the numerical and experimental examples in Section 6.2.

A similar data-driven approach is used in Chapter 4 for identification of structural modifications and inelastic impacts, as well as in Chapter 5 for substructure isolation and local monitoring.

2. More insight into the identification process is provided by distinguishing between the subspaces of *reconstructible* and *unreconstructible* components of the excitation load. Such an approach allows the underdetermined system, which arises in the case of a limited number of sensors, to be uniquely solved in the subspace of reconstructible loads. The unreconstructible subspace can be then used to construct an *observationally equivalent* excitation that optimally approximates the actual excitation. Compared to other methodologies, the approach described here is thus focused on using a limited instrumentation for identification of general dynamic loads, including loads of unknown locations as well as multiple and moving loads.

The next Section 2.2 formulates the problem. The two consecutive Sections 2.3 and 2.4 consider respectively the overdetermined and underdetermined discretized cases, which differ in the number of available sensors. In both cases the approach is aimed at identification of general dynamic loads of unknown locations, including simultaneous multiple impacts, distributed and moving loads. In the underdetermined case, this generality is attained at the cost of the uniqueness of identification, which is preserved only in the reconstructible subspace, while in the unerconstructible subspace it can only be assured by means of additional heuristic assumptions. These assumptions provide for the information that was lost in the measurement process due to the limited instrumentation (insufficient number of sensors) and masked by the measurement noise. The identi-

fication is formulated as the following optimization problem: find the excitation time-history that minimizes the discrepancy between modeled and measured responses and which is optimum according to an assumed heuristic criterion. The accuracy of identification is directly related to the number and placement of available sensors. There is a relatively large body of research in optimum sensor placement with the aim of accurate characterization of structural dynamic response, often in terms of modal coordinates, see [120, 121], or for optimum design of control systems, see [122, Chapter 7] and a review in [123]. However, it is not clear and far from obvious that the same optimality criteria should be used for the task of input identification. Astonishingly, the research on optimum sensor placement with respect to load identification seems to be very sparse. In fact, the author is aware of only two other researches devoted specifically to this problem [124, 125]. Thus, Section 2.5 formulates two complementary optimality measures and combines them in a single compound criterion. The importance of optimum sensor placement is illustrated in a numerical example in Section 2.6.

2.2 Problem formulation

First, the nonparametric model based on impulse response matrices is introduced and verified using a standard FE approach (Subsection 2.2.1). Then, in Subsections 2.2.2 and 2.2.3, it is used to formulate the direct problem and the inverse problem of load identification. Finally, certain practical problems are discussed in Subsection 2.2.4.

2.2.1 Impulse response matrices

The structures considered in this chapter are assumed to be spatially discretized and to satisfy the standard form of the equation of motion:

$$\mathbf{M}\ddot{\mathbf{u}}(t) + \mathbf{C}\dot{\mathbf{u}}(t) + \mathbf{K}\mathbf{u}(t) = \mathbf{p}(t). \quad (2.1a)$$

where \mathbf{M} , \mathbf{C} and \mathbf{K} denote the structural mass, damping and stiffness matrices that have forms suitable to the particular problem. The mass matrix \mathbf{M} is assumed to be nonsingular (all numerical examples in this book use a consistent mass matrix). The vector $\mathbf{p}(t)$ is the externally applied excitation force, and $\mathbf{u}(t)$ is the vector of the displacement response. The number of degrees of freedom (DOFs) is denoted by N_{dof} , so that \mathbf{M} , \mathbf{C} and \mathbf{K} are $N_{\text{dof}} \times N_{\text{dof}}$ matrices, while $\mathbf{u}(t)$ and $\mathbf{p}(t)$ are vectors of N_{dof} elements. Zero initial conditions are assumed,

$$\mathbf{u}(0^-) = \mathbf{0}, \quad \dot{\mathbf{u}}(0^-) = \mathbf{0}. \quad (2.1b)$$

In practice, the structure is usually excited in only a limited number N_r of its DOFs, $N_r \leq N_{\text{dof}}$. Placement of the excitations is encoded in the form of an $N_{\text{dof}} \times N_e$ zero-one matrix \mathbf{L}^f , which is called the load allocation matrix,

$$\mathbf{p}(t) = \mathbf{L}^f \mathbf{f}^0(t), \quad (2.2)$$

where $\mathbf{f}^0(t)$ is the N_e -element vector of the nonvanishing excitations. Similarly, the structural response $\mathbf{a}(t)$ is usually measured with a limited number N_r of sensors, $N_r < N_{\text{dof}}$. The sensors are assumed to be linear (displacement, strain, velocity or acceleration); their placement and types are encoded in three $N_r \times N_{\text{dof}}$ sensor placement matrices \mathbf{L}_0^a , \mathbf{L}_1^a and \mathbf{L}_2^a ,

$$\mathbf{a}(t) = \mathbf{L}_0^a \mathbf{u}(t) + \mathbf{L}_1^a \dot{\mathbf{u}}(t) + \mathbf{L}_2^a \ddot{\mathbf{u}}(t). \quad (2.3)$$

The methodology discussed in this chapter relies on a nonparametric model of the loaded structure, which is given in terms of the impulse response matrix. The above parametric formulation is used in the following only to introduce the nonparametric modeling methodology and to verify its validity.

2.2.1.1 Full impulse response matrices

By an analogy to the standard Green's function, the (full) impulse response matrix of a structure that satisfies (2.1a) is defined to be the solution to the following matrix equation:

$$\mathbf{M}\ddot{\mathbf{H}}(t) + \mathbf{C}\dot{\mathbf{H}}(t) + \mathbf{K}\mathbf{H}(t) = \delta(t)\mathbf{I}, \quad (2.4)$$

where $\delta(t)$ denotes the Dirac delta function (a unit impulse at $t = 0$), and \mathbf{I} is the $N_{\text{dof}} \times N_{\text{dof}}$ identity matrix. The solution $\mathbf{H}(t)$ to (2.4) is also an $N_{\text{dof}} \times N_{\text{dof}}$ matrix,

$$\mathbf{H}(t) = \begin{bmatrix} H_{11}(t) & H_{12}(t) & \cdots & H_{1N_{\text{dof}}}(t) \\ H_{21}(t) & H_{22}(t) & \cdots & H_{2N_{\text{dof}}}(t) \\ \vdots & \vdots & \ddots & \vdots \\ H_{N_{\text{dof}}1}(t) & H_{N_{\text{dof}}2}(t) & \cdots & H_{N_{\text{dof}}N_{\text{dof}}}(t) \end{bmatrix}, \quad (2.5)$$

whose each element $H_{ij}(t)$ denotes the displacement impulse response function, that is the displacement response in the i th structural DOF to a unit impulse excitation in the j th structural DOF. Notice that the impulse response matrix can be treated as a dynamic counterpart of the static compliance matrix. This analogy will become particularly clear in Subsection 2.2.2, where the matrix

$\mathbf{H}(t)$ is used in a simple linear operation of convolution to solve the direct problem.

The matrix $\mathbf{H}(t)$ is composed of displacement responses to unit impulses. It is thus often called the *displacement impulse response matrix*. The (full) velocity and acceleration impulse response matrices, $\dot{\mathbf{H}}(t)$ and $\ddot{\mathbf{H}}(t)$, can be defined by an analogy: they are respectively composed of the velocity and acceleration responses in all DOFs to unit impulses applied separately in all DOFs, $\dot{H}_{ij}(t)$ and $\ddot{H}_{ij}(t)$, $i, j = 1, 2, \dots, N_{\text{dof}}$. There are important differences between the displacement, velocity and acceleration impulse response matrices, which are mainly related to the impulsive excitation at $t = 0$ and which can be summarized as follows:

- The displacement does not change stepwise, and so $H_{ij}(t)$ is a continuous function. In particular, the structure is initially at rest, so that

$$\mathbf{H}(0) = \mathbf{0}. \quad (2.6)$$

- The force impulse is equal to the change in momentum,

$$\mathbf{I} = \mathbf{M} \left(\dot{\mathbf{H}}(0) - \dot{\mathbf{H}}(0^-) \right), \quad (2.7)$$

and the structure is initially at rest (see (2.1b)), so that

$$\dot{\mathbf{H}}(0^-) = \mathbf{0}, \quad \dot{\mathbf{H}}(0) = \mathbf{M}^{-1}, \quad (2.8)$$

that is the velocity impulse response is discontinuous at $t = 0$.

- Such a step change in velocity at $t = 0$ must correspond to an impulsive component in the acceleration impulse response, which can be stated explicitly in the following form:

$$\ddot{\mathbf{H}}(t) = \mathbf{M}^{-1}\delta(t) + \ddot{\mathbf{H}}_\delta(t), \quad (2.9a)$$

where $\ddot{\mathbf{H}}_\delta(t)$ is the nonimpulsive component of the response,

$$\ddot{\mathbf{H}}_\delta(t) := \begin{cases} \lim_{t \rightarrow 0^+} \ddot{\mathbf{H}}(t) & \text{if } t = 0, \\ \ddot{\mathbf{H}}(t) & \text{if } t \neq 0. \end{cases} \quad (2.9b)$$

2.2.1.2 Reduced impulse response matrix

Matrices $\mathbf{H}(t)$, $\dot{\mathbf{H}}(t)$ and $\ddot{\mathbf{H}}(t)$ are called *full* impulse response matrices, since they are $N_{\text{dof}} \times N_{\text{dof}}$, that is they relate the response in each DOF to an impulsive

excitation in each DOF. Such full matrices can be obtained experimentally only for very simple systems. However, if only a limited number N_e of excitation forces and N_r of sensors is considered, then the respectively *reduced* $N_r \times N_e$ impulse response matrix $\mathbf{B}^0(t)$ is more convenient to use. It is defined through the following operation:

$$\mathbf{B}^0(t) := (\mathbf{L}_0^a \mathbf{H}(t) + \mathbf{L}_1^a \dot{\mathbf{H}}(t) + \mathbf{L}_2^a \ddot{\mathbf{H}}(t)) \mathbf{L}^f. \quad (2.10)$$

If an acceleration sensor is used, the reduced impulse response matrix can contain an impulsive term. In an analogy to (2.9), it can be stated explicitly:

$$\mathbf{B}^0(t) = \mathbf{L}_2^a \mathbf{M}^{-1} \mathbf{L}^f \delta(t) + \mathbf{B}_\delta^0(t), \quad (2.11a)$$

where $\mathbf{B}_\delta^0(t)$ is the nonimpulsive component,

$$\mathbf{B}_\delta^0(t) = (\mathbf{L}_0^a \mathbf{H}(t) + \mathbf{L}_1^a \dot{\mathbf{H}}(t) + \mathbf{L}_2^a \ddot{\mathbf{H}}_\delta(t)) \mathbf{L}^f. \quad (2.11b)$$

2.2.1.3 Example

Example 2.1 (impulse responses of an undamped oscillator). Consider a simple undamped oscillator of unit mass with the circular velocity ω , which is equipped with a displacement sensor and a velocity sensor. The full displacement, velocity and acceleration impulse response matrices are 1×1 and thus equal to the respective impulse response functions. They can be computed by solving

$$\ddot{H}(t) + \omega^2 H(t) = \delta(t), \quad (2.12)$$

which yields

$$H(t) = \Theta(t) \frac{1}{\omega} \sin \omega t, \quad (2.13a)$$

$$\dot{H}(t) = \Theta(t) \cos \omega t, \quad (2.13b)$$

$$\ddot{H}(t) = \delta(t) - \Theta(t) \omega \sin \omega t, \quad (2.13c)$$

$$\ddot{H}_\delta(t) = -\Theta(t) \omega \sin \omega t, \quad (2.13d)$$

where $\Theta(t)$ denotes the Heavyside theta function (a unit step at $t = 0$),

$$\Theta(t) = \begin{cases} 0 & \text{for } t < 0, \\ 1 & \text{for } t \geq 0. \end{cases} \quad (2.14)$$

The load allocation and sensors placement matrices are given by

$$\mathbf{L}^f = [1], \quad \mathbf{L}_0^a = \begin{bmatrix} 1 \\ 0 \end{bmatrix}, \quad \mathbf{L}_1^a = \begin{bmatrix} 0 \\ 1 \end{bmatrix}, \quad \mathbf{L}_2^a = \begin{bmatrix} 0 \\ 0 \end{bmatrix}. \quad (2.15)$$

The reduced impulse response matrix is 2×1 and given by

$$\mathbf{B}^0(t) = \Theta(t) \begin{bmatrix} \omega^{-1} \sin \omega t \\ \cos \omega t \end{bmatrix}. \quad (2.16)$$

Notice that the reduced impulse response matrix has the dimensions of 2×1 , which is larger than the dimensions of the full matrix. This is due to the simplicity of the example and unlikely to happen in practice.

2.2.2 Direct problem

As defined at the beginning of the chapter, the direct problem considered here is the problem of computing the response $\mathbf{a}(t)$ of a structure, given its input $\mathbf{f}^0(t)$ and a nonparametric model specified in terms of the reduced impulse response matrix $\mathbf{B}^0(t)$. The problem in this form is considered in Subsection 2.2.2.2. Before that, in the next subsection, the full formulation is used to derive and verify the formulas; it is based on the equation of motion (2.1a), the input in the form of the full excitation vector $\mathbf{p}(t)$, the model represented by the full impulse response matrix $\mathbf{H}(t)$ and the full response vector $\mathbf{u}(t)$ being the desired output.

2.2.2.1 Full formulation

For a structure initially at rest, the solution to the full direct problem, that is the structural response $\mathbf{u}(t)$ in all DOFs to a given full vector $\mathbf{p}(t)$ of the excitation forces, can be expressed in the form of the following convolution of the excitation with the full impulse response matrix:

$$\mathbf{u}(t) = \int_0^t \mathbf{H}(t - \tau) \mathbf{p}(\tau) d\tau. \quad (2.17a)$$

The velocity response is obtained by differentiating (2.17a),

$$\dot{\mathbf{u}}(t) = \mathbf{H}(0)\mathbf{p}(t) + \int_0^t \dot{\mathbf{H}}(t - \tau) \mathbf{p}(\tau) d\tau = \int_0^t \dot{\mathbf{H}}(t - \tau) \mathbf{p}(\tau) d\tau, \quad (2.17b)$$

where the first term has vanished due to (2.6). Another differentiation yields the acceleration response. The impulsive component $\mathbf{M}^{-1}\delta(t)$ in the acceleration impulse response $\ddot{\mathbf{H}}(t)$, see (2.9), results in the presence of a nonvanishing feed-through term, which by (2.8) equals $\mathbf{M}^{-1}\mathbf{p}(t)$,

$$\begin{aligned}\ddot{\mathbf{u}}(t) &= \dot{\mathbf{H}}(0)\mathbf{p}(t) + \int_0^t \ddot{\mathbf{H}}(t-\tau)\mathbf{p}(\tau) d\tau \\ &= \mathbf{M}^{-1}\mathbf{p}(t) + \int_0^t \ddot{\mathbf{H}}(t-\tau)\mathbf{p}(\tau) d\tau.\end{aligned}\tag{2.17c}$$

The impulsive component in the acceleration impulse response is already reflected in the feed-through term, so that it has no influence on the convolution term, which, due to (2.9b) and the definition of an improper integral, depends only on the nonimpulsive component $\ddot{\mathbf{H}}_\delta(t)$,

$$\int_0^t \ddot{\mathbf{H}}(t-\tau)\mathbf{p}(\tau) d\tau = \lim_{t_0 \rightarrow t^-} \int_0^{t_0} \ddot{\mathbf{H}}(t-\tau)\mathbf{p}(\tau) d\tau = \int_0^t \ddot{\mathbf{H}}_\delta(t-\tau)\mathbf{p}(\tau) d\tau.\tag{2.18}$$

The validity of the solution given by (2.17) can be verified by a direct substitution into the equation of motion (2.1a),

$$\begin{aligned}\mathbf{M}\ddot{\mathbf{u}}(t) + \mathbf{C}\dot{\mathbf{u}}(t) + \mathbf{K}\mathbf{u}(t) &= \mathbf{M} \left(\mathbf{M}^{-1}\mathbf{p}(t) + \int_0^t \dot{\mathbf{H}}(t-\tau)\mathbf{p}(\tau) d\tau \right) \\ &\quad + \mathbf{C} \int_0^t \dot{\mathbf{H}}(t-\tau)\mathbf{p}(\tau) d\tau + \mathbf{K} \int_0^t \mathbf{H}(t-\tau)\mathbf{p}(\tau) d\tau \\ &= \mathbf{p}(t) + \int_0^t \left(\mathbf{M}\ddot{\mathbf{H}}(t-\tau) + \mathbf{C}\dot{\mathbf{H}}(t-\tau) + \mathbf{K}\mathbf{H}(t-\tau) \right) \mathbf{p}(\tau) d\tau \\ &= \mathbf{p}(t) + \lim_{t_0 \rightarrow t^-} \int_0^{t_0} \delta(t-\tau)\mathbf{p}(\tau) d\tau \\ &= \mathbf{p}(t),\end{aligned}\tag{2.19}$$

where the definition of an improper integral and (2.4) have been used.

The operator notation allows (2.17) to be stated in a more concise form,

$$\mathbf{u}(t) = (\mathcal{H}\mathbf{p})(t), \quad (2.20a)$$

$$\dot{\mathbf{u}}(t) = (\dot{\mathcal{H}}\mathbf{p})(t), \quad (2.20b)$$

$$\begin{aligned} \ddot{\mathbf{u}}(t) &= \mathbf{M}^{-1}\mathbf{p}(t) + (\ddot{\mathcal{H}}_{\delta}\mathbf{p})(t) \\ &= (\ddot{\mathcal{H}}\mathbf{p})(t), \end{aligned} \quad (2.20c)$$

where \mathcal{H} , $\dot{\mathcal{H}}$ and $\ddot{\mathcal{H}}_{\delta}$ denote the matrix operators of convolution with the respective impulse response matrices and $\ddot{\mathcal{H}} = \mathbf{M}^{-1}\mathcal{I} + \ddot{\mathcal{H}}_{\delta}$, where \mathcal{I} is the identity operator.

2.2.2.2 Reduced formulation

The corresponding formulas for the reduced version of the direct problem can be obtained by using (2.2) in (2.20) in place of the full excitation vector $\mathbf{p}(t)$, and then by substituting the result into (2.3). This yields

$$\begin{aligned} \mathbf{a}(t) &= (\mathbf{L}_0^a \mathcal{H} \mathbf{L}^f \mathbf{f}^0)(t) + (\mathbf{L}_1^a \dot{\mathcal{H}} \mathbf{L}^f \mathbf{f}^0)(t) \\ &\quad + \mathbf{L}_2^a \mathbf{M}^{-1} \mathbf{L}^f \mathbf{f}^0(t) + (\mathbf{L}_2^a \ddot{\mathcal{H}}_{\delta} \mathbf{L}^f \mathbf{f}^0)(t), \end{aligned} \quad (2.21)$$

which, by (2.11) and the definition of the operators \mathcal{H} , $\dot{\mathcal{H}}$, $\ddot{\mathcal{H}}$ and the improper integral, reduces to

$$\begin{aligned} \mathbf{a}(t) &= \mathbf{G}\mathbf{f}^0(t) + (\mathcal{B}_{\delta}^0 \mathbf{f}^0)(t) \\ &= (\mathcal{B}^0 \mathbf{f}^0)(t), \end{aligned} \quad (2.22a)$$

where the matrix \mathbf{G} represents the feed-through term,

$$\mathbf{G} = \mathbf{L}_2^a \mathbf{M}^{-1} \mathbf{L}^f, \quad (2.22b)$$

the matrix operator \mathcal{B}_{δ}^0 corresponds to the convolution with the reduced impulse response matrix $\mathbf{B}_{\delta}^0(t)$,

$$\mathcal{B}_{\delta}^0 = (\mathbf{L}_0^a \mathcal{H} + \mathbf{L}_1^a \dot{\mathcal{H}} + \mathbf{L}_2^a \ddot{\mathcal{H}}_{\delta}) \mathbf{L}^f, \quad (2.22c)$$

and $\mathcal{B}^0 = \mathbf{G}\mathcal{I} + \mathcal{B}_{\delta}^0$. Due to the presence of \mathbf{L}_2^f , the feed-through matrix \mathbf{G} can be nonvanishing only if accelerometer sensors are used.

In the integral notation, (2.22a) takes the following form:

$$\mathbf{a}(t) = \mathbf{G}\mathbf{f}^0(t) + \int_0^t \mathbf{B}^0(t-\tau)\mathbf{f}^0(\tau) d\tau, \quad (2.23)$$

where, as in (2.17c), the possible impulsive component in $\mathbf{B}^0(t)$ is reflected in the feed-through term, so that it has no influence on the convolution term, which depends only on the nonimpulsive component $\mathbf{B}_\delta^0(t)$,

$$\begin{aligned} \int_0^t \ddot{\mathbf{B}}^0(t-\tau)\mathbf{p}(\tau) d\tau &= \lim_{t_0 \rightarrow t^-} \int_0^{t_0} \ddot{\mathbf{B}}^0(t-\tau)\mathbf{p}(\tau) d\tau \\ &= \int_0^t \ddot{\mathbf{B}}_\delta^0(t-\tau)\mathbf{p}(\tau) d\tau. \end{aligned} \quad (2.24)$$

2.2.3 Inverse problem

The inverse problem of load identification is the problem of identifying the unknown excitation forces $\mathbf{f}^0(t)$, given the reduced impulse response matrix $\mathbf{B}^0(t)$ (or, equivalently, the corresponding operator \mathcal{B}^0), which is in fact a reduced nonparametric model of the structure, and the vector of sensor measurements $\mathbf{a}^M(t)$. The unknown excitation is identified by comparing the structural response $\mathbf{a}(t)$ modeled by (2.23) with the actually measured response $\mathbf{a}^M(t)$ and finding such a vector $\mathbf{f}^0(t)$ that makes them equal. This yields the following equation:

$$\begin{aligned} \mathbf{a}^M(t) &= \mathbf{G}\mathbf{f}^0(t) + \int_0^t \mathbf{B}^0(t-\tau)\mathbf{f}^0(\tau) d\tau \\ &= \mathbf{G}\mathbf{f}^0(t) + (\mathcal{B}_\delta^0\mathbf{f}^0)(t) \\ &= (\mathcal{B}^0\mathbf{f}^0)(t), \end{aligned} \quad (2.25)$$

which is a linear system of Volterra integral equations with a continuous or weakly singular kernel, see Definition A.10. A theoretically important, even if idealized case occurs if the feed-through matrix \mathbf{G} is square and nonsingular. The problem of identification is then equivalent to solving

$$\mathbf{G}^{-1}\mathbf{a}^M(t) = \mathbf{f}^0(t) + \mathbf{G}^{-1}(\mathcal{B}_\delta^0\mathbf{f}^0)(t), \quad (2.26)$$

which is a linear system of Volterra integral equations of the second kind, and as such, it is well-posed and uniquely solvable for every measurement vector $\mathbf{a}^M(t)$, see Theorem A.16. The identification is usually performed in a certain time interval $t \in [0, T]$, where T is the total measurement time.

For reasons discussed in Subsection 2.2.4.1, only first kind Volterra equations (2.29) might be encountered in practice. Moreover, only discretized versions of (2.25) or (2.26) are used in real applications, as discussed in Subsection 2.2.4.2. They are both extremely ill-conditioned and can be numerically treated in a similar way, see Sections 2.3, 2.4 and 2.5.

2.2.4 Practical considerations

The inverse problem, as formulated in Subsection 2.2.3, relies on two following assumptions:

1. The reduced impulse response matrix $\mathbf{B}^0(t)$ is available.
2. The time is continuous.

Both assumptions are hard to justify in practice, and so the formulation should be respectively modified to take it into account.

2.2.4.1 Experimental quasi impulsive excitations

The reduced impulse response matrix $\mathbf{B}^0(t)$ is composed of the responses to impulsive excitations. If an updated parametric model of the considered structure is unavailable to perform numerical simulations, these responses must be measured experimentally. However, an ideal impulse excitation is impossible to apply and so the exact impulse responses cannot be obtained. Nevertheless, it is still possible to measure the responses $B_{ij}(t)$ of the considered sensors, $i = 1, \dots, N_r$, to any quasi impulsive excitation $q_j(t)$, $j = 1, \dots, N_e$, which is technically feasible and easy to apply (for example with a modal hammer). These responses compose the reduced *quasi impulse response matrix* $\mathbf{B}(t)$. The quasi impulsive excitations are assumed to vanish for $t < 0$, that is $q_j(t) = 0$ and $\mathbf{B}(t) = \mathbf{0}$ for $t < 0$.

The reduced quasi impulse response matrix $\mathbf{B}(t)$ constitutes a nonparametric model of the structure that is reduced with respect to the considered placement of sensors and excitations, which is exactly the same as in the case of the reduced impulse response matrix $\mathbf{B}^0(t)$, but $\mathbf{B}(t)$ is additionally reduced also with respect to the experimentally applied quasi impulsive excitations $q_j(t)$.

Direct problem. The reduced impulse response matrix $\mathbf{B}^0(t)$ can be used to express the sensor response to any excitation, while the reduced quasi impulsive matrix $\mathbf{B}(t)$ can be used to express the response to an excitation only if it can be expressed (as a convolution) in terms of the quasi impulsive excitations $q_j(t)$. That is, if the excitations $f_j^0(t)$ can be expressed for all $j = 1, \dots, N_e$ in the following form:

$$f_j^0(t) = \int_0^t q_j(t - \tau) f_j(\tau) d\tau, \quad t \in [0, T], \quad (2.27a)$$

where $f_j(t)$ are certain unknown functions, or, in the operator notation, if the excitation vector $\mathbf{f}^0(t)$ satisfies

$$\mathbf{f}^0(t) = (\mathcal{Q}\mathbf{f})(t), \quad (2.27b)$$

where \mathcal{Q} denotes the diagonal matrix convolution operator that corresponds to (2.27a) collected for all $j = 1, \dots, N_e$, then the sensor response to $\mathbf{f}^0(t)$ can be obtained through a substitution of (2.27b) into (2.22a). This yields

$$\mathbf{a}(t) = (\mathcal{B}\mathbf{f})(t), \quad t \in [0, T], \quad (2.28a)$$

where the matrix operator \mathcal{B} ,

$$\begin{aligned} \mathcal{B} &= \mathbf{G}\mathcal{Q} + \mathcal{B}_\delta^0\mathcal{Q} \\ &= \mathcal{B}^0\mathcal{Q}, \end{aligned} \quad (2.28b)$$

corresponds to the convolution with the experimentally measured quasi impulse responses $B_{ij}(t)$ to the actually applied quasi impulsive excitations $q_j(t)$, that is

$$\mathbf{a}(t) = \int_0^t \mathbf{B}(t - \tau)\mathbf{f}(\tau) d\tau, \quad t \in [0, T]. \quad (2.28c)$$

Technically speaking, as a result of limitations of instrumentation, the space of considered excitations is restricted to the range of the matrix integral operator \mathcal{Q} . In practice, the quasi impulsive excitations can be generated by a modal hammer and have then the form of narrow diffuse peaks. Then the operator \mathcal{Q} effectively corresponds to a low-pass filter with a relatively high cut-off level that slightly limits the frequency content of the considered excitations; in practice, such a limitation might be numerically beneficial due to the well-known stronger ill-conditioning of high frequency components in deconvolution-type problems [111, 126].

Inverse problem. Similar as in Subsection 2.2.3, solving the inverse problem amounts to comparing the experimentally measured response $\mathbf{a}^M(t)$ to the response modeled with (2.28a), finding the function $\mathbf{f}(t)$ that solves the resulting equation, and finally computing the corresponding excitation by (2.27b). As a result, the two crucial equations in this case are:

$$\mathbf{a}^M(t) = (\mathcal{B}\mathbf{f})(t), \quad (2.29a)$$

$$\mathbf{f}^0(t) = (\mathcal{Q}\mathbf{f})(t). \quad (2.29b)$$

In the considered case, the experimentally applied excitations $q_j(t)$ are only quasi impulsive and not impulsive, so that the resulting quasi impulse response matrix $\mathbf{B}(t)$ contains no impulsive terms, and (2.29) is a linear system of Volterra integral equations of the first kind. However, notice that if the exact impulse responses are known (or a parametric structural model is available for simulations), then $\mathcal{Q} = \mathcal{I}$, $\mathbf{f}^0(t) = \mathbf{f}(t)$ and (2.29) reduces to (2.25).

2.2.4.2 Time discretization

In applications, the measurement process discretizes the responses by sampling them at equally spaced time instances t_1, \dots, t_{N_t} . Similarly, numerically simulated solution is also advanced in discrete time steps. In practice, the impulse response functions will be thus discrete, whether obtained from measurements or from numerical simulations, so that (2.29) should be discretized with respect to time. Due to the discrete nature of measurements and impulse responses, the quadrature discretization method is appropriate, see Subsection A.2.3.1. For the first equation, (2.29a), the method yields N_t discrete linear systems that all share the same unknowns $f_i(t_k)$,

$$\mathbf{a}^M(t_k) = \sum_{l=1}^k \alpha_{kl} \mathbf{B}(t_k - t_l) \mathbf{f}(t_l), \quad k = 1, \dots, N_t, \quad (2.30)$$

where α_{kl} are quadrature weights and N_t is the number of time steps. All these systems can be merged together and stated in the form of a single large matrix linear equation. Together with a similarly discretized (2.29b), they read

$$\mathbf{a}^M = \mathbf{B}\mathbf{f}, \quad (2.31a)$$

$$\mathbf{f}^0 = \mathcal{Q}\mathbf{f}, \quad (2.31b)$$

where the vector \mathbf{a}^M collects for all time steps the discrete measurements of all sensors, and the vectors \mathbf{f} and \mathbf{f}^0 collect the discretized convolution function

$\mathbf{f}(t)$ and the excitations in all potential excitation points, respectively. With a proper ordering of the components of these vectors, the matrix \mathbf{B} in (2.31a) takes the form of a large structured matrix: it is an $N_r N_t \times N_e N_t$ block matrix with Toeplitz blocks, where each block is square ($N_t \times N_t$), lower triangular and relates the discrete response of a single sensor to the discrete excitation in a single excitation point, $[B_{ij}(t_k - t_l)]_{k,l}$, see an example in Fig. 2.3. As mentioned in the previous subsection, if the discrete impulse responses are obtained from numerical simulations or by deconvolving the measurements, then $\mathbf{Q} = \mathbf{I}$ and $\mathbf{f}^0(t) = \mathbf{f}(t)$.

Matrix \mathbf{B} is dense, even if it is structured, and the numbers of equations and unknowns are both proportional to the number N_t of the time steps. If the time discretization is dense or a longer sampling time T is used, the system can become prohibitively large and hardly manageable computationally. However, if $\mathbf{Q} = \mathbf{I}$ and a (piecewise) continuity of excitations is expected, then the time discretization can be often assumed to be dense enough as to allow the load to be effectively approximated by splines or wavelets, load shape functions [56, 60], etc. This would reduce the numerical costs and improve the numerical conditioning. Equations (2.31) take then the following form:

$$\mathbf{a}^M = \mathbf{B}\mathbf{N}\boldsymbol{\alpha}, \quad (2.32a)$$

$$\mathbf{f}^0 \approx \mathbf{N}\boldsymbol{\alpha}, \quad (2.32b)$$

where $\mathbf{f}^0 = \mathbf{f}$ and the columns of the matrix \mathbf{N} contain the approximating functions and the approximating coefficients $\boldsymbol{\alpha}$ are far fewer in number than the original unknowns \mathbf{f}^0 .

2.2.4.3 Regularization and numerical solution

Equation (2.29a) is usually of the first kind, so that solving a load identification problem amounts theoretically to applying an (approximate) inverse of a compact integral operator. Since the inverse of such an operator cannot be bounded (Theorem A.7), the original continuous-time identification problem is inherently ill-posed, see Subsection A.2.2.1. Consequently, its discretized version (2.31a) has a seemingly contradictory property: the finer time discretization is used, the more ill-conditioned they become. As a result, a naive direct solution is hardly possible, unless the considered setup is extremely simplistic. In practice, the discretized system is always extremely ill-conditioned [127], even in the idealized case of the second kind equation (2.26), and as a rule, a robust numerical regularization technique is necessary, see [67, 109–112, 128–132] or a short overview in Subsection A.3.2.

This book uses the following three general schemes of numerical solution of (2.31), which have significantly different properties in terms of their time complexity; two of them are based on well-known approaches of numerical regularization. In the following, the time complexities are assessed under the assumption that the decisive factor is the number N_t of the time steps, so that $N_r \ll N_t$ and $N_e \ll N_t$.

Conjugate gradient least squares (CGLS). If the system is overdetermined, which depends on the number of excitations and sensors that provide independent measurements (and possible additional a priori assumptions as in (2.35)), and the number of time steps is relatively large, the time-domain iterative approach of the CGLS method is used [111, 128]. The CGLS method has well-known regularizing properties, and it is also relatively fast and convenient in implementation. The number of iterations N_{iter} depends on the spectral characteristics of the excitation and the measurement noise level, and it plays the role of the regularization parameter (well-conditioned low frequency components of the excitation are extracted before the ill-conditioned high-frequency components); as a rule, it is significantly smaller than the dimensions of the system, see [109–111, 126]. Moreover, the system matrix \mathbf{B} is used in the algorithm only in the form of matrix–vector multiplications, and as a structured matrix it can be stored in memory in a reduced form, so that the multiplications can be quickly computed by embedding the Toeplitz submatrices of \mathbf{B} in larger circulant matrices and using the fast Fourier transform (FFT) in time $O(N_t \log N_t)$ instead of $O(N_t^2)$, see [133]. As a result, the overall time complexity is $O(N_{\text{iter}} N_t \log N_t)$.

Deconvolution in frequency domain. In a few suitable cases (Sections 4.3 and 5.5), the overdetermined system is solved in frequency domain, which significantly improves the computational efficiency, because (2.31a) reduces then to a series of N_t small independent systems ($N_r \times N_e$), so that the overall time complexity is $O(N_t \log N_t)$ and a larger number of time steps N_t can be then used. However, this approach does not offer such a direct control over the level of numerical regularization as the other two approaches (CGLS, SVD), so that serious inaccuracies related to the spectral leakage of the finite length FFT are often introduced, and a proper selection of the windowing function and the window decay rate is extremely important.

Singular value decomposition (SVD). In other cases, the SVD of the matrix \mathbf{B} is performed [128]. If the system is underdetermined, the SVD allows the reconstructible and unreconstructible excitation subspaces to be determined and

separately analyzed; it is also required by the proposed criteria of sensor placement optimality. The time complexity of computing the SVD is $O(N_t^3)$ [133], so that it is a numerically costly operation, which can be applied only in cases of relatively short time intervals. If an analysis in a longer time interval is necessary, it might be pursued using a moving time window technique, as in Section 6.2. However, for a given system, the SVD needs to be computed only once, and each subsequent identification uses the already computed decomposition and it is thus an order of magnitude quicker.

2.3 Overdetermined case

If the discretized (2.31a) is not underdetermined, it has a unique least squares solution, which can be found by minimizing the norm of the residuum of the system. The underdeterminacy depends on many factors, such as the topology of the structure as well as the number, placement and types of available sensors, and for large matrices it is not easy to be quickly verified in practice. However, as a rule of thumb, the equation might be supposed to have a unique least squares solution, if all of the following general conditions are satisfied:

1. There are at least as many sensors as excitations ($N_r \geq N_e$) in order to ensure that the equations are not fewer in number than the unknowns.
2. The sensors are placed reasonably close to the excitations, to ensure a high signal-to-noise ratio.
3. The sensors are placed not too close to each other, to make their measurements independent.

The unique least-squares solution can be computed directly by using the Moore–Penrose pseudoinverse of the system matrix \mathbf{B} ,

$$\mathbf{B}^+ = (\mathbf{B}^T \mathbf{B})^{-1} \mathbf{B}^T. \quad (2.33)$$

The pseudoinverse can be also computed via the singular value decomposition of the matrix \mathbf{B} [128]. The SVD also allows too small singular values to be directly truncated, which is a common regularization technique (TSVD). However, as the system matrix is usually very large, a quicker and less memory-consuming way is to use a regularizing iterative method. The CGLS method¹ minimizes

¹An alternative name used for the CGLS method is the method of conjugate gradient normal equations (CGNE).

the norm of the residuum of (2.31) by using the conjugate gradient iterations to solve the associated normal equation,

$$\mathbf{B}^T \mathbf{a}^M = \mathbf{B}^T \mathbf{B} \mathbf{f}. \quad (2.34)$$

The CGLS seems to be appropriate, as it quickly converges and has very good regularizing properties, see [128, Chapter 11]. A comprehensive discussion of this and other iterative solvers for Toeplitz systems can be found in [134], see also [109, 111]. In these methods, the number of iterations usually plays the role of the regularization parameter: the more iterations, the less regularized is the solution. As a result, the iteration has to be stopped after a certain number of steps. If the CGLS iteration is stopped too early, the computed solution is inaccurate due to the still too large residuum of (2.34) or (2.31a); if it is stopped too late, the solution is inaccurate due to the ill-conditioning and amplification of the measurement errors. Thus, a proper termination condition is crucial. As it is not always easy to be properly formulated, sometimes hybrid methods are advocated [109, 128], which compute the least squares solution of the following augmented system:

$$\begin{bmatrix} \mathbf{B} \\ \alpha \mathbf{TQ} \end{bmatrix} \mathbf{f} = \begin{bmatrix} \mathbf{a}^M \\ 0 \end{bmatrix}, \quad (2.35)$$

where $\alpha \geq 0$ is the Tikhonov regularization coefficient that controls the regularization level. The matrix \mathbf{T} is usually the identity matrix of appropriate dimensions, but, in order to account for smoother loads, it can be also the matrix of the first or second differences with respect to time and/or space. A common method of assigning a value to the regularization parameter, whether it is α or the number of the iterations, is the L-curve technique [67, 111, 135]. The rest of this section contains a concise derivation of the classic version of the CGLS optimization algorithm as applied to the inverse problem of load identification that is considered here. Notice that there are many alternative formulations, which are mathematically equivalent in the exact arithmetic, but may have different properties in floating point arithmetics, as well as different time complexities and storage requirements [128, 136, 137].

The CGLS solution is retrieved iteratively by minimizing the norm of the residuum $\mathbf{r}(\mathbf{f})$ of either (2.31a) or (2.35). In both cases, the objective function can be stated as

$$F(\mathbf{f}) = \frac{1}{2} \|\mathbf{r}(\mathbf{f})\|^2, \quad \mathbf{r}(\mathbf{f}) := \mathbf{a}^M - \mathbf{B}\mathbf{f}, \quad (2.36)$$

where either the original matrix \mathbf{B} and vector \mathbf{a}^M or their augmented versions (2.35) are used. The gradient and the (positive semidefinite) Hessian of the

objective function with respect to the excitation vector \mathbf{f} can be computed as

$$\nabla F(\mathbf{f}) = -\mathbf{B}^T \mathbf{r}(\mathbf{f}), \quad \nabla^2 F(\mathbf{f}) = \mathbf{B}^T \mathbf{B}. \quad (2.37)$$

The optimization starts with the first approximation \mathbf{f}_0 (which may be equal to $\mathbf{0}$) and proceeds iteratively according to

$$\mathbf{f}_{n+1} := \mathbf{f}_n + s_n \Delta \mathbf{f}_n, \quad (2.38)$$

where $s_n \in \mathbb{R}$ minimizes the objective function $F(\mathbf{f}_n + s_n \Delta \mathbf{f}_n)$ along the direction of optimization $\Delta \mathbf{f}_n$, which is computed as a certain linear combination of the steepest descent direction $-\nabla F$ and the direction of optimization from the previous iteration:

$$\Delta \mathbf{f}_0 := \mathbf{B}^T \mathbf{r}(\mathbf{f}_0), \quad (2.39a)$$

$$\Delta \mathbf{f}_n := \mathbf{B}^T \mathbf{r}(\mathbf{f}_n) + \eta_{n-1} \Delta \mathbf{f}_{n-1}. \quad (2.39b)$$

The combination coefficient $\eta_{n-1} \in \mathbb{R}$ is chosen in such a way that the directions $\Delta \mathbf{f}_n$ and $\Delta \mathbf{f}_{n-1}$ are conjugate with respect to the Hessian,

$$\Delta \mathbf{f}_n^T (\mathbf{B}^T \mathbf{B}) \Delta \mathbf{f}_{n-1} = 0, \quad (2.40)$$

which, together with (2.39a), automatically ensures that all the directions of optimization are conjugate, see [128, 137]. The result of this conjugacy and the whole rationale behind the conjugate gradient method is that, in each iteration, \mathbf{f}_n is the minimum in the subspace spanned by all the previous directions of optimization, $\Delta \mathbf{f}_0, \dots, \Delta \mathbf{f}_{n-1}$, or, equivalently (see (2.39) and (2.37)), in the subspace spanned by all the gradients $-\mathbf{B}^T \mathbf{r}(\mathbf{f}_0), \dots, -\mathbf{B}^T \mathbf{r}(\mathbf{f}_{n-1})$. Consequently, the gradient at \mathbf{f}_n is orthogonal to this subspace, and the following two formulas hold:

$$(\mathbf{B}^T \mathbf{r}(\mathbf{f}_n))^T \Delta \mathbf{f}_{n-1} = 0, \quad (2.41)$$

$$(\mathbf{B}^T \mathbf{r}(\mathbf{f}_{n+1}))^T \mathbf{B}^T \mathbf{r}(\mathbf{f}_n) = 0, \quad (2.42)$$

which state that the gradient in a given iteration is orthogonal to the previous direction of optimization as well as to the gradient in the next iteration.

Left-multiplication of (2.39b) by $\mathbf{B}^T \mathbf{r}(\mathbf{f}_n)$ transposed yields, due to the orthogonality (2.41),

$$(\mathbf{B}^T \mathbf{r}(\mathbf{f}_n))^T \Delta \mathbf{f}_n = \|\mathbf{B}^T \mathbf{r}(\mathbf{f}_n)\|^2. \quad (2.43)$$

The objective function is quadratic. Therefore, due to (2.37) and (2.43),

$$F(\mathbf{f}_{n+1}) = F(\mathbf{f}_n + s_n \Delta \mathbf{f}_n) = F(\mathbf{f}_n) - s_n \|\mathbf{B}^T \mathbf{r}(\mathbf{f}_n)\|^2 + \frac{1}{2} s_n^2 \|\mathbf{B} \Delta \mathbf{f}_n\|^2, \quad (2.44)$$

and this is a convex quadratic function with respect to s_n , which has the minimum at

$$s_n = \frac{\|\mathbf{B}^T \mathbf{r}(\mathbf{f}_n)\|^2}{\|\mathbf{B} \Delta \mathbf{f}_n\|^2}. \quad (2.45)$$

Substitution of (2.39b) into the conjugacy criterion (2.40) yields

$$\eta_n = -\frac{(\mathbf{B} \Delta \mathbf{f}_n)^T \mathbf{B} \mathbf{B}^T \mathbf{r}(\mathbf{f}_{n+1})}{\|\mathbf{B} \Delta \mathbf{f}_n\|^2}. \quad (2.46)$$

The iteration formula (2.38) leads to the following iteration for the residual vectors:

$$\mathbf{r}(\mathbf{f}_{n+1}) = \mathbf{r}(\mathbf{f}_n) - s_n \mathbf{B} \Delta \mathbf{f}_n, \quad (2.47)$$

which, left-multiplied by $\mathbf{B} \mathbf{B}^T \mathbf{r}(\mathbf{f}_{n+1})$ transposed and due to (2.42), (2.45) and (2.46), finally yields

$$\eta_n = \frac{\|\mathbf{B}^T \mathbf{r}(\mathbf{f}_{n+1})\|^2}{\|\mathbf{B}^T \mathbf{r}(\mathbf{f}_n)\|^2}. \quad (2.48)$$

Flow of computations of the CGLS algorithm is outlined in Table 2.1. If the original unregularized (2.31a) is being solved, the stop condition for terminating the iterations has to be based on online analysis of the L-curve; otherwise, if the augmented (2.35) is used, the norm $\|\mathbf{r}\|$ of the residuum vector can be used for this purpose.

Notice that the most time-consuming operations in each loop are the calculations of the matrix-vector products $\mathbf{B} \Delta \mathbf{f}$ (response, line 1) and $\mathbf{B}^T \mathbf{r}$ (steepest descent, line 5), especially if the matrix \mathbf{B} is of large dimensions. However, such products can be relatively quickly computed by taking into account that the system matrix \mathbf{B} is a structured (block matrix with Toeplitz blocks). The fast Fourier transform can be thus used for accurate computations of matrix-vector products in frequency domain, which decreases the numerical costs from $O(N_r N_e N_t^2)$ to $O(N_r N_e N_t \log N_t)$ [133, 138]. This is a significant difference, as the number of time steps N_t in most applications can be expected to be much larger than the numbers of sensors and excitations, N_r and N_e .

Table 2.1. Flow of computations of the CGLS algorithm for load identification in the linear overdetermined case.

Initialization	
1) first approximation	$\mathbf{f} = \mathbf{f}_0$
2) residuum vector	$\mathbf{r} = \mathbf{a}^M - \mathbf{B}\mathbf{f}$
3) steepest descent direction	$\mathbf{d} = \mathbf{B}^T \mathbf{r}$
4) optimization direction	$\Delta\mathbf{f} = \mathbf{d}$
5) gradient norm	$d_1 = \mathbf{d}^T \mathbf{d}$
The loop	
1) response to $\Delta\mathbf{f}$	$\mathbf{q} = \mathbf{B}\Delta\mathbf{f}$
2) line minimum	$s = d_1 / \mathbf{q}^T \mathbf{q}$
3) update load vector	$\mathbf{f}^+ = s\Delta\mathbf{f}$
4) update residuum vector	$\mathbf{r}^- = s\mathbf{q}$
5) steepest descent direction	$\mathbf{d} = \mathbf{B}^T \mathbf{r}^-$
6) temporary storage	$d_2 = d_1$
7) gradient norm	$d_1 = \mathbf{d}^T \mathbf{d}$
8) combination coefficient	$\eta = d_1 / d_2$
9) update optimization direction	$\Delta\mathbf{f} = \mathbf{d} + \eta\Delta\mathbf{f}$

2.4 Underdetermined case

All research in indirect load identification of which the author is aware of deals with the overdetermined case only. However, in intended general practical applications, the discretized linear system (2.31a) will be usually severely underdetermined, that is there will be significantly fewer equations than unknowns. The reason is twofold:

1. In real-world applications the number of sensors is limited by practical reasons. Thus, unless a specific setup is considered, in many situations there will be much more potentially load-exposed DOFs than available sensors.
2. Even with a sufficiently large number of sensors, excessive ill-conditioning or a specific topology of the considered structure can decrease the numerical rank of the system matrix \mathbf{B} and make it effectively underdetermined or rank-deficient.

As the result, in the overdetermined case the generality of the identified excitation must be significantly limited. In literature, it is often assumed to be a single

stationary (or moving at a constant velocity) point-wise force, whose location is assumed to be known in advance or determined in an additional outer-loop nonlinear optimization; distributed, freely moving or multiple excitations are usually not considered. The approach proposed here aims to address the general underdetermined case directly and allows all general excitation patterns to be taken into account. However, in an underdetermined system part of the information is lost and unrecoverable from the measurements, and therefore such a generality is possible only at the cost of the uniqueness of identification, which can be attained by additional a priori assumptions only. Such assumptions can be used to complete the missing information by specifying expected or typical characteristics of the excitation.

In general, in the underdetermined case, the unknown discrete vector \mathbf{f} can be identified in two ways, which differ in their accuracies and numerical costs per single identification (in terms of computation time, memory storage, etc.):

Single-stage identification (Subsection 2.4.2). The simpler but less accurate approach, which transforms the underdetermined system (2.31a) into a larger overdetermined system by means of the mentioned additional assumptions (that may also have a regularizing effect on the solution). If the assumptions are based on the ℓ^2 norm, then the augmented system is linear and it can be solved using the CGLS method presented in Table 2.1; direct solution techniques are also possible, but they can be prohibitive in terms of the numerical costs. Otherwise, the augmented objective function can be minimized using standard optimization techniques.

Decomposition of excitation (Subsection 2.4.1), which is the more accurate approach. It makes use of the singular value decomposition of the matrix \mathbf{B} , which is a numerically costly operation, but needs to be performed only once irrespective of the number of the intended identifications. Thereupon, given a measured response vector \mathbf{a}^M , two complementary components of the corresponding excitation \mathbf{f}^0 can be relatively quickly identified: the reconstructible component and the unreconstructible component. The former is fully specified by the measurements, while the latter is related via \mathbf{Q} to the effective null space of \mathbf{B} and can be identified based on the additional a priori assumptions.

2.4.1 Decomposition of excitation

The system matrix \mathbf{B} , which is assumed here to be underdetermined, has a singular value decomposition, which is the finite-dimensional counterpart of the

singular value expansion (SVE) of the corresponding integral operator, see [110–112],

$$\mathbf{B} = \mathbf{U}\Sigma\mathbf{V}^T. \quad (2.49)$$

The matrices \mathbf{U} and \mathbf{V} are square and unitary,

$$\mathbf{U}^T\mathbf{U} = \mathbf{U}\mathbf{U}^T = \mathbf{I}, \quad \mathbf{V}^T\mathbf{V} = \mathbf{V}\mathbf{V}^T = \mathbf{I}. \quad (2.50)$$

The columns of \mathbf{U} constitute thus an orthonormal base in the space of discrete measurements, while the columns of \mathbf{V} form such a base for the space of vectors \mathbf{f} . The dimensions of \mathbf{U} and \mathbf{V} equal respectively the total number $N_r N_t$ of measurements (rows of \mathbf{B}) and the total number $N_e N_t$ of unknown excitations (columns of \mathbf{B}). The matrix Σ is a rectangular diagonal matrix of appropriate dimensions; its diagonal values σ_i are called the singular values of \mathbf{B} and are ordered nonincreasing. The SVD is unique up to the permutation of the singular values [139].

Due to the inherent ill-conditioning or ill-posedness of the considered inverse problem, the discretized system (2.31a) is, as a rule, extremely ill-conditioned. This is indicated by the fact that its singular values span across several orders of magnitude, see Subsection A.2.2.1. Numerical regularization is therefore necessary and, computed the SVD, it can be straightforwardly performed by zeroing too small singular values, which is an approach called the truncated singular value decomposition, see Subsection A.3.2. The threshold level is assumed here to be the expected relative measurement accuracy $\epsilon \geq 0$. In this way, the modified diagonal and system matrices Σ^ϵ , \mathbf{B}^ϵ are obtained and (2.49) takes the following regularized form:

$$\mathbf{B}^\epsilon = \mathbf{U}\Sigma^\epsilon\mathbf{V}^T. \quad (2.51)$$

In the idealized case of $\epsilon = 0$ (no measurement error), all singular values are preserved and $\mathbf{B}^\epsilon = \mathbf{B}$.

Let $\mathbb{F} = \mathbb{R}^{N_e N_t}$ denote the linear space of all vectors \mathbf{f} . Let split the matrix \mathbf{V} into two submatrices \mathbf{V}_1^ϵ and \mathbf{V}_2^ϵ ,

$$\mathbf{V} = [\mathbf{V}_1^\epsilon \ \mathbf{V}_2^\epsilon], \quad (2.52)$$

by including in \mathbf{V}_1^ϵ these columns of \mathbf{V} that correspond to singular values greater than ϵ . The columns of \mathbf{V}_1^ϵ and \mathbf{V}_2^ϵ span two orthogonal and complementary linear subspaces \mathbb{F}_1^ϵ and \mathbb{F}_2^ϵ of \mathbb{F} :

$$\mathbb{F}_1^\epsilon = \text{span } \mathbf{V}_1^\epsilon, \quad \mathbb{F}_2^\epsilon = \text{span } \mathbf{V}_2^\epsilon, \quad \mathbb{F} = \mathbb{F}_1^\epsilon \oplus \mathbb{F}_2^\epsilon. \quad (2.53)$$

Moreover, the columns of \mathbf{V}_2^ϵ correspond to the singular values $\sigma_i < \epsilon$ that vanish in \mathbf{B}^ϵ . Thus, \mathbb{F}_2^ϵ is the null space of \mathbf{B}^ϵ and

$$\mathbf{B}^\epsilon \mathbf{V}_2^\epsilon = \mathbf{0}. \quad (2.54)$$

As a result, the regularized system matrix \mathbf{B}^ϵ is a linear operator that represents the (discretized) measurement process, which effectively:

1. Transforms \mathbb{F} orthonormally by \mathbf{V} .
2. Uses Σ^ϵ to
 - (a) Irreversibly lose a part of the information by a projection onto \mathbb{F}_1^ϵ .
 - (b) Rescale the resulting subspace along the base directions by the remaining singular values.
3. Transforms the result orthonormally by \mathbf{U} .

Therefore, \mathbb{F}_1^ϵ is the *reconstructible* subspace of \mathbb{F} and the null space \mathbb{F}_2^ϵ is its *unreconstructible* subspace with respect to the regularized system matrix \mathbf{B}^ϵ . As a result, given the relative measurement accuracy $\epsilon \geq 0$, each vector $\mathbf{f} \in \mathbb{F}$ can be uniquely decomposed into a sum of two orthogonal components that belong to \mathbb{F}_1^ϵ and \mathbb{F}_2^ϵ :

$$\mathbf{f} = \mathbf{V}_1^\epsilon \mathbf{m}_1 + \mathbf{V}_2^\epsilon \mathbf{m}_2 = \mathbf{f}_R^\epsilon + \mathbf{V}_2^\epsilon \mathbf{m}_2. \quad (2.55)$$

Consequently, see (2.54),

$$\mathbf{B}^\epsilon \mathbf{f} = \mathbf{B}^\epsilon \mathbf{f}_R^\epsilon. \quad (2.56)$$

In other words, the first component in (2.55),

$$\mathbf{f}_R^\epsilon = \mathbf{V}_1^\epsilon \mathbf{m}_1, \quad (2.57)$$

is a linear combination of the columns of the matrix \mathbf{V}_1^ϵ ; it is thus uniquely *reconstructible* from the measurements \mathbf{a}^M . The second component, $\mathbf{V}_2^\epsilon \mathbf{m}_2$, is a linear combination of the columns of \mathbf{V}_2^ϵ and so it belongs to the null space of \mathbf{B}^ϵ . As a result, this component is *unreconstructible*: due to (2.54) all respective information is lost in the measurement process or masked by the measurement noise, and thus effectively not retained in the measurement vector \mathbf{a}^M .

In the above, the space \mathbb{F} of all vectors \mathbf{f} is decomposed into a sum of two complementary subspaces \mathbb{F}_1^ϵ and \mathbb{F}_2^ϵ . Due to (2.31b), the space of all considered excitation vectors \mathbf{f}^0 is given by $\mathbf{Q}\mathbb{F}$, and $\mathbf{Q}\mathbb{F}_1^\epsilon$ and $\mathbf{Q}\mathbb{F}_2^\epsilon$ are its *reconstructible* and *unreconstructible* subspaces. Consequently, each excitation vector \mathbf{f}^0 can be decomposed into a sum of two components, of which one is reconstructible from the measurements and the other is unreconstructible.

2.4.1.1 Reconstructible component

Assume that the (noisy) measurements \mathbf{a}^M and the regularized system matrix \mathbf{B}^ϵ are known. The unique regularized reconstructible component \mathbf{f}_R^ϵ of the corresponding vector \mathbf{f} is the minimum-norm solution of the regularized version of (2.31a). It can be directly computed as

$$\mathbf{f}_R^\epsilon = (\mathbf{B}^\epsilon)^+ \mathbf{a}^M. \quad (2.58)$$

The matrix $(\mathbf{B}^\epsilon)^+$ is the Moore–Penrose pseudoinverse of the regularized matrix \mathbf{B}^ϵ ,

$$(\mathbf{B}^\epsilon)^+ = \mathbf{V} (\boldsymbol{\Sigma}^\epsilon)^+ \mathbf{U}^T, \quad (2.59)$$

where the diagonal matrix $(\boldsymbol{\Sigma}^\epsilon)^+$ is computed from $\boldsymbol{\Sigma}^\epsilon$ by a transposition and replacement of all its nonzero elements by their reciprocals.

Alternatively, the regularized reconstructible component \mathbf{f}_R^ϵ can be also found by solving in the least square sense the system

$$\mathbf{a}^M = \mathbf{B}^\epsilon \mathbf{V}_1^\epsilon \mathbf{m}_1^\epsilon \quad (2.60)$$

using any suitable direct or iterative method, for example the CGLS technique described above for the overdetermined systems. Equation (2.60) is already regularized, hence the criterium for termination of iterations can be based on the norm of the residuum, without an additional Tikhonov regularization term. Given \mathbf{m}_1^ϵ , (2.57) can be used to compute \mathbf{f}_R^ϵ .

Finally, by (2.31b), given the regularized reconstructible component of \mathbf{f} , the equivalent regularized reconstructible component of the excitation vector \mathbf{f}^0 is equal to $\mathbf{Q}\mathbf{f}_R^\epsilon$.

2.4.1.2 Unreconstructible component

As confirmed by (2.54) and (2.56), given the regularized reconstructible component \mathbf{f}_R^ϵ , any linear combination of the columns of \mathbf{V}_2^ϵ can be added to \mathbf{f}_R^ϵ with no or a negligible² effect on the response \mathbf{a}^M . Therefore, all vectors of the form

$$\mathbf{f}(\mathbf{m}_2) = \mathbf{f}_R^\epsilon + \mathbf{V}_2^\epsilon \mathbf{m}_2, \quad (2.61)$$

where \mathbf{m}_2 is a vector of arbitrary coefficients, are valid solutions to (2.31a); by (2.31b), they all correspond to excitation vectors that are observationally indistinguishable.

²Negligible, that is below the assumed level ϵ of the measurement noise.

As a result, the choice of the particular vector of coefficients \mathbf{m}_2 and the corresponding excitation vector

$$\begin{aligned}\mathbf{f}^0(\mathbf{m}_2) &= \mathbf{Qf}(\mathbf{m}_2) \\ &= \mathbf{Qf}_R^\epsilon + \mathbf{QV}_2^\epsilon \mathbf{m}_2,\end{aligned}\tag{2.62}$$

must be based on additional criteria, which have to be formulated in advance, for example based on anticipated or typical characteristics of the excitation, such as nonnegativity, norm-minimality, smoothness, sparsity, etc.

Nonnegativity. Such a case seems to occur relatively often in practice, for example in identification of moving vehicular loads or impact type excitations; it is thus of practical significance. Such a criterion can be formalized by requiring that $\mathbf{f}^0(\mathbf{m}_2)$ has the minimum norm of its negative components, that is by minimizing the following objective function:

$$F_2(\mathbf{m}_2) := \frac{1}{2} \sum_i \left(f_i^0(\mathbf{m}_2) \mathbb{I}_{f_i^0(\mathbf{m}_2) < 0} \right)^2, \tag{2.63}$$

where $f_i^0(\mathbf{m}_2)$ is the i th component of the excitation vector $\mathbf{f}^0(\mathbf{m}_2)$ and \mathbb{I}_p denotes the indicator function,

$$\mathbb{I}_p := \begin{cases} 1 & \text{if } p \text{ is true,} \\ 0 & \text{otherwise.} \end{cases} \tag{2.64}$$

The objective function (2.63) has two important advantages:

1. It can be quickly computed together with its gradient.
2. It is a convex function with respect to \mathbf{m}_2 , so that each its local minimum is also a global minimum.

Norm-minimality, smoothness, etc. These criteria can be formalized, e.g., by requiring that \mathbf{m}_2 minimizes

$$F_2(\mathbf{m}_2) := \frac{1}{2} \|\mathbf{Tf}^0(\mathbf{m}_2)\|^2. \tag{2.65}$$

The result depends on the matrix \mathbf{T} , which, depending on the application, can be for example the matrix of the first or second differences with respect to time and/or space³ Minimization of $F_2(\mathbf{m}_2)$ is equivalent to computing the solution of

$$\mathbf{TQV}_2^\epsilon \mathbf{m}_2 = -\mathbf{TQf}_R^\epsilon \tag{2.66}$$

³It makes not much sense to select the identity matrix: the reconstructible component is orthogonal to the null space of \mathbf{B}^ϵ , and so if \mathbf{T} is the identity matrix, then the optimum excitation is obtained for $\mathbf{m}_2 = \mathbf{0}$.

in the least squares sense, which can be performed using the CGLS algorithm from Table 2.1 or even directly, provided the dimensions of the matrices make it feasible. In the latter case, see (2.33),

$$\mathbf{f}^0 = (\mathbf{I} - \mathbf{Q}\mathbf{V}_2^\epsilon (\mathbf{T}\mathbf{Q}\mathbf{V}_2^\epsilon)^+ \mathbf{T}) \mathbf{Q}\mathbf{f}_R^\epsilon. \quad (2.67)$$

Notice that the optimum excitation \mathbf{f}^0 is linearly dependent on the regularized reconstructible excitation component $\mathbf{Q}\mathbf{f}_R^\epsilon$ as well as on the measurement vector \mathbf{a}^M , see (2.58).

In both of the above cases, a scrupulous analysis would reveal that upper bounds should be in principle imposed on the moduli of the entries of \mathbf{m}_2 that correspond to the columns of \mathbf{V}_2^ϵ that do not belong to \mathbf{V}_2^0 . These columns correspond to very small positive singular values (less than ϵ) and represent the excitations that do influence the measurement vector \mathbf{a}^M , but below the assumed noise level. Such a formulation would require a constrained least squares problem to be solved to find \mathbf{m}_2 and the related optimum excitation.

Sparsity. The objective function (2.63) is based on the ℓ^2 norm of the vector $\mathbf{T}\mathbf{f}^0(\mathbf{m}_2)$. If $\mathbf{T} = \mathbf{I}$, then this norm prefers even distribution of the excitation in time and space over sparsity, which in many practical cases might be exactly the opposite of the expected characteristics of the load [80]. The requirement of sparsity might be formalized in terms of the “ ℓ^0 norm” (the number of nonvanishing elements), which however leads to NP-hard combinatorial optimization problems [140]. A solution commonly used in this case is the ℓ^1 norm. The corresponding optimization problem,

$$F_2(\mathbf{m}_2) := \|\mathbf{T}\mathbf{f}^0(\mathbf{m}_2)\|_1, \quad (2.68)$$

remains convex and it is thus numerically treatable, while it still seems to prefer sparse solutions [140].

2.4.2 Single-stage identification

In the single-stage identification approach, no distinction is made between the reconstructible and unreconstructible subspaces of the excitation space: both components are retrieved simultaneously. The numerically costly singular value decomposition is not required. However, this is at the expense of a higher numerical cost of each identification. The approach is simpler but generally less accurate, because both identified components are influenced by the a priori assumptions, while in the two-stage approach described above they influence only

the unreconstructible component (the reconstructible component is identified based only on the measurements).

The original system (2.31a) is assumed to be underdetermined and to have an infinite number of solutions. Thus the norm of its residuum, (2.36), does not have a strict minimizer. However, the squared norm of the residuum of the augmented system (2.35),

$$F(\mathbf{f}) = \frac{1}{2} \|\mathbf{a}^M - \mathbf{B}\mathbf{f}\|^2 + \frac{1}{2}\alpha \|\mathbf{TQf}\|^2, \quad (2.69)$$

includes also the Tikhonov term, which can be thought of as playing a double role:

1. Numerical regularization of the solution to alleviate the ill-conditioning of the matrix \mathbf{B} .
2. Supplying the additional information, which is used (in the place of the information lost due to underdetermination) in order to guarantee the uniqueness of identification.

Therefore, the unique solution can be found by a direct minimization of the augmented objective function (2.69), which corresponds to finding the least squares solution of (2.35) and can be performed by the CGLS method described in Table 2.1. Besides the Tikhonov term, the additional information can be supplied in other forms, for example by imposing soft nonnegativity constraints on \mathbf{f} , which amounts to minimizing

$$F(\mathbf{f}) = \frac{1}{2} \|\mathbf{a}^M - \mathbf{B}\mathbf{f}\|^2 + \frac{1}{2} \sum_i (f_i^0 \mathbb{I}_{f_i < 0})^2. \quad (2.70)$$

As discussed below (2.63), such a function is relatively easy to minimize.

2.5 Optimum sensor placement

The problem of accuracy is crucial for any strategy of load identification. It is related to the conditioning and determinacy of the discretized measurement operator \mathbf{B} . And they depends directly on the number and placement of the available sensors with respect to the points, in which the unknown excitations can occur. There is a relatively large bulk of research devoted to the problem of optimum sensor placement with respect to the objectives of optimum structural control, optimum characterization of structural dynamic response, and to a lesser extent of structural health monitoring, see, e.g., [120, 121, 123, 141–143],

[122, Chapter 7] or [144] for a related problem in identification of solidification parameters. Astonishingly, the objective of optimum identification of excitation loads seems to be relatively neglected. Even if it seems to be closely related to the previously mentioned objectives, it is intrinsically different and should not be automatically assumed to be equivalent.

In fact, the author is aware of only two other researches in the topic: Said and Staszewski use in [125] a genetic algorithm and the mutual information approach to find the optimum placement of sensors on a composite plate for the more basic purpose of detecting only the amplitude of a pointwise impact. In [124], Jacquelain *et al.* consider a continuous structure and the identification problem of a full time-history of an excitation load in a single sensor-single force (SISO) setting; a relation is observed between conditioning of the identification problem and certain characteristics of the frequency response function (alternate succession of resonances and antiresonances). This is an interesting, but still phenomenological and qualitative relation, which can be potentially used also in multi-sensor and multi-load (MIMO) cases in order to designate a limited-size discrete set of candidate sensor locations to choose from based on more quantitative optimality criteria. This section describes three such general estimates of the accuracy of identification; they have been originally proposed in [32].

Due to masking by measurement noise and possible underdetermination of (2.31), a part of the information about the actual excitation is completely lost in the measurement process and not retained in the measurements. The corresponding component of the excitation belongs to $\mathbf{Q}\mathbb{F}_2^\epsilon$, where \mathbb{F}_2^ϵ is the null space of the regularized measurement operator \mathbf{B}^ϵ , and it is thus unreconstructible: there is no way to identify it directly from the measurement, even if it can be computed (or, actually, rather *assumed*) using certain *a priori* criteria that express the anticipated characteristics of the excitation, see Section 2.4. Therefore, any accurate *a posteriori* accuracy measure is impossible. However, accuracy is associated with the reconstructible excitation subspace $\mathbf{Q}\mathbb{F}_1^\epsilon$ that depends directly on the number and placement of sensors. Accuracy can be thus *a priori* maximized by a proper distribution of the available sensors. The optimum distribution should ensure that $\mathbf{Q}\mathbb{F}_1^\epsilon$ is possibly large and informative with respect to certain criteria. In [32], the author proposes two such criteria, which are based either on the dimensionality of the reconstructible subspace for the noiseless case (via the correlated feature of conditioning of the matrix \mathbf{B}) or on its informative content, which is quantified in terms of the coincidence with a given set of expected or typical excitations. These criteria are found in numerical examples to be negatively correlated, hence they are combined in a compound

criterion, which can be seen as a single general a priori measure of the accuracy of identification.

In the following, sensor placement is denoted by π , which is a nonempty subset of $\{1, 2, \dots, N_{r_{\max}}\}$, where $N_{r_{\max}}$ is the number of all possible locations of a single sensor throughout the structure. The system matrix corresponding to sensor placement π is denoted by \mathbf{B}_π .

2.5.1 Criterion of conditioning

The conditioning criterion assigns to each sensor location π the following measure $q_1(\pi)$ of ill-conditioning of the corresponding system matrix \mathbf{B}_π :

$$q_1(\pi) := \log \frac{\sigma_{\max}(\mathbf{B}_\pi)}{\sigma_{\text{median}}(\mathbf{B}_\pi)}, \quad (2.71)$$

where $\sigma_{\max}(\mathbf{B}_\pi)$ and $\sigma_{\text{median}}(\mathbf{B}_\pi)$ denote respectively the maximum and the median singular values of \mathbf{B}_π .

Notice that the standard measure of conditioning of a matrix (its condition number) involves the minimum singular value instead of the median singular value. The median is used here, as in a floating-point arithmetic it is more reliable: computed minimum singular values of a significantly ill-conditioned matrix usually lie at a predefined cut-off level that is more related to the accuracy of the arithmetic used than to the matrix itself.

2.5.2 Criterion of informativity

In underdetermined systems, conditioning alone is not a sufficient measure of identification accuracy. The identification process can be very well-conditioned, but it is of no practical use, if identified excitations differ much from the actual excitations. Accuracy depends thus also on the *informativity* of the subspace of reconstructible excitations and, for each excitation, it can be quantified in terms of the distance between the excitation and its reconstructible component. The actual excitation is unknown, hence a general measure of informativity has to be defined with respect to a given set of N_l expected or typical unit excitations $\{\mathbf{f}_1, \mathbf{f}_2, \dots, \mathbf{f}_{N_l}\}$:

$$q_2(\pi) := \frac{1}{N_l} \sum_{i=1}^{N_l} \left\| \mathbf{f}_i^0 - \mathbf{f}_i^0|_{\mathbf{Q}\mathbb{F}_{\pi,1}^0} \right\|^2, \quad (2.72)$$

where $\mathbf{Q}\mathbb{F}_{\pi,1}^0$ is the subspace of reconstructible excitations for a given sensor placement π and at the noise level $\epsilon = 0$, and $\mathbf{f}_i^0|_{\mathbf{Q}\mathbb{F}_{\pi,1}^0}$ denotes the projection of

the vector \mathbf{f}_i^0 onto this subspace. The projection can be relatively easily found, as due to (2.53), the reconstructible subspace is spanned by the column vectors of the matrix $\mathbf{Q}\mathbf{V}_{\pi,1}^0$. Usefulness of q_2 depends in practice on the set of unit excitations $\{\mathbf{f}_1, \mathbf{f}_2, \dots, \mathbf{f}_{N_1}\}$, which should retain characteristic features of the excitations that are expected in the considered system.

Both criteria, q_1 and q_2 , are computed for the noiseless case (at $\epsilon = 0$), which allows them to be general measures of the quality of sensor placement, irrespective of the actual noise level in the measurement system.

2.5.3 Compound criterion

The criteria of conditioning and informativity tend in practice to be negatively correlated, see a numerical example in Fig. 2.5(left). Moreover, most of the reconstructible subspace computed for the noiseless case, $\mathbf{Q}\mathbb{F}_1^0$, is actually hardly reconstructible, because it corresponds to negligibly small singular values. Therefore, a practical criterion has to weight conditioning against informativity and to take into account the relative measurement noise level ϵ . This can be achieved by measuring the accuracy of the identification process as performed with the regularized system matrix \mathbf{B}_π^ϵ instead of the original matrix \mathbf{B}_π :

$$q_2^\epsilon(\pi) := \frac{1}{N_1} \sum_{i=1}^{N_1} \left\| \mathbf{f}_i^\epsilon - \mathbf{f}_i^0 |_{\mathbf{Q}\mathbb{F}_{\pi,1}^\epsilon} \right\|^2. \quad (2.73)$$

2.6 Numerical example

2.6.1 The structure

Figure 2.2 shows the 3D truss structure modeled in the numerical example. The structure is 6 m long, and all its elements are 0.5 m long with the exception of the 12 diagonal elements of the lower plane, which are $0.5\sqrt{2}$ m long; each element is 10 mm^2 in its cross-section and made of steel with the density of 7800 kg/m^3 and Young's modulus of 200 GPa. Additionally, the mass of each node is 0.23 kg. There are a total of 107 elements and 38 nodes. The two left-hand side bottom corner nodes have restrained all the degrees of freedom (DOFs) and are thus turned into fixed support, while the two opposite right-hand side bottom corner nodes have restrained only the vertical DOFs and are free to move in the horizontal plane.

The modeled time interval $T = 75$ ms is discretized into 250 time steps of $\Delta t = 0.3$ ms each. Such a time step corresponds to the sampling frequency of

3333 Hz, which is more than twice as large as the highest natural frequency of the structure (1368 Hz). Unknown excitation loads can occur only vertically in each of the twelve upper nodes of the structure. A maximum of eleven strain sensors can be placed in any of the eleven upper elements ($0 < N_r \leq N_{r_{\max}} = 11$) that join the twelve nodes potentially exposed to the unknown excitation loads. Discrete structural impulse responses are numerically simulated by means of the unconditionally stable Newmark integration scheme [145–148] with the standard parameters $\gamma = 1/2$ and $\beta = 1/4$, which is applied to (2.4) with a consistent mass matrix. The impulse response matrix \mathbf{B}_π is $250N_r \times 3000$ in dimensions and thus underdetermined. Figure 2.3 illustrates the structure of the full matrix \mathbf{B} : its row blocks correspond to the eleven sensors, while the column blocks correspond to the twelve DOFs potentially exposed to unknown excitations. Since there are 250 time steps, each block is a 250×250 lower triangular Toeplitz matrix. For each sensor placement π , the corresponding matrix \mathbf{B}_π is obtained by selecting the appropriate block rows from the full matrix depicted in Fig. 2.3. Such a matrix, even if dense, is of moderate dimensions and so computation of its SVD is feasible. Thus the more accurate approach of decomposition of the excitation and separate identifications of its reconstructible and unreconstructible components is followed.

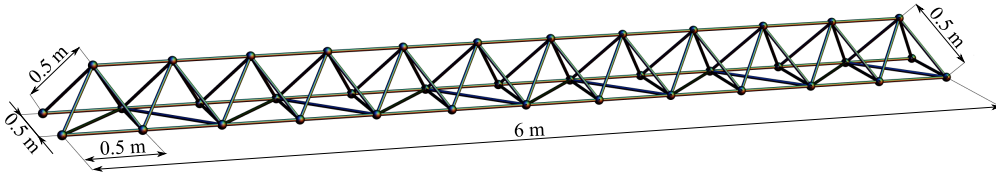


Figure 2.2. The 3D truss structure modeled in the numerical example.

2.6.2 Optimum placement of sensors

Up to $N_{r_{\max}} = 11$ strain sensors are used in the identification process. Therefore, there are as many as $2^{11} - 1 = 2047$ different ways to place the sensors and 2047 different impulse response matrices \mathbf{B}_π . For each of them, the SVD and the sensor placement criteria q_1 and q_2 defined in (2.71) and (2.72) are computed.

The criterion q_2 requires the set of N_l expected or typical unit excitations $\{\mathbf{f}_1, \mathbf{f}_2, \dots, \mathbf{f}_{N_l}\}$ to be specified. For this purpose, load shape functions [56, 60] are used, which are cubic Hermite polynomials that are piecewise combined in two neighboring time intervals to obtain the two C^1 -smooth functions depicted

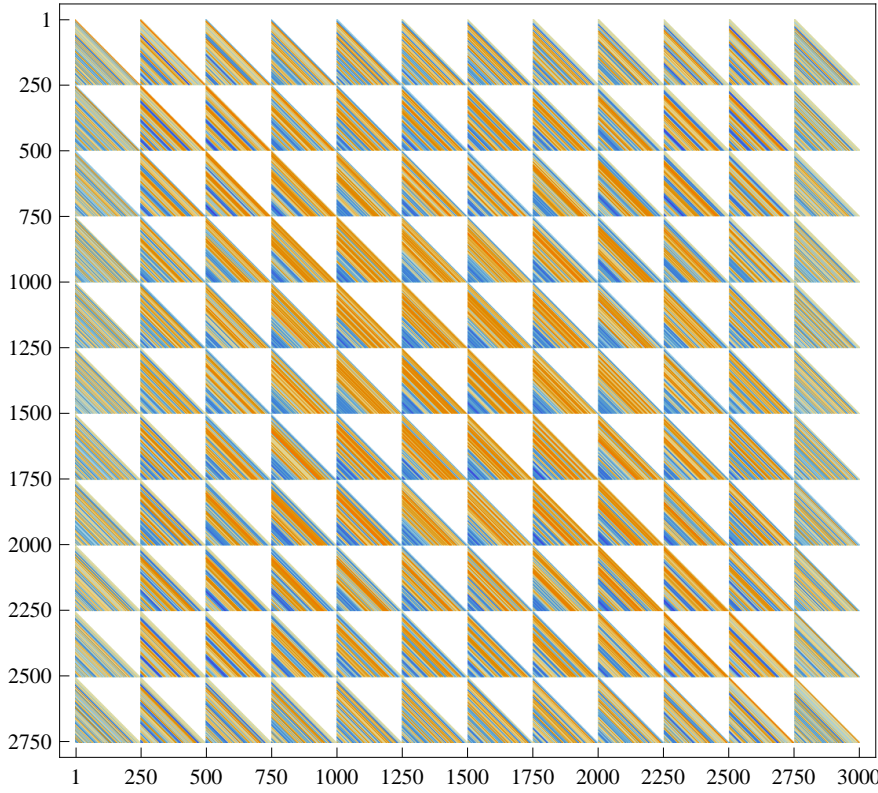


Figure 2.3. The 11×12 block Toeplitz structure of the full impulse response matrix \mathbf{B} .

in Fig. 2.4. The time-history of the excitation in each of the twelve potentially load-exposed DOFs is divided into eleven equal intervals. The division points (at the time steps no. 25, 50, 75, ..., 225) are used to obtain 22 load shape functions for each DOF by shifting the simple patterns plotted in Fig. 2.4. These 22 time evolutions are normalized and independently replicated for each of the twelve considered DOFs to yield a total of $N_l = 264$ excitations \mathbf{f}_i . Notice that such a set spans a subspace of all excitations that preserves the resolution with respect to space, but is of reduced resolution with respect to time.

Figure 2.5(left) plots q_2 versus q_1 ; each dot corresponds to one sensor placement π . The negative correlation is clearly visible. Clear groups that correspond to the number of sensors N_r can be distinguished: the more sensors, the larger (worse) the conditioning q_1 and the smaller (better) the informativity q_2 . Within the individual groups a negative correlation can also be observed, even if significantly less pronounced.

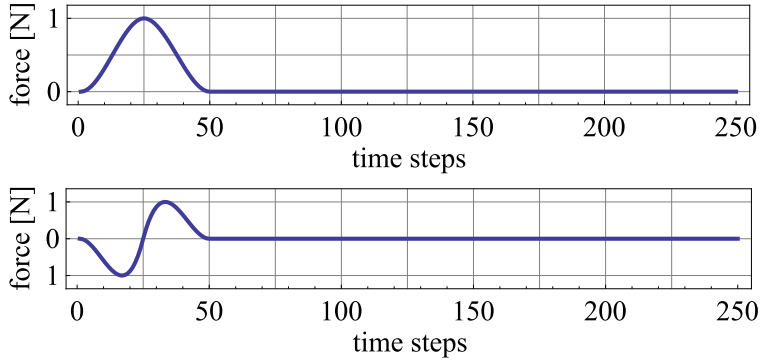


Figure 2.4. The two basic excitation patterns that are shifted in time to form all the load shape functions for a given DOF.

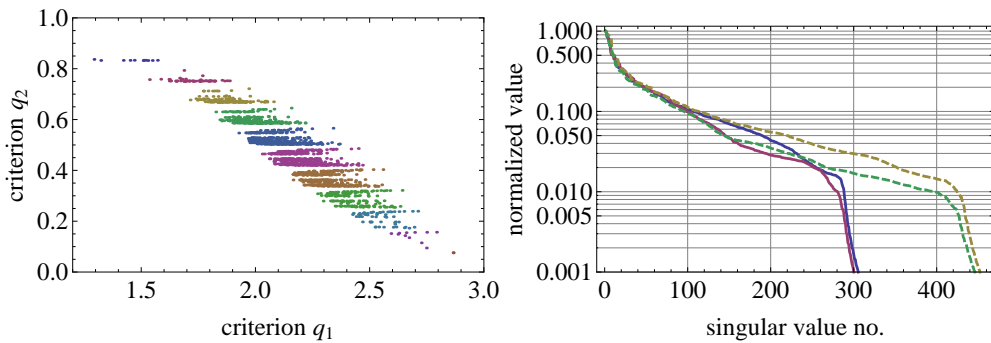


Figure 2.5. (left) Correlation plot for sensor placement criteria q_1 and q_2 ; (right) Normalized singular values of the impulse response matrices \mathbf{B} corresponding to the $q_2^{5\%}$ -best and $q_2^{5\%}$ -worst placements of two (continuous) and three (dashed) sensors.

The measurement noise at 5% rms level is assumed, and such a level is used to compute the compound criterion $q_2^{5\%}$, (2.73). Table 2.2 lists the best and worst placements of two to five sensors according to $q_2^{5\%}$. The best placements seem to distribute the sensors more or less evenly along the length of the structure, while the worst placements group the sensors together near the supports. A qualitatively similar distributions have been obtained in [32], even if a different set of excitations was used there to compute q_2 . In an example of a cantilever beam reported in [35], the worst placements were grouped near the free end of the beam, while the best placements were more evenly distributed, but still nearer the fixed end.

For each given number of available sensors, the difference between the best and the worst placements in terms of conditioning and dimensionality of the 5%-reconstructible space can be clearly illustrated by plotting the normalized singular values of the corresponding impulse response matrices, see Fig. 2.5(right) for the results obtained in the cases of the $q_2^{5\%}$ -best and $q_2^{5\%}$ -worst placements of two or three sensors. The related 5%-reconstructible spaces have the dimensions of 189 and 145 in the case of two sensors and 219 and 144 in the case of three sensors. In other words, even in the best placement of two sensors only the first 189 singular vectors out of 3000 stay above the assumed 5% noise level, which means that almost 94% of the available information is lost in the measurement process or masked by the measurement noise. The remaining 6% is confined to the 5%-reconstructible subspace of all excitations; the basis of this subspace consists of the right singular vectors, that is of the columns of the matrix $\mathbf{V}_2^{5\%}$. As an example, the excitations corresponding to the 1st and the 5th right singular vectors in the case of the $q_2^{5\%}$ -best placement of two sensors are depicted in Fig. 2.6. Notice the increasing oscillations: in general, the consecutive singular vectors introduce more and more high frequency components. This is typical for Toeplitz matrices [109] and also consistent with the characteristics of the excitation set used to compute $q_2^{5\%}$.

Table 2.2. Best and worst placements of two, three, four and five strain sensors with respect to the compound criterion $q_2^{5\%}$. An “o” denotes an element with a sensor; a dash “-” denotes an element without a sensor.

	2 sensors	3 sensors	4 sensors	5 sensors
$q_2^{5\%}$ -best	O-----O-	O--O----O-	O--O----OO	O---O---O-OO
	O-----O--	O--O----O-	OO-O-----O	O---O---O-OO
	-O-----O-	-O-O----O-	O--O---O-O-	OO-O---O---O
	O---O-----	O-----O-O-	O---O----OO	OO-O---O-O-
	O-----O--	-O-----O-O-	OO-O-----O-	O---O---O-OO
$q_2^{5\%}$ -worst	-----OO	OOO-----	--OO---OO---	-----OO-OOO
	OO-----	-----OOO	-OOO---O---	-----OOO-OO
	-OO-----	--OO---O---	-----O-OOO	-----OOO-OO-
	-----OO-	--O---OO-	-----OO---OO	-----OOOOOO--
	--OO-----	-----OOO-	-----OO---OO	-----OOOOOO-

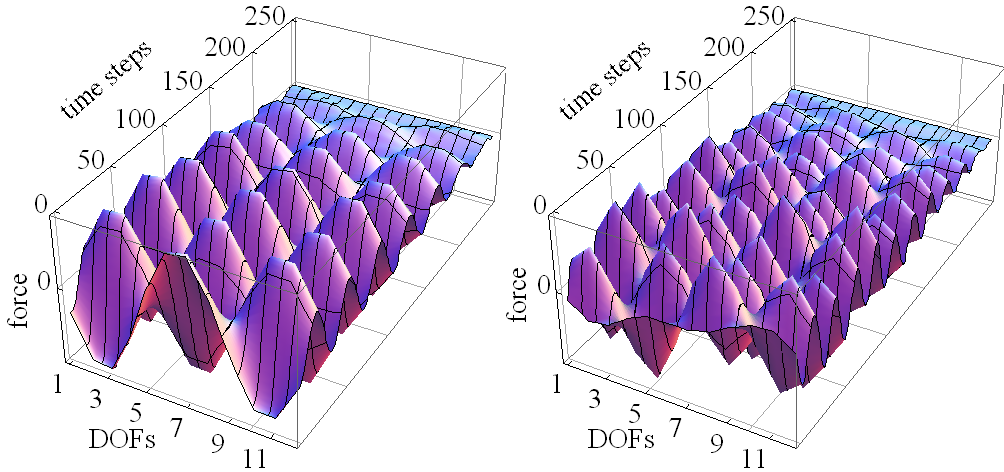


Figure 2.6. Unnormalized excitations corresponding to the first and the fifth right singular vector computed for the $q_2^{5\%}$ -best placement of two sensors.

2.6.3 Actual excitation

Figure 2.7 depicts the evolution of the assumed actual excitation, which is identified in the following with the discussed approaches. The excitation models a constant moving load of 1000 N. This load is distributed in the form of a set of two vertical forces, each of 500 N and 0.5 m apart from each other, which move from right to left along the whole length of the modeled structure. In each time instance, each of these two forces is transferred to the nearest structural nodes proportionally to its position along the element. The unconditionally stable Newmark integration scheme with $\gamma = 1/2$ and $\beta = 1/4$ is used to simulate the exact responses of the eleven considered strain sensors, see Fig. 2.8, where the solid lines mark the responses of the three $q_2^{5\%}$ -best placed sensors (no. 1, 4 and 10). In order to simulate the measurement error, all the responses are contaminated with a numerically generated independent Gaussian noise at 5% rms level before being used in computations. Spectral analysis of the noisy response shows that as much as 99% of its energy is conveyed below 53 Hz, which confirms that the selected time discretization is fine enough.

2.6.4 Identification results

Based on the simulated noisy responses of the considered sensors, the corresponding reconstructible and unreconstructible components of the excitation

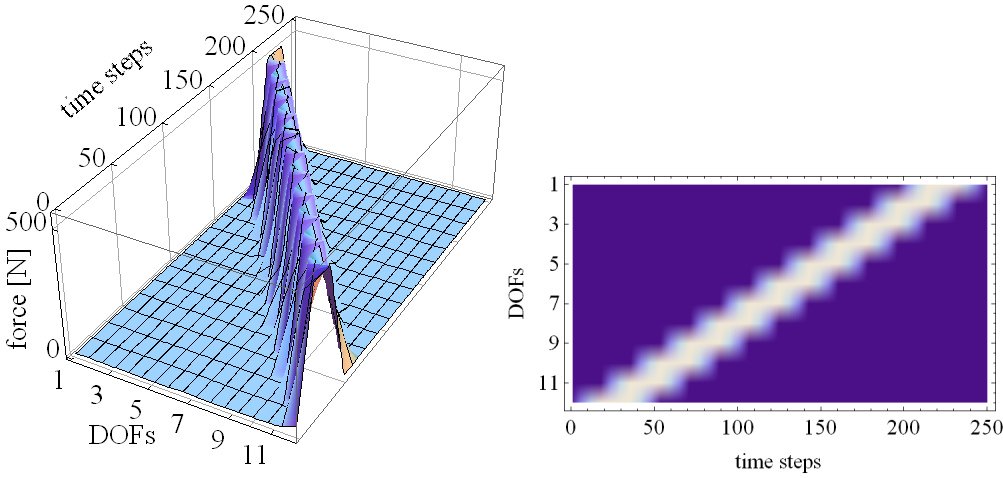


Figure 2.7. Assumed actual excitation of the truss structure: 3D plot and a density plot.

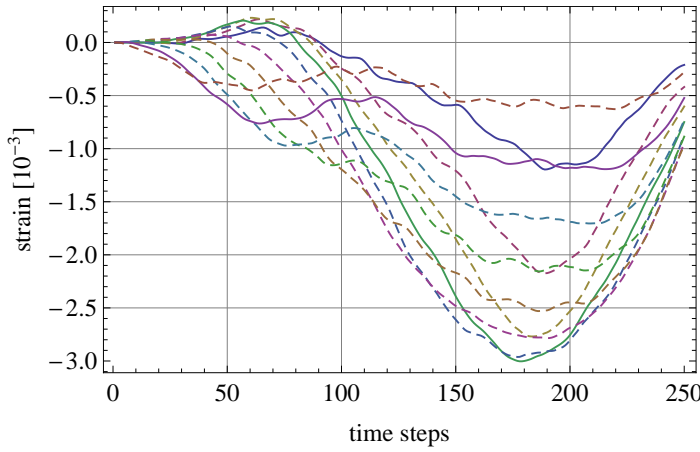


Figure 2.8. Simulated exact responses of the eleven strain sensors to the assumed actual excitation. The responses of the $q_2^{5\%}$ -best placement of three sensors (no. 1, 4, 10) are marked with solid lines.

are separately identified. Given the SVDs of the impulse response matrices (2.51), the reconstructible component is computed directly by (2.58). The unreconstructible component is identified based on the assumption of nonnegativity of the excitation, that is by minimization of (2.63).

First, the $q_2^{5\%}$ -best placements of two and three sensors are used. The results are shown in the form of density and 3D plots in Figs. 2.9 and 2.10, respectively. In both figures, the left and right columns correspond to the number of sensors used in identification (respectively two and three). The top rows show the

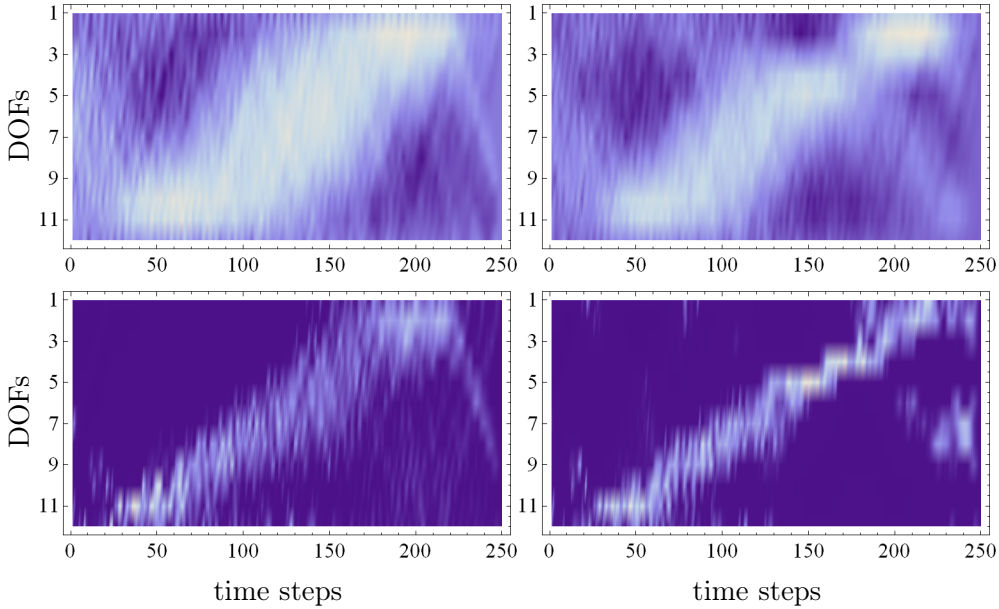


Figure 2.9. Identification results, density plots: (left column) using the $q_2^{5\%}$ -best placement of two sensors, (right column) using the $q_2^{5\%}$ -best placement of three sensors; (top row) reconstructible components, (bottom row) results of full identification, where the assumption of nonnegativity (2.63) is used to identify the unreconstructible excitation components.

reconstructible components, and the bottom rows show the identified full excitations (2.61) which include also the unreconstructible components. All of qualitative features of the actual excitation are identified properly, including its location and characteristic movement. In quantitative terms, the magnitude is identified only approximately. This is, however, not surprising, given that as much as 93% of the total information about the actual excitation is not retained in the available measurements: it is either masked by the measurement noise or completely lost due to the insufficient number of sensors. A comparison of the results shown in the top and bottom rows of Figs. 2.10 and 2.9 confirms that a proper choice of the additional information used for identification of the unreconstructible component might be crucial.

For comparison purposes, the identification is repeated using the $q_2^{5\%}$ -worst placement of five sensors. The results are shown in Fig. 2.11. In comparison to the results obtained with the optimally placed two or three sensors, the accuracy is significantly worse even though considerably more sensors are used. It clearly emphasizes the importance of the optimum distribution of the available sensors in the structure and confirms the usefulness of the proposed optimality criterion.

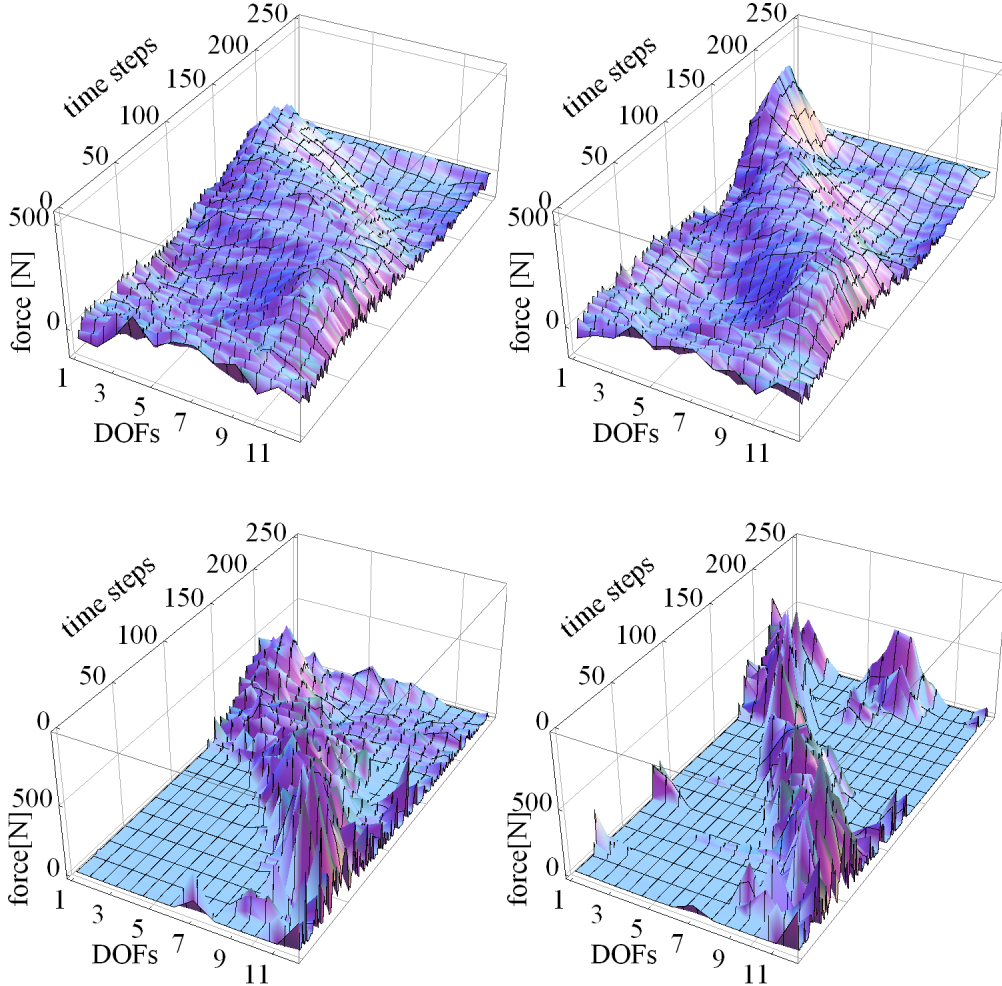


Figure 2.10. Identification results, 3D plots: (left column) using the $q_2^{5\%}$ -best placement of two sensors, (right column) using the $q_2^{5\%}$ -best placement of three sensors; (top row) reconstructible components, (bottom row) results of full identification, where the assumption of nonnegativity (2.63) is used to identify the unreconstructible excitation components.

In this example, the criterion of nonnegativity is used to identify the excitation in the unreconstructible subspace. A similar example is considered in [32], but with the criterion of smoothness of excitation. Figs. 7.5 and 7.4 in Section 7.4 plot the results of identification of the same excitation, but in a structure that features elastoplastic material characteristics (bilinear isotropic hardening).

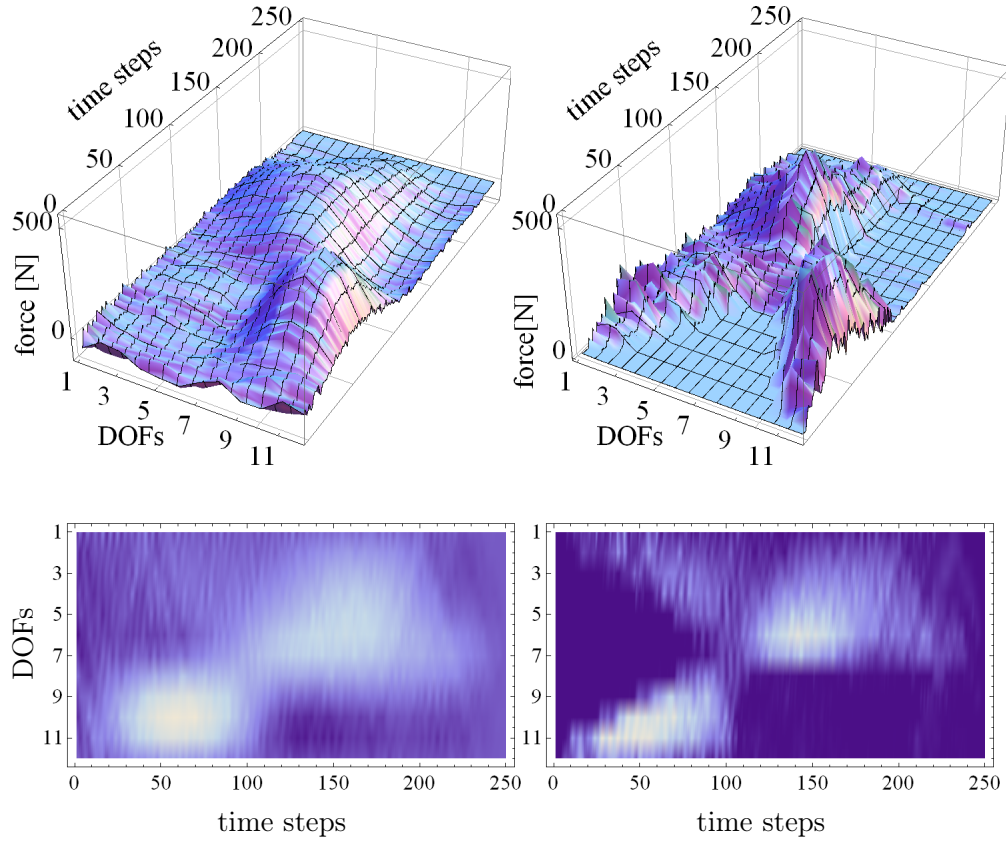


Figure 2.11. Identification results for the $q_2^{5\%}$ -worst placement of five sensors, 3D and density plots: (left column) reconstructible components, (right column) results of full identification, where the assumption of nonnegativity (2.63) is used to identify the unreconstructible excitation components.

3

Virtual distortion method

The virtual distortion method (VDM) [27] is a quick reanalysis method that has been developed in the Institute of Fundamental Technological Research (IPPT PAN) since the mid 1980s. The term *distortion* originates from a book on the theory of elasticity by professor Nowacki [149], where distortions are used to model material dislocations and thermoelastic interactions. Earlier related work includes the Eshelby's analysis of elastic inclusions [150] and the research on initial strains or eigenstrains by Kröner [151, 152], Argyris [153] and Maier [154]; there is also a parallel research on the theorems of structural variation by Majid and Celik [155], which was performed mainly in the context of the phenomenon of plasticity. In 1989, Holnicki-Szulc and Gierliński [156] have coined the term *virtual distortion* and proposed the concept of the influence matrix, which is the distinguishing factor of the VDM that provides for its numerical effectiveness.

Initially, the VDM was inspired by a research in static analysis of prestressed structures [157]. Thereupon, analysis of progressive collapse and various problems of structural design, redesign and control were included [28, 156, 158–161], and the methodology was successively expanded to include reanalysis in time-domain, applications to inverse problems of structural health monitoring and to the design of adaptive structures, see, e.g., [27, 32, 162, 163]. In its current formulation, the VDM is applicable in deterministic static and dynamic reanalysis of structures, including time and frequency domains. It has been also used for modeling of stochastic response of truss structures with uncertain parameters under static [164] and dynamic loads [165].

As it is convenient in the intended applications to structural health monitoring, this chapter is focused on deterministic time-domain formulation of the VDM in direct and inverse problems of dynamics. In comparison to earlier formulations, a new continuous-time notation is used, which is not only more concise than the original discrete-time notation, but it also emphasizes the mathematical structure and properties of the problem and its relation to the inverse problem of load identification. The derivation here sets out from the equation of motion of the original structure, which seems to be more natural than the

postulate of equality of local strains and element forces. Moreover, in the inverse problem of damage identification, a distinction is introduced (Subsection 3.1.2.2) between a damage of a known type and a damage of an unknown type; the former requires only selected damage parameters to be identified (such as stiffness reduction ratio), while in the latter case the type of the damage (such as a “breathing crack” or a “constant reduction of stiffness”) needs to be additionally identified, which is discussed in detail and further developed in Section 6.2.

3.1 Introduction

3.1.1 Structural reanalysis

The VDM is a reanalysis technique, that is a technique for a repeated analysis. In general, the purpose of any reanalysis technique is to compute the structural response of a modified (damaged, plastically yielded, additionally supported, etc.) structure in a numerically efficient way without a brute force solution of the full set of modified structural equations, based on the information already contained in the original response of the unmodified structure. To this end, three components are necessary:

1. the original response of the unmodified structure,
2. definition of the modifications and
3. certain model of the unmodified structure.

The probably most widely known reanalysis method is the approximate reanalysis by the method of combined approximations (CA), which has been developed by Kirsch *et al.* [166] and is basically equivalent to a preconditioned conjugate gradient method [167]. The CA requires the full parametric model of the unmodified structure to be known, which might be a limiting factor in purely experimental investigations of complex real structures. Within the VDM, a nonparametric model of the unmodified structure is used. Such a model is called the influence matrix, and it contains global responses of the unmodified linear structure to local strain distortions or pseudo loads. The influence matrix is thus a nonparametric structural model, which is reduced with respect to structural elements and/or DOFs affected by the modeled modifications, and which can be obtained either numerically or experimentally (see Chapter 4). Given such a model, computation of the response of the modified structure can be performed in a single step, without iterations that are necessary in most of other approaches.

As demonstrated in [168], the VDM, the CA and the theorems of structural variations can be in their static formulations tracked back to the Sherman–Morrison–Woodbury formula [169]. For a general review of other static reanalysis approaches, see [170–172] and also [27, Section 2].

3.1.2 Overview of the VDM

For the purpose of notational clarity, this chapter considers modifications that affect structural stiffness and structural mass. This is not restricting, since the formulation of the VDM is flexible and can be straightforwardly adapted to include plastic yielding (Chapter 7 or [27, 32]), breathing cracks (Section 6.2 or [57]), moving masses (Section 6.3 or [39, 40, 55]), material damping [173, 174], additional supports (Chapter 5 or [46, 47]), etc. Within the framework considered in this chapter, some types of modifications affect only stiffness (modifications of Young’s modulus, plastic yielding, etc.), some affect only mass (concentrated mass modifications), while others can affect both parameters (material redistribution, changes in element cross-sections, etc.). The VDM models stiffness-related effects of modifications with the vector κ^0 of virtual distortions, which are intentionally introduced additional strains that are imposed on the involved intact finite elements. The inertial effects of mass modifications are modeled using the equivalent unequilibrated pseudo loads \mathbf{p}^0 that act in the involved structural degrees of freedom (DOFs). Even if the virtual distortions can be expressed in terms of the equivalent pseudo loads (as in Chapter 4), in some applications it is convenient to maintain the distinction and treat the virtual distortions and pseudo loads separately, which is discussed in Subsection 3.3.2.

The original undamaged structure is assumed to be linear¹. With the assumption of zero initial conditions, the response \mathbf{a} of the modified structure to an external excitation can be thus represented by a sum of the

1. response \mathbf{a}^L of the original undamaged structure to the same external excitation and the
2. response of the original undamaged structure to the imposed virtual distortions κ^0 and pseudo loads \mathbf{p}^0 ,

that is by the following formula:

$$\mathbf{a} = \mathbf{a}^L + \mathcal{B}^{av} \boldsymbol{\nu}^0, \quad (3.1)$$

¹If necessary, potential material nonlinearities can be modeled using additional fields of virtual (or plastic) distortions, as in Chapter 7; see also [175] for a coupled analysis.

where the vector $\boldsymbol{\nu}^0$ collects the pseudo loads and virtual distortions,

$$\boldsymbol{\nu}^0 = \begin{bmatrix} \mathbf{p}^0 \\ \boldsymbol{\kappa}^0 \end{bmatrix}, \quad (3.2)$$

and their effect on the response is modeled by the linear matrix operator $\mathcal{B}^{a\nu}$ of convolution with the respective impulse response functions of the original undamaged structure. These impulse response functions can be either precomputed or even directly measured, if the parametric numerical model of the original structure is unknown [29]. The vector $\boldsymbol{\nu}^0$ depends on the type and extent of the damage and is related in an implicit way to the vector $\boldsymbol{\mu}$ of damage parameters by the following equation:

$$\mathbf{0} = \mathbf{R}(\boldsymbol{\nu}^0, \boldsymbol{\mu}, \mathbf{a}), \quad (3.3)$$

which is stated here in a general form, as the specific form of the function \mathbf{R} depends on the type of the considered damages, modifications or nonlinearities; for example, in the case of the damages considered in this chapter it takes the form of (3.28) or (3.30).

3.1.2.1 Direct problem

The direct problem is the problem of computing the response \mathbf{a} of the modified structure to a certain external excitation, given

1. the response \mathbf{a}^L of the original undamaged structure to the same excitation,
2. the damage, defined by the damage type (function \mathbf{R}) and damage parameters $\boldsymbol{\mu}$, and
3. certain characteristics of the original structure (expressed in the form of the operator $\mathcal{B}^{a\nu}$ and based on the impulse responses of the original undamaged structure).

The solution scheme is simple: first, (3.1) is substituted into (3.3) and the resulting equation

$$\mathbf{0} = \mathbf{R}(\boldsymbol{\nu}^0, \boldsymbol{\mu}, \mathbf{a}^L + \mathcal{B}^{a\nu}\boldsymbol{\nu}^0), \quad (3.4)$$

is solved with respect to the vector $\boldsymbol{\nu}^0$. In time domain, this is usually equivalent to a linear integral equation of the Volterra type, and in the case of a localized damage, the number of unknowns (elements of $\boldsymbol{\nu}^0$) is considerably smaller than the number of structural DOFs. Then, the computed vector $\boldsymbol{\nu}^0$ is substituted back into (3.1) to obtain the response \mathbf{a} . In this way, the response of the damaged

structure is expressed in terms of (convolutions of) selected structural impulse responses of the original unmodified structure, so that time-consuming brute force simulation of the updated finite element (FE) model is avoided. In other words, the VDM uses a reduced (fewer unknowns) and essentially nonparametric (that is based on the impulse responses) approach to structural modeling, which is an outstanding feature of the VDM in comparison to other reanalysis approaches, such as the CA [166, 167], that usually operate directly on the full structural FE model. Notice that the VDM, similarly as the CA and most other reanalysis methods, relies on the assumption of small deformations (geometric linearity).

3.1.2.2 Inverse problem

Within the framework of the VDM, the inverse problem of damage identification is the problem of identifying the damage, given

1. the measured response \mathbf{a}^M of the damaged structure to a certain external testing excitation,
2. the response \mathbf{a}^L of the original undamaged structure to the same testing excitation, and
3. certain characteristics of the original structure (expressed in the form of the operator $\mathcal{B}^{a\nu}$ and based on the impulse responses of the original undamaged structure).

Additionally, the type of the damage can be either known or unknown, so that the function \mathbf{R} in (3.3) is respectively either known or unknown, too. In both cases, the identification is stated in the form of the problem of finding a certain least-squares solution to the following equation:

$$\begin{aligned}\mathbf{a}^M &= \mathbf{a}^L + \mathcal{B}^{a\nu} \boldsymbol{\nu}^0 \\ &= \mathbf{a},\end{aligned}\tag{3.5}$$

which equates the measured and the modeled responses of the damaged structure. The least-squares solution is found with respect to either $\boldsymbol{\mu}$ or $\boldsymbol{\nu}^0$, which is then used to identify the damage type \mathbf{R} .

Damage of a known type. If the function \mathbf{R} is known, only the vector $\boldsymbol{\mu}$ of damage parameters needs to be identified. This is usually performed in the standard way, that is by minimizing the norm of the residuum of (3.5),

$$F(\boldsymbol{\mu}) := \frac{1}{2} \|\mathbf{a}^M - \mathbf{a}\|,\tag{3.6}$$

with respect to the vector μ . The response \mathbf{a} of the damaged structure depends on μ and is computed as in the direct problem. Such a formulation is described in detail in this chapter. Its important feature is that it allows an effective exact first and second order sensitivity analysis to be performed with respect to μ . As a result, fast gradient-based and even second order optimization approaches can be used to minimize the objective function. Besides, the formulation in the form of a least-squares problem allows also the Hessian of the objective function to be quickly approximated along the lines of the Gauss–Newton approach at the computational cost of a first order analysis.

Damage of an unknown type. If the type of the damage is not known, both \mathbf{R} and μ have to be identified. First, (3.5) is solved with respect to the vector ν^0 , which is equivalent to finding a solution to a linear least-squares problem. This yields the pseudo loads and/or virtual distortions that explain the observed discrepancies between the measured response \mathbf{a}^L of the damaged structure and the response \mathbf{a} of the original undamaged structure. Then, several versions of (3.3) are constructed that correspond to various potential damage types \mathbf{R}_i , $i = 1, 2, \dots$. In each case, the particular damage parameters are found by minimizing the norm of the residuum $\|\mathbf{R}_i(\nu^0, \mu, \mathbf{a}^L)\|$ (or of its physically more meaningful equivalent) with respect to μ . The best-fitting damage type (that is \mathbf{R}_i with the smallest residuum norm) together with its fitted parameters are assumed to represent the actual damage. Such an approach is considered in Section 6.2 and further developed into a tool for simultaneous identification of excitations and damages.

3.1.3 Introductory examples

This subsection uses two simple examples to illustrate the scheme of application of the VDM in direct problems of structural reanalysis, discuss the difference to a direct solution in terms of the required data and numerical effectiveness, as well as to introduce two specific forms of (3.3).

3.1.3.1 Mass modification in a 1-DOF system

Consider a 1-DOF system that satisfies the standard form of the equation of motion:

$$m\ddot{u}^L(t) + c\dot{u}^L(t) + ku^L(t) = f_{\text{test}}(t). \quad (3.7)$$

Denote its acceleration impulse response function by $\ddot{\mathcal{B}}^{\text{up}}(t)$, and let $\ddot{\mathcal{B}}^{\text{up}}$ denote the respective operator, defined as in (2.20). Assume zero initial conditions and

let $u^L(t)$ and $\ddot{\mathcal{B}}^{up}$ be known. Consider a mass modification Δm ; the equation of motion of the modified system under the same testing excitation $f_{test}(t)$ can be then stated as

$$(m + \Delta m)\ddot{u}(t) + c\dot{u}(t) + ku(t) = f_{test}(t), \quad (3.8)$$

where $u(t)$ denotes the response of the modified structure that is different from the original response $u^L(t)$. The modification term can be moved to the right-hand side of the equation, which effectively transforms the modification into a pseudo load $p^0(t)$ that acts in the original system and models the inertial effects of the modification:

$$m\ddot{u}(t) + c\dot{u}(t) + ku(t) = f_{test}(t) + p^0(t), \quad (3.9a)$$

where

$$p^0(t) = -\Delta m\ddot{u}(t). \quad (3.9b)$$

Equation (3.9a) is the equation of motion of the original system, which is excited by the same external excitation $f_{test}(t)$ as in (3.7) and additionally by the pseudo load $p^0(t)$. As a result, the acceleration response of the modified system is the sum of the responses of the original system to $f_{test}(t)$ and to $p^0(t)$. In the operator notation, as in (2.20), the response can be expressed in the following form:

$$\ddot{u}(t) = \ddot{u}^L(t) + (\ddot{\mathcal{B}}^{up}p^0)(t). \quad (3.10)$$

Notice that (3.9b) is a counterpart of (3.3), while (3.10) corresponds to (3.1).

To solve the direct problem using the VDM approach, (3.10) is first substituted into (3.9b). It yields the following integral equation of the Volterra type:

$$\left((\mathcal{I} + \Delta m\ddot{\mathcal{B}}^{up}) p^0 \right) (t) = -\Delta m\ddot{u}^L(t), \quad (3.11)$$

which is solved with respect to the pseudo load $p^0(t)$. The result is then substituted into (3.10) to obtain the response of the modified system. Such a VDM-based scheme can be compared with a direct solution of the modified equation of motion (3.8). Two important points should be noted:

- *Required data.* In any direct solution of (3.8), the excitation $f_{test}(t)$ and the parametric model of the system defined by m , c and k have to be known. On the other hand, the VDM requires $\ddot{\mathcal{B}}^{up}$ and $u^L(t)$ to be known, that is a nonparametric model of the system and its response to the considered excitation, which are both easy to obtain directly from experimental measurements.

- *Numerical effectiveness.* In this example, the VDM has no computational advantage over a direct solution: both (3.8) and (3.11) have a single unknown, while the Volterra integral equation (3.11) might be computationally more costly than a simple ordinary differential equation (3.8). The reason is that the system considered here has a single DOF only, so that its modification is not localized; compare it with the next example.

3.1.3.2 Stiffness modification of a truss element

Consider a single truss element of an arbitrarily large linear structure and denote by $\varepsilon^L(t)$ its response to an external excitation of the global structure. Consider a modification of the stiffness of the element and let it be quantified by the stiffness reduction ratio

$$\mu := \frac{\tilde{E}}{E}, \quad (3.12)$$

where \tilde{E} and E are the modified and original Young's moduli. Assume zero initial conditions. The VDM models stiffness modification of a truss element with a time-dependent virtual distortion $\varepsilon^0(t)$ (an additional strain) imposed on the original unmodified element. Let $B^{\varepsilon\varepsilon}(t)$ denote the strain response of the original element to an impulsive virtual distortion, that is to an excitation by a pair of self-equilibrated axial forces $\pm EA\delta(t)$ applied at its ends, where A denotes the cross-sectional area and $\delta(t)$ is Dirac's delta. Assume that the original response $\varepsilon^L(t)$ and the response $B^{\varepsilon\varepsilon}(t)$ (or the corresponding convolution operator $\mathcal{B}^{\varepsilon\varepsilon}$) are both known.

The direct problem is the problem of computing the response $\varepsilon(t)$ of the modified element to the same external excitation. The axial force in the actually modified element should be the same as in the element with the modification modeled by the virtual distortion, that is

$$\tilde{E}A\varepsilon(t) = EA(\varepsilon(t) - \varepsilon^0(t)), \quad (3.13)$$

which yields the following counterpart of (3.3):

$$\varepsilon^0(t) = (1 - \mu)\varepsilon(t). \quad (3.14)$$

The original structure is linear, thus the response of the modified element is the sum of its original response $\varepsilon^L(t)$ and its response to the virtual distortion,

$$\varepsilon(t) = \varepsilon^L(t) + (\mathcal{B}^{\varepsilon\varepsilon}\varepsilon^0)(t), \quad (3.15)$$

which is the counterpart of (3.1). Substitution of (3.15) into (3.14) yields the following integral equation of the Volterra type:

$$\varepsilon^0(t) - (1 - \mu) (\mathcal{B}^{\varepsilon\varepsilon} \varepsilon^0)(t) = (1 - \mu) \varepsilon^L, \quad (3.16)$$

which is solved to obtain $\varepsilon^0(t)$. The response $\varepsilon(t)$ of the modified element is obtained then by a substitution into (3.15). As in the previous example, two points should be noted:

- *Required data.* In any attempt at direct solution, the external excitation and the full parametric structural model of the global structure should be known, which can be difficult to obtain and update, and whose size depends on the number of structural DOFs and can be thus very large. On the other hand, irrespective of the size of the global structure, the VDM requires only two scalar functions $B^{\varepsilon\varepsilon}(t)$ and $\varepsilon^L(t)$ to be known, which are both relatively easy to obtain directly from measurements.
- *Numerical effectiveness.* In this example, the computational advantage of the VDM over the direct solution is very clear: the VDM requires only a single integral equation (3.16) with a single unknown to be solved, while any direct solution would require a solution of the full equation of motion of the global structure, which might be a time-consuming process in a case of a large structure. This advantage can be traced back to the fact that the modification considered here is localized and that the VDM uses a nonparametric structural model which is reduced in size to the number of the virtual distortions (or pseudo loads).

3.1.4 VDM and load identification

Throughout the rest of this book, the VDM is extensively used, mostly in time domain, as a convenient vehicle for formalization of various modeling and/or identification problems related to SHM. Similar as the inverse problem of load identification (Chapter 2), the VDM is formulated in terms of Volterra integral equations and relies on deconvolution procedures, which can be seen in the formal similarity of (2.26) to (3.5) (or to its three specific forms: (3.11), (3.16) and (3.32)). This is not a coincidence, since load identification is at the core of the methodology and occurs in the direct problem as well as in the inverse problem:

- In the direct problem the damages are assumed, and in order to compute the corresponding response, the methodology computes the equivalent pseudo loads or virtual distortions by solving (3.4) or any of its specific

version such as (3.32). The latter equation has a formally identical form as (2.26), and essentially it is thus an inverse problem of load identification. Load identification occurs also in the inverse problem of identification of a damage of a known type (see Subsection 3.1.2.2), because it proceeds by a repetitive solution of the direct problem.

- Identification of a damage of an unknown type starts with identification of the pseudo loads or virtual distortions that explain the observed discrepancies between the responses of the original structure and the damaged structures. It requires computing a solution to (3.1), which is a prime example of a load identification problem.

Moreover, the VDM can be seamlessly merged with the load identification procedures outlined in the previous chapter to form a unified approach for simultaneous identification of excitations and damages, see Chapter 6 and especially Section 6.2.

3.2 Distortions of a finite element

3.2.1 Basis distortions and equivalent element loads

The effects of stiffness modification of a finite element are modeled within the VDM using the equivalent virtual distortions. Their number and forms can be analyzed using the eigenvalue problem of the local stiffness matrix \mathbf{K}_i of the involved finite element, which is expressed in local coordinate system (the subscript i stands for the i th element). The matrix is positive semi-definite, hence its eigenvectors are of two kinds only: unit distortion vectors φ_{ij} that correspond to positive eigenvalues λ_{ij} and unit rigid motion vectors that correspond to zero eigenvalues. Thus, the matrix \mathbf{K}_i can be expressed in terms of its positive eigenvalues and the corresponding eigenvectors as follows:

$$\mathbf{K}_i = \sum_j \lambda_{ij} \varphi_{ij} \varphi_{ij}^T. \quad (3.17)$$

The eigenvector φ_{ij} is called the *jth basis distortion vector* of the i th finite element and corresponds to the following vector of local loads of the element:

$$\mathbf{n}_{ij} := \mathbf{K}_i \varphi_{ij} = \lambda_{ij} \varphi_{ij}. \quad (3.18)$$

Example 3.1 (distortions of a 2D beam element). *In its local coordinate system $\{x_1, y_1, \theta_1, x_2, y_2, \theta_2\}$, a 2D Euler–Bernoulli beam element of length L has the following stiffness matrix:*

$$\mathbf{K}_i = \begin{bmatrix} \frac{EA}{L} & 0 & 0 & -\frac{EA}{L} & 0 & 0 \\ 0 & \frac{12EI}{L^3} & \frac{6EI}{L^2} & 0 & -\frac{12EI}{L^3} & \frac{6EI}{L^2} \\ 0 & \frac{6EI}{L^2} & \frac{4EI}{L} & 0 & -\frac{6EI}{L^2} & \frac{2EI}{L} \\ -\frac{EA}{L} & 0 & 0 & \frac{EA}{L} & 0 & 0 \\ 0 & -\frac{12EI}{L^3} & -\frac{6EI}{L^2} & 0 & \frac{12EI}{L^3} & -\frac{6EI}{L^2} \\ 0 & \frac{6EI}{L^2} & \frac{2EI}{L} & 0 & -\frac{6EI}{L^2} & \frac{4EI}{L} \end{bmatrix},$$

where E is the Young modulus, A is the beam's cross-section and I is the second moment of area of the cross-section. Such a matrix has the three following positive eigenvalues:

$$\lambda_{i1} = \frac{2AE}{L}, \quad \lambda_{i2} = \frac{2EI}{L}, \quad \lambda_{i3} = \frac{6EI(4 + L^2)}{L^3}.$$

The three corresponding eigenvectors,

$$\begin{aligned} \varphi_{i1} &= \{-1, 0, 0, 1, 0, 0\}, && (\text{axial distortion}) \\ \varphi_{i2} &= \{0, 0, -1, 0, 0, 1\}, && (\text{bending distortion}) \\ \varphi_{i3} &= \{0, 2/L, 1, 0, -2/L, 1\}, && (\text{shear/bending distortion}) \end{aligned}$$

constitute the three basis distortion vectors of the element; their forms are illustrated in Fig. 3.1. Notice that bar elements, whether 2D or 3D, have only a single axial distortion.

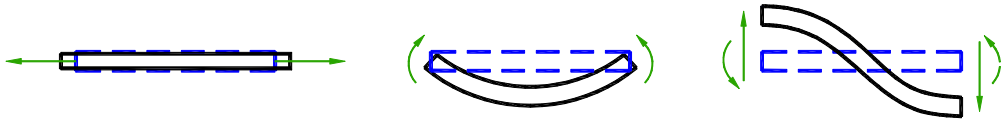


Figure 3.1. The three basis distortions of a 2D beam finite element: axial, bending and shear/bending.

3.2.2 Total distortions

A vector $\mathbf{u}_i(t)$ of local nodal displacements (expressed in local coordinates) can be represented in the eigenbasis of \mathbf{K}_i . The coordinates $\kappa_{ij}(t)$ that correspond to the basis distortion vectors $\varphi_{ij}(t)$,

$$\kappa_{ij}(t) := \varphi_{ij}^T \mathbf{u}_i(t), \quad (3.19)$$

are called the *total distortions*.

3.2.3 Decomposition of global elastic forces

Let \mathbf{L}_i be the transformation matrix from the global coordinate system to the local coordinates of the i th element, so that

$$\mathbf{u}_i(t) = \mathbf{L}_i \mathbf{u}(t), \quad (3.20)$$

where $\mathbf{u}(t)$ is the global displacement vector expressed in the global coordinate system. The global stiffness matrix \mathbf{K} of the original undamaged structure can be assembled from local stiffness matrices as

$$\mathbf{K} = \sum_i \mathbf{L}_i^T \mathbf{K}_i \mathbf{L}_i. \quad (3.21)$$

Using (3.17) to (3.21), the vector $\mathbf{K}\mathbf{u}(t)$ of global elastic forces can be decomposed into a linear combination of total distortions $\kappa_{ij}(t)$ and the corresponding vectors of local nodal loads \mathbf{n}_{ij} , that is it can be expressed in the form of the following sum:

$$\mathbf{K}\mathbf{u}(t) = \sum_i \mathbf{L}_i^T \mathbf{K}_i \mathbf{u}_i(t) = \sum_{i,j} \kappa_{ij}(t) \mathbf{L}_i^T \mathbf{n}_{ij}. \quad (3.22)$$

3.2.4 Equation of motion of the original structure

Let the vector $\mathbf{f}_{\text{test}}(t)$ denote an external excitation. Denote the corresponding response of the original unmodified structure by $\mathbf{u}^L(t)$ (global displacements) and $\kappa_{ij}^L(t)$ (total distortions). The equation of motion of the unmodified structure can be stated as, see (3.22),

$$\mathbf{M}\ddot{\mathbf{u}}^L(t) + \mathbf{C}\dot{\mathbf{u}}^L(t) + \sum_{i,j} \kappa_{ij}^L(t) \mathbf{L}_i^T \mathbf{n}_{ij} = \mathbf{f}_{\text{test}}(t), \quad (3.23)$$

where \mathbf{M} and \mathbf{C} denote respectively the mass and damping matrices of the unmodified structure. The superscript L stands for “linear” and emphasizes the linearity of the original unmodified structure, whose response constitutes the baseline response for further reanalysis and computations. The baseline response is modified by the effects of the virtual distortions and/or pseudo loads that are used to model structural modifications and damages, which can in general introduce nonlinearity into the structure, such as a breathing crack (Section 6.2) or plastic yielding (Chapter 7).

3.3 Direct problem

3.3.1 Structural modifications and damages

The direct problem is the problem of computing the response $\mathbf{a}(t)$ of the modified structure, given the vector $\boldsymbol{\mu}$ of damage parameters. This chapter considers two kinds of structural modifications and/or damages:

1. *Stiffness-related damages*, which are represented by constant uniform stiffness reductions of the affected finite elements and quantified in relative terms by the ratio μ_i between the original local stiffness matrix \mathbf{K}_i and the modified local stiffness matrix $\tilde{\mathbf{K}}_i$,

$$\tilde{\mathbf{K}}_i = \mu_i \mathbf{K}_i, \quad (3.24)$$

where i indexes the elements. This approach seems to be typical for global SHM methods, see, e.g., Dems and Mróz [176, 177] or Dems and Turrant [178], where from the practical point of view the most important factor is often the remaining stiffness expressed in relative terms as a percentage of the original stiffness. These damages are modeled with virtual distortions of the affected finite elements. However, if absolute stiffness modifications $\Delta\mathbf{K}$ are required, which may happen, e.g., in the case of additional reinforcing elements, they need to be modeled by pseudo loads, see Chapter 4.2.1.2.

2. *Mass-related modifications*, which are described here in absolute terms as a certain unknown modification $\Delta\mathbf{M}$ to the original structural mass matrix \mathbf{M} . This is a natural way of modeling the influence of added masses. If a relative formulation is required, it can be obtained in an analogous way to (3.24) as $\Delta\mathbf{M} = \sum_i \mu_i \mathbf{M}_i$; notice that mass modification will be then coupled to stiffness modification by the common modification coefficients μ_i .

For notational simplicity, it is assumed here that the modifications do not considerably affect the material damping properties of the involved elements. If it is not the case, the damping can be modeled in a similar way to the modifications of stiffness and mass, see, e.g., [173, 174] and [162, Section 6.4]. Notice also that the modifications considered here preserve the linearity of the structure. However, the approach can be straightforwardly extended to include the case of time-varying stiffness modifications (breathing cracks, plasticity, etc.), as discussed, e.g., in [27, 32, 40, 57] or in Chapters 6 and 7.

3.3.2 Pseudo loads and virtual distortions

If an external excitation $\mathbf{f}_{\text{test}}(t)$, the same as in (3.23), is applied to the modified structure, it results in the response $\mathbf{u}(t)$, which is described by the following equation of motion:

$$(\mathbf{M} + \Delta\mathbf{M}) \ddot{\mathbf{u}}(t) + \mathbf{C}\dot{\mathbf{u}}(t) + \sum_i \mathbf{L}_i^T \tilde{\mathbf{K}}_i \mathbf{u}_i(t) = \mathbf{f}_{\text{test}}(t). \quad (3.25)$$

The terms that quantify the modifications are moved to the right-hand side, which yields the following equivalent form:

$$\begin{aligned} & \mathbf{M}\ddot{\mathbf{u}}(t) + \mathbf{C}\dot{\mathbf{u}}(t) + \sum_i \mathbf{L}_i^T \mathbf{K}_i \mathbf{u}_i(t) \\ &= \mathbf{f}_{\text{test}}(t) - \Delta\mathbf{M}\ddot{\mathbf{u}}(t) + \sum_i (1 - \mu_i) \mathbf{L}_i^T \mathbf{K}_i \mathbf{u}_i(t), \end{aligned} \quad (3.26)$$

or, see (3.22),

$$\mathbf{M}\ddot{\mathbf{u}}(t) + \mathbf{C}\dot{\mathbf{u}}(t) + \sum_{i,j} \kappa_{ij}(t) \mathbf{L}_i^T \mathbf{n}_{ij} = \mathbf{f}(t) + \mathbf{p}^0(t) + \sum_{i,j} \kappa_{ij}^0(t) \mathbf{L}_i^T \mathbf{n}_{ij}, \quad (3.27)$$

where

$$\mathbf{p}^0(t) = -\Delta\mathbf{M}\ddot{\mathbf{u}}(t), \quad (3.28a)$$

$$\kappa_{ij}^0(t) = (1 - \mu_i) \kappa_{ij}(t). \quad (3.28b)$$

Actually, (3.27) is the equation of motion of the unmodified structure, which is subjected, besides the original excitation $\mathbf{f}_{\text{test}}(t)$, to the pseudo load $\mathbf{p}^0(t)$ and the virtual distortions $\kappa_{ij}^0(t)$ that model the considered structural modifications. The equivalency between the modifications and the pseudo load/virtual distortions is expressed in an implicit way by (3.28), which are a particular case of the equation (3.3). In general, their specific form depends on the type of the assumed modifications and it is different for modifications of other types; for another example see (5.6), which is a kinematic compatibility condition that describes the reaction forces of modeled virtual supports.

A virtual distortion $\kappa_{ij}^0(t)$ of a finite element can be identified with an additionally introduced time-dependent strain. For simulation purposes, it is modeled with the corresponding vector $\kappa_{ij}^0(t) \mathbf{n}_{ij}$ of self-equilibrated generalized forces applied locally in the DOFs of the involved element. Mass modifications are modeled with the vector $\mathbf{p}^0(t)$ of pseudo loads, which are unequilibrated

generalized forces applied in the DOFs related to mass modifications. In principle, it is possible to decompose virtual distortions into local nodal loads and merge them with $\mathbf{p}^0(t)$ in order to use a single vector of pseudo loads for the dual purpose of modeling both types of modifications simultaneously. It can be practically useful in purely experimental approaches, because forces are easier to generate experimentally than distortions, and such a possibility is further investigated in Chapter 4. However, in the general formulation it is advantageous to maintain the distinction between pseudo loads and virtual distortions because of the following practical as well as conceptual reasons:

- A finite element has a smaller number of distortions than DOFs (e.g., a 3D truss element needs six pseudo loads, but only a single distortion to model a modification of its stiffness).
- There is a natural gradation of virtual distortions of an element in terms of their importance, which is related to the order of the distortion (the magnitude of the corresponding eigenvalue) and to the excitation. Simulation or common engineering sense can be often used to determine which distortions of an element are dominant in its response and which are insignificant and can be thus neglected. A quantitative measure of importance is proposed in [58].
- The intuitiveness of the relation between the stiffness modification and the corresponding virtual distortions is conceptually appealing. It is especially apparent in the case of a truss element.

As confirmed by (3.27), the response $\mathbf{u}(t)$ of the damaged structure can be modeled by the following sum of the responses of the original unmodified structure to the external excitation $\mathbf{f}_{\text{test}}(t)$, the pseudo load $\mathbf{p}^0(t)$ and the virtual distortions $\kappa_{ij}^0(t)$:

$$\ddot{\mathbf{u}}(t) = \ddot{\mathbf{u}}^L(t) + (\ddot{\mathbf{B}}^{\text{up}} \mathbf{p}^0)(t) + \sum_{i,j} (\ddot{\mathbf{B}}_{ij}^{\text{uk}} \kappa_{ij}^0)(t), \quad (3.29a)$$

$$\kappa_{ij}(t) = \kappa_{ij}^L(t) + (\mathbf{B}_{ij}^{\text{kp}} \mathbf{p}^0)(t) + \sum_{k,l} (\mathbf{B}_{ijkl}^{\text{kk}} \kappa_{kl}^0)(t), \quad (3.29b)$$

which are a specific form of (3.1) and counterparts of (3.10), (3.15) and (2.20). The response to the pseudo loads and virtual distortions is expressed here through the respective matrix operators that are based on convolutions with the corresponding impulse response functions of the unmodified structure: $\ddot{\mathbf{B}}^{\text{up}}(t)$, which is the matrix of acceleration responses in all involved DOFs to impulse excitations in all involved DOFs; $\ddot{\mathbf{B}}_{ij}^{\text{uk}}(t)$, which is the vector of acceleration responses in all involved DOFs to an impulsive unit distortion φ_{ij} (local impulsive

load \mathbf{n}_{ij}); $\mathbf{B}_{ij}^{\kappa p}(t)$, which is the response vector of the j th distortion of the i th finite element to impulse excitations in all involved DOFs; and $B_{ijkl}^{\kappa\kappa}(t)$, which is the response of the j th distortion of the i th finite element to an impulsive unit distortion φ_{kl} (local impulsive load \mathbf{n}_{kl}). If the excitation and response DOFs are collocated, the respective acceleration impulse response functions contain an impulsive term at time $t = 0$, which affects the respective matrix operator as in (2.20c).

For notational simplicity, (3.28) and (3.29) are stated together in the following concise forms:

$$\boldsymbol{\nu}^0(t) = \mathbf{P}(\boldsymbol{\mu})\mathbf{a}(t), \quad (3.30)$$

$$\mathbf{a}(t) = \mathbf{a}^L(t) + (\mathcal{B}^{av}\boldsymbol{\nu}^0)(t), \quad (3.31)$$

where the vector $\boldsymbol{\nu}^0(t)$ collects together the pseudo load vector $\mathbf{p}^0(t)$ and all the virtual distortions $\kappa_{ij}^0(t)$ as defined in (3.2), the vector $\mathbf{a}(t)$ collects together the involved responses of the modified/damaged structure, that is $\ddot{\mathbf{u}}(t)$ and all the distortion responses $\kappa_{ij}(t)$, the vector $\mathbf{a}^L(t)$ collects all the baseline responses $\ddot{\mathbf{u}}^L(t)$ and $\kappa_{ij}^L(t)$ of the original intact structure, the vector $\boldsymbol{\mu}$ collects all the damage and modification parameters (all μ_i together with all the mass-related parameters that define $\Delta\mathbf{M}$), the matrix $\mathbf{P}(\boldsymbol{\mu})$ is a block matrix composed of $\Delta\mathbf{M}$ and a diagonal block with $1 - \mu_i$ on the diagonal, see (3.28), and the matrix operator \mathcal{B}^{av} collects all the matrix operators from (3.29) ordered in the way that match the internal order of the elements of the vectors $\mathbf{a}(t)$ and $\boldsymbol{\nu}^0(t)$. Notice that (3.30) and (3.31) are specific forms of (3.3) and (3.1), respectively.

3.3.3 Solution scheme

Equation (3.31) can be used to compute the response $\mathbf{a}(t)$ of the modified structure, provided the vector $\boldsymbol{\nu}^0(t)$ of pseudo loads and virtual distortions is known. However, (3.30) states $\boldsymbol{\nu}^0(t)$ in an implicit way and cannot be used for a direct computation. Hence, as outlined in Subsection 3.1.2.1, (3.31) is substituted into (3.30) to obtain the following system of Volterra integral equations:

$$\mathbf{P}(\boldsymbol{\mu})\mathbf{a}^L(t) = \boldsymbol{\nu}^0(t) - \mathbf{P}(\boldsymbol{\mu})(\mathcal{B}^{av}\boldsymbol{\nu}^0)(t), \quad (3.32)$$

where, apart from the unknown vector $\boldsymbol{\nu}^0(t)$, all the other terms are known. For modifications small enough, (3.32) constitutes a system of Volterra integral equations of the second kind and is thus uniquely solvable, see Theorem A.16 in Appendix or [112]. Solved (3.32), the response $\mathbf{a}(t)$ of the damaged structure is obtained from (3.31) by a substitution of the vector $\boldsymbol{\nu}^0(t)$.

Two important points should be noted here, which parallel the observations made in Subsection 3.1.3:

- *Required data.* Equations (3.30), (3.31) and (3.32) involve, besides the modification parameters $\boldsymbol{\mu}$, only selected local characteristics of the original unmodified structure (responses to $\mathbf{f}_{\text{test}}(t)$ and the matrix operators based on the reduced impulse responses). As a result, FE models of neither original nor modified structure are required to compute the response of the modified structure.
- *Numerical effectiveness.* According to (3.28), the pseudo loads vanish in all DOFs that are not directly related to the mass modifications $\Delta\mathbf{M}$ and, similarly, the virtual distortions are nonzero only in the damaged finite elements. As a result, the dimension of the system (3.32) is significantly reduced, which makes numerical computations more feasible. In other words, for localized modifications, only a small submatrix of the full impulse response matrix is required to construct $\mathbf{B}^{a\nu}$.

This is in agreement with the fact repeatedly mentioned in Section 3.1: the VDM uses a nonparametric model of the original structure which is reduced in size to the number of the virtual distortions and pseudo loads.

3.3.4 Time discretization

In practice, all the responses are either measured or obtained via numerical simulations and thus discrete. As a result, not the continuous-time (3.30), (3.31) and (3.32), but rather their discretized counterparts are usually used. In the matrix notation, they take the following forms of large linear equations:

$$\boldsymbol{\nu}^0 = \mathbf{P}(\boldsymbol{\mu})\mathbf{a}, \quad (3.33a)$$

$$\mathbf{a} = \mathbf{a}^L + \mathbf{B}^{a\nu}\boldsymbol{\nu}^0, \quad (3.33b)$$

$$\mathbf{P}(\boldsymbol{\mu})\mathbf{a}^L = [\mathbf{I} - \mathbf{P}(\boldsymbol{\mu})\mathbf{B}^{a\nu}] \boldsymbol{\nu}^0, \quad (3.33c)$$

where \mathbf{I} denotes the identity matrix of appropriate dimensions. The vectors \mathbf{a} , \mathbf{a}^L and $\boldsymbol{\nu}^0$ are the discrete-time counterparts of $\mathbf{a}^L(t)$, $\mathbf{a}(t)$ and $\boldsymbol{\nu}^0(t)$ sampled and collected in all considered time instants. Similarly, the matrix $\mathbf{B}^{a\nu}$ is the discretized counterpart of the corresponding matrix operator; with proper ordering of the discrete data, it has the form of a block matrix with Toeplitz blocks, similar in structure to that seen in Fig. 2.3 or in Fig. 4.2. For notational simplicity, the same symbols are used in (3.33) and in (3.30), (3.31) and (3.32) to denote vectors that depend on time and their discrete-time counterparts

(e.g., $\mathbf{a}(t)$ vs. \mathbf{a}). However, ambiguity can be avoided, because functions can be always distinguished from their discretized versions by the explicitly specified time argument t .

For an assumed modification scenario, quantified by the vector $\boldsymbol{\mu}$ of mass and stiffness modification parameters, (3.33c) is solved to obtain the equivalent vector $\boldsymbol{\nu}^0$ of pseudo loads and virtual distortions. As (3.33c) is a discretized version of a Volterra integral equation, it is usually significantly ill-conditioned and requires numerical regularization. The response of the modified structure is then computed using (3.33b). To this end, the solution vector $\boldsymbol{\nu}^0$ is multiplied by the matrix \mathbf{B}^{av} , which, as a discrete-time counterpart of a matrix operator based on convolution, acts as a smoothing operator that alleviates the effects of a potential under-regularization of (3.33c). As a result, the computed discrete response \mathbf{a} turns out in practice to be stable for a wide range of regularization parameters.

3.4 Inverse problem

The inverse problem, as outlined in Subsection 3.1.2.2, is the problem of characterizing a damage (or a modification) of a structure, given the measured response $\mathbf{a}^M(t)$ of the damaged/modified structure to a testing excitation $\mathbf{f}_{\text{test}}(t)$. Selected local characteristics of the original unmodified structure, that is the matrix operator \mathbf{B}^{av} and the response $\mathbf{a}^L(t)$ to the testing excitation, are required for this purpose. In practice, the discrete-time formulation is used, and the identification is based on (3.33). As in the direct problem, a nonparametric model is used, which is additionally reduced with respect to the placement of the testing excitation, sensors and potential structural damages. No full parametric structural model of neither the original nor the damaged structure is thus necessary for identification. As a result, no time-consuming repeated modifications and brute force simulations of the full model are required to account for the damages. This is an important advantage of the VDM-based reanalysis, which allows identification of localized modifications to be performed quickly.

Subsection 3.1.2.2 distinguishes between two general kinds of inverse problems: inverse problems with a known damage type and inverse problems with an unknown damage type or, in other words, between inverse problems with a known and an unknown function \mathbf{R} in (3.3). This chapter considers the former case: the damage is modeled here with certain modifications of structural stiffness and mass, see Subsection 3.3.1, so that (3.3) takes the specific form of (3.28) or (3.30).

3.4.1 Objective function

Assumed the type of the damage, the identification amounts to minimization of the discrepancy $F(\boldsymbol{\mu})$ between the measured response $\mathbf{a}^M(t)$ of the modified structure to a certain testing excitation and the corresponding simulated response $\mathbf{a}(t)$. The standard l^2 norm is usually used with the residuum of (3.5) and the objective function is then defined as in (3.6):

$$\begin{aligned} F(\boldsymbol{\mu}) &:= \frac{1}{2} \int_0^T \|\mathbf{d}(t)\|^2 dt \\ &= \frac{1}{2} \|\mathbf{d}\|^2 \\ &= \frac{1}{2} \langle \mathbf{d}, \mathbf{d} \rangle, \end{aligned} \tag{3.34a}$$

where $\boldsymbol{\mu}$ is the vector of the unknown damage parameters that need to be identified and $\langle \cdot, \cdot \rangle$ denotes the standard scalar product of two functions defined on the considered time interval $[0, T]$. The vector $\mathbf{d}(t)$ is the discrepancy between the modeled and measured responses,

$$\mathbf{d}(t) := \mathbf{a}^M(t) - \mathbf{a}(t), \tag{3.34b}$$

where $\mathbf{a}(t)$ is the response as simulated using the VDM and $\mathbf{a}^M(t)$ is the measured response of the modified structure to the same testing excitation. Alternatively, it may be sometimes beneficial to normalize the responses in order to equate the influence of the individual sensors on the objective function,

$$F(\boldsymbol{\mu}) := \frac{1}{2} \sum_i \frac{\|a_i^M - a_i\|^2}{\|a_i^M\|^2}, \tag{3.35}$$

where the subscript i indexes the sensors used for identification. As these two formulas differ in the constant terms only, (3.34a) is used in the following. The respective formulas corresponding to (3.35) can be obtained by a simple normalization of the summands.

Depending on the particular meaning of the modification parameters $\boldsymbol{\mu}$, they may be subjected to common sense constraints. For example, a stiffness modification parameter μ_i , as defined in (3.24), usually must obey at least a constraint of the form $0 \leq \mu_i \leq 1$.

3.4.2 Sensitivity analysis

First and second order sensitivity analysis of the identification problem is possible using either the direct differentiation method (DDM) or the adjoint variable method (AVM) [179–182]. As a result, exact Newton optimization techniques can be used for fast convergence of the optimization process [137] and quick identification.

The DDM performs sensitivity analysis of any response-based function directly via sensitivity analysis of the structural response, that is by using pre-computed derivatives of the response. On the other hand, the AVM uses a vector of the adjoint variables, which are specific to the analyzed objective function (or a constraint function). The most time-consuming operations are repetitive solutions of the differentiated or adjoint versions of (3.32), that is (3.37) or (3.43) respectively. All other operations are significantly faster. The total time of the first order analysis is then $O(N_\mu)$ for the DDM and $O(N_F)$ for the AVM, where N_μ denotes the number of damage parameters and N_F denotes the total number of the analyzed functions (the objective function $F(\boldsymbol{\mu})$ and the constraints). Notice also that certain optimization techniques do not require sensitivity analysis of the soft constraints (for example, a penalty function might be used instead). In such a case, the AVM significantly outperforms the DDM. For the second order analysis, the time complexities are $O(N_\mu^2)$ for the direct–direct method and $O(N_\mu + N_F)$ for the direct–adjoint method. In the following, both methods are described with respect to the objective function $F(\boldsymbol{\mu})$. The same derivation can be followed for constraints or other response-based functions.

3.4.2.1 First order sensitivity analysis

Direct differentiation of the objective function (3.34a) with respect to the parameter μ_i yields the following formula:

$$\begin{aligned} F_i(\boldsymbol{\mu}) &:= \frac{\partial}{\partial \mu_i} F(\boldsymbol{\mu}) \\ &= -\langle \mathbf{d}, \mathbf{a}_i \rangle, \end{aligned} \tag{3.36a}$$

where

$$\begin{aligned} \mathbf{a}_i(t) &:= \frac{\partial}{\partial \mu_i} \mathbf{a}(t) \\ &= (\mathcal{B}^{\alpha\nu} \boldsymbol{\nu}_i^0)(t) \end{aligned} \tag{3.36b}$$

is the i th derivative of the response vector $\mathbf{a}(t)$ obtained by a direct differentiation of (3.31). Other response-based functions, such as constraints, would yield

formulas different from (3.36a); however, they would always involve $\mathbf{a}_i(t)$. Equation (3.36b) expresses $\mathbf{a}_i(t)$ through the derivative $\boldsymbol{\nu}_i^0(t)$ of the vector $\boldsymbol{\nu}^0(t)$ of pseudo loads and virtual distortions, which is computed by the DDM using the differentiated (3.32),

$$\mathbf{P}_i(\boldsymbol{\mu})\mathbf{a}(t) = \boldsymbol{\nu}_i^0(t) - \mathbf{P}(\boldsymbol{\mu}) (\mathbf{B}^{av} \boldsymbol{\nu}_i^0)(t) \quad (3.37)$$

that needs to be solved anew separately for each i , that is a total of $N_{\boldsymbol{\mu}}$ times. Solved (3.37), the derivatives of any function $F(\boldsymbol{\mu})$ can be obtained by a simple substitution of the computed $\boldsymbol{\nu}_i^0(t)$ into (3.36), which is an operation significantly faster than solving (3.37).

In contrast to the DDM, the AVM collects all the terms in (3.37) on the right-hand side,

$$\mathbf{0} = \boldsymbol{\nu}_i^0(t) - \mathbf{P}(\boldsymbol{\mu}) (\mathbf{B}^{av} \boldsymbol{\nu}_i^0)(t) - \mathbf{P}_i(\boldsymbol{\mu})\mathbf{a}(t), \quad (3.38)$$

and takes the scalar product with a vector $\boldsymbol{\lambda}(t)$ of adjoint variables,

$$0 = \langle \boldsymbol{\lambda}, \mathbf{0} \rangle = \langle \boldsymbol{\lambda}, \boldsymbol{\nu}_i^0 - \mathbf{P}(\boldsymbol{\mu}) \mathbf{B}^{av} \boldsymbol{\nu}_i^0 - \mathbf{P}_i(\boldsymbol{\mu}) \mathbf{a} \rangle. \quad (3.39)$$

The result is added to (3.36a) in which (3.36b) has been substituted for $\mathbf{a}_i(t)$,

$$F_i(\boldsymbol{\mu}) = -\langle \mathbf{d}, \mathbf{B}^{av} \boldsymbol{\nu}_i^0 \rangle + \langle \boldsymbol{\lambda}, \boldsymbol{\nu}_i^0 - \mathbf{P}(\boldsymbol{\mu}) \mathbf{B}^{av} \boldsymbol{\nu}_i^0 - \mathbf{P}_i(\boldsymbol{\mu}) \mathbf{a} \rangle. \quad (3.40)$$

All the terms that contain the derivative $\boldsymbol{\nu}_i^0(t)$ are collected together to yield

$$F_i(\boldsymbol{\mu}) = \langle -(\mathbf{B}^{av})^* \mathbf{d} + \boldsymbol{\lambda} - (\mathbf{B}^{av})^* \mathbf{P}(\boldsymbol{\mu}) \boldsymbol{\lambda}, \boldsymbol{\nu}_i^0 \rangle - \langle \boldsymbol{\lambda}, \mathbf{P}_i(\boldsymbol{\mu}) \mathbf{a} \rangle, \quad (3.41)$$

where the symmetry of $\mathbf{P}(\boldsymbol{\mu})$ is used and the superscript \star denotes the adjoint operator, see (A.33),

$$(\mathbf{B} \cdot)(t) = \int_0^t \mathbf{B}(t-\tau) \cdot (\tau) d\tau, \quad (3.42a)$$

$$(\mathbf{B}^* \cdot)(t) = \int_t^T \mathbf{B}^T(\tau-t) \cdot (\tau) d\tau. \quad (3.42b)$$

The derivative $\boldsymbol{\nu}_i^0(t)$ is eliminated from (3.41) by choosing the vector $\boldsymbol{\lambda}(t)$ of the adjoint variables in such a way that the first scalar product vanishes as a whole.

It happens if the left multiplier of the scalar product vanishes, that is if $\boldsymbol{\lambda}(t)$ is a solution to

$$((\mathcal{B}^{av})^* \mathbf{d})(t) = \boldsymbol{\lambda}(t) - ((\mathcal{B}^{av})^* \mathbf{P}(\boldsymbol{\mu}) \boldsymbol{\lambda})(t), \quad (3.43)$$

which is called the adjoint integral equation. Equation (3.43), as (3.32), is a Volterra integral equation of the second kind, and for modification small enough it is uniquely solvable. Finally, given the adjoint variable $\boldsymbol{\lambda}(t)$, the first scalar product in (3.41) vanishes and the derivative $F_i(\boldsymbol{\mu})$ can be computed simply and quickly as

$$F_i(\boldsymbol{\mu}) = -\langle \boldsymbol{\lambda}, \mathbf{P}_i(\boldsymbol{\mu}) \mathbf{a} \rangle. \quad (3.44)$$

Notice that the adjoint variable $\boldsymbol{\lambda}(t)$ is independent of i , so that the full gradient $\nabla F(\boldsymbol{\mu})$ of the analyzed function can be computed at the cost of a single solution of the adjoint integral equation (3.43), instead of multiple solutions of (3.37) as required by the DDM. On the other hand, the left-hand side of the adjoint equation (3.43) depends on the analyzed function and so the equation needs to be solved separately for each of the analyzed functions (a total of N_F times). The time complexities of the DDM and AVM are thus proportional to the number of the parameters and analyzed functions, respectively.

3.4.2.2 Second order sensitivity analysis

If required, second order sensitivity analysis can be performed using the direct–direct method or, alternatively, the direct–adjoint method, which seems to be the fastest from the family of the second order adjoint methods [181]. Both methods require the first order derivatives $\boldsymbol{\nu}_i^0(t)$ to be computed using the DDM, that is by solving (3.37) a total of $N_\boldsymbol{\mu}$ times (once for each parameter μ_i), and then substituted into (3.36b) in order to obtain $\mathbf{a}_i(t)$. Double differentiation of the objective function with respect to the i th and j th parameters yields a formula analogous to (3.36a),

$$\begin{aligned} F_{ij}(\boldsymbol{\mu}) &:= \frac{\partial^2}{\partial \mu_i \partial \mu_j} F(\boldsymbol{\mu}) \\ &= \langle \mathbf{a}_j, \mathbf{a}_i \rangle - \langle \mathbf{d}, \mathbf{a}_{ij} \rangle, \end{aligned} \quad (3.45a)$$

where $\mathbf{a}_{ij}(t)$ denotes the second derivative of the response vector $\mathbf{a}(t)$,

$$\begin{aligned} \mathbf{a}_{ij}(t) &:= \frac{\partial^2}{\partial \mu_i \partial \mu_j} \mathbf{a}(t) \\ &= (\mathcal{B}^{av} \boldsymbol{\nu}_{ij}^0)(t). \end{aligned} \quad (3.45b)$$

Although other response-based functions can yield formulas that are different from (3.45a), they will always involve $\mathbf{a}_{ij}(t)$, which is expressed in (3.45b) through the second order derivative $\boldsymbol{\nu}_{ij}^0(t)$. The direct–direct method computes $\boldsymbol{\nu}_{ij}^0(t)$ by solving the twice differentiated (3.32),

$$\mathbf{P}_i(\boldsymbol{\mu})\mathbf{a}_j(t) + \mathbf{P}_j(\boldsymbol{\mu})\mathbf{a}_i(t) = \boldsymbol{\nu}_{ij}^0(t) - \mathbf{P}(\boldsymbol{\mu}) (\mathcal{B}^{av} \boldsymbol{\nu}_{ij}^0)(t), \quad (3.46)$$

which needs to be performed separately for each pair of indices i and j , that is a total of $\frac{1}{2}N_{\boldsymbol{\mu}}(N_{\boldsymbol{\mu}} + 1)$ times. The direct–direct method has thus the time complexity of $O(N_{\boldsymbol{\mu}}^2)$. It is assumed in (3.46) that $\mathbf{P}_{ij}(\boldsymbol{\mu})$ vanishes, because it is a linear function of $\boldsymbol{\mu}$, see (3.28) and (3.30). Solved (3.46), the second order derivatives and the Hessian of $F(\boldsymbol{\mu})$ can be obtained by a simple substitution of the computed $\boldsymbol{\nu}_{ij}^0(t)$ into (3.45), which is an operation much faster than solving (3.46).

The direct–adjoint method uses the adjoint variable $\boldsymbol{\lambda}(t)$ to eliminate $\boldsymbol{\nu}_{ij}^0(t)$ from (3.45a) and thus to avoid repetitive solutions of (3.46). The procedure is analogous to the procedure outlined in (3.38) to (3.44) and yields

$$F_{ij}(\boldsymbol{\mu}) = \langle \mathbf{a}_i, \mathbf{a}_j \rangle - \langle \boldsymbol{\lambda}, \mathbf{P}_i(\boldsymbol{\mu})\mathbf{a}_j + \mathbf{P}_j(\boldsymbol{\mu})\mathbf{a}_i \rangle, \quad (3.47)$$

where $\boldsymbol{\lambda}(t)$ is the same as used in the first order analysis, that is a solution to (3.43). The direct–adjoint method requires a separate solution of (3.37) for each parameter μ_i (a total of $N_{\boldsymbol{\mu}}$ solutions) as well as a separate solution of (3.43) for each of the analyzed functions (N_F solutions). Therefore, it has a linear time complexity with respect to the sum of the numbers of parameters and analyzed functions $O(N_{\boldsymbol{\mu}} + N_F)$, and it is thus preferable to the direct–direct method, unless $N_{\boldsymbol{\mu}} \ll N_F$.

Notice also that if the second order analysis is performed using the direct–adjoint method, both $\boldsymbol{\nu}_i^0(t)$ and $\boldsymbol{\lambda}(t)$ are known. Thus, the gradient of the objective function can be additionally computed at a low cost by (3.36) and compared for verification purposes to that obtained by (3.44).

3.4.3 Time discretization

In practice, the inverse problem is always solved in the discrete time setting using the discretized counterparts of the continuous-time formulas, see (3.33).

3.4.3.1 Objective function

In the discrete time setting, the objective function (3.34a) assumes the following form:

$$F(\boldsymbol{\mu}) := \frac{1}{2} \mathbf{d}^T \mathbf{d}, \quad (3.48a)$$

where the vector \mathbf{d} denotes the difference between the measured and the simulated discrete responses,

$$\mathbf{d} := \mathbf{a}^M - \mathbf{a}. \quad (3.48b)$$

Both the DDM and the AVM can be used to perform sensitivity analysis. The time complexities are summarized in Table 3.1. They are the same as in the continuous time setting, provided that solving (3.33c) (more exactly, its differentiated and adjoint versions) takes significantly more time than other operations.

Table 3.1. Time complexity of sensitivity analysis of the inverse problem ($N_{\boldsymbol{\mu}}$ is the number of identified parameters; N_F is the number of analyzed functions).

	DDM	AVM
First order analysis	$O(N_{\boldsymbol{\mu}})$	$O(N_F)$
Second order analysis	$O(N_{\boldsymbol{\mu}}^2)$	$O(N_F + N_{\boldsymbol{\mu}})$

3.4.3.2 Sensitivity analysis

The first and second order direct derivatives of $F(\boldsymbol{\mu})$ are given by

$$F_i(\boldsymbol{\mu}) = -\mathbf{d}^T \mathbf{a}_i, \quad (3.49)$$

$$F_{ij}(\boldsymbol{\mu}) = \mathbf{a}_i^T \mathbf{a}_j - \mathbf{d}^T \mathbf{a}_{ij}, \quad (3.50)$$

where \mathbf{a}_i and \mathbf{a}_{ij} are the first and second order derivatives of the response vector,

$$\mathbf{a}_i = \mathbf{B}^{a\nu} \boldsymbol{\nu}_i^0, \quad (3.51)$$

$$\mathbf{a}_{ij} = \mathbf{B}^{a\nu} \boldsymbol{\nu}_{ij}^0. \quad (3.52)$$

The DDM computes them by solving the differentiated versions of (3.33c),

$$\mathbf{P}_i(\boldsymbol{\mu}) \mathbf{a} = [\mathbf{I} - \mathbf{P}(\boldsymbol{\mu}) \mathbf{B}^{a\nu}] \boldsymbol{\nu}_i^0, \quad (3.53)$$

$$\mathbf{P}_i(\boldsymbol{\mu}) \mathbf{a}_j + \mathbf{P}_j(\boldsymbol{\mu}) \mathbf{a}_i = [\mathbf{I} - \mathbf{P}(\boldsymbol{\mu}) \mathbf{B}^{a\nu}] \boldsymbol{\nu}_{ij}^0, \quad (3.54)$$

where \mathbf{a}_i is computed in a similar way as \mathbf{a}_i in (3.51). Equation (3.53) needs to be solved N_μ times, while (3.54) requires as many as $\frac{1}{2}N_\mu(N_\mu + 1)$ solutions. However, notice that (3.33c), (3.53) and (3.54) differ by the left-hand side only and all have the same system matrix, so that successive solutions might be significantly faster than the first solution.

The AVM computes the derivative of $F(\boldsymbol{\mu})$ as

$$F_i(\boldsymbol{\mu}) = -\boldsymbol{\lambda}^T \mathbf{P}_i(\boldsymbol{\mu}) \mathbf{a}, \quad (3.55)$$

where $\boldsymbol{\lambda}$ is the adjoint vector that satisfies the equation adjoint to (3.33c), that is

$$[\mathbf{B}^{av}]^T \mathbf{d} = [\mathbf{I} - \mathbf{B}^T \mathbf{P}(\boldsymbol{\mu})] \boldsymbol{\lambda}. \quad (3.56)$$

Equation (3.56) needs to be solved once for each of the analyzed functions, that is a total of N_F times.

Solved (3.53) and (3.56) (a total of $N_\mu + N_F$ solutions), the second derivatives of $F(\boldsymbol{\mu})$ can be computed using the direct–adjoint method as

$$F_{ij}(\boldsymbol{\mu}) = \mathbf{a}_i^T \mathbf{a}_j - \boldsymbol{\lambda}^T \mathbf{P}_i(\boldsymbol{\mu}) \mathbf{a}_j - \boldsymbol{\lambda}^T \mathbf{P}_j(\boldsymbol{\mu}) \mathbf{a}_i, \quad (3.57)$$

which is the discrete-time counterpart of (3.47). Such an approach is usually faster than that of the DDM and (3.50), and it additionally allows the gradient of $F(\boldsymbol{\mu})$ to be quickly computed using (3.55) as well as (3.49), which can be used for verification purposes.

4

Model-free structural health monitoring

The previous chapter has introduced the virtual distortion method in a time-domain formulation, emphasizes its characteristically nonparametric approach to structural modeling and hints at the possibility of a purely experimental modeling based on experimentally measured impulse response functions. This chapter aims at exploring this possibility: it presents, discusses and verifies experimentally a VDM-based approach to structural health monitoring that directly utilizes the experimentally measured structural impulse responses. Even though the approach allows parametrized modifications and damages to be identified, the response of the modified structure is modeled in an essentially local and nonparametric or data-driven way. The approach obviates the need for a parametric numerical modeling and for laborious initial model updating. Moreover, no topological information about the global structure is required, besides potential locations of the modifications given in the terms of the set of the related degrees of freedom (DOFs). In the field of SHM, these features are characteristic enough to warrant the name of a *model-free* approach. The chapter revises and extends the research presented in [29, 30, 38, 41–45].

The first section offers an overview of the state-of-the-art and an introduction. The second section states the time-domain formulation, including the direct problem of modeling the response of the modified structure, the inverse problem of identification of structural modifications along with its sensitivity analysis, and discusses the discretization process. A corresponding formulation in frequency domain is presented in the third section. The fourth section discusses a possible extension to identification of inelastic impacts. Finally, selected experimental results are presented in the last section. A 3D truss structure with 70 elements and 26 nodes is used. The approach is tested in identification of mass modifications that occur in a single node or in two nodes concurrently. Given the initially measured local quasi impulse responses, even a single sensor and a single testing excitation are sufficient for identification.

4.1 State-of-the-art and introduction

A general motivation behind the research on the nonparametric approach investigated in this chapter is the need for a practical identification technique that could be used in black-box type global monitoring systems for identification of modifications, external dynamic loads and damages of real-world, large and complex structures.

Most of the low-frequency methods used for global structural health monitoring [11, 12, 15, 183–186] can be classified into the two following general groups:

- *Model-based methods*, which rely on a parametric numerical model of the monitored structure. Various types of such models can be used, including modal models [81, 187, 188], models based on various formulations of the Finite Element (FE) method [57, 189–193] or on a continuous formulation [194]. The identification is stated in the form of the problem of a minimization of the discrepancy between the measured response¹ of the damaged structure and the computed response of the modeled structure. A set of parameters of the model needs to be designated that is assumed to capture important characteristics of the involved structural modifications; these parameters are then used as the optimization variables. The optimization is performed either in an analytical way [195] or using computational intelligence techniques, such as genetic algorithms [194, 196–198] or others [199].
- *Pattern recognition methods* rely on a database of numerical fingerprints of low dimension that are extracted from several responses of the modified structure [200–204]. The responses that are used to form the database need to be collected ahead of the identification either by simulations or by experimental measurements of the involved structure with various modification scenarios implemented [205]. The fingerprints should discriminate well between the unmodified structure and the scenarios considered for identification. Given the database and the measured response of the monitored structure, the actual modification is identified using the fingerprints only, without a direct insight into their actual mechanical meaning. Techniques of computational intelligence, such as neural networks [206–210], are usually used for this purpose. As a result, neither a numerical model of the structure nor simulation is required at the identification stage.

¹Or certain structural characteristics, which can be extracted from measured response, such as modal parameters (natural frequencies, mode shapes or curvatures, damping ratios, etc.).

Most of these methods can be used for full identification, that is they are capable of detecting, localizing and quantifying the unknown modification or damage, see [186] for a comparison of two specific methods. However, in case of many structures, it may not be possible to actually introduce the modifications in order to perform the measurements and build the fingerprint database. Similarly, an accurate numerical model of a complex real-world structure may be hard to obtain and not available [211–213].

Therefore, there is a third group of methods, which rely on certain *structural invariants* of the monitored structure that can be computed directly from the measured response [214]. Most often, these invariants are modal [15] or based on wavelet or time series analysis [215]. Compatibility of the strain tensor and the corresponding spatial filters are considered in [216, 217]. Lyapunov exponents are used for monitoring of a nonlinear structure in [218], while [219] tests the invariants related to recurrence plots and [220] deals with trajectory patterns in diagnostics of rotating machinery. The response surface methodology is discussed in [221, 222]. Modification is detected by assessing the discrepancy between the invariants of the original undamaged structure and the invariants computed from the performed measurements. By a proper spatial distribution of sensors in the structure, these invariants can be compared locally, which may allow the detected modification to be also approximately localized.

The approach described in this chapter avoids actual modifications as well as parametric numerical modeling of the structure, and so it could be classified to the third group. On the other hand, it has no clearly defined invariant, and unlike other methods from this group, it is capable of quantification of parametrically expressed damages. The damages are assumed here to be quantified in terms of absolute modifications $\Delta\mathbf{M}$ and $\Delta\mathbf{K}$ to the structural mass and stiffness matrices. In line with the general methodology of the VDM, these modifications are modeled by the equivalent pseudo loads $\mathbf{p}^0(t)$ that act in the related degrees of freedom (DOFs) of the unmodified structure. As defined in (4.7), the pseudo loads consist of two parts: one imitates the inertial effects of mass modifications, while the other implements the virtual distortions. As a result, a single vector of the pseudo loads models mass modifications and stiffness-related damages, which is unlike the more intuitive standard approach of the VDM, where separate virtual distortions $\boldsymbol{\kappa}^0(t)$ are used for modeling of uniform stiffness modifications of the involved finite elements, see (3.28). However, such distortions are not easy to be applied experimentally, which confines them to applications with a known FE model of the structure.

Given the modifications, the *direct problem* consists of computing the response of the damaged structure to a certain testing excitation, given the base-

line response of the original unmodified structure and a set of its experimentally obtained impulse response functions. The influence of modifications on the response is computed by convolving the equivalent pseudo loads with the impulse responses. In time domain, the pseudo loads are given in the form of a unique solution to a certain linear integral equation of the Volterra type, which is discretized into a large ill-conditioned structured linear system. The system is solved using the conjugate gradient least squares algorithm [128], which has regularizing properties. The block Toeplitz structure of the system matrix allows the necessary matrix–vector products to be quickly computed using the fast Fourier transform, while the matrix is stored in computer memory in a reduced form. In frequency domain, the pseudo loads can be found at a smaller numerical cost for each frequency of interest separately; however, this is at the cost of losing the direct control over the regularization level of the solution.

As in the previous chapter, the *inverse problem* of identification of structural modifications is formulated as an optimization problem of minimizing the discrepancy between the measured and the modeled structural responses to a given testing excitation. The adjoint variable method [179–181] is employed for fast and exact first and second order sensitivity analysis, so that quickly convergent Newton optimization algorithms can be used in order to speed up the identification.

4.2 Time-domain formulation

The time-domain formulation is directly based on the general formulation of the VDM, which is described in Chapter 3. The derivations of the direct and the inverse problems are analogical to those presented in Sections 3.3 and 3.4 respectively. However, there are two important differences that stem from the intended experimental and nonparametric character of the approach:

- Only pseudo loads are used for modeling the structural damages.
- Experimentally obtained responses to quasi impulsive excitations have to be used instead of the exact impulse responses (Subsection 4.2.1.4), since the latter are impossible to obtain experimentally.

4.2.1 The direct problem

In agreement with the general methodology of the VDM, structural modifications are modeled with the equivalent pseudo loads, which are coupled to the response and act in the unmodified structure to imitate the effects of the

modifications. Hence, similarly as in (3.1) and (3.31), the time-domain response $\mathbf{a}(t)$ of the modified structure to a given external excitation $\mathbf{p}(t)$ is expressed as a sum of

1. the response $\mathbf{a}^L(t)$ of the original unmodified structure to the same external excitation, which is called the *linear response*, and
2. the response of the same unmodified structure to the pseudo loads $\mathbf{p}^0(t)$, which is called the *residual response* and denoted by $\mathbf{u}^R(t)$.

The response is found in two steps: first the pseudo loads are computed and then the corresponding response. The pseudo loads are coupled to the response, hence they are given in an implicit form and have to be found in the first step by solving the integral equation (4.9b), which is the counterpart of (3.32).

4.2.1.1 Residual response

Let $\mathbf{p}^0(t)$ be a vector of certain pseudo loads that excite the original unmodified structure, and denote by $\mathbf{u}^R(t)$ the vector of the corresponding structural response. The structure is assumed to be linear and governed by the following equation of motion:

$$\mathbf{M}\ddot{\mathbf{u}}^R(t) + \mathbf{C}\dot{\mathbf{u}}^R(t) + \mathbf{K}\mathbf{u}^R(t) = \mathbf{p}^0(t), \quad (4.1)$$

where \mathbf{M} , \mathbf{C} and \mathbf{K} are respectively the mass, damping and stiffness matrices of the unmodified structure.

The structure is linear, hence the response can be expressed as in (2.17), that is in the form of a convolution of the pseudo load vector $\mathbf{p}^0(t)$ with the structural impulse responses that are collected in the matrix $\mathbf{H}(t)$,

$$\mathbf{u}^R(t) = \int_0^t \mathbf{H}(t-\tau) \mathbf{p}^0(\tau) d\tau, \quad (4.2a)$$

$$\ddot{\mathbf{u}}^R(t) = \mathbf{M}^{-1} \mathbf{p}^0(t) + \int_0^t \ddot{\mathbf{H}}(t-\tau) \mathbf{p}^0(\tau) d\tau, \quad (4.2b)$$

or, using the operator notation, as in (2.20),

$$\mathbf{u}^R(t) = (\mathcal{H}\mathbf{p}^0)(t), \quad (4.3a)$$

$$\begin{aligned} \ddot{\mathbf{u}}^R(t) &= \mathbf{M}^{-1}\mathbf{p}^0(t) + (\ddot{\mathcal{H}}_\delta\mathbf{p}^0)(t) \\ &= (\ddot{\mathcal{H}}\mathbf{p}^0)(t), \end{aligned} \quad (4.3b)$$

where \mathcal{H} and $\ddot{\mathcal{H}}_\delta$ are the matrix Volterra operators that correspond to convolutions with the respective impulse responses, and $\ddot{\mathcal{H}} = \mathbf{M}^{-1}\mathcal{I} + \ddot{\mathcal{H}}_\delta$, where \mathcal{I} is the identity operator. Notice that the measured impulse responses are discrete, so that the impulsive term is in practice incorporated into the response at time $t = 0$ and the discretized versions of the operators \mathcal{H} and $\ddot{\mathcal{H}}$ can be obtained directly from the experimental measurements, see Subsection 4.2.3.

4.2.1.2 Structural modifications and the equivalent pseudo load

Let $\mathbf{f}_{\text{test}}(t)$ be an external excitation (testing excitation) and denote by $\mathbf{u}^L(t)$ the corresponding response of the unmodified structure. The equation of motion can be stated as

$$\mathbf{M}\ddot{\mathbf{u}}^L(t) + \mathbf{C}\dot{\mathbf{u}}^L(t) + \mathbf{K}\mathbf{u}^L(t) = \mathbf{f}_{\text{test}}(t). \quad (4.4)$$

The modified structure, if subjected to the same testing excitation $\mathbf{f}_{\text{test}}(t)$, responds with $\mathbf{u}(t)$. This response satisfies the following equation of motion, compare with (3.25):

$$(\mathbf{M} + \Delta\mathbf{M})\ddot{\mathbf{u}}(t) + \mathbf{C}\dot{\mathbf{u}}(t) + (\mathbf{K} + \Delta\mathbf{K})\mathbf{u}(t) = \mathbf{f}_{\text{test}}(t), \quad (4.5)$$

where the structural modification (damage) is defined by $\Delta\mathbf{M}$ and $\Delta\mathbf{K}$, and where it is assumed that these modifications do not considerably influence the damping properties for the reasons mentioned in Subsection 3.3.1. The modification terms in (4.5) can be moved to the right-hand side to yield the following analogue of (3.27):

$$\mathbf{M}\ddot{\mathbf{u}}(t) + \mathbf{C}\dot{\mathbf{u}}(t) + \mathbf{K}\mathbf{u}(t) = \mathbf{f}_{\text{test}}(t) + \mathbf{p}^0(t), \quad (4.6)$$

which is the equation of motion of the original unmodified structure, in which the structural modification are modeled with the equivalent pseudo load vector $\mathbf{p}^0(t)$,

$$\mathbf{p}^0(t) = -\Delta\mathbf{M}\ddot{\mathbf{u}}(t) - \Delta\mathbf{K}\mathbf{u}(t). \quad (4.7)$$

Unlike in (3.28), a single pseudo load vector is used here to model both types of modifications simultaneously and it is thus a sum of the two respective parts.

According to (4.6), the response $\mathbf{u}(t)$ depends on the excitation $\mathbf{f}_{\text{test}}(t)$ and on the pseudo load $\mathbf{p}^0(t)$. The structure is linear, and by a comparison of (4.1), (4.4) and (4.6), the response $\mathbf{u}(t)$ turns out to be the sum of the linear response $\mathbf{u}^L(t)$ and the residual response $\mathbf{u}^R(t)$,

$$\mathbf{u}(t) = \mathbf{u}^L(t) + \mathbf{u}^R(t), \quad (4.8a)$$

$$\ddot{\mathbf{u}}(t) = \ddot{\mathbf{u}}^L(t) + \ddot{\mathbf{u}}^R(t). \quad (4.8b)$$

Equations (4.3) is substituted into (4.8); a subsequent substitution of the result into (4.7) yields the following system of Volterra integral equations of the second kind with the pseudo load vector $\mathbf{p}^0(t)$ as the unknown:

$$\begin{aligned} -\Delta \mathbf{M}\ddot{\mathbf{u}}^L(t) - \Delta \mathbf{K}\mathbf{u}^L(t) \\ = (\mathbf{I} + \Delta \mathbf{M}\mathbf{M}^{-1}) \mathbf{p}^0(t) + ((\Delta \mathbf{M}\ddot{\mathcal{H}}_\delta + \Delta \mathbf{K}\mathcal{H}) \mathbf{p}^0)(t). \end{aligned} \quad (4.9a)$$

In practice, such a system is usually significantly ill-conditioned. However, it follows from the Riesz theory [112] that it is well-posed, provided the matrix $\mathbf{I} + \Delta \mathbf{M}\mathbf{M}^{-1}$ is nonsingular or, equivalently, if the matrix $\mathbf{M} + \Delta \mathbf{M}$ is nonsingular. Therefore, (4.9a) has a unique solution, if the considered mass modification is small enough to uphold the positive definiteness of the modified mass matrix $\mathbf{M} + \Delta \mathbf{M}$. This is a requirement that is satisfied in all practical cases, unless the modification is large enough to remove all the mass related to selected DOFs of the global structure. Otherwise, (4.9a) becomes an ill-posed problem, so that in certain uncommon cases its solution may then not exist (for example in the case of the testing excitation applied in a detached massless DOF, which is impossible in practice).

If the operator $\ddot{\mathcal{H}}$ is used instead of $\ddot{\mathcal{H}}_\delta$, then (4.9a) takes the following form:

$$-\Delta \mathbf{M}\ddot{\mathbf{u}}^L(t) - \Delta \mathbf{K}\mathbf{u}^L(t) = \mathbf{p}^0(t) + ((\Delta \mathbf{M}\ddot{\mathcal{H}} + \Delta \mathbf{K}\mathcal{H}) \mathbf{p}^0)(t), \quad (4.9b)$$

which does not directly involve the unknown mass matrix \mathbf{M} . Even though the formulation of (4.9b) is not standard, it seems to be more practical: the experimentally measured impulse response incorporates an impulsive term at $t = 0$, so that in practice a discretized version of $\ddot{\mathcal{H}}$ is easier to be obtained than that of $\ddot{\mathcal{H}}_\delta$. Notice that, besides the unknown pseudo load, all the terms in (4.9b) are known in an experiment. Thus, given the modifications, the equation can be formed and solved to obtain the equivalent pseudo load vector $\mathbf{p}^0(t)$. Notice also that it can be deduced from (4.7) or (4.9b) that $\mathbf{p}^0(t)$ is nonzero only in the DOFs that are directly related to the modifications (correspond to nonzero rows/columns of the modification matrices $\Delta \mathbf{M}$ and $\Delta \mathbf{K}$). Consequently, the actual dimensions of (4.9b) are significantly reduced with respect to the total number of all structural DOFs, and only a correspondingly reduced impulse response matrix is required to form the equation instead of the full matrix $\mathbf{H}(t)$.

4.2.1.3 Response of the modified structure

The modifications are modeled with the equivalent pseudo load $\mathbf{p}^0(t)$ that acts in the original unmodified structure. Given the response $\mathbf{u}^L(t)$ of unmod-

ified structure to the testing excitation, the pseudo load equivalent to a given modification can be obtained by solving the system (4.9b). Using (4.8) and (4.3), the response of the modified structure to the same testing excitation can be found to be the sum of the response of the unmodified structure and the cumulative effects of the pseudo loads,

$$\mathbf{u}(t) = \mathbf{u}^L(t) + (\mathcal{H}\mathbf{p}^0)(t), \quad (4.10a)$$

$$\ddot{\mathbf{u}}(t) = \ddot{\mathbf{u}}^L(t) + (\ddot{\mathcal{H}}\mathbf{p}^0)(t). \quad (4.10b)$$

4.2.1.4 Experimental quasi impulse responses

The solution to the direct problem outlined so far assumes that the structural impulse response functions are measured and available. However, exact impulse responses are hardly available in practice: one can measure only responses to quasi impulsive excitations that last several time steps. Two solutions are possible:

1. either the measured responses are deconvolved with respect to the actually applied quasi impulsive excitations in order to obtain the exact impulse responses
2. or, as in Subsection 2.2.4.1, the measured responses are directly used in computations by a representation of the pseudo load in terms of the experimentally applied quasi impulsive excitations.

The first approach requires a separate ill-conditioned deconvolution to be performed for each pair of a quasi impulsive excitation and the corresponding response. This is avoided in the second approach, which implicitly embeds the deconvolutions in a modified version of (4.9b). The pseudo loads are expressed in the form of a convolution of the actually applied quasi impulsive excitations $q_i(t)$, which all have to satisfy $q_i(t) = 0$ for $t \leq 0$, with certain unknown functions $p_i(t)$,

$$p_i^0(t) = (q_i * p_i)(t) = \int_0^t q_i(t - \tau) p_i(\tau) d\tau, \quad (4.11a)$$

where i indexes all DOFs related to the considered modifications and subjected to the excitation $q_i(t)$. Equation (4.11a) can be collected for all involved DOFs and stated in the operator notation as

$$\mathbf{p}^0(t) = (\mathcal{Q}\mathbf{p})(t), \quad (4.11b)$$

where \mathbf{Q} is the corresponding diagonal matrix convolution operator. A substitution of (4.11b) into (4.9b) and (4.10) yields their following counterparts:

$$-\Delta \mathbf{M}\ddot{\mathbf{u}}^L(t) - \Delta \mathbf{K}\mathbf{u}^L(t) = \left((\mathbf{Q} + \Delta \mathbf{M}\ddot{\mathcal{H}} + \Delta \mathbf{K}\mathcal{H}) \mathbf{p} \right) (t), \quad (4.12)$$

and

$$\mathbf{u}(t) = \mathbf{u}^L(t) + (\mathcal{H}\mathbf{p})(t), \quad (4.13a)$$

$$\ddot{\mathbf{u}}(t) = \ddot{\mathbf{u}}^L(t) + (\ddot{\mathcal{H}}\mathbf{p})(t), \quad (4.13b)$$

where, in comparison to the symbols used in (4.9b) and (4.10), the following substitutions have been performed:

$$\begin{aligned} \mathcal{H} &\leftarrow \mathcal{H}\mathbf{Q}, \\ \ddot{\mathcal{H}} &\leftarrow \ddot{\mathcal{H}}\mathbf{Q}. \end{aligned} \quad (4.14)$$

In both cases the resulting \mathcal{H} and $\ddot{\mathcal{H}}$ are the matrix integral operators that correspond to the convolutions with the experimentally measured responses to the actually applied quasi impulsive excitations. Notice that if the experimentally applied excitation is indeed impulsive, then $\mathbf{Q} = \mathbf{I}$ and (4.12) and (4.13) simplify to (4.9b) and (4.10).

4.2.1.5 Required data and computations

The VDM-based procedure described above uses essentially a local nonparametric model of the unmodified structure that consists of its

- Structural impulse responses, which can be (Subsection 4.2.1.4) either exact or approximate, and which are used to form the required matrix integral operators.
- Structural responses $\mathbf{u}^L(t)$ and $\ddot{\mathbf{u}}^L(t)$ to the testing excitation $\mathbf{f}_{\text{test}}(t)$.

These characteristics can be measured experimentally prior to modeling of the modifications. According to (4.7), the pseudo loads vanish in the DOFs that are not directly related to the modification. As a result, only a reduced impulse response matrix is required: the responses that constitute the model need to be measured only by the sensors intended for identification and in the DOFs related to potential modifications. Depending on the assumed form of these modifications, they can form only a small subset of all structural DOFs. As a result, full instrumentation of the involved structure is not necessary, which makes experimental investigations more feasible.

Given such a model of the unmodified structure and a modification defined by $\Delta\mathbf{M}$ and $\Delta\mathbf{K}$, the corresponding response of the modified structure to the same testing excitation $\mathbf{f}(t)$ is computed in two steps:

1. The equivalent pseudo load vector $\mathbf{p}^0(t)$ or the corresponding convolution function $\mathbf{p}(t)$ is found by solving respectively (4.9b) or (4.12).
2. The response is computed by (4.10) or (4.13).

Notice that all these computations are based directly on the experimentally measured data, so that a parametric numerical model of neither the unmodified nor the modified structure needs to be built and updated.

4.2.2 The inverse problem

In time domain, the inverse problem is stated in the standard form of an optimization problem of minimization of the mean square distance between the measured and the modeled displacement responses of the modified structure to a certain testing excitation $\mathbf{f}_{\text{test}}(t)$. The direct differentiation method as well as the adjoint variable method are employed for an exact first and second order sensitivity analysis; for a single objective function the latter method is faster by one order of magnitude, see Table 3.1 or [179–181]. Thanks to the fast second order sensitivity analysis, Newton optimization methods can be used for fast convergence and identification [137]. Basically, a similar formulation is used as in Section 3.4, despite that only pseudo loads and experimental quasi impulse responses are used for modeling purposes.

4.2.2.1 Objective function

Given the testing excitation $\mathbf{f}_{\text{test}}(t)$, the time-domain identification of the unknown modification is based on the comparison between the measured response $\mathbf{u}^{\text{M}}(t)$ of the modified structure and its modeled response $\mathbf{u}(t)$. The identification is equivalent to the minimization of the objective function defined as in (3.34a):

$$F(\boldsymbol{\mu}) := \frac{1}{2} \langle \mathbf{d}, \mathbf{d} \rangle, \quad (4.15a)$$

where $\boldsymbol{\mu}$ is a vector of parameters that fully define the modification $\Delta\mathbf{K}$ and $\Delta\mathbf{M}$, and $\mathbf{d}(t)$ is the difference between the measured and the modeled response defined as in (3.34b),

$$\mathbf{d}(t) := \mathbf{u}^{\text{M}}(t) - \mathbf{u}(t). \quad (4.15b)$$

4.2.2.2 Direct differentiation method

Gradient. Similar as in (3.34), a direct differentiation of the displacement response (4.13a) with respect to the i th modification parameter μ_i yields

$$\begin{aligned}\mathbf{u}_i(t) &:= \frac{\partial}{\partial \mu_i} \mathbf{u}(t) \\ &= (\mathcal{H}\mathbf{p}_i)(t),\end{aligned}\tag{4.16a}$$

so that

$$\begin{aligned}F_i(\boldsymbol{\mu}) &:= \frac{\partial}{\partial \mu_i} F(\boldsymbol{\mu}) \\ &= -\langle \mathbf{d}, \mathbf{u}_i \rangle \\ &= -\langle \mathbf{d}, \mathcal{H}\mathbf{p}_i \rangle.\end{aligned}\tag{4.16b}$$

Equations (4.16) involve the derivatives $\mathbf{p}_i(t)$ of the convolution function. The DDM computes them by solving (separately for each modification parameter μ_i) the differentiated (4.12),

$$-\Delta\mathbf{M}_i \ddot{\mathbf{u}}(t) - \Delta\mathbf{K}_i \mathbf{u}(t) = \left((\mathcal{Q} + \Delta\mathbf{M}\ddot{\mathcal{H}} + \Delta\mathbf{K}\mathcal{H}) \mathbf{p}_i \right) (t).\tag{4.17}$$

Hessian. Direct differentiation of (4.16) with respect to μ_j yields the second derivative $\mathbf{u}_{ij}(t)$ of the displacement response,

$$\begin{aligned}\mathbf{u}_{ij}(t) &:= \frac{\partial^2 \mathbf{u}(t)}{\partial \mu_i \partial \mu_j} \\ &= (\mathcal{H}\mathbf{p}_{ij})(t),\end{aligned}\tag{4.18a}$$

and the second derivative of the objective function,

$$\begin{aligned}F_{ij}(\boldsymbol{\mu}) &:= \frac{\partial^2 F(\boldsymbol{\mu})}{\partial \mu_i \partial \mu_j} \\ &= \langle \mathbf{u}_i, \mathbf{u}_j \rangle - \langle \mathbf{d}, \mathbf{u}_{ij} \rangle.\end{aligned}\tag{4.18b}$$

Equations (4.18) involve the first and second derivatives of the pseudo loads. The DDM computes the first derivatives by solving (4.17) separately for each i , while the second derivatives $\mathbf{p}_{ij}(t)$ are computed using (4.17) differentiated once again,

$$\begin{aligned}-\Delta\mathbf{M}_i \ddot{\mathbf{u}}_j(t) - \Delta\mathbf{K}_i \mathbf{u}_j(t) - \Delta\mathbf{M}_j \ddot{\mathbf{u}}_i(t) - \Delta\mathbf{K}_j \mathbf{u}_i(t) \\ = \left((\mathcal{Q} + \Delta\mathbf{M}\ddot{\mathcal{H}} + \Delta\mathbf{K}\mathcal{H}) \mathbf{p}_{ij} \right) (t),\end{aligned}\tag{4.19}$$

where it is assumed that $\Delta\mathbf{M}$ and $\Delta\mathbf{K}$ depend linearly on the modification parameters μ_i and μ_j , so that their second derivatives vanish, $\Delta\mathbf{M}_{ij} = \Delta\mathbf{K}_{ij} = \mathbf{0}$, which happens for example if the modification parameters are simply the added or removed masses, cross-sections of elements or their stiffnesses, etc. Equation (4.19) needs to be solved several times, separately for each pair of i and j .

4.2.2.3 Adjoint variable method

If the number of modification parameters is denoted by N_μ , then the DDM needs N_μ solutions of (4.17) to compute the gradient of the objective function and as many as $O(N_\mu^2)$ solutions of (4.19) to compute its Hessian. Both equations are systems of Volterra integral equations, and hence sensitivity analysis via the DDM is numerically costly to a significant degree. If a single objective function is used, the AVM allows these costs to be reduced by one order of magnitude, see Table 3.1.

Gradient. Similarly as described in Subsection 3.4.2.1, the AVM collects all the terms in (4.17) on the right-hand side and takes the scalar product with a vector $\boldsymbol{\lambda}(t)$ of adjoint variables. The result vanishes, and so it can be added to (4.16b),

$$\begin{aligned} F_i(\boldsymbol{\mu}) = -\langle \mathbf{d}, \mathcal{H}\mathbf{p}_i \rangle + \left\langle \boldsymbol{\lambda}, \left(\mathcal{Q} + \Delta\mathbf{M}\ddot{\mathcal{H}} + \Delta\mathbf{K}\mathcal{H} \right) \mathbf{p}_i \right. \\ \left. + \Delta\mathbf{M}_i\ddot{\mathbf{u}} + \Delta\mathbf{K}_i\mathbf{u} \right\rangle. \end{aligned} \quad (4.20)$$

All the terms containing $\mathbf{p}_i(t)$ in (4.20) are collected together to yield

$$\begin{aligned} F_i(\boldsymbol{\mu}) = \left\langle -\mathcal{H}^*\mathbf{d} + \left(\mathcal{Q}^* + \ddot{\mathcal{H}}^*\Delta\mathbf{M} + \mathcal{H}^*\Delta\mathbf{K} \right) \boldsymbol{\lambda}, \mathbf{p}_i \right\rangle \\ + \langle \boldsymbol{\lambda}, \Delta\mathbf{M}_i\ddot{\mathbf{u}} + \Delta\mathbf{K}_i\mathbf{u} \rangle, \end{aligned} \quad (4.21)$$

where the superscript $*$ denotes the adjoint operator, see (3.42) or (A.33). The derivatives $\mathbf{p}_i(t)$ of the convolution functions are eliminated from (4.21) by choosing the vector $\boldsymbol{\lambda}(t)$ of the adjoint variables in such a way that the first scalar product vanishes. As a result,

$$F_i(\boldsymbol{\mu}) = \langle \boldsymbol{\lambda}, \Delta\mathbf{M}_i\ddot{\mathbf{u}} + \Delta\mathbf{K}_i\mathbf{u} \rangle, \quad (4.22)$$

provided that $\boldsymbol{\lambda}(t)$ is a solution to the adjoint integral equation,

$$(\mathcal{H}^*\mathbf{d})(t) = \left(\left(\mathcal{Q}^* + \ddot{\mathcal{H}}^*\Delta\mathbf{M} + \mathcal{B}^*\Delta\mathbf{K} \right) \boldsymbol{\lambda} \right) (t), \quad (4.23)$$

which is a counterpart of (3.43).

Notice that the adjoint variable $\boldsymbol{\lambda}(t)$ is independent of i , hence the gradient of the objective function $\nabla F(\boldsymbol{\mu})$ can be computed at the cost of only a single solution of the adjoint integral equation instead of N_μ solutions of (4.17) required by the DDM. Nevertheless, the solution needs to be repeated separately for each analyzed objective function.

Hessian. The direct–adjoint method, which seems to be the quickest from the family of the second order adjoint variable methods, see, e.g., [181], is employed here to reduce the numerical costs of computing the Hessian of the objective function by one order of magnitude, that is from $O(N_\mu^2)$ to $O(N_\mu)$. In exactly the same way as in the first order sensitivity analysis, the second derivatives $\mathbf{p}_{ij}(t)$ of the convolution function are eliminated from (4.18b) by using the scalar product of the vector $\boldsymbol{\lambda}(t)$ of the adjoint variables and (4.19). A considerably simpler formula for the element $F_{ij}(\boldsymbol{\mu})$ of the Hessian can be obtained this way,

$$F_{ij}(\boldsymbol{\mu}) = \langle \mathbf{u}_i, \mathbf{u}_j \rangle + \langle \boldsymbol{\lambda}, \Delta \mathbf{M}_i \ddot{\mathbf{u}}_j + \Delta \mathbf{M}_j \ddot{\mathbf{u}}_i + \Delta \mathbf{K}_i \mathbf{u}_j + \Delta \mathbf{K}_j \mathbf{u}_i \rangle, \quad (4.24)$$

where the first derivatives $\mathbf{p}_i(t)$ of the convolution function have to be obtained using the DDM, that is by solving N_μ times (4.17), and

$$\begin{aligned} \ddot{\mathbf{u}}_i(t) &:= \frac{\partial}{\partial \mu_i} \ddot{\mathbf{u}}(t) \\ &= (\ddot{\mathcal{B}} \mathbf{p}_i)(t) \end{aligned} \quad (4.25)$$

is the vector of the derivatives of the acceleration response.

In order to perform the second-order analysis, $\mathbf{u}_i(t)$ and $\mathbf{p}_i(t)$ have to be known. The gradient of the objective function can be thus quickly computed using (4.16b) and verified against the gradient obtained by (4.22).

4.2.2.4 Required data

The inverse problem is solved by iterative optimization. The objective function is computed in its each step, possibly along with the gradient and the Hessian. The following purely experimental data are required for this purpose:

- the measured response $\mathbf{u}^M(t)$ of the modified structure to a certain reproducible testing excitation $\mathbf{f}_{\text{test}}(t)$;
- the measured responses $\mathbf{u}^L(t)$ and $\ddot{\mathbf{u}}^L(t)$ of the original unmodified structure to the same testing excitation $\mathbf{f}_{\text{test}}(t)$;
- the matrices $\mathbf{H}(t)$ and $\ddot{\mathbf{H}}(t)$ of measured responses of the unmodified structure to quasi impulsive excitations $q_i(t)$, which are respectively used to form the required matrix integral operators \mathcal{B} , $\ddot{\mathcal{B}}$ and \mathcal{Q} .

As it is the case in the direct problem, measurements of the responses of the unmodified structure are restricted only to the sensors intended for identification and to the DOFs related to potential modifications (only a reduced quasi impulse response matrix is required). The response of the modified structure needs to be measured only by the sensors intended for identification.

4.2.3 Time discretization and numerical solution

All the required responses are in practice discrete and not continuous, that is they are vectors sampled in discrete time points every Δt . As mentioned in Subsection 4.2.1.4, two formulations of the direct and the inverse problems are possible, which use either the exact impulse responses or the experimentally obtained quasi impulse responses. In the first case, the direct problem uses (4.9b) and (4.10), and in the second case (4.12) and (4.13) are used. In the discrete-time setting, the exact discrete impulse responses, denoted here by $\mathbf{D}(t)$ and $\ddot{\mathbf{D}}(t)$, are the discrete responses to one-time-step unit excitations (which can be obtained by a deconvolution), so that

$$\mathbf{D}(t) \approx \mathbf{H}(t)\Delta t, \quad (4.26a)$$

$$\ddot{\mathbf{D}}(t) \approx \begin{cases} \mathbf{M}^{-1} + \ddot{\mathbf{H}}_\delta(0)\Delta t & \text{if } t = 0, \\ \ddot{\mathbf{H}}(t)\Delta t & \text{otherwise,} \end{cases} \quad (4.26b)$$

where the impulsive component of $\ddot{\mathbf{H}}(t)$ is included in $\ddot{\mathbf{D}}(0)$, compare to (4.3b). If measured discrete responses to multistep quasi impulsive excitations are used, then simply

$$\mathbf{D}(t) \approx \mathbf{H}(t)\Delta t, \quad (4.27a)$$

$$\ddot{\mathbf{D}}(t) \approx \ddot{\mathbf{H}}(t)\Delta t, \quad (4.27b)$$

$$\mathbf{Q}(t) \leftarrow \mathbf{Q}(t)\Delta t, \quad (4.27c)$$

where the right-hand side matrix $\mathbf{Q}(t)$ contains on the diagonal the experimentally applied quasi impulsive excitations $q_i(t)$ and zeros elsewhere.

4.2.3.1 Direct problem

Exact impulse responses. By the time discretization defined in (4.26), the integral equation (4.9b) is transformed at each considered time step t into the following discretized linear system:

$$\sum_{\tau=0}^t \left(\delta_{\tau t} \mathbf{I} + \Delta \mathbf{M} \ddot{\mathbf{D}}(t-\tau) + \Delta \mathbf{K} \mathbf{D}(t-\tau) \right) \mathbf{p}^0(\tau) = -\Delta \mathbf{M} \ddot{\mathbf{u}}^L(t) - \Delta \mathbf{K} \mathbf{u}^L(t), \quad (4.28)$$

where $\delta_{\tau t}$ is Kronecker's delta and \mathbf{I} denotes the identity matrix of appropriate dimensions. Equation (4.28) is then collected for all the considered time steps t and stated in the following form of a single large linear system,

$$\mathbf{A} \mathbf{p}^0 = -\Delta \mathbf{M} \ddot{\mathbf{u}}^L - \Delta \mathbf{K} \mathbf{u}^L, \quad (4.29)$$

where \mathbf{p}^0 , $\ddot{\mathbf{u}}^L$ and \mathbf{u}^L are the vectors that collect the pseudo loads and the respective responses of the unmodified structure in all time steps and in all DOFs related to structural modifications. The system matrix \mathbf{A} is a structured block matrix with $N_t \times N_t$ lower triangular Toeplitz blocks, where N_t is the number of time steps. The structure of a typical matrix is illustrated in Fig. 4.2. The number of blocks depends on the type of the structure. For example, 3D trusses have three DOFs per node, and so \mathbf{A} has $3N_n \times 3N_n$ blocks, where N_n is the number of the nodes related to structural modifications. For 2D trusses, which have two DOFs per node, it has $2N_n \times 2N_n$ blocks. In the general case, there can be $6N_n \times 6N_n$ blocks.

Equation (4.29) is solved to obtain the vector \mathbf{p}^0 of the discretized pseudo loads; the modeled discrete responses of the modified structure are then computed by the following discretized counterparts of (4.10):

$$\mathbf{u} = \mathbf{u}^L + \mathbf{D} \mathbf{p}^0, \quad (4.30a)$$

$$\ddot{\mathbf{u}} = \ddot{\mathbf{u}}^L + \ddot{\mathbf{D}} \mathbf{p}^0, \quad (4.30b)$$

where the matrices \mathbf{D} and $\ddot{\mathbf{D}}$ are block matrices with Toeplitz blocks that are the discretized counterparts of the integral operators in (4.3).

Experimental quasi impulse responses. If the experimentally measured responses to multistep quasi impulse excitations are directly used, then the discretization defined in (4.27) is applied to (4.12). In each time instance t it yields

$$\sum_{\tau=0}^t \left(\mathbf{Q}(t-\tau) + \Delta \mathbf{M} \ddot{\mathbf{D}}(t-\tau) + \Delta \mathbf{K} \mathbf{D}(t-\tau) \right) \mathbf{p}(\tau) = -\Delta \mathbf{M} \ddot{\mathbf{u}}^L(t) - \Delta \mathbf{K} \mathbf{u}^L(t), \quad (4.31)$$

which, if it is collected for all time steps t , takes the same formal form as (4.29),

$$\mathbf{A} \mathbf{p} = -\Delta \mathbf{M} \ddot{\mathbf{u}}^L - \Delta \mathbf{K} \mathbf{u}^L, \quad (4.32)$$

although the block matrix \mathbf{A} is constructed here in a different way. Given the initial data, (4.32) needs to be solved first, and then the resulting vector \mathbf{p} is substituted into discretized (4.13),

$$\mathbf{u} = \mathbf{u}^L + \mathbf{D}\mathbf{p}, \quad (4.33a)$$

$$\ddot{\mathbf{u}} = \ddot{\mathbf{u}}^L + \ddot{\mathbf{D}}\mathbf{p}, \quad (4.33b)$$

to obtain the discrete response of the modified structure.

4.2.3.2 Inverse problem and sensitivity analysis

As in the case of continuous time setting, sensitivity analysis is illustrated here using the formulation with experimentally measured responses to multistep quasi impulsive excitations, and the AVM is used. Due to the formal similarity of (4.29) to (4.32) and of (4.30) to eq:ch04-discreteResponseNonimp, the case of exact impulse responses can be treated in an analogous manner.

Identification of the unknown modification parameters $\boldsymbol{\mu}$ that fully define the unknown damage $\Delta\mathbf{K}$ and $\Delta\mathbf{M}$ is equivalent to the minimization of the following objective function:

$$\begin{aligned} F(\boldsymbol{\mu}) &:= \frac{1}{2} \mathbf{d}^T \mathbf{d} \\ &= \frac{1}{2} \langle \mathbf{d}, \mathbf{d} \rangle, \end{aligned} \quad (4.34)$$

where

$$\mathbf{d} := \mathbf{u}^M - \mathbf{u} \quad (4.35)$$

and the vector \mathbf{u}^M denotes the measured discrete response of the modified structure (collected in all time steps and in all considered sensors) to the testing excitation $\mathbf{f}_t(t)$.

The derivative $F_i(\boldsymbol{\mu})$ of the objective function with respect to μ_i can be computed using the discrete version of (4.22),

$$F_i(\boldsymbol{\mu}) = \langle \boldsymbol{\lambda}, \Delta\mathbf{M}_i \ddot{\mathbf{u}} + \Delta\mathbf{K}_i \mathbf{u} \rangle, \quad (4.36)$$

where the vector $\boldsymbol{\lambda}$ collects the discretized adjoint variables that can be obtained at the cost of a single solution of the discrete adjoint equation,

$$\mathbf{A}^T \boldsymbol{\lambda} = \mathbf{B}^T \mathbf{d}, \quad (4.37)$$

which is the discrete-time counterpart of the continuous adjoint integral equation (4.23). The Hessian of the objective function can be computed similarly,

$$F_{ij}(\boldsymbol{\mu}) = \langle \mathbf{u}_i, \mathbf{u}_j \rangle + \langle \boldsymbol{\lambda}, \Delta \mathbf{M}_i \ddot{\mathbf{u}}_j + \Delta \mathbf{M}_j \ddot{\mathbf{u}}_i + \Delta \mathbf{K}_i \mathbf{u}_j + \Delta \mathbf{K}_j \mathbf{u}_i \rangle, \quad (4.38)$$

where

$$\mathbf{u}_i = \mathbf{D}\mathbf{p}_i, \quad (4.39a)$$

$$\ddot{\mathbf{u}}_i = \ddot{\mathbf{D}}\mathbf{p}_i, \quad (4.39b)$$

and the vector \mathbf{p}_i of the first order derivatives of the discrete convolution coefficients has to be obtained by solving (separately for each modification parameter μ_i) the discrete-time counterpart of (4.17),

$$\mathbf{A}\mathbf{p}_i = -\Delta \mathbf{M}_i \ddot{\mathbf{u}} - \Delta \mathbf{K}_i \mathbf{u}. \quad (4.40)$$

As in (4.19), it is assumed in (4.38) that the second derivatives $\Delta \mathbf{M}_{ij}$ and $\Delta \mathbf{K}_{ij}$ of the modifications vanish. The time complexity of Hessian computation is linear with respect to the number N_μ of the considered parameters of modification, instead of the quadratic complexity of the DDM, and Table 3.1 applies. Notice that the second order sensitivity analysis requires computation of \mathbf{u}_i , which can be then used in the discrete-time counterpart of (4.16b),

$$F_i(\boldsymbol{\mu}) = -\langle \mathbf{u}_i, \mathbf{d} \rangle, \quad (4.41)$$

for a low-cost verification of the gradient obtained via (4.36).

Given the quasi impulse response matrices \mathbf{D} and $\ddot{\mathbf{D}}$, experimentally applied quasi impulsive excitations \mathbf{Q} , as well as the discrete responses \mathbf{u}^M , \mathbf{u}^L and $\ddot{\mathbf{u}}^L$ to the testing excitation, the computations required for a first order and a second order sensitivity analysis are summarized in Table 4.1.

4.2.3.3 Numerical solution

Given the required discrete measurement data, identification of structural modifications amounts to an iterative minimization of the objective function and might seem to be straightforward. In each iteration, a sensitivity analysis is performed as described in Table 4.1. Two square linear systems, (4.32) and (4.37), have to be solved to obtain \mathbf{p} and $\boldsymbol{\lambda}$; if a second order optimization method is used, then also all \mathbf{p}_i have to be computed by solving (4.40) separately for each optimization variable μ_i . In all cases, the system matrix is either \mathbf{A} or \mathbf{A}^T . However, all responses are stored and processed in time domain, which

Table 4.1. Computations required for a first order and a second order sensitivity analysis in the discrete time setting. It is assumed that \mathbf{D} , $\ddot{\mathbf{D}}$, \mathbf{Q} , \mathbf{u}^M , \mathbf{u}^L and $\ddot{\mathbf{u}}^L$ are known.

1 st order	2 nd order	Formula	Computation
×	×	(4.31)	system matrix \mathbf{A}
×	×	(4.32)	convolution functions \mathbf{p}
×	×	(4.33)	modeled responses \mathbf{u} and $\ddot{\mathbf{u}}$
×	×	(4.35)	residual vector \mathbf{d}
×	×	(4.34)	objective function $F(\boldsymbol{\mu})$
×	×	(4.37)	discrete adjoint variables $\boldsymbol{\lambda}$
	×	(4.40)	derivatives \mathbf{p}_i for all i
×	×	(4.36)	gradient of the objective function $\nabla F(\boldsymbol{\mu})$
	×	(4.41)	gradient of the objective function $\nabla F(\boldsymbol{\mu})$
	×	(4.38)	Hessian of the objective function

often results in large dimensions of these matrices. In the case of a 3D truss, \mathbf{A} is a dense $3N_n \times 3N_n$ block matrix with $N_t \times N_t$ blocks, where N_t is the number of time steps and N_n is the number of the nodes related to the modifications. The total dimensions are thus $3N_n N_t \times 3N_n N_t$, and in case of a longer time interval or a larger number of potential modifications, the matrices can become huge and unmanageable by standard numerical techniques. Moreover, as can be expected from the Toeplitz structure of its blocks [109], the matrix is significantly ill-conditioned, and a regularization technique must be used in order to obtain meaningful solutions.

Three effective numerical techniques can be used to address the problems caused by the size and ill-conditioning of the matrix \mathbf{A} :

1. The involved systems are solved using the fast iterative algorithm of conjugate gradient least squares [128]. There are two main reasons behind the choice of the CGLS:
 - The CGLS method has good regularizing properties. The number of iterations plays the role of the regularization parameter: the more iterations, the more exact but less regularized (that is more influenced by the measurement error) is the solution;
 - The system matrix \mathbf{A} is used only in the form of the matrix–vector products \mathbf{Ax} and $\mathbf{A}^T\mathbf{y}$. No costly matrix decompositions, factorizations and even no direct access to its elements are necessary. In fact, the CGLS requires just two black-box procedures that implement the respective multiplications.

2. In the CGLS method, the system matrix \mathbf{A} is present only implicitly in the form of matrix–vector products, which can be quickly computed if the block Toeplitz structure of \mathbf{A} is exploited: For each $N_t \times N_t$ Toeplitz block, the exact product can be computed in frequency domain using an embedding in a circulant matrix and the FFT in time $O(N_t \log N_t)$ instead of $O(N_t^2)$, see, e.g., [133].
3. Each block of \mathbf{A} is an $N_t \times N_t$ lower triangular Toeplitz block, hence it can be stored in computer memory in a reduced form using only N_t elements instead of N_t^2 .

The next section presents another approach that converts the modeling and identification problems into frequency domain and solves them separately for each frequency line of interest. The total numerical cost is smaller; however, the direct control over the regularization level is lost.

4.3 Frequency-domain formulation

The described problem is essentially transient, so that the time-domain formulation described in the previous section seems to be quite natural. Moreover, the numerical solution techniques like the CGLS allow for a good control over the amount of regularization embedded into the computed solution. Nevertheless, this is at the cost of the computational time, since the time-domain formulation makes extensive use of the operation of convolution. The basic equation used to model the pseudo loads that are equivalent to the modifications, (4.9b) or (4.12), as well as its differentiated and adjoint versions, (4.17) and (4.23), are all systems of linear integral equations of the Volterra type. Numerical solution of such systems is considerably time-consuming, even with the effective numerical techniques mentioned in Subsection 4.2.3.3.

In this section, the problem is transferred into frequency domain. As a result, the original systems of Volterra integral equations are converted into a series of simple decoupled discretized linear equations (a separate independent equation for each frequency line of interest), which can be solved at a significantly smaller total numerical cost. If necessary, the computed frequency-domain response can be transformed back into time domain to obtain the time-domain responses. As a result, the original objective function (4.15a) and the fast sensitivity analysis based on the AVM are still possible. Alternatively, the frequency-domain formulation highlights also the possibility of other objective functions based on modal characteristics of the structure such as its natural frequencies.

4.3.1 The direct problem

By applying the Fourier transform \mathcal{F} to both sides of (4.4), the equilibrium equation of the unmodified structure takes in frequency domain the following quasi static form:

$$(-\omega^2 \mathbf{M} + i\omega \mathbf{C} + \mathbf{K}) \mathbf{u}^L(\omega) = \mathbf{f}_{\text{test}}(\omega), \quad (4.42)$$

where the vectors $\mathbf{u}^L(\omega)$ and $\mathbf{f}(\omega)$ are the frequency-domain response and the testing excitation respectively. Given the excitation, the response can be expressed as

$$\mathbf{u}^L(\omega) = \mathbf{H}(\omega) \mathbf{f}_{\text{test}}(\omega), \quad (4.43)$$

where $\mathbf{H}(\omega)$ is the frequency response matrix,

$$\mathbf{H}(\omega) = (-\omega^2 \mathbf{M} + i\omega \mathbf{C} + \mathbf{K})^{-1}. \quad (4.44)$$

The structural modifications have been defined in terms of the modifications to the structural mass and stiffness matrices, $\Delta \mathbf{M}$ and $\Delta \mathbf{K}$. The equilibrium equation of the modified structure,

$$(-\omega^2 (\mathbf{M} + \Delta \mathbf{M}) + i\omega \mathbf{C} + \mathbf{K} + \Delta \mathbf{K}) \mathbf{u}(\omega) = \mathbf{f}_{\text{test}}(\omega), \quad (4.45)$$

can be transformed into the equilibrium equation of the original unmodified structure,

$$(-\omega^2 \mathbf{M} + i\omega \mathbf{C} + \mathbf{K}) \mathbf{u}(\omega) = \mathbf{f}_{\text{test}}(\omega) + \mathbf{p}^0(\omega), \quad (4.46)$$

where the modifications are modeled with the vector $\mathbf{p}^0(\omega)$ of the equivalent pseudo loads,

$$\mathbf{p}^0(\omega) = (\omega^2 \Delta \mathbf{M} - \Delta \mathbf{K}) \mathbf{u}(\omega). \quad (4.47)$$

Equations (4.42), (4.44) and (4.46) yield together

$$\mathbf{u}(\omega) = \mathbf{u}^L(\omega) + \mathbf{H}(\omega) \mathbf{p}^0(\omega), \quad (4.48)$$

which, if substituted into (4.47), yields the following frequency-domain counterpart of (4.9b):

$$(\mathbf{I} - \omega^2 \Delta \mathbf{M} \mathbf{H}(\omega) + \Delta \mathbf{K} \mathbf{H}(\omega)) \mathbf{p}^0(\omega) = -(-\omega^2 \Delta \mathbf{M} + \Delta \mathbf{K}) \mathbf{u}^L(\omega), \quad (4.49)$$

where \mathbf{I} is the identity matrix of appropriate dimensions. Notice that $\Delta \mathbf{M}$ and $\Delta \mathbf{K}$ have nonvanishing entries only in the rows and columns that correspond to the DOFs directly related to the modifications. In all other DOFs the pseudo

loads vanish according to (4.47), so that (4.49) is in practice reduced to a small linear system with dimensions $3N_n \times 3N_n$ for a truss structure or $6N_n \times 6N_n$ in the general case, where N_n is the number of the nodes directly related to the modifications. Accordingly, only the corresponding small submatrix of the full frequency response matrix $\mathbf{H}(\omega)$ needs to be estimated experimentally prior to modeling and identification.

Given the required characteristics of the structure, that is the response $\mathbf{u}^L(\omega)$ of the original unmodified structure and its frequency response matrix $\mathbf{H}(\omega)$, as well as the assumed structural modifications $\Delta\mathbf{M}$ and $\Delta\mathbf{K}$, first the equivalent vector $\mathbf{p}^0(\omega)$ of the pseudo loads is found by solving (4.49) and then the response $\mathbf{u}(\omega)$ of the modified structure is computed by (4.48). The computations need to be repeated separately for each frequency line ω of interest.

4.3.2 The inverse problem

Given the frequency-domain response, various formulations of the objective function are possible. The objective function can be based on fitting selected modal characteristics, such as natural frequencies, as expressed for example by the following:

$$F(\boldsymbol{\mu}) := \sum_i \left(\frac{\omega_i^M - \omega_i(\boldsymbol{\mu})}{\omega_i^M} \right)^2, \quad (4.50)$$

where ω_i^M is the i th natural frequency of the modified structure identified in a direct analysis of the measured response $\mathbf{u}^M(\omega)$, while $\omega_i(\boldsymbol{\mu})$ is the corresponding natural frequency identified from the modeled response $\mathbf{u}(\omega)$. Given the frequency-domain response, the natural frequencies can be often found by a simple peak-picking procedure or by the eigensystem realization algorithm (ERA) [223], so that the corresponding value of the objective function (4.50) is readily available. However, sensitivity analysis of (4.50) is more difficult: computation of the derivatives of the natural frequencies requires the corresponding mode shapes to be known [224–226], which in general might be also identified by means of the ERA, but in practice less accurately than the natural frequencies. Given the simplicity of (4.49) and (4.48) and the relatively narrow involved frequency ranges, it might turn out that simple zero-order search techniques are more reliable than gradient-based optimization algorithms.

In another formulation, the inverse Fourier transform \mathcal{F}^{-1} (or, in practice, the inverse fast Fourier transform) might be employed to obtain the time-domain response. The standard time-domain objective function (4.15a) might be then used, where

$$\mathbf{d}(t) := \mathbf{u}^M(t) - (\mathcal{F}^{-1}\mathbf{u})(t). \quad (4.51)$$

Under reasonable assumptions² quick first and second order sensitivity analysis based either on the DDM or on the AVM can be straightforwardly applied in the similar way as in the time-domain case.

4.3.3 FFT and windowing function

In principle, the frequency-domain responses and the frequency response functions can be obtained from time-domain measured responses and quasi impulsive excitations by employing the Fourier transform. However, in practice all the measurements are discrete and of finite length, hence the fast Fourier transform needs to be used together with a suitable windowing function, which is required in order to decrease the inevitable spectral leakage. Out of various windowing functions possible (see, e.g., Subsection 5.5.2), the exponential window seems to provide best results, which is related to the quasi impulsive character of the excitations.

4.4 Identification of inelastic impacts

This section discusses a possible extension of the described methodology to identification of inelastic impacts. It is assumed that such an impact is fully defined by the following parameters:

- impacting mass m ,
- components v_x , v_y and v_z of the impact velocity,
- and possibly, also the number k of the impacted DOF.

An inelastic impact can be relatively easily mimicked experimentally by

1. Attaching a single additional mass m in the k th node (impacted node).
2. Applying a quasi impulsive excitation to the attached mass in the impact direction defined by (v_x, v_y, v_z) .

If the quasi impulsive excitation is measured, then the equivalent impact velocity can be straightforwardly calculated by dividing the impulse of force by the attached mass.

²In general, the derivative $\mathbf{u}_i(\omega)$ ought exist and be continuous with respect to ω and μ_i , which is required by the Leibniz integral rule. In practice, it is always satisfied for real-world structures.

4.4.1 The direct problem

The inelastically impacting mass attaches to the impacted node, and can be thus treated as an added mass. Therefore, structural response to an inelastic impact can be modeled in a similar way as the response of a structure with a single added mass. To this end, mass modification $\Delta\mathbf{M}$ and the response $\mathbf{u}^L(t)$ of the unmodified structure to the impulsive excitation need to be known. The former is defined by the mass m and the impacted node k . The latter depends on the impulsive excitation $\mathbf{f}_{\text{test}}(t)$, which, unlike in the preceding section, is not arbitrary and has to model the actual impact excitation:

$$\mathbf{f}_{\text{test}}(t) := m(v_x \mathbf{e}_{k_x} + v_y \mathbf{e}_{k_y} + v_z \mathbf{e}_{k_z}) \delta(t), \quad (4.52)$$

where $\delta(t)$ is the Dirac delta function, the impact occurs in the k th node along the DOFs k_x , k_y and k_z , and the corresponding vectors are denoted by \mathbf{e}_{k_x} , \mathbf{e}_{k_y} and \mathbf{e}_{k_z} . Notice that in (4.52) the time-history of the excitation $\delta(t)$ has to be assumed in advance, and that in practice certain quasi impulsive functions, like the half-sine, might be considered instead of the Dirac delta.

The excitation (4.52) depends on impact parameters, hence the corresponding response of the unmodified structure $\mathbf{u}^L(t)$ cannot be measured in advance and needs to be calculated as

$$\mathbf{u}^L(t) := m(v_x \mathbf{u}_{k_x}^L(t) + v_y \mathbf{u}_{k_y}^L(t) + v_z \mathbf{u}_{k_z}^L(t)), \quad (4.53)$$

that is as the respective combination of the structural responses to unit impulsive excitations $\mathbf{u}_{k_x}^L(t)$, $\mathbf{u}_{k_y}^L(t)$ and $\mathbf{u}_{k_z}^L(t)$.

4.4.2 The inverse problem

Given the measured response of the structure to an inelastic impact (either real or mimicked as described above), the assumed parameters of the impact can be identified by minimizing the discrepancy between the measured and the modeled structural responses. The unknown impact parameters are treated as the optimization variables. The standard time-domain formulation (4.15a) of the objective function can be used. If a frequency-domain formulation is used instead, then besides the natural frequencies also the amplitude of the frequency response have to be included in order to be able to differentiate between various impact velocities, which affect the amplitude, but not the frequency content of the response.

4.5 Selected experimental results

This section presents selected experimental results to verify the practical applicability of the described methodology. A 3D truss structure is used in a problem of nonparametric identification of nodal mass modifications. The average relative error of identification of a single modifications is less than 5%. The identification errors are larger in the case of two concurrent modifications, which is a result of the ill-conditioning of the identification problem. The accuracy of results depends on the characteristics, number and placement of the testing excitations and sensors, as well as on the placement of modifications. The problem of estimation of the limiting resolution of the methodology based on the experimentally obtained nonparametric model of the unmodified structure is a interesting area of further research.

The results presented in this section are obtained in time domain. Selected results of mass identification obtained in a frequency-domain analysis can be found in [43]. An example preliminary result of identification of stiffness modification of a truss element is available in [30]; identification of an inelastic impact is reported in [41].

4.5.1 The structure

The experimental verification uses a 3D truss structure with 26 nodes and 70 elements, see Fig. 4.1. It is constructed using a commercially available system of spherical joints and connecting tubes [31]. The structure is 4 m long, and its elements are circular steel tubes with the radius of 22 mm, the thickness of 1 mm and the lengths of 0.500 m or 0.707 m. The mass of each joint is 0.23 kg, and the total mass of the structure is approximately 32 kg. The two right-hand side nodes in the scheme are free to move in the longitudinal direction only, while the two opposite left-hand side nodes have restrained all their DOFs and are thus turned into fixed supports. Only nodal mass modifications are considered. They are implemented experimentally by attaching concentrated masses at either one or two out of the nodes marked M_1 , M_2 and M_3 in Fig. 4.1. It is assumed that the location of the modifications is known in advance and need not be identified.

4.5.2 Excitations and measurements

Figure 4.1 shows the location of the testing excitation $\mathbf{f}_{\text{test}}(t)$ and of the single sensor intended for identification and used to measure the response $\mathbf{u}^L(t)$ of the original structure and the response $\mathbf{u}^M(t)$ of the modified structure. A modal

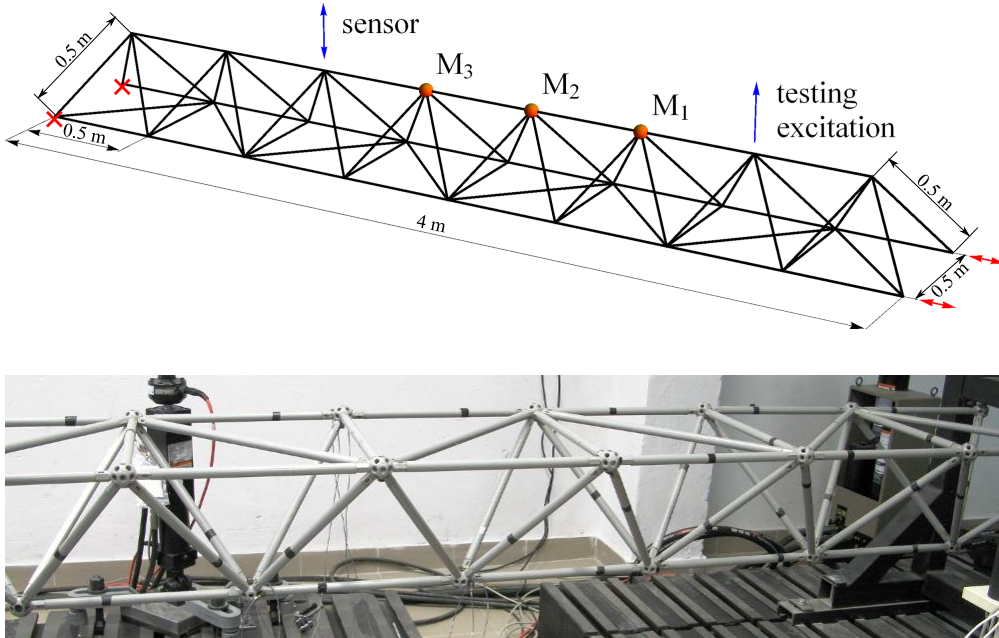


Figure 4.1. The 3D truss structure used in experimental verification: (top) scheme; (bottom) a fragment of the real structure.

hammer is used to generate the testing excitation, as well as all the quasi impulsive excitations used in measurements of the necessary quasi impulse responses. All the sensors are accelerometers; the signals from the accelerometers and from the modal hammer are collected by a Brüel & Kjær data acquisition system PULSE, sampled at 65.5 kHz and transferred to a desktop PC for further analysis. The acquisition system internally double-integrated the acceleration responses to recover the corresponding displacements. For each response, measurements are recorded independently four times and then averaged in order to diminish the adverse effects of the measurement noise. The CGLS method is used thereafter to deconvolve the averaged responses with respect to the averaged quasi impulsive excitations in order to obtain the exact discrete-time impulse responses. A total of 15 000 time steps is recorded for each response, which corresponds approximately to the time interval of 230 ms or 7.2 periods of the first natural vibration (31.5 Hz).

In the case of two nodal mass modifications, the matrix \mathbf{A} in (4.29) is a 6×6 block matrix; each of its block rows and block columns corresponds to one of the six DOFs of the two nodes considered for modifications. If the full-length

responses are used, each block is a $15\,000 \times 15\,000$ lower triangular Toeplitz submatrix, and the total matrix dimensions are thus $90\,000 \times 90\,000$; the structure of such a matrix is illustrated in Fig. 4.2³. The matrix is dense, and if stored in the full form using standard 8-byte double floating point numbers, it would require as much as 60.3 GB of memory storage. On the other hand, exploitation of its Toeplitz block structure allows the matrix to be stored in 4.1 MB only.

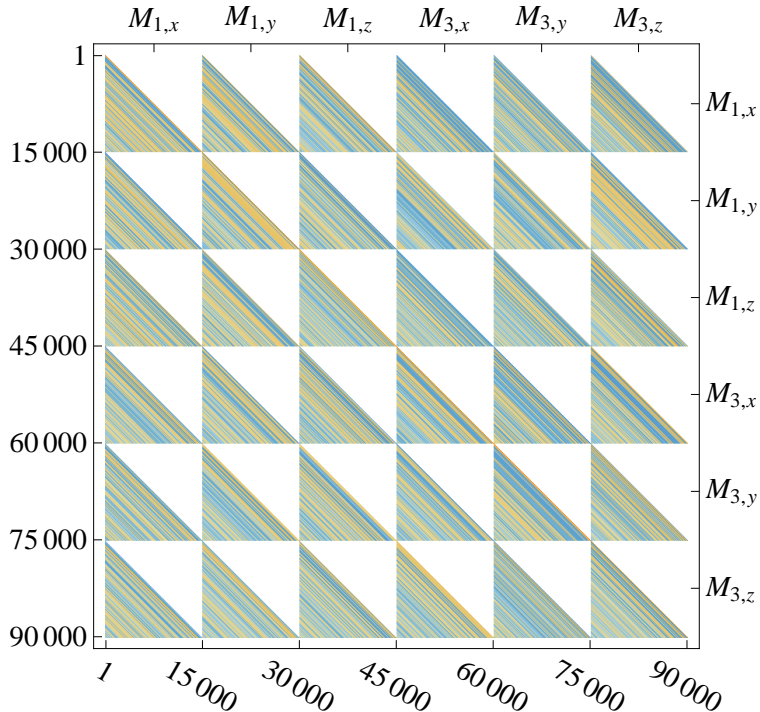


Figure 4.2. Modification of two nodal masses: structure of the system matrix \mathbf{A} in (4.29).

4.5.3 Single nodal mass modification

In the first considered scenario, a single concentrated mass is attached to one of the nodes M_1 , M_2 or M_3 ; the location of the modification is assumed to be known in advance. Four different masses of 1.36 kg, 2.86 kg, 3.86 kg and 5.36 kg are used in each of the three nodes; a total of 12 cases is thus tested. Such

³Notice the similarity of the structure of the matrix to that shown in Fig. 2.3. This emphasizes the central role of load identification and deconvolution procedures in the VDM and the nonparametric approach described in this chapter.

modifications can considerably alter the local dynamics in their neighborhood, since they range from 100% to almost 400% of the structural mass related to the modified node (joint mass plus half of the masses of the six neighboring elements, which is 1.36 kg altogether). On the other hand, in comparison to the total mass of the unmodified structure (32 kg), the relative mass modifications are much smaller and range from 4.25% to 16.75%.

All identifications are performed using the Newton optimization algorithm with exact second derivatives computed using the AVM. In each step of the optimization, the ill-conditioned system (4.29), as well as its differentiated version and the adjoint system, are iteratively solved using 1000 CGLS iterations, which allows the computed responses to stabilize numerically before being overly influenced by the measurement errors. The results of identification might depend on the length of the responses used in computations. In order to test their stability, all the identifications are performed repeatedly using the response lengths varying from 250 up to 15 000 time steps (3.8 ms to 292 ms). The results are plotted in Fig. 4.3. At short response lengths, the identification results are strongly dependent on the number of the time steps used in computations; it is thus assumed that at least 7500 time steps (115 ms or 3.6 periods of the first natural vibration) have to be used for reliable results.

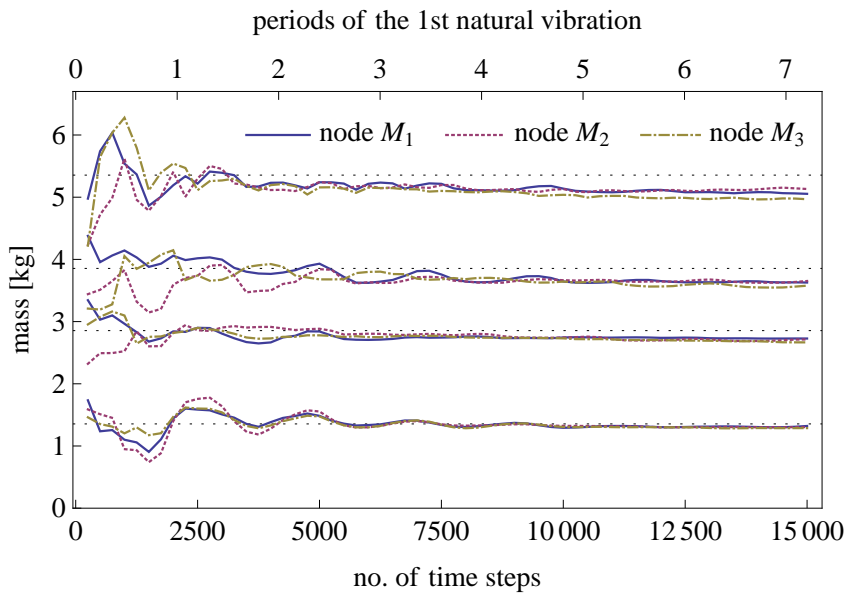


Figure 4.3. Single nodal mass modification: identification results in dependence on the length of the responses used in computations; the dotted gridlines mark the actual modifications.

In general, the results of identification underestimate the actual modifications; the relative identification errors range between -8% and $+1\%$ with the mean relative error of -4.6% . Figure 4.4 plots in the logarithmic scale the normalized objective functions that are computed using 15 000 time steps for all the four masses and the three considered nodes; the minima of all the curves are clearly distinguishable. As an example, Fig. 4.5 compares the three full-length responses that correspond to the best-fitting case of the mass 2.86 kg attached in node M_3 (identified mass 2.67 kg). The difference between $\mathbf{u}^L(t)$ and $\mathbf{u}^M(t)$, that is the influence of the added mass on the measured response, is clearly noticeable in the increase of the period of the basic oscillations; the fit between the measured and modeled responses of the modified structure is almost perfect.

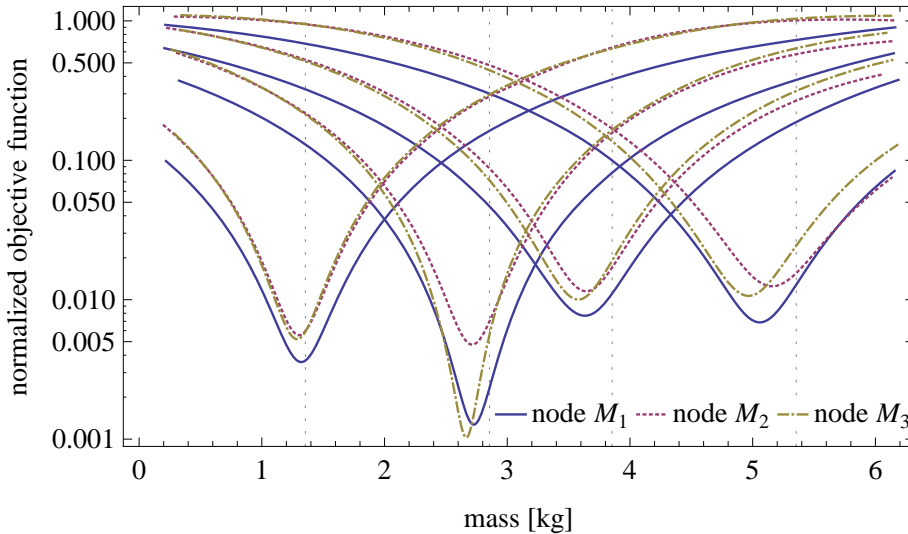


Figure 4.4. Single nodal mass modification: normalized objective functions computed using 15000 time steps for all three nodes and four tested masses; the dotted gridlines mark the actual modifications.

4.5.4 Modification of two nodal masses

In the second considered scenario, two nodal masses are simultaneously attached in two nodes of the structure (M_1 and M_3). Six different cases are tested, that is all the six possible combinations of $M_1 \in \{1.36 \text{ kg}, 2.86 \text{ kg}\}$ and $M_3 \in \{1.39 \text{ kg}, 2.89 \text{ kg}, 3.89 \text{ kg}\}$.

In order to test the stability of the results, all the identifications are performed repeatedly using the responses of different lengths: each 250 time steps

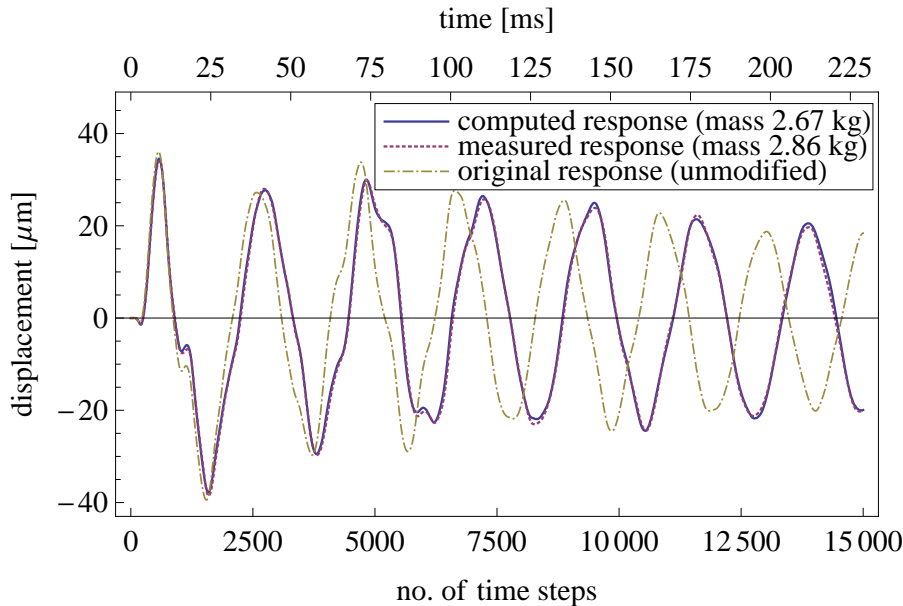


Figure 4.5. Single nodal mass modification (node M_3 , actual mass 2.86 kg, identified mass 2.67 kg): the computed response $\mathbf{u}(t)$ and the measured responses $\mathbf{u}^M(t)$ and $\mathbf{u}^L(t)$ of the modified and original structures respectively.

in the range from 7500 to 15 000 time steps, that is a total of 31 times. Figure 4.6 shows the results of all the identifications. They are obtained using a modified Newton optimization algorithm and exact Hessians. Similarly as in the case of a single nodal mass modification, the total modification mass is underestimated: the relative identification errors range between -13% and -1.6% with the mean of -5.2% .

For each of the two nodal masses, the relative identification errors are higher than in the case of a single nodal mass modification, which is the result of a significant ill-conditioning of the identification problem. As an example, Fig. 4.7 plots the contours of (the logarithm of) the objective function that corresponds to the actual mass modifications $(M_1, M_3) = (2.86 \text{ kg}, 1.39 \text{ kg})$ and is computed using 15 000 time steps. The minimum is found at $(3.05 \text{ kg}, 1.07 \text{ kg})$, so that the relative identification errors are $(7\%, 23\%)$. A high degree of ill-conditioning is apparent in the shape of the objective function, which forms a characteristic long and narrow valley. As a result, it is relatively easy to find the bottom line of the valley (which approximately corresponds to the constant sum of the two modifications), while the exact location of the minimum along the bottom line

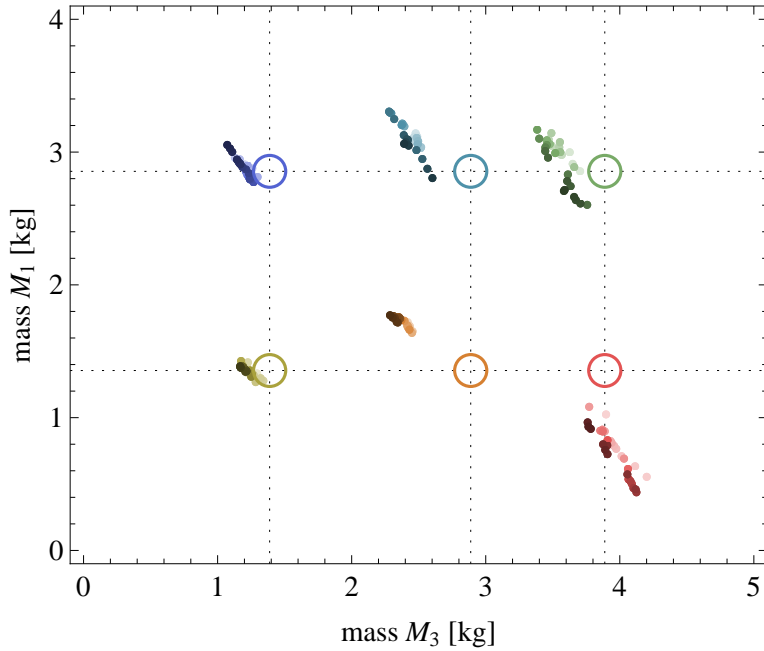


Figure 4.6. Modification of two nodal masses: identification results for different considered lengths of the responses. The circles mark the actual modifications, the dots mark the identification results computed using 7500 (light dots) to 15 000 (dark dots) time steps.

(that is the differentiation between the masses) is very sensitive to measurement errors and varies with the different numbers of time steps used in computations. The degree of ill-conditioning can be quantified by the condition number of the Hessian at the minimum, which is approximately 500; the related linear identification problem has thus the condition number of approximately 22.4. Figure 4.8 compares the three responses related to the discussed case: the measured response $\mathbf{u}^L(t)$ of the original unmodified structure, the measured response $\mathbf{u}^M(t)$ of the modified structure and the response $\mathbf{u}(t)$ as modeled for the identified mass modifications.

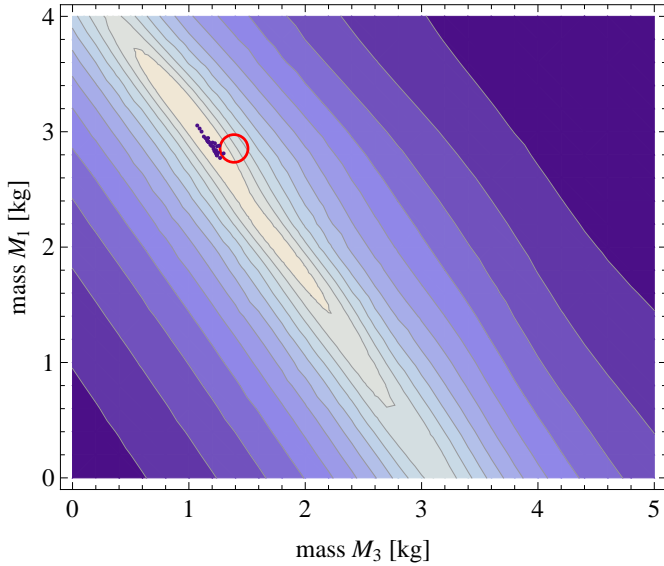


Figure 4.7. Modification of two nodal masses: contours of (the logarithm of) the objective function computed (using 15 000 time steps) for the actual modifications $M_1 = 1.36\text{ kg}$ and $M_3 = 2.89\text{ kg}$. The circle marks the actual modification, the dots mark the identification results obtained for different considered numbers of time steps (7500 to 15 000).

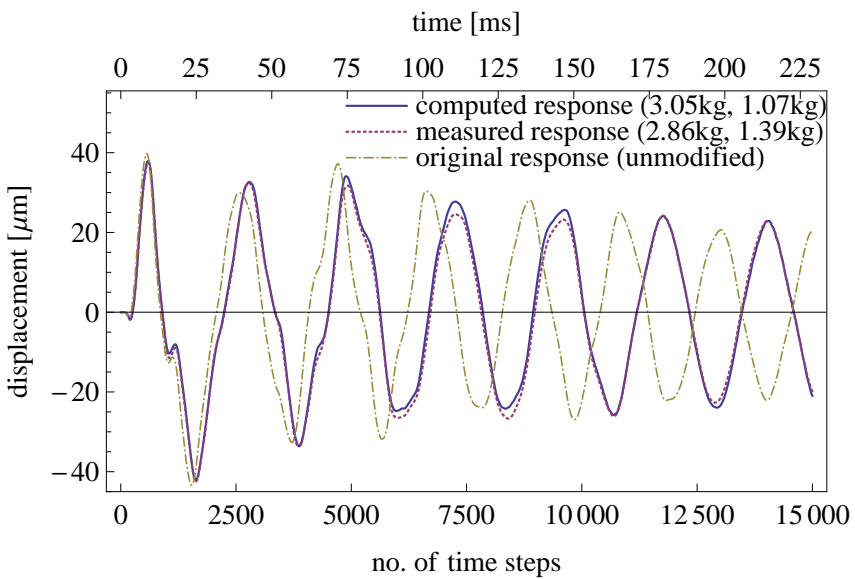


Figure 4.8. Modification of two nodal masses (M_1 , M_3): measured response at the actual masses (2.86 kg, 1.39 kg), modeled response for the identified masses (3.05 kg, 1.07 kg) and the response of the original unmodified structure.

5

Virtual isolation of substructures for local health monitoring

Chapters 3 and 4 discuss the theoretical formulation and an experimental implementation of the virtual distortion method in an inverse problem of identification of structural modifications and damages; the close relation of the methodology to load identification problems is emphasized. This chapter describes another practical application of the VDM: the problem of substructure isolation through virtual supports for the purpose of local structural health monitoring. The formulation relies on load identification in an even more straightforward way, since virtual supports are modeled in terms of their support reaction forces that are identified in a typical problem of load identification. In other words, kinematic boundary conditions on the substructural interface are modeled in terms of the equivalent load boundary conditions.

The substructure isolation methodology has been proposed in [46–53]. The next section discusses the general motivation behind the research in substructuring. The second section briefly reviews the state-of-the-art. The third section introduces the substructure isolation method and emphasizes its relation to the problem of load identification. The fourth and fifth sections describe the process of virtual isolation of a substructure in time domain and in frequency domain. The sixth section illustrates the method using a numerical example. Finally, the last section verifies it in an experimental study using a damaged aluminum cantilever beam. The setup uses up to three different global structures that share the same substructure (the original beam, the beam with an additional “sponge support” and with an additional mass) to test the robustness of the isolation with respect to unknown modifications of the outside structure. Two typical global health monitoring methods are applied at the substructural level, so that the damage is identified based on comparison of either time-domain responses of the substructure or its modal characteristics. In both cases the substructure is successfully isolated and the damages are properly identified in a local analysis.

5.1 Motivation

Research on damage identification in SHM as well as practical applications of developed techniques often focus on large specialized structures, such as bridges, tall buildings, dams, etc. Such complex structures are difficult to be monitored globally using approaches of low frequency SHM due to at least four inherent reasons:

1. *Accuracy and reliability of parametric numerical models.* Boundary conditions and nonlinear components are often hard to model or even determine, which might be reflected in a poor accuracy of any global parametric numerical model of the monitored structure, such as its finite element model.
2. *Poor numerical convergence.* In large problems of global identification or model updating the numerical convergence is usually seriously undermined by a large number of independent unknown parameters that need to be simultaneously identified. This results in significant ill-conditioning which seems to be typical in inverse problems of parametric structural identification.
3. *Large number of sensors* that are necessary to guarantee the uniqueness of the result of a global identification. The reasons are the large number of involved unknowns and low sensitivity of the global response to local damages.
4. *Unknown excitations.* Response of the global structure is often influenced by many excitations that cannot be measured and often even characterized accurately enough.

As a result, in monitoring of large and complex structures, data-driven (pattern-recognition) approaches have often to be used at the expense of accuracy and physicality of model-based SHM. However, in many practical applications only small local substructures are crucial and need monitoring, which suggests that model-based SHM approaches could be applied locally. Such small substructures have much fewer structural parameters and unknown factors that need to be identified and controlled, which makes local modeling and analysis much more feasible in comparison to global approaches. This is the motivation behind the research on substructuring in general and on the substructure isolation method in particular, including this chapter.

5.2 State-of-the-art

5.2.1 Static case

The body of research on damage detection through localized analysis is already relatively substantial. In the static case, the analysis is usually based on global or local structural flexibilities. Park *et al.* [227] decompose the global flexibility matrix into substructural flexibilities (alternatively, they can be also obtained through local measurements) and propose localized damage indicators based on their relative changes. In Park and Reich [228], damages are localized using an invariance property of the transmission zeros of the substructural frequency response functions. Bernal [229] analyzes changes of global flexibility matrix and localizes the damage using the damage locating vectors (DLVs). Duan *et al.* extend this approach in [230] to the case of incomplete measured degrees of freedom.

However, all these analyzes concern the static case only. Structural flexibility is a static characteristics of the structure that may convey less information than contained in its dynamic response. Consequently, certain damages might be masked in static response, even if they evidently manifest themselves in the dynamic response. Thus, several researches have pursued substructuring methods that use dynamic structural response.

5.2.2 Dynamic case

To detect and localize damage, one can compare locally sensitive information, such as local strain or local modal characteristics, extracted from the dynamic structural responses measured before and after the damage occurs. For example, Yun *et al.* [231] propose a method for local monitoring of stiffness modifications using a neural network, where the input vector consists of natural frequencies and locally measured incomplete global mode shapes; a numerical model of the unmodified global structure is required. Bao *et al.* [232] use the damage basic probability assignment (BPA) function of substructures for preliminary damage localization. An and Ou [233] develop a model updating method that utilizes four different cost functions and involves free vibration accelerations and local mode shapes for detection of local damage in a truss structure.

A substructure is a local part of the global structure, and so it is not independent of the global structure. In order to focus on the substructure only, most of the existing approaches separate the substructure from the global structure by partitioning the global equation of motion. The generalized interface forces are then used for coupling both structures and need to be identified together

with substructural parameters. In other words, the substructure is treated as having free boundary conditions on its interface with the global structure and the influence of the global structure is represented by the generalized interface forces. Since these forces are unknown, they need to be identified or estimated along with the unknown parameters of the substructure. The local identification is performed usually in a model-based manner and requires a general parametric numerical model of the substructure to be known beforehand.

The substructural approach has been probably first considered by Koh et al. [234] in the context of structural identification and called a substructural identification (SSI) or a divide-and-conquer strategy. The method proposed in [234] applies the extended Kalman filter with weighted global iteration to substructures with and without overlapping members; in [235], it is developed into a progressive structural identification approach, which identifies the global structure through identification of progressively growing substructures. The extended Kalman filter is used also by Oreta and Tanabe [236] for local identification of member properties in frame structures. A method for shear structures based on cross-power spectral densities is proposed by Zhang and Johnson in [237]. In [238], Yun and Lee employ an ARMAX model of the substructure and a sequential prediction error method to locally estimate unknown parameters that are related to damages; complete measurement of the substructure is necessary, including the interior excitations and the response in all its DOFs. Tee *et al.* [239] apply the substructural strategy in the field of SHM and propose two methods aimed at first and second order model identification and damage assessment at the substructural level. The methods are based on the eigensystem realization algorithm and the observer/Kalman filter; in [240], they are combined with a model condensation approach, which allows the number of necessary measurements to be reduced. In all these and similar methods, complete measurement of interface response is necessary: the measured response is treated as a known input to the substructure. A method that does not require the interface responses to be measured directly is proposed by Koh *et al.* in [241], where the generalized interface forces between the substructure and the global structure are identified simultaneously with the unknown physical parameters of the substructure using local frequency response functions. Different sets of internal response measurements are used to obtain different estimates of the interface forces; the identification procedure amounts to minimization of the discrepancy between them. Yang and Huang propose in [242, 243] a sequential nonlinear least-square method to estimate unknown excitations, physical parameters of the substructure as well as the interface forces. Lei *et al.* propose in [244] a related algorithm for identification of nonlinear substructural parameters; the al-

gorithm is based on the sequential application of the extended Kalman estimator for the nonlinear structural parameters and the least-squares indirect estimation of the unmeasured interface forces. Both methods require only a limited number of output measurements, and they can trace damages changing with time. In [245], Yuen and Katafygiotis present an output-only bayesian frequency-domain approach for substructure identification and monitoring in linear multi degree of freedom (MDOF) systems. Zhang *et al.* [246] introduce a control system to identify storey parameters in a shear structure using cross power spectral density (CPSD). A method based on multi-feature genetic algorithm was used by Trinh and Koh [247] to estimate substructural mass, damping and stiffness parameters. Xing and Mita [248] confine each substructure of a multi-storey shear building to a few DOFs only and use overlapping substructures; they apply directly the ARMAX method for local identification. Wang *et al.* [249] employ the concept of the quasi static displacement vector to simplify the generalized interface forces, and use a method based on a genetic algorithm to identify the substructure.

5.2.3 Substructure separation methods

All the methods mentioned above can be collectively called *substructure separation* methods, since they rather separate than isolate the substructure from the global structure: although separated, the substructure and the global structure remain coupled to each other via the unknown interface forces. Consequently, all the discussed identification methods need to account for the unknown interface forces besides the unknown substructural parameters. However, forces and structural parameters are variables of very different characteristics, and thus all these identification methods, although effective, are not standard and have to be specifically tailored to be used at the substructural level. As a result, none of the standard and widely-researched model updating or health monitoring methods can be directly applied to the separated substructure, which is an inherent deficiency common to all approaches based on substructure separation.

5.3 Overview of the isolation method

5.3.1 Two-stage monitoring

The *substructure isolation* method has been proposed to overcome the drawbacks of the substructure separation approaches [46–53]. The core idea of the isolation is different: instead of separating the substructure and then identifying

its parameters together with the unknown interface forces, the method splits the task of local identification into two conceptually distinct stages that are performed separately:

1. *Virtual isolation of the substructure.* This is essentially a signal processing stage, in which experimentally measured responses of the substructure are numerically processed in order to eliminate the outside influences of the global structure. The result is the response of the substructure that would be measured, if the substructure was actually isolated from the global structure by physically supporting all the degrees of freedom (DOFs) on its interface. The whole procedure is numerical and not physical, and hence the modeled supports in the interface DOFs are virtual in nature.
2. *Local analysis and identification* of the isolated substructure is performed in the second stage. The response computed in the first stage is the local response of the isolated substructure, which has the same physical parameters as the real substructure, but it is independent from the external influences of the global structure. As a result, any of the existing, well-researched methods aimed originally at global SHM can be used together with the computed response and thus effectively at the substructural level.

Such an approach places the substructure isolation method in a broader landscape of methods that use structural modifications, either physical or virtual, to increase the sensitivity of the response to selected structural parameters, see Dems and Mróz [176, 177], Hou *et al.* [250], Nalitolela *et al.* [251] or Bojczuk and Mróz [252].

Notice that there are no unknown interface forces to be accounted for in the second stage. This is a significant advantage of isolation as compared to separation, which allows any of the standard model updating or health monitoring methods to be used locally. Moreover, response of the isolated substructure is computed directly using measured responses of the substructure, so that no parametric numerical model is required at the isolation stage. The disadvantage of the isolation approach is that it requires the substructure to be linear and all interface DOFs to be instrumented.

5.3.2 Excitations, sensors and measured responses

The response of the virtually supported substructure to an internal testing excitation $\mathbf{f}_{\text{test}}(t)$ is computed in the first stage by processing four types of responses of the global structure. These responses are generated experimentally using two different types of excitations and measured using two groups of sen-

sors. The purpose of measurements is to gather enough information about local dynamics of the substructure (internal and interface) when excited either internally or from outside through the interface DOFs. The placement of excitations and sensors is illustrated in Fig. 5.1.

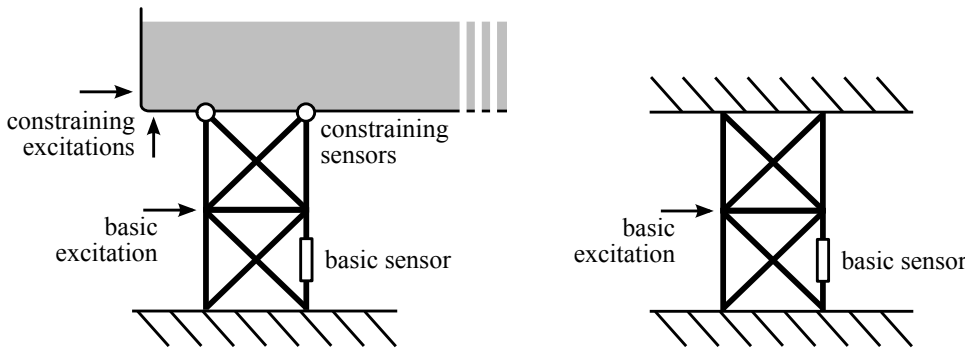


Figure 5.1. Excitations and sensors required for virtual isolation of a substructure: (left) the real substructure as a part of a larger global structure; (right) the virtually isolated substructure.

5.3.2.1 Excitations

The required excitations are divided into

1. *Basic excitation*, which is the external excitation $\mathbf{f}_{\text{test}}(t)$ that is applied inside the considered substructure.
2. *Constraining excitations*, denoted by $q_i(t)$, which are applied in the DOFs of the interface or in the outside structure. Their total number must not be smaller than the number of the interface DOFs.

Each constraining excitation $q_i(t)$ results in a vector $\mathbf{q}_i^I(t)$ of the generalized interface forces that excite the substructure. For the considered substructure, the excitation $q_i(t)$ is thus equivalent to the vector $\mathbf{q}_i^I(t)$ applied in the interface DOFs of the substructure treated as having all free boundary conditions on the interface. In other words, the response of the substructure (with all free boundary conditions on the interface) to the interface excitation $\mathbf{q}_i^I(t)$ is exactly the same as the response of the actual substructure to the constraining excitation $q_i(t)$. Notice that the relation between the constraining excitation and the equivalent interface excitation might not be linear, as the outside structure is not required to be linear.

The excitations (basic and constraining) need not be measured for the purpose of the isolation stage, even if the identification or monitoring methods applied in the subsequent stage of local analysis may require certain characteristics of the basic excitation to be known.

Basically, the constraining excitations can be of any type. However, their character and placement influence the conditioning of the isolation process, and thus the quality of the computed response of the isolated substructure. For a reliable isolation, the responses should provide full information about the internal dynamics of the substructure as excited through its interface. The following practical hints can be considered:

- In order to ensure a high signal-to-noise ratio, the constraining excitations should be placed near the interface rather than far away from it.
- The constraining excitations should be applied in different points and in various directions. In this way, there are more chances that the equivalent interface excitations and the measured responses are independent.
- The constraining excitations should not be very soft or too hard. A soft excitation may excite only low frequencies, while a hard excitation may result in only high-frequency response. In both cases, information in a certain frequency range would be lost.

5.3.2.2 Sensors

The responses of the global structure to the above excitations are measured by the two following groups of sensors:

1. *Basic sensors*, which are linear sensors placed inside the substructure.
2. *Constraining sensors*, which are linear sensors that need to be placed in all DOFs of the substructural interface.

5.3.2.3 Measured responses

Altogether, there are two types of excitations and two groups of sensors, so four different types of response are measured, which are denoted as summarized in Table 5.1. Notice that there is a single basic excitation, so that $\mathbf{u}^L(t)$ and $\mathbf{a}^L(t)$ are vectors, while $\mathbf{B}^{up}(t)$ and $\mathbf{B}^{ap}(t)$ are matrices, because there are several constraining excitations.

Table 5.1. Responses of the global structure used for virtual isolation of its substructure.

	Basic excitation $\mathbf{f}_{\text{test}}(t)$	Constraining excitations
Basic sensors	$\mathbf{u}^L(t)$	$\mathbf{B}^{up}(t)$
Constraining sensors	$\mathbf{a}^L(t)$	$\mathbf{B}^{ap}(t)$

5.3.3 Stage I: substructure isolation

The purpose of the isolation stage is to compute the response $\mathbf{u}(t)$ to the basic excitation $\mathbf{f}_{\text{test}}(t)$ that would be measured by the basic sensors, if the substructure was physically isolated from the rest of the global structure.

The isolation process is numerical, and the supports in the interface DOFs are thus only virtual and not physical. They are modeled using the general methodology of the VDM, in which their reaction forces are replaced with initially unknown pseudo loads. This can be summarized as follows:

1. It is noted that there is an effective equivalence between a physical support and its reaction force. Physical supports represent kinematic boundary condition, which affect the supported substructure by means of their reaction forces. Thus, if the reaction forces are known, the supports can be equivalently modeled using load boundary conditions defined by the known reaction forces.
2. If the supported substructure is linear, there is a linear relation (5.5) between the interface forces and the response. Equation (5.5) is the counterpart of the VDM formula (3.1).
3. The reaction forces, which would be exerted by the supports, if they were physically applied, are unknown. However, the responses in the supported DOFs must vanish, which is expressed in the form of the kinematic compatibility condition (5.6a). Together with (5.5a), this condition yields (5.6b), which can be solved to obtain the proper reaction forces. The kinematic compatibility condition (5.6a) is one of the many special forms of the general VDM formula (3.3).
4. Given the reaction forces, the effect of the corresponding load boundary conditions on the response can be computed using (5.5b).

Basically, the above process is an analogue of the method of forces applied in dynamics. According to the third point, structural response in the to-be-supported DOFs must be measured, which explains why the constraining sensors have to be placed in all the DOFs of the substructural interface. Technically speaking, these sensors implement the virtual interface supports. The whole pro-

cess is equivalent to modeling an isolated substructure, which is an independent virtual structure with the same physical parameters as the real substructure, but isolated from the global structure with virtual supports placed on the interface and modeled using proper load boundary conditions.

5.3.4 Stage II: local identification

The isolated substructure has the same physical parameters as the real substructure, but it constitutes a (virtual) system that is independent from the outside structure. The response $\mathbf{u}(t)$ computed in the first stage is thus a local response of the isolated substructure to the basic excitation $\mathbf{f}_{\text{test}}(t)$, and it does not contain any outside influences. Such a local response can be further processed to obtain certain local characteristics of the substructure, which can include its local natural frequencies and local mode shapes. As a result, local damage identification can be performed by any of the standard and well-investigated methods that have been originally aimed at global identification. In this way, modeling of the global structure is avoided, which can significantly decrease the monitoring costs in real applications.

In the numerical and experimental examples described in this chapter, the substructure is identified by updating selected parameters of its local finite element model. The updating process is based on minimization of an objective function that is formulated using either time-domain or frequency-domain responses.

5.3.4.1 Time-domain identification

Provided the basic excitation is known, local damage of the substructure is identified via a time-domain comparison of the response $\mathbf{u}(t)$ of the isolated substructure with the response $\mathbf{u}^{\text{FE}}(t, \boldsymbol{\mu})$ that is computed using a finite element model of the isolated substructure and which depends on the vector $\boldsymbol{\mu}$ of unknown structural parameters that represent the damage. The vector $\boldsymbol{\mu}$ is treated as an optimization variable, so that the damage is identified by minimizing the following objective function:

$$F(\boldsymbol{\mu}) := \frac{\|\mathbf{u} - \mathbf{u}^{\text{FE}}(\boldsymbol{\mu})\|^2}{\|\mathbf{u}\|^2}. \quad (5.1)$$

which is the normalized least-square distance between both responses.

5.3.4.2 Frequency-domain identification

If the basic excitation is a short-time quasi impulsive load, then the response $\mathbf{u}(t)$ computed in the isolation process is a free response of the isolated substructure. Such a response can be used to identify the local modal model of the isolated substructure, including its natural frequencies ω_i and mode shapes ϕ_i , e.g., by the eigensystem realization algorithm [223]. A local damage of the substructure is then identified by minimizing the following discrepancy between the identified modes and the modes computed using a local finite element model of the isolated substructure:

$$F(\boldsymbol{\mu}) := \sum_i \left| \frac{\omega_i - \omega_i^{\text{FE}}(\boldsymbol{\mu})}{\omega_i} \right|^2 + \kappa \sum_i |1 - \text{MAC}(\phi_i, \phi_i^{\text{FE}}(\boldsymbol{\mu}))|^2, \quad (5.2)$$

where $\omega_i^{\text{FE}}(\boldsymbol{\mu})$ and $\phi_i^{\text{FE}}(\boldsymbol{\mu})$ are respectively the i th natural frequency and mode shape of the local FE model of the isolated substructure, and κ is a weighting factor of the mode shape errors that are computed using the modal assurance criterion (MAC) [253].

5.3.5 Substructure isolation and load identification

Subsection 3.1.4 emphasizes the close relation between the VDM and the inverse problem of load identification. In this chapter, the methodology of the VDM is used for modeling of virtual supports in the purpose of isolation of substructures. It is noted that physical supports influence the structure through their reaction forces. Accordingly, virtual supports are modeled in terms of certain pseudo loads that are placed in the to-be-supported DOFs in order to model the reaction forces of the intended supports. This kind of formulation relies on load identification in a very direct way: the proper time histories of the pseudo loads are found by solving a typical load identification problem, that is by fitting the modeled response of the interface to (the negative of) its measured response, compare (5.6b) to (2.25).

5.4 Isolation in time domain

The substructure is virtually isolated by placing virtual supports in all DOFs of its interface with the rest part of the global structure. The supports are modeled by the pseudo load vector $\mathbf{p}^0(t)$ that would equal the generalized support reaction forces, if the substructure was physically supported. The virtual supports implement fixed boundary conditions on the interface, and thus $\mathbf{p}^0(t)$

models the corresponding generalized boundary forces and defines the equivalent load boundary conditions.

The pseudo load vector is represented in terms of (a convolution of) the generalized interface forces $\mathbf{q}_i^I(t)$ that correspond to the i th constraining excitation $q_i(t)$,

$$\mathbf{p}^0(t) = \sum_i \int_0^t \mathbf{q}_i^I(t - \tau) p_i(\tau) d\tau, \quad (5.3)$$

where i indexes the constraining excitations and $p_i(t)$ are certain unknown functions. Equation (5.3) can be stated in the operator notation as

$$\mathbf{p}^0 = \mathcal{Q}^I \mathbf{p}, \quad (5.4)$$

where \mathcal{Q}^I is the corresponding matrix convolution operator that, unlike \mathcal{Q} in Subsections 2.2.4.1 or 4.2.1.4, is not diagonal.

The considered substructure is assumed to be linear. The response of the virtually supported substructure to the basic excitation $\mathbf{f}_{\text{test}}(t)$ is the sum of the response of the actual substructure and the effects of the pseudo loads that model the supports. The former response is directly measured ($\mathbf{a}^L(t)$ and $\mathbf{u}^L(t)$), while the latter, thanks to (5.3), can be expressed in terms of the measured responses to the constraining excitations. Thus, the response of the constraining and basic sensors in the virtually supported substructure are respectively modeled as

$$\mathbf{a}(t) = \mathbf{a}^L(t) + (\mathcal{B}^{\text{ap}} \mathbf{p})(t), \quad (5.5a)$$

$$\mathbf{u}(t) = \mathbf{u}^L(t) + (\mathcal{B}^{\text{up}} \mathbf{p})(t), \quad (5.5b)$$

where \mathcal{B}^{ap} and \mathcal{B}^{up} are matrix convolution operators with the experimentally measured $\mathbf{B}^{\text{ap}}(t)$ and $\mathbf{B}^{\text{up}}(t)$, see Table 5.1. The interface responses $\mathbf{a}(t)$ vanish in a properly isolated substructure, which yields the following kinematic compatibility condition:

$$\mathbf{a}(t) = \mathbf{0}, \quad (5.6a)$$

and together with (5.5a) leads to

$$(\mathcal{B}^{\text{ap}} \mathbf{p})(t) = -\mathbf{a}^L(t). \quad (5.6b)$$

Equations (5.5b) and (5.6b) yield together the formula

$$\mathbf{u}(t) = \mathbf{u}^L(t) - \left(\mathcal{B}^{\text{up}} [\mathcal{B}^{\text{ap}}]^+ \mathbf{a}^L \right)(t), \quad (5.7)$$

which expresses the response of the isolated substructure to the basic excitation in terms of the measured responses of the actual substructure. Notice that the operator \mathbf{Q}^I does not appear in (5.7), hence neither the constraining excitations $q_i(t)$ nor the equivalent interface excitations $\mathbf{q}_i^I(t)$ need to be known. However, the character and placement of the constraining excitations affects the properties of the operator \mathcal{B}^{ap} , which is inverted in (5.7), and thus the accuracy of the isolation. Therefore, constraining excitations should be chosen with care: a few practical hints have been already provided in Subsection 5.3.2.1. In practice, quasi impulsive excitations, obtained for example with a modal hammer, tend to provide good results.

5.4.1 Isolation with other types of virtual supports

Up to now, the constraining sensors have been all assumed to measure displacement, velocity or acceleration in interface DOFs. Their responses are made vanishing in the isolated substructure, which yields fixed boundary conditions on the interface and, consequently, a kind of virtual supports that can be termed “virtual fixed supports”.

In fact, other types of boundary conditions and virtual supports can be also used, depending on the type of the substructure and sensors placed on its interface. In the following, isolation of a 2D beam is used as an illustrative example. Figure 5.2 shows the structure, the substructure to be isolated and the physical quantities of interest at the interface: the internal shear force $a_T(t)$, the internal bending moment $a_M(t)$, the vertical displacement $a_y(t)$, the rotation $a_\theta(t)$ and the longitudinal strain $a_\varepsilon(t)$, which is measured on one of the beam faces. For the moment, the axial displacement and axial force are ignored for the sake of simplicity: in their absence, the strain $a_\varepsilon(t)$ (measured off the neutral axis) is proportional to the bending moment $a_M(t)$, but much easier to measure. The mentioned quantities can be used to formulate four different types of boundary conditions,

$$a. \begin{cases} 0 = a_y(t), \\ 0 = a_\theta(t), \end{cases} \quad b. \begin{cases} 0 = a_y(t), \\ 0 = a_\varepsilon(t), \end{cases} \quad c. \begin{cases} 0 = a_T(t), \\ 0 = a_\theta(t), \end{cases} \quad d. \begin{cases} 0 = a_T(t), \\ 0 = a_\varepsilon(t), \end{cases} \quad (5.8)$$

where the strain is used as a substitute of the internal bending moment. Equations (5.8) define four kinds of nodal virtual supports that can be applied in the interface to isolate the substructure, see Fig. 5.3.

In practice, it is usually impossible to place physical supports or to apply in real time proper excitations on the interface to make its response satisfy one

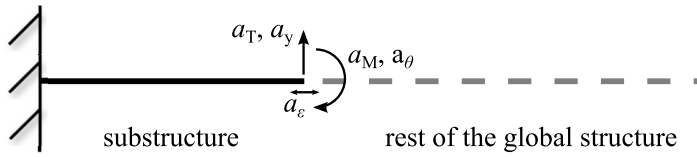


Figure 5.2. A substructure of a 2D beam (axial displacements ignored).

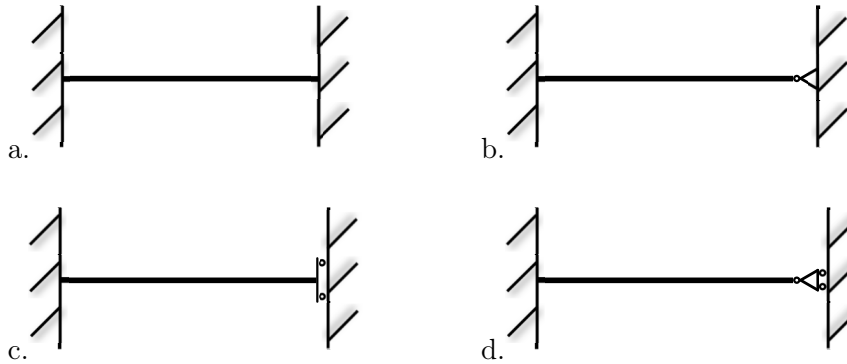


Figure 5.3. The four types of nodal virtual supports defined in (5.8) (axial displacements ignored).

of the four conditions listed in (5.8). However, as shown above, a number of nonzero interface responses can be linearly convolved to zero, so that the resulting interface response satisfies the desired boundary conditions. As a result, the type of the virtual support is determined by the types of the interface sensors. For instance, if $a_y(t)$ and $a_\theta(t)$ are measured, then the *virtual fixed support*, (5.8)a and Fig. 5.3a, can be constructed by a linear combination of the measured responses. Or, if the responses $a_y(t)$ and $a_\varepsilon(t)$ are measured, the *virtual pinned support*, (5.8)b and Fig. 5.3b, can be constructed. In real applications, the shear force $a_T(t)$ is hard to measure, so that the other two kinds of virtual supports (marked c. and d.) will be usually not used. As before, the reaction forces of the virtual supports are modeled with the equivalent vector $\mathbf{p}^0(t)$ of pseudo loads. The substructure and all the sensors are linear, so that (5.3) to (5.6b) hold. Equation (5.7) can be thus used to compute the response of the isolated substructure to the basic excitation, which satisfies the intended boundary conditions as determined by the type of the interface sensors.

In the above example, axial displacement and axial force are ignored. If they are to be considered, the longitudinal strain measured off the neutral axis is no longer a direct substitute of the internal bending moment. In such a case,

two strain sensors can be placed on the opposite faces of the beam in the same distance from its neutral axis: the axial stress and the bending moment will be then proportional to the sum and to the difference of their measurements respectively.

5.4.2 Time discretization and numerical stability

For theoretical clarity, all the responses in this section have been assumed so far to be continuous. However, in a real application only discrete data can be measured, and so all the responses are given in practice in the form of vectors that are sampled in discrete time points every Δt . Therefore, the key formula (5.7) has to be discretized into:

$$\mathbf{u} = \mathbf{u}^L - \mathbf{B}^{up} [\mathbf{B}^{ap}]^+ \mathbf{a}^L, \quad (5.9)$$

where the vectors \mathbf{u} , \mathbf{u}^L and \mathbf{a}^L collect in all time instances the respective discrete responses of all involved sensors, and the matrices \mathbf{B}^{up} and \mathbf{B}^{ap} with proper ordering of the data take the forms of large block matrices with Toeplitz blocks. As an example, Fig. 5.20 left illustrates the structure of the matrix \mathbf{B}^{ap} obtained in the experimental study described in Section 5.7. Matrices of this kind are usually extremely ill-conditioned [109, 111], and hence the superscript $+$ denotes in (5.9) the regularized pseudoinverse, which for smaller problems can be computed directly via the truncated singular value decomposition [67, 111, 128]. However, the term $[\mathbf{B}^{ap}]^+ \mathbf{a}^L$ is (the negative of) the regularized solution of the following discretized version of (5.6b):

$$\mathbf{B}^{ap} \mathbf{p} = -\mathbf{a}^L, \quad (5.10)$$

and it can be also computed as a whole using the Tikhonov regularization or, which is more convenient for large problems, an iterative regularization method such as the conjugate gradient least squares, see [67, 111, 128] and the remarks in Subsection 4.2.3.3.

In all regularization approaches, it is important to properly choose the regularization parameter, which can be, depending on the specific procedure, the number of the retained singular values, the Tikhonov weighting parameter, the number of iterations, etc. The heuristic commonly used for this purpose is the L-curve criterion [67, 111, 135]. However, note that in (5.9) the regularized solution is multiplied by \mathbf{B}^{up} , which is a matrix of a similar structure to \mathbf{B}^{ap} . Thus, \mathbf{B}^{up} acts as a smoothing operator that alleviates the effects of a potential

under-regularization. As a result, the computed discrete response \mathbf{u} of the isolated substructure turns out in practice to be stable for a wide range of values of the regularization parameter, see, e.g., Figs. 5.11 and 5.12.

5.5 Isolation in frequency domain

In the previous section, the response of the isolated substructure is constructed in time domain. It involves solving a very large and extremely ill-conditioned matrix equation (5.10), which originates from a discretization of a system of Volterra integral equations of the first kind (5.6b) and has the dimensions proportional to the number of the considered time steps N_t . Solution of such a system is difficult and time-consuming; the size of the system and thus the manageable length of the measurement time interval is significantly limited. Similar as in Section 4.3, a frequency-domain formulation can be proposed, which significantly decreases the computational effort: the method performs much faster, even if considerably longer measurement time intervals are used.

The naming convention for the responses is the same as in Table 5.1, with the exception that the responses are now complex amplitudes that depend on the frequency ω . The frequency-domain counterparts of (5.5) have the form of the following matrix equations:

$$\mathbf{a}(\omega) = \mathbf{a}^L(\omega) + \mathbf{B}^{ap}(\omega)\mathbf{p}(\omega), \quad (5.11a)$$

$$\mathbf{u}(\omega) = \mathbf{u}^L(\omega) + \mathbf{B}^{up}(\omega)\mathbf{p}(\omega), \quad (5.11b)$$

where $\mathbf{B}^{ap}(\omega)$ and $\mathbf{B}^{up}(\omega)$ are complex matrices. In contrast to (5.5), which constitute a large system of Volterra integral equations, (5.11) yield for each ω a different discrete linear system of a moderate size.

In a properly isolated substructure, the response of all the interface sensors vanish, which yields the kinematic compatibility condition

$$\mathbf{a}(\omega) = \mathbf{0}, \quad (5.12a)$$

and thus the following frequency-domain counterpart of (5.6b):

$$\mathbf{B}^{ap}(\omega)\mathbf{p}(\omega) = -\mathbf{a}^L(\omega) \quad (5.12b)$$

is a discrete matrix equation of a moderate size (the number of unknowns equals the number of the to-be-supported interface DOFs or constraining sensors) that needs to be solved separately for each ω of interest. The solution to (5.12b) can

be represented using the regularized pseudoinverse as $-[\mathbf{B}^{\text{ap}}(\omega)]^+ \mathbf{a}^L(\omega)$, which substituted into (5.11b) yields

$$\mathbf{u}(\omega) = \mathbf{u}^L(\omega) - \mathbf{B}^{\text{up}}(\omega) [\mathbf{B}^{\text{ap}}(\omega)]^+ \mathbf{a}^L(\omega). \quad (5.13)$$

In practice, even repeated solutions of (5.12b), each for a different ω , are considerably faster than a single solution of the integral equation (5.6b). The process is even less time-consuming, if only a limited number of frequencies ω is of interest instead of the full spectrum.

5.5.1 Isolation in time domain vs. isolation in frequency domain

Equations (5.12b) and (5.13) are frequency-domain counterparts of the time-domain (5.6b) and (5.7). The most important differences between the two formulations can be summarized as follows:

1. The frequency-domain (5.12b) is a separate matrix equation for each frequency line ω , and since not always all frequencies are of interest, it might be solved only a very limited number of times. The time-domain (5.6b) is a single system of Volterra integral equations that needs to be solved once and for all.
2. The frequency-domain (5.12b) is of a significantly smaller size than any discretized version of (5.6b). The former system has the dimensions of *number of interface sensors* \times *number of constraining excitations*, while in the latter system both dimensions are N_t times larger, where N_t is the number of the time steps.
3. In practice, the time-domain system is always extremely ill-conditioned. The frequency-domain system is well-conditioned for most of the frequencies ω , provided the constraining excitations are properly placed and applied, see Subsection 5.3.2.1.
4. In an application, (a discretized version of) the time-domain system is constructed directly using measured time-domain responses, while the frequency-domain system needs an initial pre-processing of the measurement data (windowing, averaging, discrete Fourier transform, etc.), see Subsection 5.5.2.

Only the last of the above points mentions an advantage of the time-domain formulation; the former three points list clear advantages of the frequency-domain approach.

5.5.2 FFT of the time-domain responses

In real applications the measured time-domain response is discrete, so the frequency-domain formulation requires the fast Fourier transform to be employed to compute the frequency-domain responses. If the time-domain signal is of a finite length and does not tend to zero in the integration time, spectral leakage is inevitable. As demonstrated in the numerical example below (Sub-section 5.6.2), it can significantly impair the accuracy of the frequency-domain response computed using (5.13). To minimize the adverse effect of the spectral leakage, the windowing process is usually employed before performing the FFT. Here, three windowing functions are tested: $w_e(t, \eta)$ (exponential window), $w_h(t)$ (hanning window) and, for comparison purposes, $w_1(t)$ (rectangular window, that is no windowing),

$$w_e(t, \eta) := \begin{cases} e^{-\eta t} & \text{for } 0 \leq t \leq T, \\ 0 & \text{elsewhere,} \end{cases} \quad (5.14a)$$

$$w_h(t) := \begin{cases} \frac{1}{2} + \frac{1}{2} \cos(\frac{\pi t}{T}) & \text{for } 0 \leq t \leq T, \\ 0 & \text{elsewhere.} \end{cases} \quad (5.14b)$$

$$w_1(t) := \begin{cases} 1 & \text{for } 0 \leq t \leq T, \\ 0 & \text{elsewhere.} \end{cases} \quad (5.14c)$$

A useful feature of the exponential window can be considered in order to support its feasibility: compare the free response of an n -DOF structure in $t \in [0, T]$ with the same response after exponential windowing,

$$\mathbf{u}(t) = \sum_i A_i \phi_i e^{-\omega_i \xi_i t} \sin(\omega_{di} t + \theta_i), \quad (5.15a)$$

$$\mathbf{u}(t) w_e(t, \eta) = \sum_i A_i \phi_i e^{-\omega_i (\xi_i + \eta/\omega_i) t} \sin(\omega_{di} t + \theta_i), \quad (5.15b)$$

where ϕ_i is the shape of the i th structural mode, A_i denotes the amplitude, ω_i is the i th natural frequency, ξ_i is the corresponding damping ratio, and $\omega_{di} = \omega_i(1 - \xi_i^2)^{0.5}$. The exponential window increases the damping ratio of the free response by η/ω_i , but does not change its frequency content, which is unlike other windows including the hanning window.

5.6 Numerical examples

Two simple mass-spring systems are used for initial verification of the isolation method and to illustrate the principles of its application. Time-domain as

well as frequency-domain isolation with the three considered windowing functions are used. The influence of the regularization level on the accuracy of the results is tested.

5.6.1 2-DOF mass-spring system

This example considers an elementary 2-DOF mass-spring system shown in Fig. 5.4(left). The value of each lumped mass is m ; the stiffness and the damping of each spring are k and c respectively. The system matrices are thus

$$\mathbf{M} := \begin{bmatrix} m & 0 \\ 0 & m \end{bmatrix}, \quad \mathbf{C} := \begin{bmatrix} 2c & -c \\ -c & c \end{bmatrix}, \quad \mathbf{K} := \begin{bmatrix} 2k & -k \\ -k & k \end{bmatrix}. \quad (5.16)$$



Figure 5.4. Numerical example of the 2-DOF mass-spring system: (left) the global system and (right) its isolated substructure.

Let the substructure consist of the second mass and the spring, as shown in Fig. 5.4(right). There is a single DOF only (the first mass) on the interface, thus a single constraining excitation is necessary, which has to be applied to the first mass. In frequency domain, the constraining excitation is unit harmonic. If the basic excitation is also unit harmonic, then the basic and constraining displacement responses are the respective entries of system frequency response matrix $\mathbf{H}(\omega)$, see Table 5.1,

$$\mathbf{H}(\omega) = \begin{bmatrix} \mathbf{B}^{ap}(\omega) & \mathbf{a}^L(\omega) \\ \mathbf{B}^{up}(\omega) & \mathbf{u}^L(\omega) \end{bmatrix} = \frac{1}{A} \begin{bmatrix} k + ic\omega - m\omega^2 & k + ic\omega \\ k + ic\omega & 2k + 2ic\omega - m\omega^2 \end{bmatrix}, \quad (5.17)$$

where $A = (k^2 + 2ick\omega - (c^2 + 3km)\omega^2 - 3icm\omega^3 + m^2\omega^4)^{-1}$. Equation (5.13) can be now used to obtain the response of the isolated substructure to the basic excitation,

$$\mathbf{u}(\omega) = \frac{1}{k + ic\omega - m\omega^2}, \quad (5.18)$$

which is obviously the same as the frequency response function of the single DOF system shown in Fig. 5.4(right). The substructure is thus successfully isolated.

Table 5.2. Numerical example of the 6-DOF massspring system: naming convention.

	Basic excitation f_6	Constraining excitation f_3
Basic sensor x_5	$\mathbf{u}^L(\omega), \mathbf{u}^L(t)$	$\mathbf{B}^{up}(\omega), \mathbf{B}^{up}(t)$
Constraining sensor x_3	$\mathbf{a}^L(\omega), \mathbf{a}^L(t)$	$\mathbf{B}^{ap}(\omega), \mathbf{B}^{ap}(t)$

5.6.2 6-DOF mass-spring system

5.6.2.1 The structure, excitations and sensors

Consider a 6-DOF mass-spring system shown in Fig. 5.5(left). The stiffness of each spring is $k = 2 \text{ kN/m}$ and all the lumped masses are $m = 4 \text{ kg}$. The proportional damping model is used, and the 1st and 2nd order damping ratios are 1%. The substructure to be isolated and locally monitored consists of the 4th, 5th and 6th mass, as shown in Fig. 5.5(right), while the interface DOF that should be fixed is the 3rd mass. These data are used to obtain FE models (mass, damping and stiffness matrices) of the global system and of the isolated substructure.

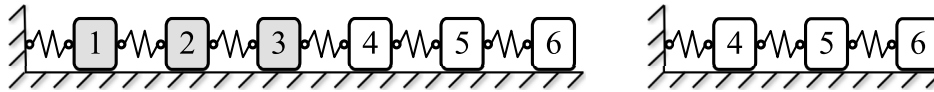


Figure 5.5. Numerical example of the 6-DOF mass-spring system: (left) the global system and (right) its isolated substructure.

Assume that two acceleration sensors, denoted by x_3 and x_5 , are placed respectively on the 3rd and the 5th mass, and that two excitations, denoted f_3 and f_6 , can be applied respectively to the 3rd and the 6th mass. In the following, the FE model of the global system is used in frequency domain and in time domain to compute the corresponding four responses, which are denoted in the plots by x_i-f_j for the purpose of notational clarity. They are treated as measured responses, and the FE model of the global system is not used anymore. These responses play the role of the four responses used in (5.6b) and (5.13) to construct the response of the isolated substructure, see the naming convention in Table 5.2. The accuracy of the constructed response is verified using the FE model of the isolated substructure, by comparison with the directly simulated response of the 5th mass to the excitation of the 6th mass provided that the 3rd mass is fixed.

5.6.2.2 Isolation using exact frequency-domain responses

Figure 5.6(left) plots the exact acceleration frequency response functions (accelerance FRFs) of the global system, as simulated using its FE model. They are directly used in (5.13) to construct the accelerance FRF of the isolated substructure,

$$\mathbf{u}(\omega) = \mathbf{u}^L(\omega) - \frac{\mathbf{B}^{up}(\omega)}{\mathbf{B}^{ap}(\omega)} \mathbf{a}^L(\omega). \quad (5.19)$$

Figure 5.6(right) compares the result to the accurate accelerance FRF computed using the FE model of the isolated substructure. Amplitudes of both responses are the same (the discrepancies are of the order of the accuracy of the floating point arithmetic), which confirms that the considered substructure can be successfully isolated in frequency domain by means of the exact accelerance FRFs.

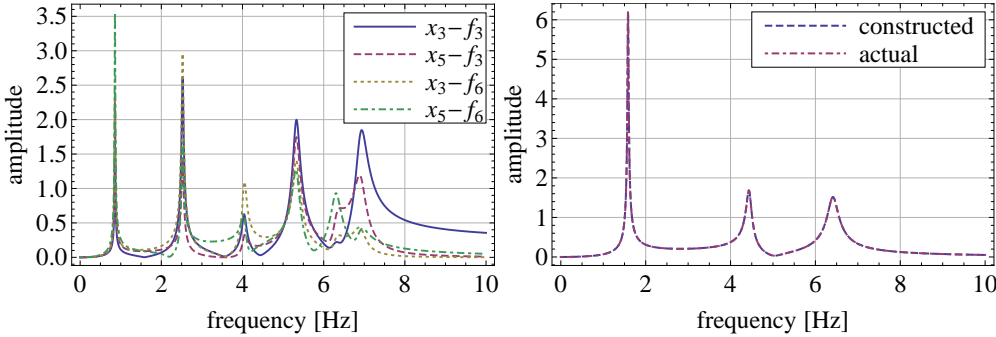


Figure 5.6. Numerical example of the 6-DOF mass-spring system: (left) amplitudes of the accelerance FRFs of the global system; (right) constructed and actual accelerance FRFs of the isolated substructure.

5.6.2.3 Isolation using noisy time-domain responses

In order to emulate a real application with time-domain excitations, a simulated hammer excitation is applied to the 3rd and 6th mass, see the left-hand side of Fig. 5.7. The sampling frequency is 200 Hz and the time interval is $T = 5$ s, which results in a total of 1000 time steps. In order to simulate the responses of the global system, the Newmark integration scheme [145–148] with the standard parameters $\gamma = 1/2$ and $\beta = 1/4$ is used to integrate the equation of motion of its FE model, see the right-hand side plot. In the same way, the time-domain responses of the isolated substructure are directly computed based on its FE model and used in the following for comparison purposes.

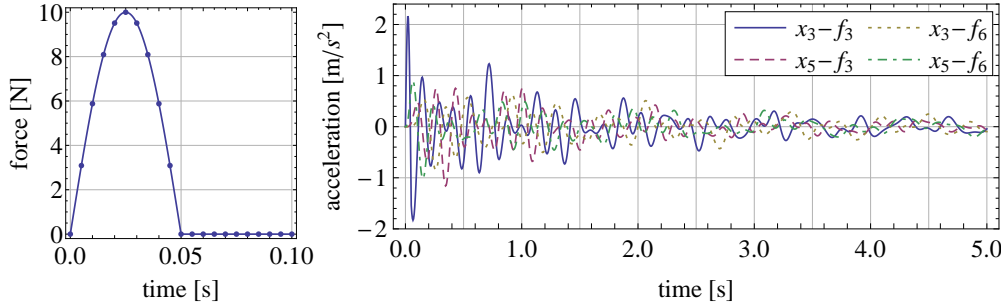


Figure 5.7. Numerical example of the 6-DOF mass-spring system: (left) simulated hammer excitation; (right) simulated responses of the global structure.

First, in the following, the simulated responses are used to construct the accelerance FRF of the isolated substructure using the windowing functions discussed in Subsection 5.5.2. By comparison with the FRF obtained using the directly simulated responses of the isolated substructure, only the exponential window is selected for further computations. Then, all the generated responses are contaminated with uncorrelated Gaussian noise at 5% rms level and used again in frequency- and time-domain isolation. The time-domain responses of the isolated substructure obtained this way are used with the ERA [223] to identify basic modal parameters of the substructure (natural frequencies and damping ratios). The relative accuracy of the results (time-histories of the responses and the identified modal parameters) is compared in terms of the decay rate of the FFT window and in terms of the regularization level (CGLS iterations).

FFT and windowing. All the three windowing functions mentioned in Subsection 5.5.2 (exponential window, hanning window and no windowing) are tested. The exponential window depends on the window decay rate η . Here, it is specified through the attenuation ratio $r = w_e(T, \eta)$ at the end of time interval T ; both quantities are related to each other by

$$r = \exp(-\eta T) = e^{-\eta T}, \quad \eta = -\frac{\ln r}{T}. \quad (5.20)$$

Three different values of the attenuation ratio r are initially tested: 10^{-1} , 10^{-2} and 10^{-3} . Before performing the FFT, in order to increase its frequency resolution, several zeros are added in front of the windowed hammer excitation and the responses (the time interval is increased tenfold and filled with zeros at the beginning).

The results of the FFT are used to construct the frequency-domain response of the isolated substructure by (5.13); this response is divided by the FFT of the simulated hammer excitation to obtain the constructed FRF of the isolated substructure. The FEM-based response of the substructure is processed in the same way, and using the same windowing functions, to compute the FEM-based FRF of the isolated substructure for verification purposes. Figure 5.8 (top left, top right and bottom left) compares the amplitudes of the constructed and FEM-based FRFs. Only the exponential window (top left) is able to yield consistent results. Even if the hanning window (top right) yields almost the same positions of the peaks, the amplitudes deviate significantly. The destructive effect of spectral leakage is clearly evident in the case of no windowing (bottom left).

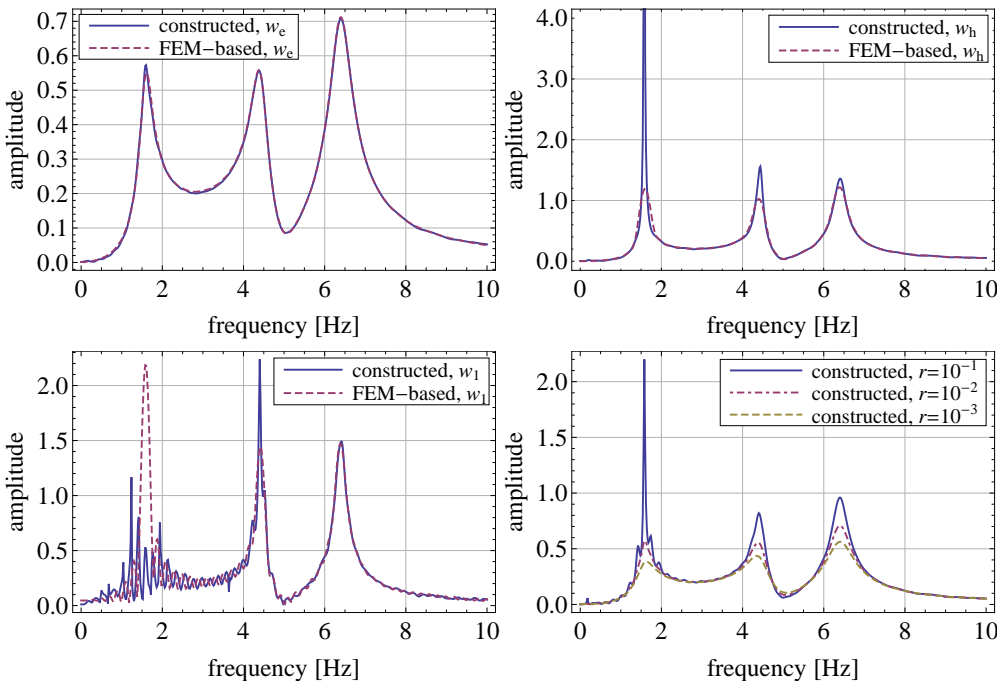


Figure 5.8. Numerical example of the 6-DOF mass-spring system. Comparison of the constructed and FEM-based accelerance FRFs of the isolated substructure: (top left) exponential window, $r = 10^{-2}$; (top right) hanning window; (bottom left) no windowing. Exponential window, spectral leakage and effective damping: (bottom right) accelerance FRF constructed using exponential windows with different decay rates.

As mentioned in Subsection 5.5.2, the exponential window increases the effective system damping. Figure 5.8 (bottom right) compares the amplitudes of the FRFs constructed with different values of the window attenuation ratio. For $r = 10^{-1}$, there are obvious oscillations, which suggests that the window decay rate is not large enough to reduce the spectral leakage. On the other hand, too small r introduces too much damping into the system. As a result, a compromise value should be chosen.

Isolation in frequency domain. The inverse FFT is applied to the response of the isolated substructure constructed using exponential windows with the attenuation ratio r varying in the range from 1 (no windowing) to 10^{-4} . After the first 50 ms of the constructed response is discarded, see Fig. 5.7(left), the remaining part is the free response of the isolated substructure and can be thus used with the ERA to retrieve modal parameters of the substructure. The raw constructed response is windowed, which means that either

1. The ERA is applied directly to the windowed response. In order to account for the damping effect of the exponential window, the identified damping ratios are corrected by η/ω , see Subsection 5.5.2 and (5.20). Or
2. The response is first unwindowed (divided by the exponential window) and then used with the ERA. The identified damping ratios do not need to be corrected.

In both cases, the accuracy of the identification results depends on the particular value of the ratio r used in computations. Figure 5.9 plots the relative root mean square (RMS) errors of the identified eigenvalues, damping ratios and the time-histories of the constructed responses in dependence on r . The first case (windowed response) is shown in the left-hand side figure; the right-hand side figure plots the second case (unwindowed responses). An example comparison of a time-domain response of the isolated substructure constructed using a compromise value of $r = 10^{-2}$ with the actual time-domain response (both of which are windowed and unwindowed using the same exponential window) is shown in Fig. 5.10.

Notice that the results are clearly unstable for too small attenuation of the windowing function ($r > 10^{-1}$), which has to be attributed to the insufficiently reduced spectral leakage. On the other hand, too much damping (too small r) results in pronounced oscillations at the end of the time interval that occur in the constructed unwindowed response; they can be checked to increase dramatically with decreasing attenuation ratio r . Between $r = 10^{-2}$ and $r = 10^{-3}$ the oscillations lead to serious numerical instability, which cause the regularization procedures that are in-built into the used software packages to intervene. This

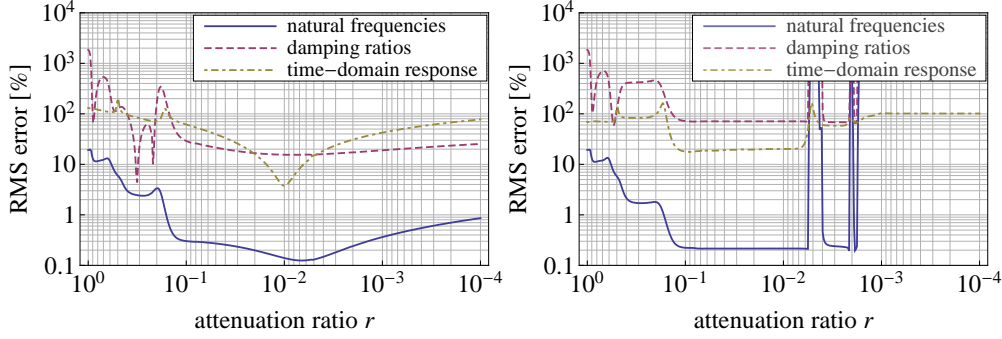


Figure 5.9. Numerical example of the 6-DOF mass-spring system. Isolation in frequency domain. Relative root mean square errors of identified natural frequencies, damping ratios and time-domain responses in dependence on the attenuation ratio r of the exponential window. Identification and comparison performed using: (left) windowed responses; (right) unwindowed responses. Notice the effect of the undamped oscillations for $r < 10^{-2}$ and the related intervention of the regularization procedures in-built into the inverse FFT routine.

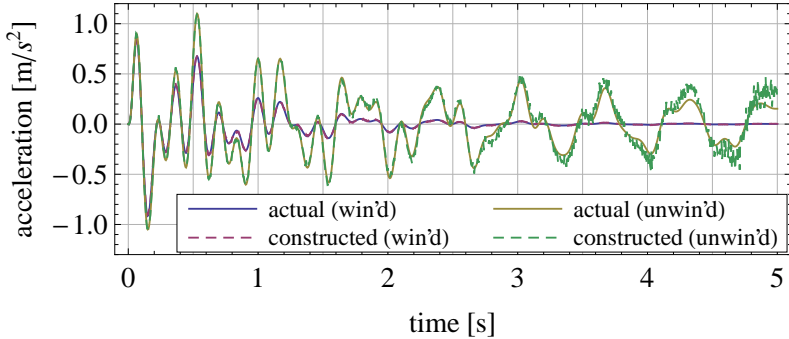


Figure 5.10. Numerical example of the 6-DOF mass-spring system. A comparison of the windowed and unwindowed time-domain responses of the isolated substructure (isolation in frequency domain, exponential FFT window with the attenuation ratio $r = 10^{-2}$).

can be seen in Fig. 5.9(right): after initial spikes, for $r < 10^{-3}$ the constructed unwindowed response stays exactly the same, irrespective of the attenuation ratio and with a high constant level of the oscillations. The destructive effect of the oscillations can be partially countered by applying the ERA to the windowed responses, which increases the relative weight of the initial part of the constructed response.

Isolation in time domain. The time-domain responses x_3 and x_5 of the global system to the constraining excitation f_3 are used to build the lower triangu-

lar Toeplitz matrices \mathbf{B}^{ap} and \mathbf{B}^{up} , which are the discretized versions of the corresponding Volterra convolution operators, see Subsection 5.4.2. The iterative algorithm of CGLS is used to solve (5.10); the result is substituted into (5.9) to obtain the time-domain response of the isolated substructure. The first 50 ms of the constructed response is discarded, and the remaining part is used with the ERA to retrieve the modal parameters of the substructure. Due to ill-conditioning of (5.9), the constructed time-domain responses have small oscillations near the end of the time interval. Although similar oscillations appear also in the responses constructed using frequency-domain isolation, they are masked there by the exponential window, see Fig. 5.10, while in time-domain isolation there is no such a natural attenuating window. Thus, besides the full-length constructed responses, their first halves are also used with the ERA. The accuracy of the results depends on the regularization level of the computed solution to (5.10), that is on the number of CGLS iterations used to solve it. Figure 5.11 plots the relative RMS errors of identification results in dependence on the number of CGLS iterations; the results computed using full- and half-length responses are distinguished by using thick and thin lines respectively. An example comparison of time-domain responses of the isolated substructure (constructed using 100, 200 and 400 CGLS iterations) with the actual time-domain response is shown in Fig. 5.12.

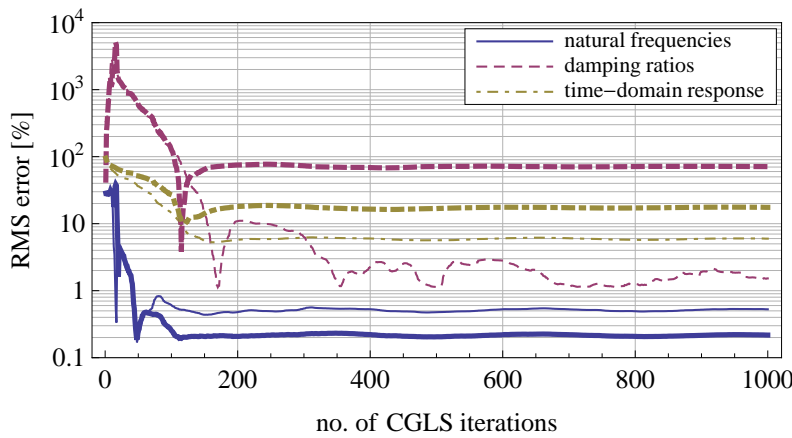


Figure 5.11. Numerical example of the 6-DOF mass-spring system. Isolation in time domain. Relative root mean square errors of identified natural frequencies, damping ratios and time-domain responses in dependence on the number of CGLS iterations. The results obtained with full-length responses are plotted using thick lines; thin lines denote the results obtained for half-length responses.

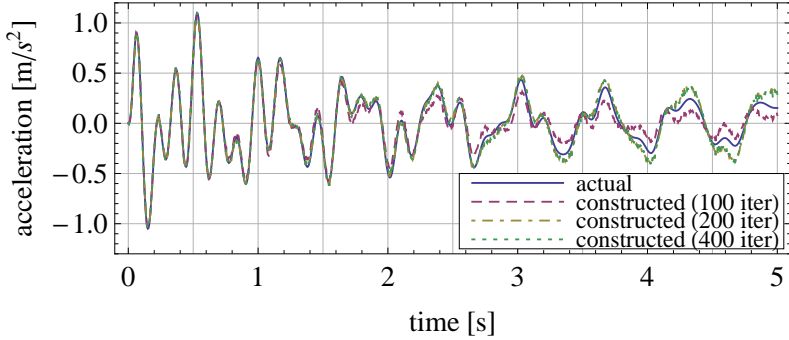


Figure 5.12. Numerical example of the 6-DOF mass-spring system. A comparison of the time-domain responses of the isolated substructure (isolation in time domain; 100, 200 and 400 CGLS iterations).

The results attest the stability of the CGLS-based isolation in time domain. The results are unstable only if the solution to (5.9) is overregularized, that is if too few CGLS iterations are used. Then, after passing a certain threshold number of iterations, the constructed response and the identified modal parameters remain stable irrespective of the number of iterations used. In general, half-length responses yield considerably better results, at least in terms of the time-histories of the responses and the modal damping ratios. On the other hand, the natural frequencies obtained with full-length responses are more accurate, but the difference is negligible in practice (0.2% vs. 0.5% relative error).

Practical conclusions. The results allow the following practical conclusions to be drawn:

- The numerical example confirms the effectiveness of the substructure isolation method. The constructed responses of the virtually isolated substructures are accurate and stable enough to be used for local monitoring: at simulated 5% rms error of the time-domain responses of the global structure, the relative errors of substructural identification can be kept one order of magnitude lower for natural frequencies and at the same order of magnitude for modal damping ratios and the time-histories of the responses.
- Isolation in frequency domain is much quicker than in time domain. However, the exponential FFT window with a proper decay rate must be used for stable results. The accuracy can strongly depend on the decay rate and the window of proper decay rates can be relatively narrow: the at-

tenuation must be large enough to prevent spectral leakage and small enough to prevent numerical inaccuracies in the inverse FFT routine.

- Isolation in time domain is relatively time-consuming: the cost of a single step of CGLS iteration (two FFT-based matrix–vector products) is comparable to the cost of a full frequency-domain isolation. However, after passing a relatively small threshold number of iterations, the results remain stable irrespectively of the actual number of iterations.

5.7 Experimental verification

This section verifies the substructure isolation method in an experimental example. Time-domain and frequency-domain isolation is respectively used to construct the time-domain responses of the isolated substructure to a windowed sine pulse and to an impact excitation by a modal hammer. These responses are used to identify a local damage of the substructure. Structural parameters of a local FE model of the isolated substructure are updated based on fitting either the time-histories of the responses or the substructural natural frequencies. Two modifications of the global structure are used to test the robustness of the isolation with respect to unknown modifications and nonlinearities of the outside structure.

5.7.1 Experimental setup

The experimental setup is shown in Fig. 5.13. The specimen, a slender aluminum cantilever beam, has a rectangular cross-section of 2.7 cm × 0.31 cm and the length of 136.15 cm. The beam is vertically suspended from a stable frame, which is seen in blue on the left-hand side of the figure. Young's modulus of the beam is 70 GPa, and the density is 2700 kg/m³. The upper part of the beam (of length 79.4 cm) is the substructure to be identified. It is damaged by cutting even notches near the fixed end on the length of 10.2 cm, which decreases the bending stiffness of the damaged segment to 42% of its original stiffness and leaves the mass nearly unchanged, see Fig. 5.14(left). Up to three different global structures that share the same substructure are used in order to verify the robustness of the isolation with respect to unknown modifications or nonlinearities of the outside structure, see Table 5.3 and Fig. 5.13. Based on the same beam, the outside structure is modified by fixing an unknown additional mass or by mounting a “sponge support” in place of the free end. The sponge support can increase the structural damping and may have nonlinear characteristics.

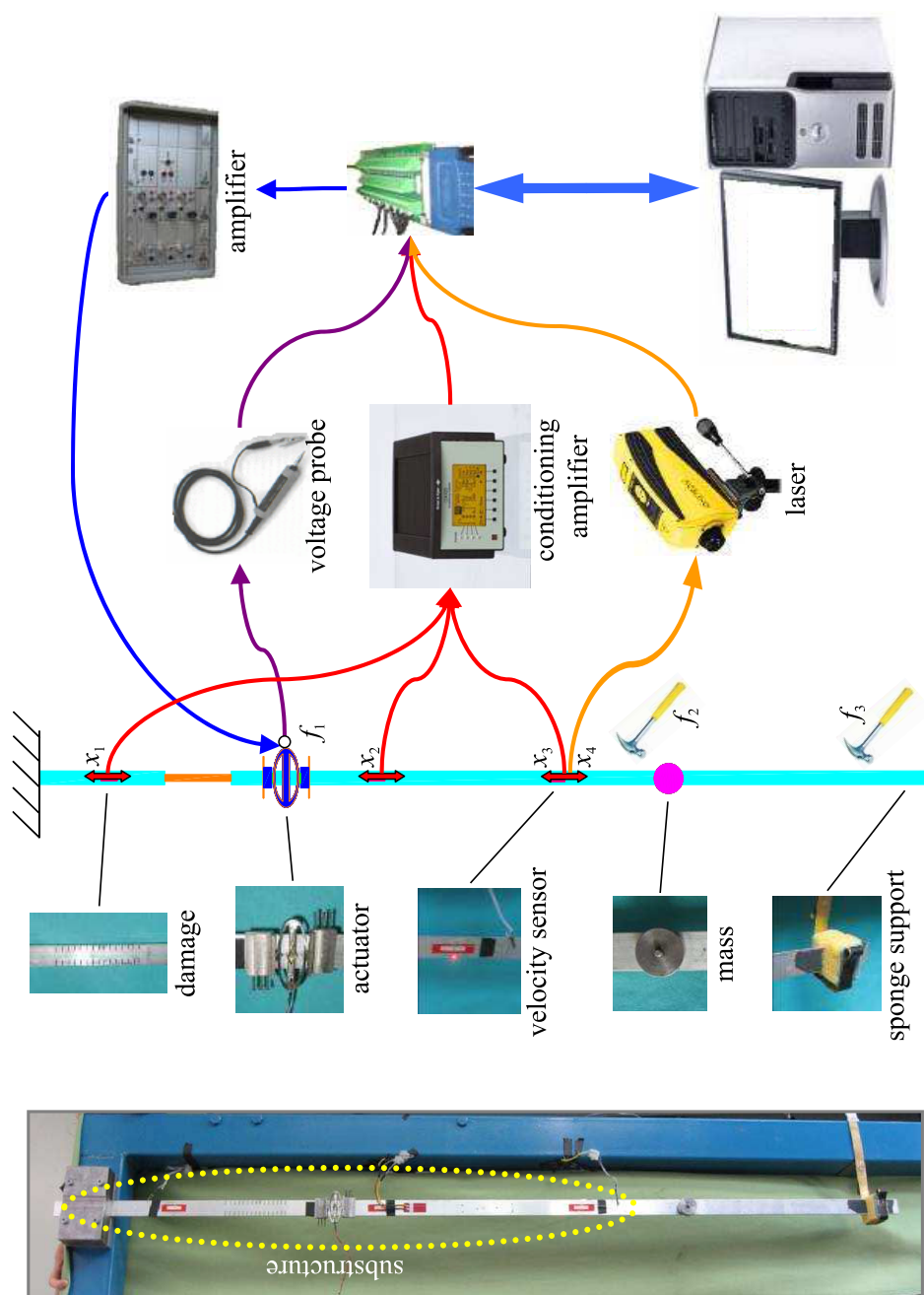


Figure 5.13. Experimental example. The setup.

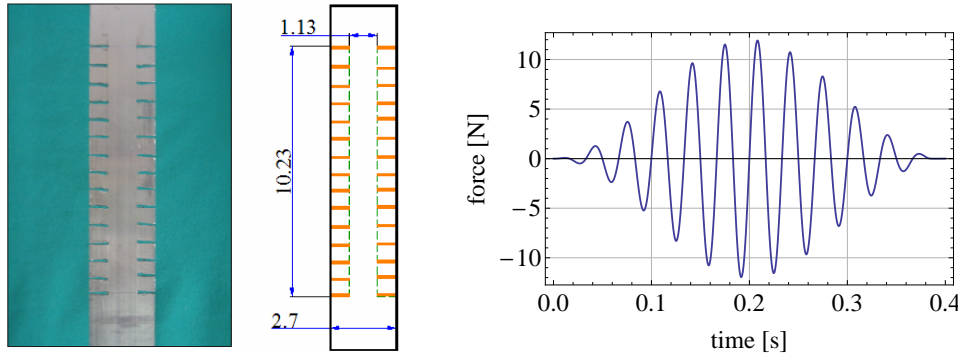


Figure 5.14. Experimental example. (left) The to-be-identified damage of a section of the beam (bending stiffness decreased to 42%, mass nearly unchanged); (right) Basic excitation f_1 for time-domain identification: a windowed sine pulse $\sin 60\pi t$ applied using the piezo actuator (APA).

Table 5.3. Experimental example. The three global structures with the same substructure.

Symbol	Outside structure
b_1	original beam
b_2	original beam with an additional unknown mass
b_3	original beam with a “sponge support”

Inside the substructure, two kinds of the basic excitation f_1 are separately applied to be used with different isolation and identification methods:

1. For isolation and identification in time-domain through (5.9) and (5.1), a windowed sine pulse $\sin(60\pi t)$ is applied using an amplified piezo actuator (APA) [254], see Fig. 5.14(right). The APA is fixed inside the substructure in such a way that it can be assumed to apply a pure moment load.
2. For isolation in frequency domain via (5.13) and identification based on fitting the natural frequencies by (5.2), the APA is not mounted and a transverse impact by a simple uninstrumented hammer is used instead in the role of the basic excitation. The excitation is not measured.

There are no axial excitations, which allows axial displacements of the neutral beam axis to be neglected.

Three piezoelectric patches are glued to one of the beam faces (off the neutral axis) to measure the longitudinal strain x_1 , x_2 and x_3 , and the transverse interface velocity x_4 is measured using a laser vibrometer, see Fig. 5.13 and Table 5.4. The measurement data is acquired and stored on a PC via the acquisition system LabVIEW. Raw voltage readings are used in computations in

order to avoid unnecessary scaling of the measurement noise. Two amplifiers are used to amplify the signals from the strain sensors (x_1 , x_2 and x_3) and the excitation signal f_1 . To reduce the measurement noise, each excitation is repeated 4 or 5 times and the averaged responses are used for identification. The sampling frequency is chosen to be 10 kHz in order to guarantee that the sampled data contain all the necessary dynamic information about the substructure. The considered sampling time is 0.4 s (4000 time steps or the length of the excitation) for the time-domain isolation and 4 s (40 000 time steps) for the frequency-domain isolation.

A single virtual pinned support is modeled in the interface node to isolate the substructure, see Fig. 5.15. As axial displacements are negligible, it is implemented by the two interface sensors: the strain sensor x_3 plays the role of the free support in the rotational DOF and constrains the bending moment, while the velocity sensor x_4 plays the role of the fixed support and constrains the transverse displacement, see Fig. 5.3(b). The two other strain sensors (x_1 and x_2) are located inside the substructure and used for damage identification.

Two virtual supports are used, and two constraining excitations are thus required. A simple uninstrumented hammer is used at two points of the outside structure to apply transverse impacts, which are denoted by f_2 and f_3 , see Table 5.5. In order to ensure that the corresponding responses are independent, f_2 and f_3 are placed far from each other.

Let the substructure be divided into five segments, as shown in Fig. 5.15. The damage is modeled by decreasing the bending stiffnesses of the segments, and it is represented by the vector $\mu = \{\mu_1, \mu_2, \dots, \mu_5\}$ of their stiffness reduction

Table 5.4. Experimental example. Sensors and responses.

Symbol	Measurand	Position
x_1	strain 1	upper substructure
x_2	strain 2	lower substructure
x_3	strain 3	interface
x_4	transverse velocity	interface

Table 5.5. Experimental example. Excitations.

Symbol	Excitor	Position
f_1	piezo actuator/hammer	substructure
f_2	hammer	upper outside structure
f_3	hammer	lower outside structure

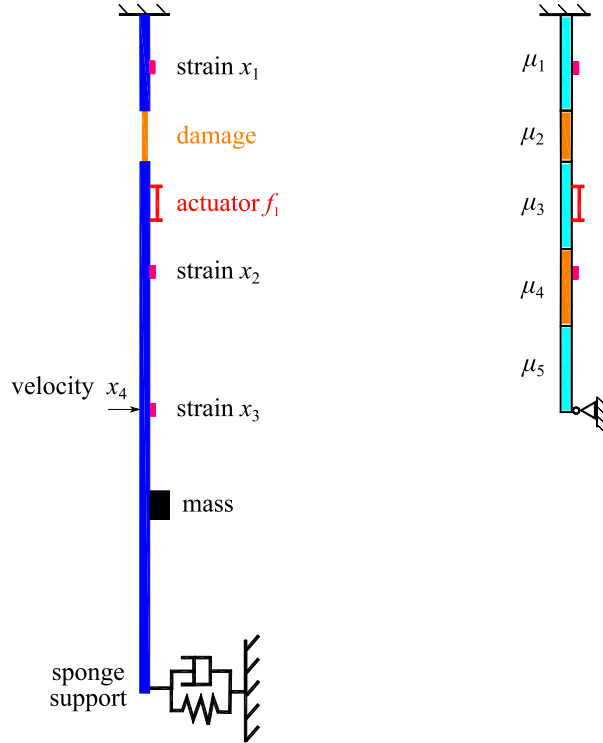


Figure 5.15. Experimental example. Isolation of the substructure with a single virtual pinned support in the interface node (free support in the rotational DOF, fixed support in the transverse DOF, negligible axial distortions): (left) the global structure; (right) the isolated substructure and its division into five segments.

ratios, where $\mu_i \in (0, 1]$ is the ratio of the decreased stiffness of the i th segment to its original stiffness, see (3.24). In the experiment, only the second segment is actually damaged, and the actual, to-be-identified damage is represented by

$$\boldsymbol{\mu}_{\text{actual}} := [1.00, 0.42, 1.00, 1.00, 1.00]^T. \quad (5.21)$$

A local FE model of the undamaged isolated substructure is built and updated. The beam is slender and vertically suspended, the model includes thus the effects of the gravity. The axial distortions are neglected, since all excitations are either moment or transverse loads. Such a local substructural model is used for the purpose of local damage identification. No FE model of the global structure is used. This is consistent with the fact that the global structure is modeled only nonparametrically: the three considered global structures b_1 , b_2 and b_3 are represented exclusively by their experimentally measured responses $b_i - x_j - f_k$.

5.7.2 Isolation and identification in time domain

For time-domain isolation, the piezo actuator is used to apply the basic excitation f_1 depicted in Fig. 5.14(right). The corresponding responses of the four sensors x_1 to x_4 are measured in all three global structures b_1 to b_3 and shown in Fig. 5.16. The responses of the three structures differ significantly, which confirms that the structures are substantially different. The only exception is the strain x_2 : the sensor is located close to the actuator, and it responds mainly to the excitation. The responses to the impulsive constraining excitations f_2 and f_3 are shown in Fig. 5.17. Notice that there are significant differences between the three structures b_1 , b_2 and b_3 , too.

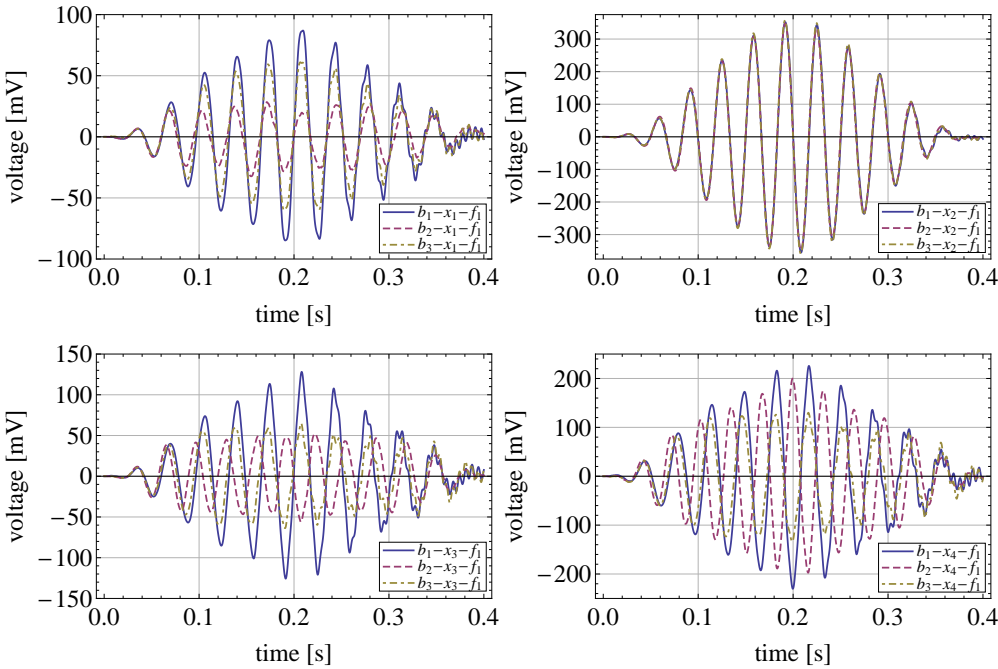


Figure 5.16. Experimental example. Isolation in time domain. Measured responses of the three considered global structures to the basic excitation f_1 by the APA: (top left) strain x_1 ; (top right) strain x_2 ; (bottom left) strain x_3 ; (bottom right) transverse velocity x_4 .

The substructure is isolated by (5.9). The isolation process makes use of the responses to the basic and constraining excitations, which can be measured in any of the three global structures b_1 , b_2 or b_3 . Figure 5.18 compares the constructed responses x_1 and x_2 of the (damaged) isolated substructure to the responses of the undamaged substructure as simulated using its FE model. The

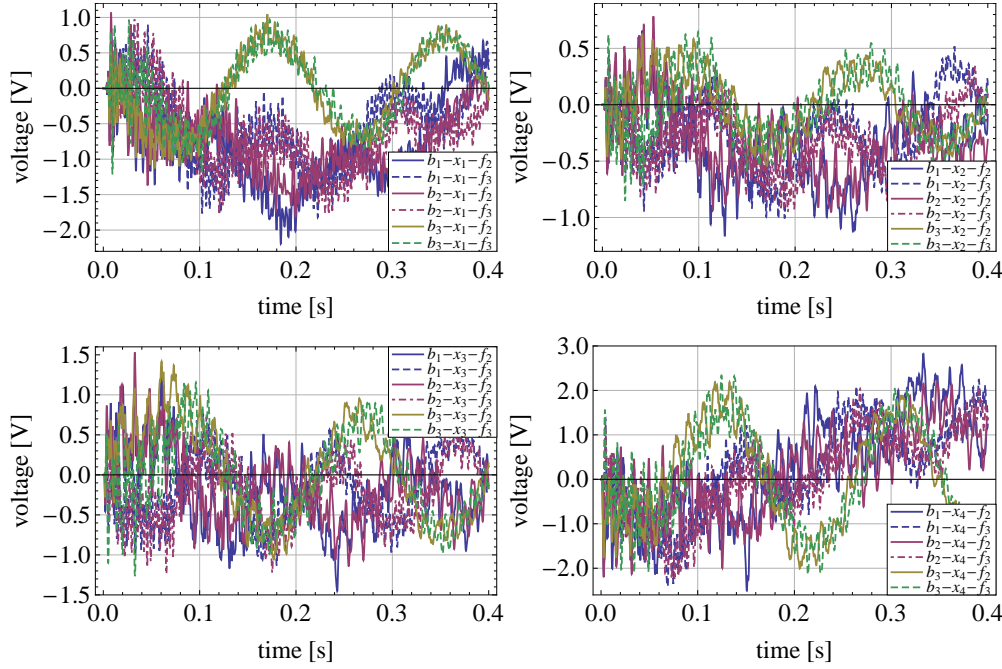


Figure 5.17. Experimental example. Isolation in time domain. Measured responses of the three considered global structures to the constraining excitations f_2 and f_3 : (top left) strain x_1 ; (top right) strain x_2 ; (bottom left) strain x_3 ; (bottom right) transverse velocity x_4 .

constructed responses are visually indistinguishable, which is consistent with the fact that all three global structures share the same substructure. The influences of its outside, including the additional mass and the sponge support, are successfully eliminated. The clearly noticeable difference between the constructed and the simulated responses is related to the local damage and can be exploited for its identification.

Each of the constructed responses in Fig. 5.18 is constructed using the measurements of the same global structure, out of the three possible. In order to verify the robustness of the isolation method in a case of a global structure that changes during the measurements, the responses to the basic and constraining excitations are measured in different global structures. As there are three global structures, there are nine possible combinations, which are denoted by “Bi–Cj”¹. Figure 5.19 plots all the nine responses constructed this way. They

¹That is, “B1–C2” denotes that the respective response is constructed using measurements to the basic (B) excitation of the global structure b_1 and measurements to the constraining (C) excitations of b_2 .

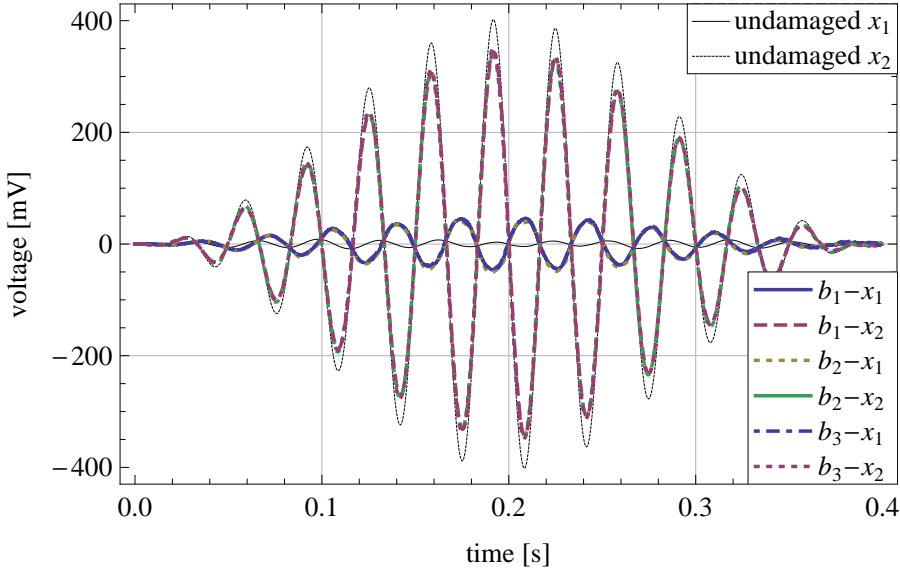


Figure 5.18. Experimental example. Isolation in time domain. Constructed responses x_1 and x_2 of the same substructure, isolated out of the three considered global structures b_1 , b_2 and b_3 , and compared to the FEM-based responses of the undamaged substructure.

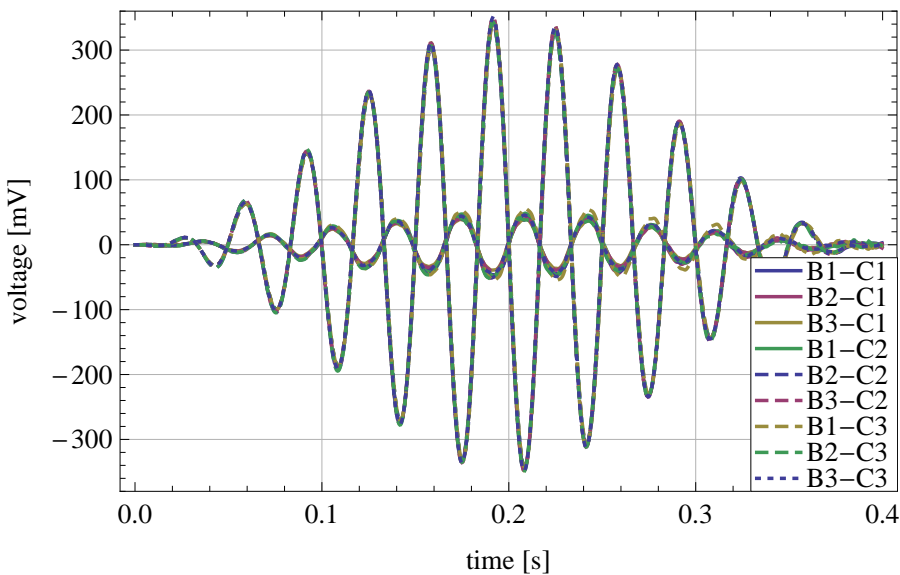


Figure 5.19. Experimental example. Isolation in time domain. The nine constructed responses of the isolated substructure. “ B_i-C_j ” denotes the result obtained with the responses to the basic and constraining excitations measured respectively in global structures b_i and b_j .

all match each other well, which confirms that the constructed response is not influenced by an even developing unknown modification of the outside structure, provided the substructure remains the same. Figure 5.20(left) illustrates the block Toeplitz structure of the matrix \mathbf{B}^{ap} as obtained for structure b_1 .

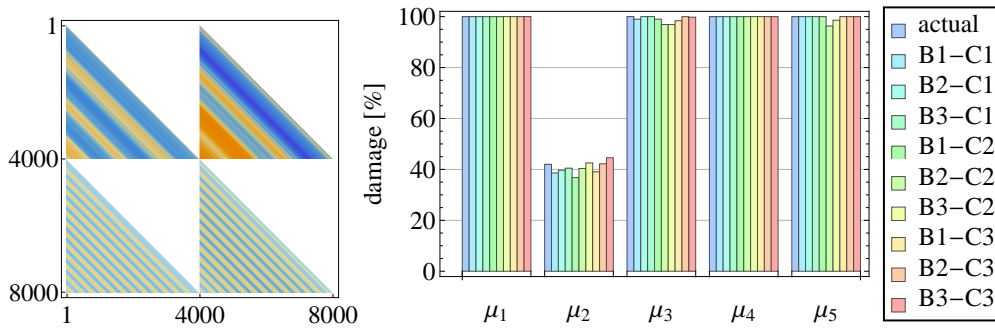


Figure 5.20. Experimental example. Isolation in time domain. (left) Block Toeplitz structure of the matrix \mathbf{B}^{ap} as measured in the global structure b_1 ; (right) Actual and identified damage. “ B_i-C_j ” denotes the result obtained with the responses to the basic and constraining excitations measured respectively in global structures b_i and b_j .

Damage identification in time domain is equivalent to the minimization of the objective function (5.1) with respect to the five stiffness reduction ratios μ_1 to μ_5 , subject to the common sense constraints $0 < \mu_i \leq 1$. The identification results are shown in Fig. 5.20(right) and compared to the actual values. Both the location and the extent of the damage are identified with a high accuracy, even though the outside structures were different or changing. Note that the damage is identified at the substructural level, that is no FE model of the global structure is used for this purpose. Moreover, constructed the response of the isolated substructure, there is no need for time-consuming repeated identification of the generalized interface forces in each optimization step.

5.7.3 Isolation and identification in frequency domain

For isolation in frequency domain by (5.13), the beams b_1 and b_3 are used without the APA. Instead, a transverse impulsive excitation of a simple uninstrumented hammer is applied at the same location and used in the role of the basic excitation f_1 . The corresponding responses of all the four sensors x_1 to x_4 measured in the two global structures are shown in Fig. 5.21. The identification is based on fitting the natural frequencies, and hence a long time interval of 4 s (40 000 time steps) is used.

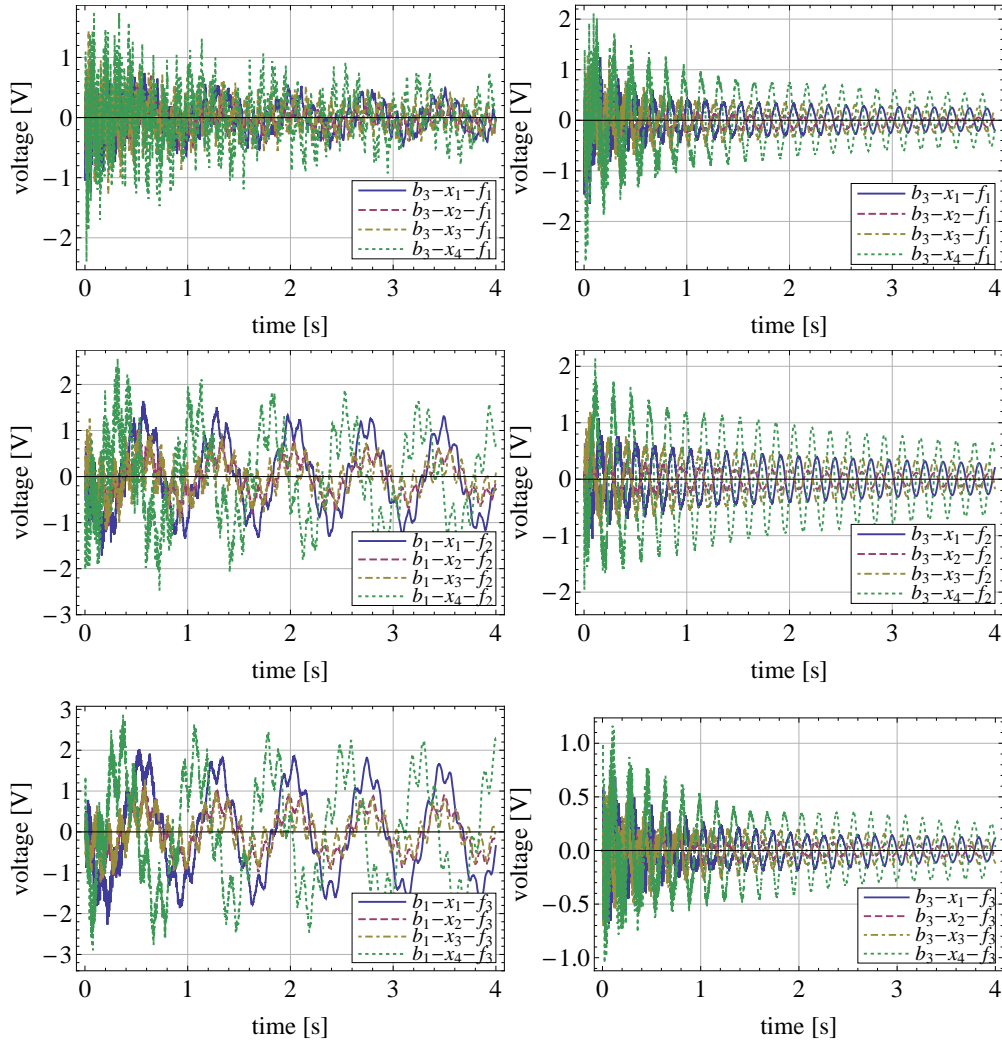


Figure 5.21. Experimental example. Isolation in frequency domain. Measured time-domain responses of the global structures b_1 and b_3 to the basic excitation by a simple hammer: (left column) global structure b_1 ; (right column) global structure b_3 . (top row) basic excitation f_1 ; (middle row) constraining excitation f_2 ; (bottom row) constraining excitation f_3 .

In a similar way as in the time-domain analysis, the responses to basic and constraining excitations can be measured in different global structures. Two global structures are used here, and there are thus four possible combinations. The corresponding spectra of the constructed responses x_1 and x_2 of the isolated substructure are shown in Fig. 5.22. The vertical gridlines mark the natural

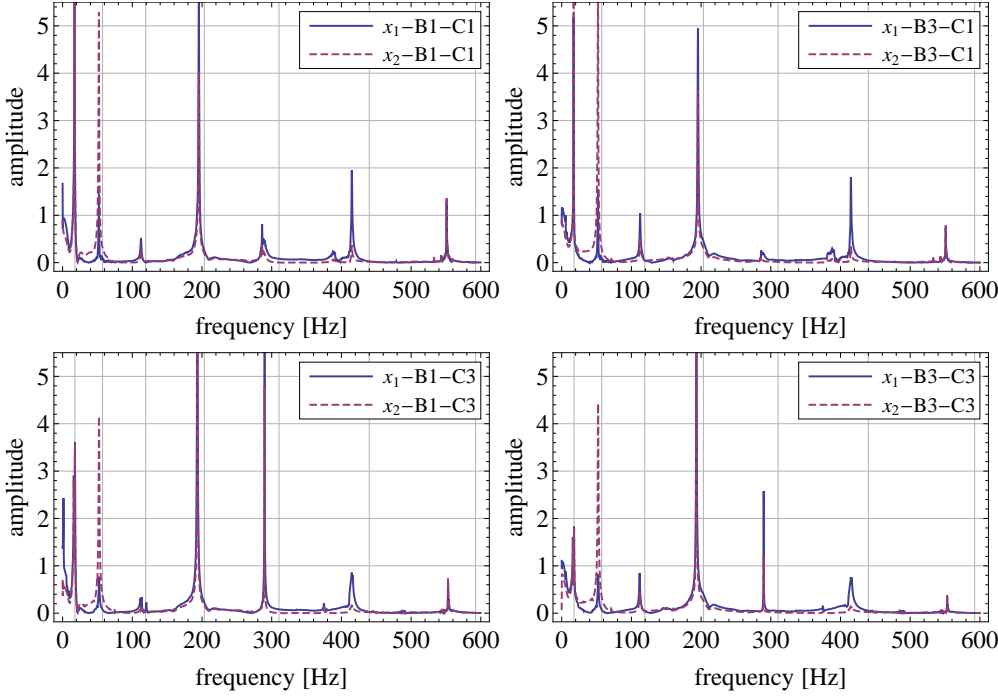


Figure 5.22. Experimental example. Isolation in frequency domain. Spectra of the four constructed responses of the isolated substructure to f_1 : (top left) B1–C1; (top right) B3–C1; (bottom left) B1–C3; (bottom right) B3–C3. “Bi–Cj” denotes the result obtained with the responses to the basic and constraining excitations measured respectively in the global structures b_i and b_j . The vertical gridlines mark the natural frequencies of the undamaged isolated substructure.

frequencies computed using the FE model of the undamaged structure. They are clearly different from the plot peaks; the differences are due to the damage and can be exploited for its local identification. To decrease the spectral leakage, the exponential window is employed with the same attenuation ratio $r = 10^{-2}$ as in the numerical example in Subsection 5.6.2. As mentioned in Subsection 5.5.2, such a window can affect modal identification of the isolated substructure. According to (5.20) and (5.15), given the attenuation ratio r , the corresponding offset of the i th damping ratio is inversely proportional to ωT . Natural frequencies ω of the isolated substructure in the experiment are much higher than those in the numerical example and the measurement time T is longer, so here the influence of the exponential window is small. The peaks of

the constructed responses (Fig. 5.22) are very pronounced, and thus the first seven natural frequencies of the isolated substructure are obtained by simple peak-picking²; they are listed in Table 5.6. The results are in good agreement with the natural frequencies computed using the FE model of the substructure and the actual damage extents (5.21), which confirms that the substructure is successfully isolated. Notice also that the identified natural frequencies are almost the same in all four combination cases, which confirms that the isolation process is independent of the outside structure: if the substructures are the same, the constructed isolated substructures are also the same, irrespective of the outside structure.

Table 5.6. Experimental example. Isolation in frequency domain. Natural frequencies of the isolated substructure in Hz.

no.	Theoretical FEM		Identified experimentally			
	intact	damaged	B1–C1	B3–C1	B1–C3	B3–C3
1	17.64	17.47	17.08	17.08	17.69	17.70
2	57.33	52.00	52.14	52.14	52.27	52.27
3	119.15	112.94	112.49	112.52	113.25	111.83
4	203.28	195.65	195.48	195.51	193.27	193.27
5	310.44	290.01	286.27	286.31	289.84	289.84
6	439.89	413.88	414.96	414.97	414.81	414.82
7	592.37	550.98	550.99	550.99	553.04	553.04

The identification of damage is based on updating the local FE model of the isolated substructure to fit in relative terms its first seven natural frequencies to the frequencies listed in Table 5.6. The first summand in (5.2) is used as the objective function. First, for illustration purposes, it is assumed that the location of the damage is known (second segment), so that only μ_2 is unknown. Figure 5.23(left) plots the four objective functions in dependence on μ_2 . All the four minima are located close to the actual value of 42%, which is marked with the vertical gridline. Then, the full identifications are performed with respect to all the five stiffness reduction ratios μ_1 to μ_5 , subject to $0 < \mu_i \leq 1$. The results are shown in the right-hand side of Fig. 5.23. Identification accuracy,

²Notice that besides the seven more pronounced peaks there are two small spurious peaks at approximately 2 Hz and 375 Hz. They correspond to the first natural frequency of the global structure and to its first torsional mode. The former is apparently not fully isolated, while the latter cannot be modeled using a plane beam model employed here.

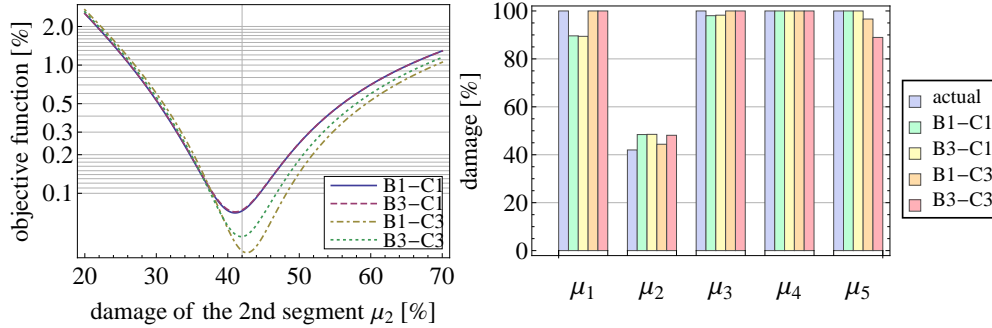


Figure 5.23. Experimental example. Isolation in frequency domain: (left) Objective functions in the four considered cases. Only μ_2 (the damage of the second segment) is assumed to be unknown. The vertical gridline mark the actual damage of 42%; (right) Actual damage and the results of full identification. “Bi–Cj” denotes the result obtained with the responses to the basic and constraining excitations measured respectively in the global structures b_i and b_j .

even if slightly lower than in the time-domain analysis, is still very good in terms of localization and quantification of the damage. As in the case of time-domain isolation, the damage is identified at the substructural level, so that only local FE modeling is necessary for this purpose. Constructed the response of the isolated substructure, the outside part, including the generalized interface forces, can be disregarded.

6

Simultaneous identification of damages and dynamic excitations

Identification of dynamic excitations and identification of damages are two crucial problems in structural health monitoring. Over the recent years, the respective identification problems have become widely researched fields and several robust methods have been proposed. However, the problems are almost always treated as decoupled:

- either the external excitations are assumed to be known and the damage is identified
- or the structure is assumed to be known in order to identify the excitations (see a review in Subsection 2.1.2).

Such an approach can be problematic in applications, where unknown damages and unknown excitations coexist, together influence the structural response and are both of interest. In such cases, the related identification problems are inherently coupled: it is in principle not possible to identify the unknown excitation independently from the unknown damage.

In general, it seems that the research on simultaneous identification of arbitrary dynamic excitations and structural damages is very limited. The main difficulty seems to lie in a very different type of the involved unknowns: excitations \mathbf{f}^0 vs. structural parameters $\boldsymbol{\mu}$, see (1.2). As a rule, due to their essentially different natures, two-step iteration procedures are adopted: the excitations and structural parameters are updated separately in each iteration, so that the optimization process proceeds in an alternate manner. This is a nonstandard optimization approach that requires dedicated identification methodologies, see Section 6.1.

This chapter briefly reviews the state-of-the-art and describes two different solutions to the problem of simultaneous identification of coexistent dynamic excitations and structural damages, see also [39, 40, 55, 57, 62]. The proposed

solutions are aimed at simplification of the identification methodologies proposed so far, especially with respect to the way the two types of the involved optimization variables are treated. Both are based on the virtual distortion method and avoid the inconveniences of the typical two-stage alternating optimization procedures. The solutions explore the two following approaches to unification of the optimization variables:

1. The first approach (Section 6.2, see [57, 62]) represents the damages in the form of virtual distortions (pseudo loads) and identifies them together with the unknown excitation using standard load identification procedures. The identified virtual distortions are used to recover the stress-strain relationships of the damaged elements, and consequently, the type and extent of the damage. As a result, the type of the damage need not be assumed *a priori*, which is a unique feature of this approach.
2. The second approach (Section 6.3, see [39, 40, 55]) proceeds the opposite way and parametrizes the excitations (moving loads are considered here). In this way, both damage and excitations are represented by a set of unified parameters that can be simultaneously updated in each iteration of the optimization procedure.

As usual in the VDM, the assumption of small deformations or geometric linearity is required.

6.1 State-of-the-art

The unknowns involved in the problem of simultaneous identification of co-existent excitations and damages are of very different types (excitations and structural parameters). Accordingly, two-step iteration procedures are usually adopted in the literature, so that the optimization process proceeds by alternating between the unknowns of both types, which are updated separately from each other. The body of related research seems to be very limited: Chen and Li [255] propose a method based on an iterative least-squares identification procedure, which requires each degree of freedom (DOF) of the monitored structure to be instrumented. A method based on sensitivity of structural responses is proposed and experimentally verified by Lu and Law in [256], which represent the unknown excitation force in the form of a sum of a constant and sinusoidal terms; the parameters of the force (amplitudes and frequencies) are identified together with the damage (modifications of element stiffnesses) with a limited number of measurements. In [257], Zhang *et al.* present a method for simultane-

ous identification of structural damage and support excitation that is modeled using a finite series of Chebyshev polynomials; their amplitudes are treated as the optimization variables together with the stiffness modification coefficients. In Zhang *et al.* [61], only damage parameters are treated as the unknown optimization variables: in each optimization step, assumed the damage, the excitation is uniquely determined from the measured responses. There is also a number of substructuring approaches based on separation of the substructure from the global structure via the generalized interface forces that need to be identified together with the unknown substructural parameters; see Subsection 5.2.2 for a short review.

In case of an unknown moving load, characteristics of the coupled vehicle-bridge system vary in time and can be significantly different from those of the bridge alone [258]. The number of publications on simultaneous identification of moving loads and damages seems to be as small as in the case of nonmoving excitations. The author is aware of only five other papers that study the problem of identification of selected additional structural parameters besides the moving load, which includes parameters such as the prestressing force [259]. Zhu and Law [260] propose a method for simultaneous identification of a moving force and damage in a simply supported beam, where the excitation models a moving vehicular load; the required number of sensors is one less than the number of the elements of the beam. A related method is considered by Lu and Liu in [261, 262], which identifies bridge and vehicle parameters using a typical two-stage optimization procedure. Hoshiya and Maruyama [263] apply a weighted global iteration procedure and the extended Kalman filter for simultaneous identification of a moving load and modal parameters of a simply supported beam. The load is parametrized either by its magnitude and velocity (a constant moving force) or by its static magnitude, velocity, damping and frequency (a moving single DOF oscillator).

Besides, there is a relatively small number of papers that use a known moving load for detection or identification of unknown damages. It includes Majumder and Manohar [264, 265], as well as Nasrellah and Manohar [266], who use a moving oscillator for damage identification in linear and nonlinear beams; the beam and the oscillator are treated together as a single coupled and time-varying system. Sieniawska, Śniady and Żukowski use in [267] a static substitute of the equation of motion to identify parameters of a linear structure from its responses to a moving force of a known constant magnitude; the approach is tested experimentally on a highway bridge. Pakrashi *et al.* present in [268] experimental monitoring of a progression of a crack in a beam using beam–vehicle interaction response. Other related researches include [269–273].

6.2 Damage-equivalent excitations

In this section, the methodology of the VDM is employed to model the unknown damages by virtual distortions [57, 62]. These are equivalent to locally applied pseudo loads, and as mentioned in Subsection 3.1.2.2, they can be directly identified together with the unknown excitation forces using standard linear load identification procedures, see Chapter 2. The identified virtual distortions are used to recover the stress-strain relationships of the damaged elements. As a result, the damages of unknown types can be identified via an analysis of the identified stress-strain curves. Therefore, no damage model needs to be assumed in advance, which is considered to be an important advantage of this approach. This advantage comes at the cost: in practice, an a priori information about the locations of the excitations and the damages is required in order to keep the number of sensors reasonably small¹.

The approach can be used off-line and online by repetitive applications in a moving time window. The numerical costs are considerably reduced by approximating the unknown excitations and virtual distortions with a set of suitable approximating functions (splines, wavelets, load shape functions, etc.). First, a numerical experiment of a truss with 5% measurement error validates that the two tested damage types (constant stiffness reduction and breathing crack) can be identified along with the excitation. A damaged cantilever aluminum beam is then used in an experimental verification; the identification is successfully performed off-line as well as online.

6.2.1 VDM-based formulation and the direct problem

For the sake of notational simplicity only truss structures, damages related to stiffness and strain sensors are considered here. These simplifications are inessential, since the methodology can be straightforwardly extended to include other damage patterns and nonlinearities as well as other types of structures and sensors, see a more general formulation of the VDM in Chapter 3. In particular, specific generalizations to plates and frames are discussed in [28, 161, 195], mass-related modifications are discussed in Chapter 4 and elastoplastic structures are considered in Chapter 7. Strain response is used here because of its straightforward relation to the virtual distortion of a truss element, see (6.5a).

¹In practical applications the information on localization might be partly provided by a dedicated external system [274, 275]. However, in further research this drawback should be also addressed directly.

A truss element has only a single virtual distortion (see Subsection 3.2.1), which is the axial distortion

$$\varepsilon_i^0(t) := \kappa_{i1}^0(t), \quad (6.1)$$

where i indexes the potentially damaged elements. Correspondingly, for a truss structure with stiffness-related damages, each line of (3.29b) can be expressed in the following integral form:

$$\varepsilon_i(t) = \varepsilon_i^L(t) + \sum_k \int_0^t B_{ik}^{\kappa\kappa}(t-\tau) \varepsilon_k^0(\tau) d\tau, \quad (6.2)$$

where $\varepsilon_i(t)$ is the strain response of the i th element in the damaged structure to a certain external excitation $\mathbf{f}^0(t)$, $\varepsilon_i^L(t)$ is the strain response to the same excitation of the same element in the intact structure, and the summation extends over all potentially damaged elements. As in (3.29b), zero initial conditions have to be assumed. In modeling the stresses of the damaged elements, the virtual distortion has to be subtracted from the total strain,

$$\sigma_i(t) = E_i (\varepsilon_i(t) - \varepsilon_i^0(t)), \quad (6.3)$$

where E_i denotes the original Young's modulus of the undamaged i th element.

The virtual distortion $\varepsilon_i^0(t)$ of the i th element models its stiffness-related defect, which is expressed in terms of the (possibly time-dependent) modified stiffness $\tilde{E}_i(t)$ or the corresponding stiffness modification coefficient $\mu_i(t)$,

$$\mu_i(t) = \frac{\tilde{E}_i(t)}{E_i}, \quad (6.4)$$

which is the direct counterpart of (3.24) for truss structures and yields the following counterpart of (3.28b):

$$\varepsilon_i^0(t) = (1 - \mu_i(t)) \varepsilon_i(t) \quad (6.5a)$$

or, equivalently,

$$\mu_i(t) = \frac{\varepsilon_i(t) - \varepsilon_i^0(t)}{\varepsilon_i(t)}. \quad (6.5b)$$

In the direct problem, the external excitation $\mathbf{f}^0(t)$ and the damages $\mu_i(t)$ are known in advance and used in a numerical simulation of the structural response. In order to determine the corresponding virtual distortions, the strain relation

(6.2) is substituted into the right-hand side of (6.5a), which yields the following simpler counterpart of (3.32):

$$\varepsilon_i^0(t) - (1 - \mu_i(t)) \sum_k \int_0^t B_{ik}^{\kappa\kappa}(t - \tau) \varepsilon_k^0(\tau) d\tau = (1 - \mu_i(t)) \varepsilon_i^L(t). \quad (6.6)$$

Equation (6.6), if collected for all potentially damaged elements i , forms a system of Volterra integral equations. Notice that in a case of a time-variable stiffness modification, the coefficient $\mu_i(t)$ often explicitly depends only on the current value of the strain $\varepsilon_i(t)$, so that (6.6) ceases to be linear and it might be difficult to solve it using standard approaches. In such a case, the equation is usually solved iteratively with respect to time, by finding $\varepsilon_i^0(t)$ in successive time steps. In each time step, the following procedure is used:

1. A trial step is taken using the values from the previous time step, $\mu_i(t) := \mu_i(t - \Delta t)$. A discretized version of (6.6),

$$\begin{aligned} \sum_k (\delta_{ik} - (1 - \mu_i(t)) D_{ik}^{\kappa\kappa}(0)) \varepsilon_k^0(t) \\ = (1 - \mu_i(t)) \left(\varepsilon_i^L(t) + \sum_k \sum_{\tau=0}^{t-1} D_{ik}^{\kappa\kappa}(t - \tau) \varepsilon_k^0(\tau) \right), \end{aligned} \quad (6.7)$$

where $D_{ik}^{\kappa\kappa}(t)$ is the discretized version of the continuous impulse response function $B_{ik}^{\kappa\kappa}(t)$, is solved for the current time step t and yields the corresponding trial values of the virtual distortions $\varepsilon_i^0(t)$, which are then used in (6.2) and (6.3) to obtain the trial values of the strain and stress responses $\varepsilon_i(t)$ and $\sigma_i(t)$.

2. The compliance of the trial strains with the assumed trial values of $\mu_i(t)$ is verified. If compliant, the trial step is accepted.
3. If not compliant, the noncompliant values of $\mu_i(t)$ are updated (for example, the value for compression is replaced with the value for tension, or vice versa) and the computations in the current time step are repeated.

The above procedure is best-suited to the case, when there is a discrete set of possible values of the coefficients $\mu_i(t)$. It includes the discussed later case of a breathing crack (two different values of μ_i to be used in tension and in compression). In such cases, updating the damage coefficients in the last of the above points is straightforward (in case of noncompliance, the other value is simply selected) and the repeated solution of (6.7) usually yields accurate

values of the virtual distortions and compliant strains. In other words, for the case of a breathing crack, possible repeated solutions of (6.7) are required only if the set of elements in tension needs to be updated, but given this set, the corresponding response is computed in a single step, without any iterations with respect to responses or virtual distortions. An analogous formulation is possible in the more general case of a constitutive law that is linear in intervals, see also Chapter 7 for the case of a bilinear isotropic hardening plasticity.

6.2.2 Off-line identification

According to (6.2), the response of the damaged structure is the sum of the

1. original response $\varepsilon_i^L(t)$ of the undamaged structure to the external excitation $\mathbf{f}^0(t)$ and the
2. cumulated effects of the virtual distortions that model the damage.

The response $\varepsilon_i^L(t)$ depends directly on the unknown excitation, and it can be represented in the form of a convolution of the excitation with the respective impulse response functions of the undamaged structure,

$$\varepsilon_i^L(t) = \sum_j \int_0^t B_{ij}^{\kappa f}(t-\tau) f_j^0(\tau) d\tau, \quad (6.8)$$

where $f_j^0(t)$ is the unknown excitation in the j th potentially load-exposed DOF, $B_{ij}^{\kappa f}(t)$ denotes the corresponding impulse response function (strain response in the i th element of the undamaged structure to an impulsive excitation in its j th DOF), and the summation extends over all DOFs that are potentially exposed to the excitation.

In the direct problem, the model of the damage is known a priori, so that the virtual distortions are uniquely determined by the damage and the excitation. However, in the inverse problem the type of the damage is unknown. Thus, the virtual distortions $\varepsilon_i^0(t)$ and the excitation $f_j^0(t)$ are treated here as independent unknowns. Substitution of (6.8) into (6.2) yields

$$\varepsilon_i(t) = \sum_j \int_0^t B_{ij}^{\kappa f}(t-\tau) f_j^0(\tau) d\tau + \sum_k \int_0^t B_{ik}^{\kappa \kappa}(t-\tau) \varepsilon_k^0(\tau) d\tau, \quad (6.9)$$

which expresses the response of the damaged structure in terms of the unknowns of both types, $f_j^0(t)$ and $\varepsilon_k^0(t)$. Equation (6.9), collected for all i -indexed sensors,

forms a system of integral equations of the Volterra type, which in the discretized form can be stated as a single large linear equation,

$$\begin{aligned}\boldsymbol{\varepsilon} &= \mathbf{B}^{\kappa f} \mathbf{f}^0 + \mathbf{B}^{\kappa \kappa} \boldsymbol{\varepsilon}^0 \\ &= \left[\begin{array}{c} \mathbf{B}^{\kappa f} \quad \mathbf{B}^{\kappa \kappa} \end{array} \right] \left[\begin{array}{c} \mathbf{f}^0 \\ \boldsymbol{\varepsilon}^0 \end{array} \right] \\ &= \mathbf{B} \mathbf{z}^0,\end{aligned}\tag{6.10}$$

where the vector \mathbf{z}^0 collects together the vectors \mathbf{f} and $\boldsymbol{\varepsilon}^0$ that contain respectively all the discretized excitations in all potentially load-exposed DOFs and all the discretized virtual distortions in all potentially damaged elements. The matrices $\mathbf{B}^{\kappa f}$ and $\mathbf{B}^{\kappa \kappa}$ are the discretized versions of the corresponding convolution operators. By a proper ordering of the elements of \mathbf{z}^0 , the matrix \mathbf{B} can be structured as a large block matrix composed of lower triangular Toeplitz matrices, which relate the discretized sensor responses to unit excitations or to unit distortions. This is the same familiar form, as that of the matrices in Figs. 2.3, 4.2 and 5.20 (bottom left).

6.2.2.1 Identification of excitations and virtual distortions

According to (6.9) or (6.10), information about the unknown excitation and damage is reflected in the response. The identification is thus equivalent to a comparison of the computed response vector $\boldsymbol{\varepsilon}$ with the measured response vector $\boldsymbol{\varepsilon}^M$ in order to solve the resulting equation,

$$\boldsymbol{\varepsilon}^M = \mathbf{B} \mathbf{z}^0,\tag{6.11a}$$

which is a large finite-dimensional linear system. For a unique solution, there should be at least as many independent sensors as the total number of the potentially load-exposed DOFs and damaged elements. In practice, it requires an information about the potential locations of the damages and excitations to be available a priori.

The system (6.11a) is dense, and the numbers of equations and unknowns are both proportional to the number of the time steps N_t : If the total number of load-exposed DOFs and damages is N and the number of sensors is N_r , then the dimension of \mathbf{B} is $N_r N_t \times N N_t$. In fact, (6.11a) is a counterpart of (2.31a) and an approximation of the forces and virtual distortions (e.g., by splines, wavelets or load shape functions [60]) can be used to reduce the numerical costs and improve the numerical conditioning. In this way, the following equation is obtained:

$$\boldsymbol{\varepsilon}^M \approx \mathbf{B} \mathbf{N} \boldsymbol{\alpha},\tag{6.11b}$$

which is a counterpart of (2.32) ($\mathbf{z}^0 \approx \mathbf{N}\boldsymbol{\alpha}$, the columns of \mathbf{N} contain the approximating functions and the approximating coefficients $\boldsymbol{\alpha}$ are far fewer in number than the original unknowns \mathbf{z}^0).

In most practical situations, solution of the linear system (6.11a) corresponds to a deconvolution. As mentioned in Subsection 2.2.4.3, this is an inherently ill-conditioned problem, so that a small disturbance of $\boldsymbol{\varepsilon}^M$ (for example by an inevitable measurement error) may cause a large error in the identified excitations and virtual distortions. Therefore, it is necessary to numerically regularize the solution, see [67, 109, 111, 112, 128–130, 137] or a short overview of regularization techniques in Subsection A.3.2.

6.2.2.2 Identification of damages

The virtual distortions and excitation forces, identified by (6.11), can be used in (6.10) to compute the strains of the damaged elements and then, by (6.3), to recover their stresses. The recovered stress-strain relationships of the damaged elements can be analyzed to identify the types of the damages and their extents. Two types of damages are considered here, both are expressible in terms of a single stiffness reduction coefficient:

- Constant reduction of stiffness (e.g., related to a corrosion),

$$\mu_i(t) = \mu_i^{\text{crs}}, \quad (6.12\text{a})$$

where $\mu_i^{\text{crs}} < 1$.

- Breathing crack model with a reduced stiffness in tension,

$$\mu_i(t) = \begin{cases} 1 & \text{if } \varepsilon_i(t) < 0 \text{ (compression),} \\ \mu_i^{\text{bc}} & \text{if } \varepsilon_i(t) \geq 0 \text{ (tension),} \end{cases} \quad (6.12\text{b})$$

where $\mu_i^{\text{bc}} < 1$. Such a model, although simple, seems to be adequate for the purposes of low-frequency SHM, see Friswell [276] or Ostachowicz and Krawczuk [277].

For each potentially damaged element, the stress-strain relationship is recovered in the form of a discrete-time sequence of pairs $(\varepsilon_i(t), \sigma_i(t))$. Given these pairs, the type and extent of each damage can be identified by square best-fitting of the theoretical curves, which has to be performed separately for each considered damage type,

$$\begin{aligned}\mu_i^{\text{crs}} &:= \frac{1}{2} \sum_t (\sigma_i(t) - \mu_i E_i \varepsilon_i(t))^2 \\ &= \frac{1}{E_i} \frac{\sum_t \varepsilon_i(t) \sigma_i(t)}{\sum_t \varepsilon_i^2(t)}\end{aligned}\quad (6.13a)$$

and

$$\begin{aligned}\mu_i^{\text{bc}} &:= \frac{1}{2} \sum_t (\sigma_i(t) - \mu_i E_i \varepsilon_i(t))^2 \mathbb{I}_{\varepsilon_i(t)>0} \\ &= \frac{1}{E_i} \frac{\sum_t \varepsilon_i(t) \sigma_i(t) \mathbb{I}_{\varepsilon_i(t)>0}}{\sum_t \varepsilon_i^2(t) \mathbb{I}_{\varepsilon_i(t)>0}},\end{aligned}\quad (6.13b)$$

where $\mathbb{I}_{\varepsilon_i(t)>0}$ is the indicator function defined in (2.64), and then by choosing the damage type that better fits the stress-strain relationship, that is yields a smaller least-square distance

$$\frac{\sum_t [\sigma_i(t) - \mu_i(t) E_i \varepsilon_i(t)]^2}{\sum_t \sigma_i^2(t)}. \quad (6.14)$$

6.2.3 Online identification

The main task in identification of coexistent external excitation and damage is to solve (6.11), which is basically equivalent to solving a discretized deconvolution problem. The quality of the solution and the computational effort depend mainly on the matrix \mathbf{B} or, for (6.11b), \mathbf{BN} . When the sampling time is long, these matrices can be prohibitively large, and each solution might be time-consuming and prone to numerical errors. Moreover, (6.11) can be used only for off-line identification. In order to eliminate the drawbacks and to make online identification possible, repetitive identification in a moving time window is employed here. The assumed linearity of the original undamaged structure is utilized.

The damaged structure, including the nonlinear case of a breathing crack, is converted by the VDM into a linear distorted structure (the original intact linear structure with the imposed virtual distortions). This is indicated by (6.9), which assumes zero initial conditions. Let the sampling time interval be divided into several (possibly overlapping) time sections. The response of the distorted

structure in the n th section can be expressed by the following modified version of (6.9):

$$\begin{aligned}\varepsilon_i^{(n)}(t) &= \bar{\varepsilon}_i^{(n)}(t) + \sum_j \int_0^t B_{ij}^{\kappa f}(t-\tau) f_j^{0(n)}(\tau) d\tau \\ &\quad + \sum_k \int_0^t B^{\kappa\kappa}(t-\tau) \varepsilon_k^{0(n)}(\tau) d\tau,\end{aligned}\tag{6.15}$$

which takes into account also the free vibrations $\bar{\varepsilon}_i^{(n)}(t)$ of the undamaged structure caused by the nonzero initial conditions at the beginning of the n th time section.

The strains computed by a discretized version of (6.15) can be compared to the measured strains and stated in the form of a single matrix equation similar to (6.11a),

$$\boldsymbol{\varepsilon}^{M(n)} - \bar{\boldsymbol{\varepsilon}}^{(n)} = \mathbf{B}^{(n)} \mathbf{z}^{0(n)},\tag{6.16}$$

which is formed separately for each time section, and where $\mathbf{B}^{(n)}$ is the matrix \mathbf{B} reduced according to the length of the n th section, while the vector $\boldsymbol{\varepsilon}^{M(n)}$ collects the discretized strains measured in the n th time section. Equation (6.16) covers only one time section and is thus much smaller and easier to solve than (6.11). If the excitations and virtual distortions in the previous time sections are already identified, the initial conditions of the successive time section and the corresponding free vibrations can be computed straightforwardly. Equation (6.16) can be thus used online, in successive time sections, to obtain iteratively all the unknown excitations and virtual distortions in the whole considered time interval.

As observed in practice, the identified excitations tend to drift away from the exact solution, which causes a lower accuracy near the end of each time section. A practical way to improve the accuracy is to consider partly overlapping time sections, so that less accurate results from the previous section can be improved using the identification results from the successive time section.

6.2.4 Numerical example

6.2.4.1 The structure

Figure 6.1 shows the modeled truss structure. The structure is 2.5 m long, and all its elements are 0.5 m long with the exception of the five diagonal

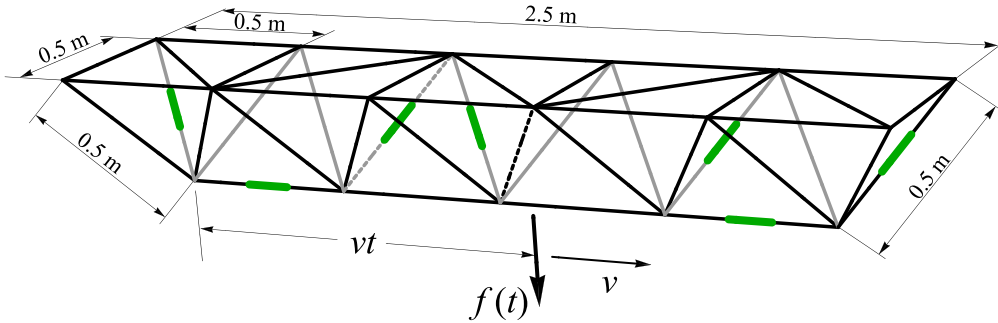


Figure 6.1. Truss structure modeled in the numerical example. Dashed lines mark the damaged elements (no. 3 and 5); strain sensors are marked with shorter solid green lines (elements no. 1, 2, 3, 4, 6, 7 and 8). The moving force is proportionally transferred to the two nearest nodes.

elements of the upper plane, which are $0.5\sqrt{2}$ m long. All the elements are 10 mm^2 in cross-section and made of steel with the density 7800 kg/m^3 and Young's modulus of 210 GPa. Additionally, the mass of each node is 0.13 kg. The two left-hand side corner nodes of the upper plane are fixed, while the two opposite right-hand side corner nodes have restrained only the vertical DOF and are free to move in the horizontal plane.

It is assumed that the structure is excited by a moving vertical force, which is transferred to the lower five nodes of the structure as via a system of rigid beams. More specifically, the transferred nodal forces are nonzero only in the two nodes nearest to the moving force, for which they are equal to $(1 - p)F(t)$ and $pF(t)$, where p is the percentage of the distance between the nodes already covered by the force (25% if the force has advanced $1/4$ of the distance, 50% if it is already in the middle point between the nodes, etc.).

Two damages are assumed to occur in elements no. 3 and 5; these elements are drawn in Fig. 6.1 using dashed lines. Seven strain sensors are placed on elements no. 1, 2, 3, 4, 6, 7 and 8, which are marked with shorter parallel solid lines. The considered time interval is $T = 48$ ms in total, and it is discretized into 241 time steps of 0.2 ms each. The dimensions of the full matrix \mathbf{B} are thus 1687×1687 . The matrix is generated numerically using the Newmark integration scheme [145–148] and the equation of motion of the FE model of the structure. The matrix has a 7×7 block structure: seven block rows correspond to the seven sensors, while five block columns correspond to the five excited DOFs and the two other block columns correspond to the two damaged elements; there are 241 time steps, and hence each block is a 241×241 lower triangular Toeplitz matrix.

6.2.4.2 Actual damages and excitations

Figure 6.2a plots the time-history of the assumed actual excitation, which is identified in the following section with the discussed approaches. The excitation simulates a time-dependent load that moves along the structure at a constant velocity of $v = 41.667$ m/s. As described, the load is transferred to the two nearest structural nodes; Fig. 6.2b plots the corresponding nodal excitations. The computed exact responses of the considered strain sensors in the undamaged structure are plotted in Fig. 6.2c. In order to test the damage identification, two damage types are considered:

1. Breathing 40% crack (bc) in the element no. 3 (Young's modulus is reduced by 40% when the element is in tension),

$$\mu_3(t) = \begin{cases} 1 & \text{if } \varepsilon_3(t) \leq 0, \\ 0.6 & \text{if } \varepsilon_3(t) > 0. \end{cases} \quad (6.17a)$$

2. Constant stiffness reduction (csr) in the element no. 5 (Young's modulus is reduced by 70%),

$$\mu_5(t) = 0.3. \quad (6.17b)$$

These damage types and extents are used to simulate the response of the damaged structure, which is then contaminated with numerically generated uncorrelated Gaussian noise at the 5% rms level in order to simulate the measurement error, see Fig. 6.2d. By a comparison with the response of the undamaged structure (Fig. 6.2c) a relatively small influence of the considered damages might be noticed. The (exaggerated) deformed state of the damaged structure in selected time steps is shown in Fig. 6.3.

6.2.4.3 Identification results

Both online and off-line identification schemes are tested; for online identification, the total time interval of 241 time steps (48 ms) is divided into three time sections each of 120 time steps with overlapping parts of 60 time steps. In each case, identification is performed by (6.11a) as well as by (6.11b) with excitations and virtual distortions approximated by load shape functions, see Fig. 2.4. In the off-line case, eighteen approximating functions are used, while in the online case fourteen functions are used for each of the three considered time sections. Table 6.1 lists the dimensions of the resulting matrices **B** or **BN** of the linear systems (6.11).

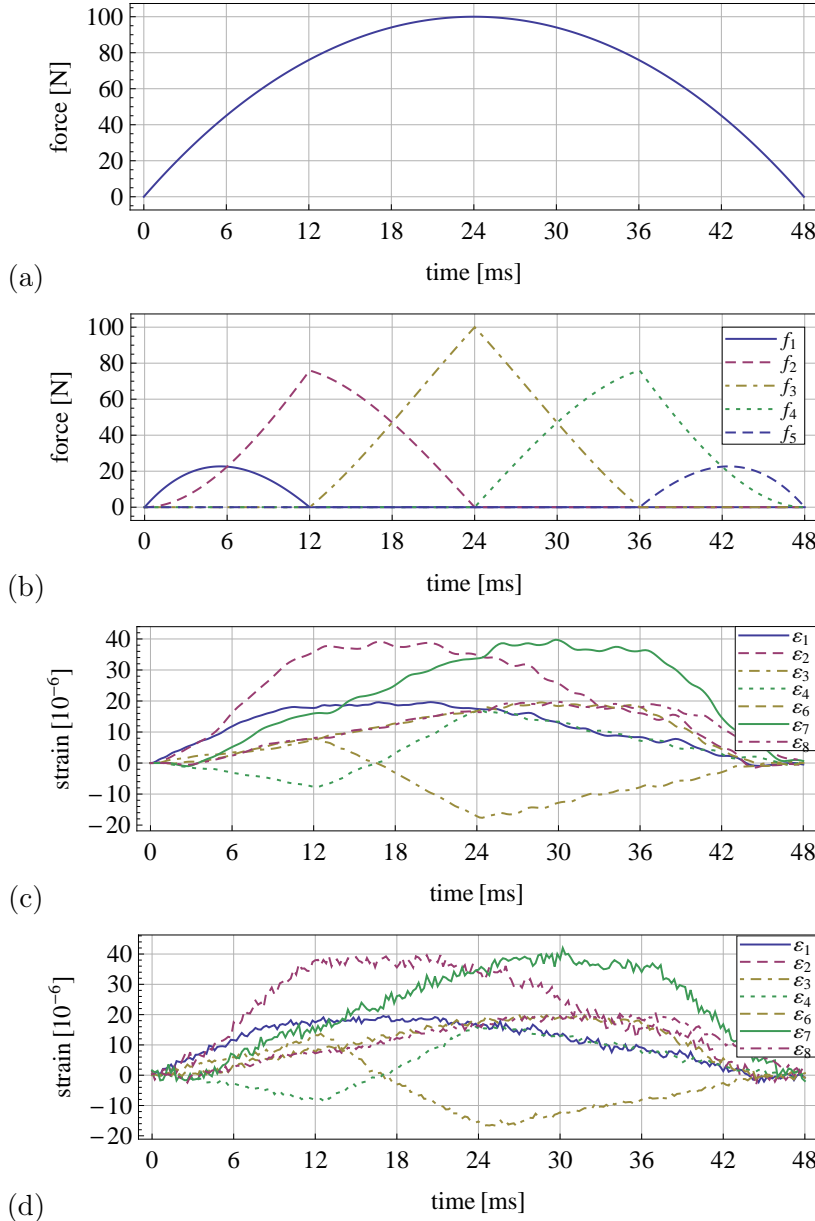


Figure 6.2. Assumed actual excitation and the corresponding simulated responses: (a) Assumed actual load; (b) Corresponding equivalent nodal excitations; (c) Exact response of the undamaged structure; (d) Response of the damaged structure contaminated with 5% rms Gaussian uncorrelated noise.

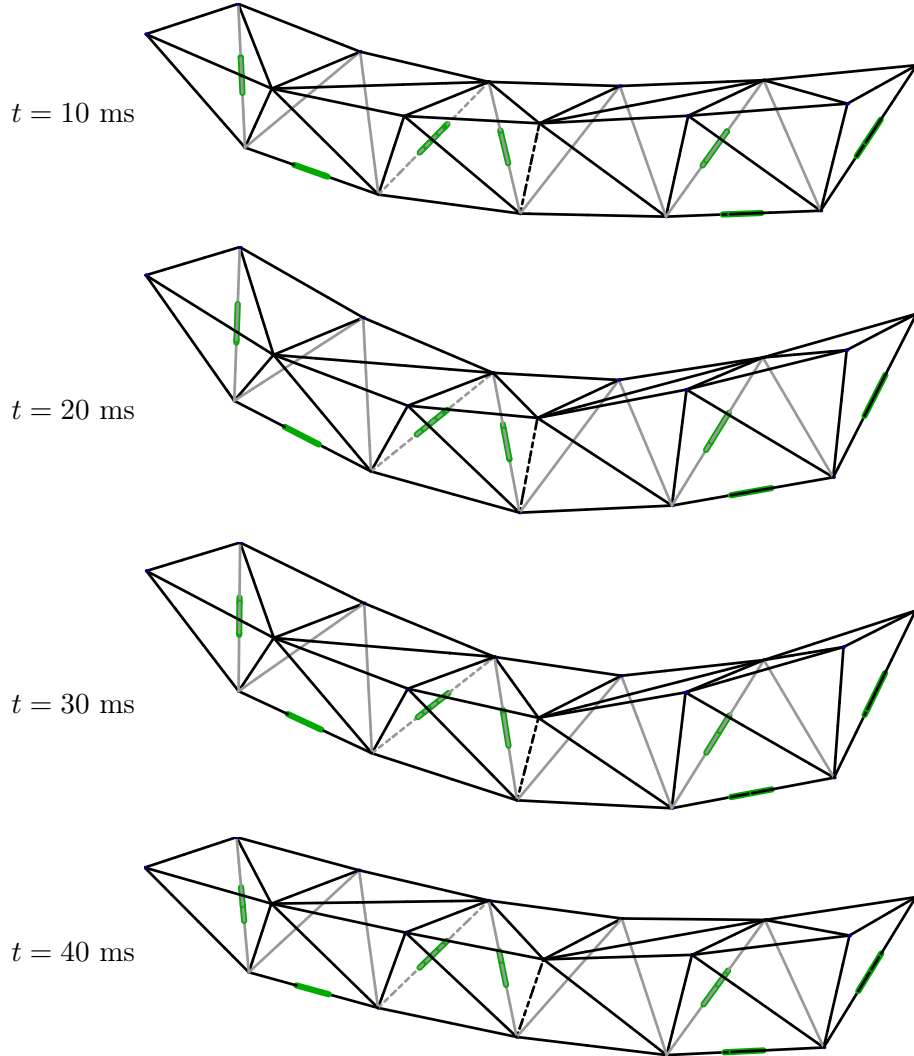


Figure 6.3. Deformed damaged structure in time steps $t = 10 \text{ ms}, 20 \text{ ms}, 30 \text{ ms}, 40 \text{ ms}$ (exaggeration factor 1500).

Table 6.1. Dimensions of the linear systems (6.11).

	Off-line case	Online case
Full (B)	1687×1687	847×847
Approximated (BN)	1687×126	847×98

The system matrices are ill-conditioned, but not of unmanageable dimensions, hence the solutions are computed using the truncated singular value decomposition. The regularization level is defined by the number k_{TSVD} of the truncated singular values. In each case it is determined separately using the L-curve technique, that is by weighting in the log-log scale the residual against the norm of the first differences of the solution, see, e.g., [67, 135] or Subsection A.3.2. In the full off-line case, the corner of the L-curve corresponds to $k_{\text{TSVD}} \approx 350$, see Fig. 6.4 (left); it is thus assumed that $k_{\text{TSVD}} = 357$, that is all singular values less than 0.1% of the maximum singular value are discarded. For the full online case $k_{\text{TSVD}} = 194$ has been chosen in a similar way, which corresponds to the truncation level of 0.2%. The L-curves corresponding to the approximated cases, see an example in Fig. 6.4 (right) for the off-line case, consist of the lower branches only, which confirms the well-conditioning of the approximated problems. Here, a low value of $k_{\text{TSVD}} = 5$ is used to guarantee the reliability.

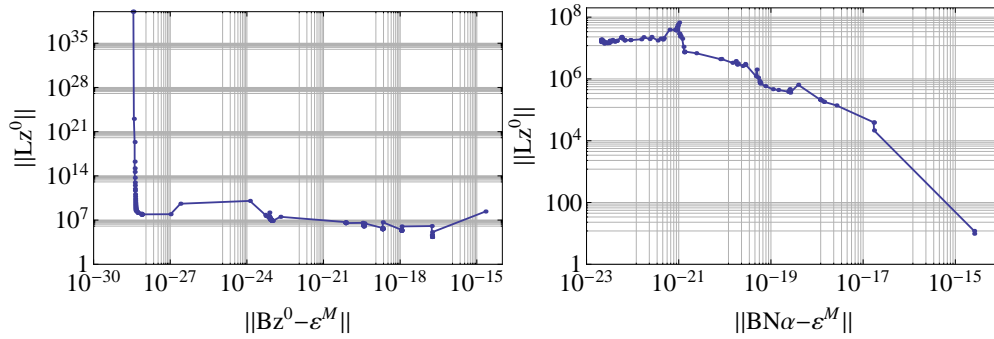


Figure 6.4. The L-curve (norm of the first differences vs. the residual, \mathbf{L} is the matrix of the first differences), off-line identification: (left) full matrix \mathbf{B} ; (right) approximated matrix \mathbf{BN} .

The computational cost of a single identification depends mainly on the cost of the singular value decomposition of the system matrix, which for an $m \times n$ matrix ($m \geq n$) is of order $O(mn^2)$ [139]. Hence, as seen in Table 6.1, the cost can be reduced by almost two orders of magnitude by using the approximations. The reduction due to the repetitive smaller identifications in the online case, which use the same system matrix and hence require only a single decomposition, is less pronounced (below one order of magnitude). In the case of several repetitive identifications, both off-line and online, the numerically costly SVD has to be computed only once, and thus the total cost of a single identification is smaller by one order of magnitude.

Identification of excitations. The actual nodal excitations and the excitations identified in the four considered cases are compared in Fig. 6.5. If it is known in advance, or deduced from the characteristic features of the identified nodal forces, that all the excitations correspond to a load moving at a constant velocity, then it can be also constructed from the identified time-histories; the results are shown in Fig. 6.6. Although the identified excitations have some oscillations due to the simulated measurement noise, they are all reconstructed with a good accuracy. Notice that the approximation of the excitations and the virtual distortions by the load shape functions not only reduces the numerical costs, but also filters out the noise to a certain degree while preserving the accuracy.

Identification of damages. For each of the two damaged elements, the best-fitting extents of the damages of both types (μ_i^{csr} and μ_i^{bc} , $i \in \{3, 5\}$) are computed by (6.13) and used to identify the type of the damage by choosing the better fit via (6.14). The results are listed in Tables 6.2 and 6.3. Figure 6.7 plots the actual, raw identified and fitted stress-strain relationships.

Table 6.2. Off-line identification of damage extent (by (6.13)) and of damage type (by smaller fit (6.14)) for elements no. 3 and 5.

Full matrix extent	Approximated extent	Actual value
fit	fit	
$\mu_3^{\text{csr}}=0.9046$	$\mu_3^{\text{csr}}=0.9048$	—
$\mu_3^{\text{bc}}=0.5950$	$\mu_3^{\text{bc}}=0.5972$	$\mu_3^{\text{bc}}=0.6$
$\mu_5^{\text{csr}}=0.2741$	$\mu_5^{\text{csr}}=0.2765$	$\mu_5^{\text{csr}}=0.3$
$\mu_5^{\text{bc}}=0.2699$	$\mu_5^{\text{bc}}=0.2706$	—
0.0424	0.0363	
0.0068	0.0008	
0.0360	0.0464	
0.2480	0.1247	

In general, type of the damage can be properly identified by selecting the type that fits better the recovered stress-strain relationship, that is minimizes the fit (6.14). However, in online identification with short time sections, a damaged element may happen to be almost only in tension during the whole time section (e.g., as element no. 5 in time section I). In such a case, the damage type cannot be reliably estimated in that specific section, since compression data are necessary for distinguishing between both tested damage types. Similarly, if an element with a breathing crack damage is in compression almost the whole time section (as element no. 3 in time section III), reliable differentiation between a marginal reduction of stiffness and a breathing crack is not possible. Nevertheless, these shortcomings are unavoidable; the proper damage type in such cases can be deduced only by comparing the results obtained in all time sections.

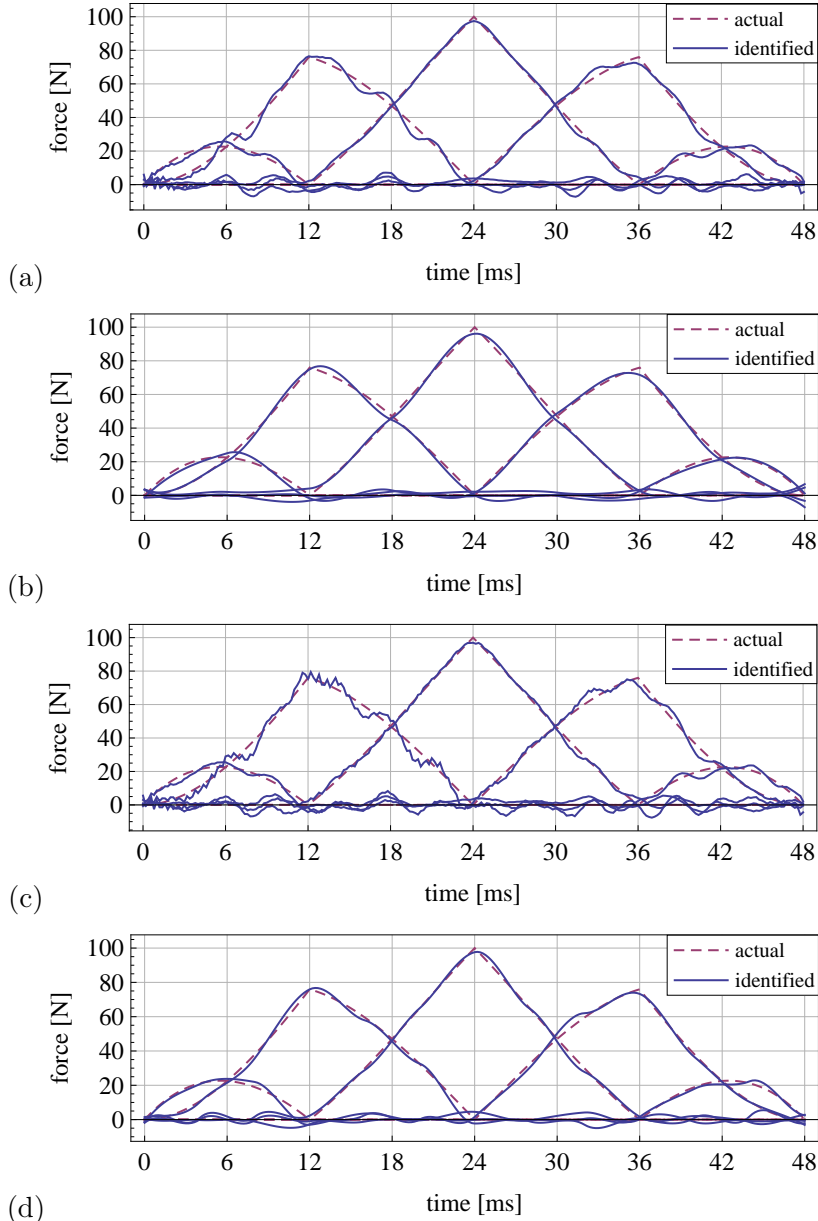


Figure 6.5. Identified equivalent nodal excitations: (a) off-line, full matrix (no approximations); (b) off-line, approximated; (c) online, full matrix (no approximations); (d) online, approximated.

Table 6.3. Online identification of damage extent (by (6.13)) and of damage type (by smaller fit (6.14)) for elements no. 3 and 5.
 Column “tension” lists the percentage of the time steps in tension.

	Time section I		Time section II		Time section III		Mean value	Actual value
	extent	fit	tension	extent	fit	tension	extent	fit
μ_3^{CSR} =0.651	0.135	70.0%	$\mu_3^{\text{CSR}}=0.947$	0.027	20.8%	$\mu_3^{\text{CSR}}=0.998$	0.005	10.8%
μ_3^{BC} =0.596	0.034	70.0%	$\mu_3^{\text{BC}}=0.583$	0.006	—	$\mu_3^{\text{BC}}=0.409$	0.005	—
μ_5^{CSR} =0.281	0.155	89.2%	$\mu_5^{\text{CSR}}=0.273$	0.035	85.8%	$\mu_5^{\text{CSR}}=0.266$	0.087	$\mu_5^{\text{CSR}}=0.529$
μ_5^{BC} =0.285	0.163	89.2%	$\mu_5^{\text{BC}}=0.273$	0.040	—	$\mu_5^{\text{BC}}=0.251$	0.739	$\mu_5^{\text{BC}}=0.273$
full matrix								
μ_3^{CSR} =0.732	0.070	70.8%	$\mu_3^{\text{CSR}}=0.953$	0.020	21.7%	$\mu_3^{\text{CSR}}=0.999$	0.001	12.5%
μ_3^{BC} =0.597	0.002	70.8%	$\mu_3^{\text{BC}}=0.593$	0.001	—	$\mu_3^{\text{BC}}=0.501$	0.001	—
μ_5^{CSR} =0.282	0.011	95.0%	$\mu_5^{\text{CSR}}=0.272$	0.018	85.0%	$\mu_5^{\text{CSR}}=0.275$	0.071	$\mu_5^{\text{CSR}}=0.276$
approx.								
μ_5^{BC} =0.282	0.019	95.0%	$\mu_5^{\text{BC}}=0.271$	0.088	—	$\mu_5^{\text{BC}}=0.256$	0.532	—

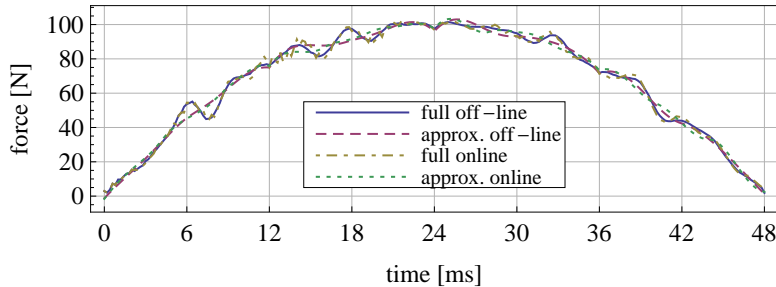


Figure 6.6. Reconstructed moving force for the four considered cases (off-line full matrix, off-line approximated, online full matrix and online approximated), compare with the actual force in Fig. 6.2a.

Because of the influence of noise, the recovered stress-strain relationships of the damaged elements are scattered around the actual relationships (Fig. 6.7). The damage extents are estimated by least-square fitting. Notice that, in the online identification, the identification accuracy varies between the time sections due to the measurement error. However, all the tested identification schemes (off-line and online, with and without approximations) yield satisfactory results, which is especially important provided the considerably smaller numerical cost (by two to three orders of magnitude) of the online approximated method.

6.2.5 Experimental example

6.2.5.1 The structure

The described approach is verified experimentally using an aluminum cantilever beam and the setup used also in Section 5.7. The experimental setup is shown in Fig. 6.8. Its physical parameters are listed in Section 5.7. No “sponge support” and no additional mass are used.

6.2.5.2 Actual damage and excitation

The beam is intentionally damaged by cutting even notches near its fixed end on the section of a length of 10.23 cm. The stiffness of the damaged section is reduced to 42% of the original stiffness, while the mass remains almost unchanged.

The excitation is applied using an Amplified Piezo Actuator (APA, [254]), which is fixed on the beam in such a way that it can be assumed to apply a pure moment load. The structural dynamic responses are measured by three piezoelectric patches glued to the beam (denoted in the following by x_1 , x_2

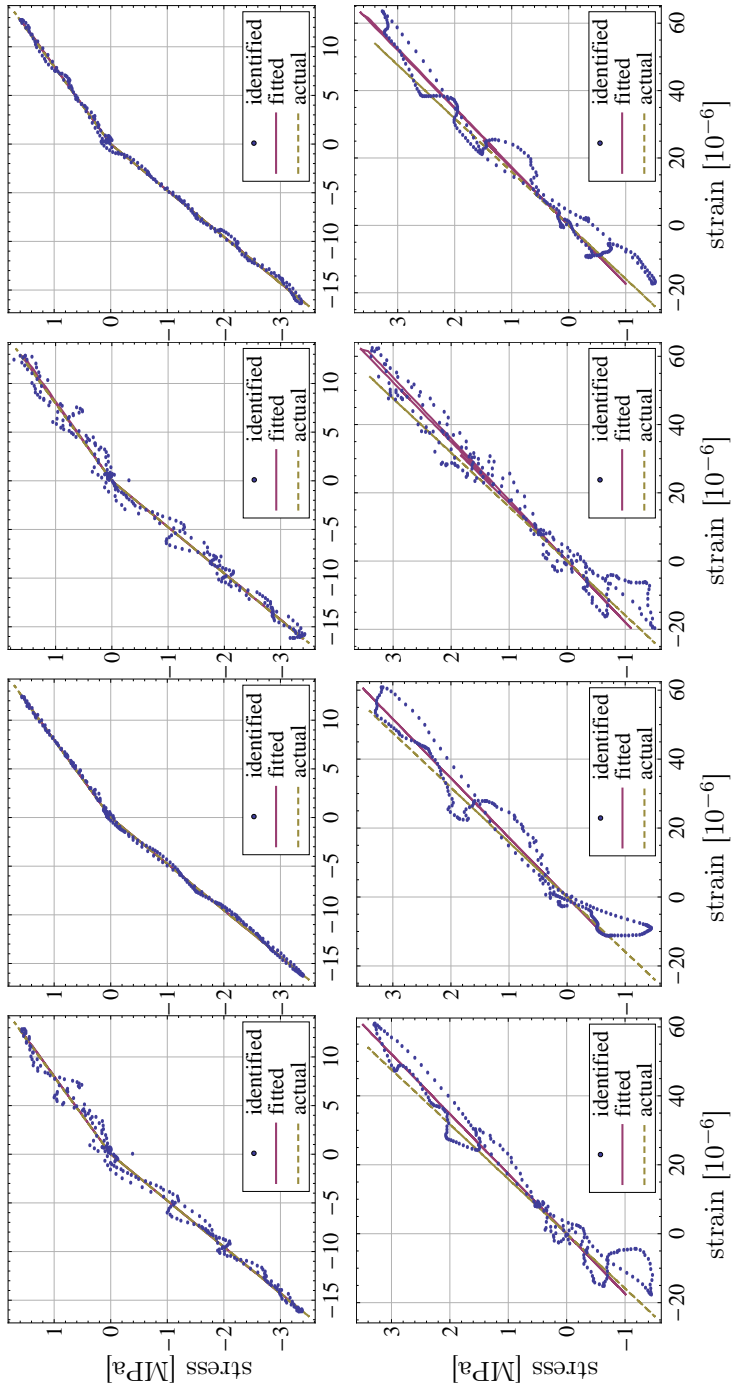


Figure 6.7. Actual, raw identified and fitted stress-strain relationships for elements no. 3 (breathing crack, first row) and 5 (constant stiffness reduction, second row): (1st column) off-line, full matrix; (2nd column) off-line approximated; (3rd column) online, full matrix; (4th column) online approximated.

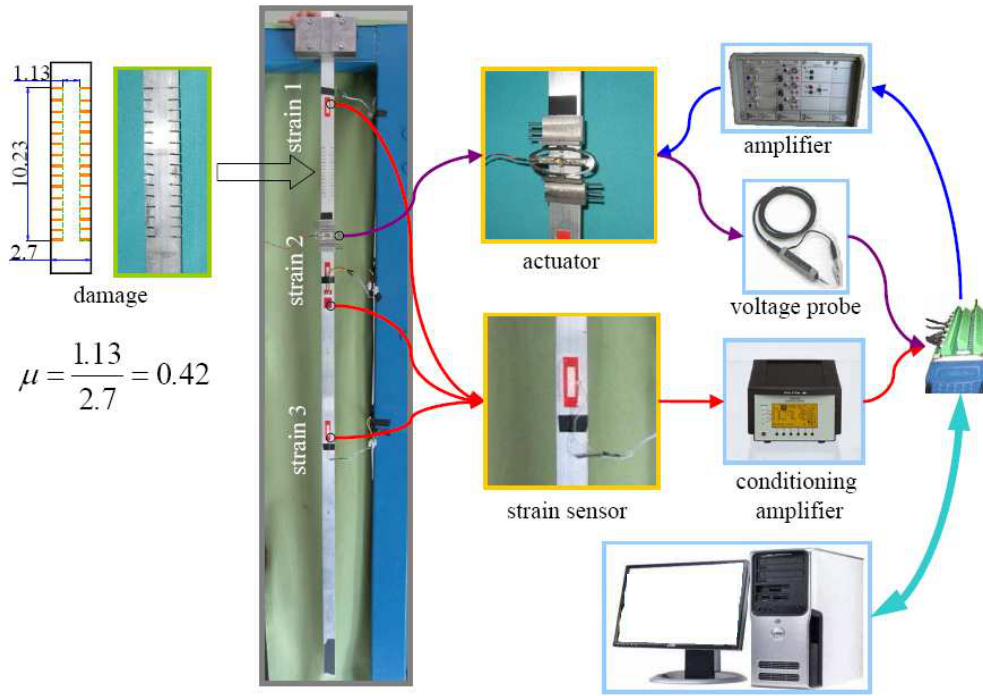


Figure 6.8. Experimental setup.

and x_3). In the considered setup, they measure axial strain off the neutral axis of the beam, which is proportional to the local curvature. Applied excitation is also measured; Fig. 6.9 (top) plots the time-history of the force applied to the actuator clamps. The sampling frequency is 2500 Hz. The measured responses are shown in the bottom plot of Fig. 6.9. The analyzed time interval is 3.52 s.

6.2.5.3 Identification results

A finite element model of the undamaged beam is assembled and updated; the damaged section is assumed to be a single element. The model considers the influence of gravity and the presence of the actuator and sensors. A generic 2D beam element has three virtual distortions. However, a pure moment excitation is applied here, which results in mainly bending distortions, hence the other two distortions (axial and shear/bending, see Subsection 3.2.1) are neglected in the analysis. Therefore, one external excitation and one damage-related virtual distortion are the unknowns to be identified, and at least two sensors are required to obtain a unique solution.

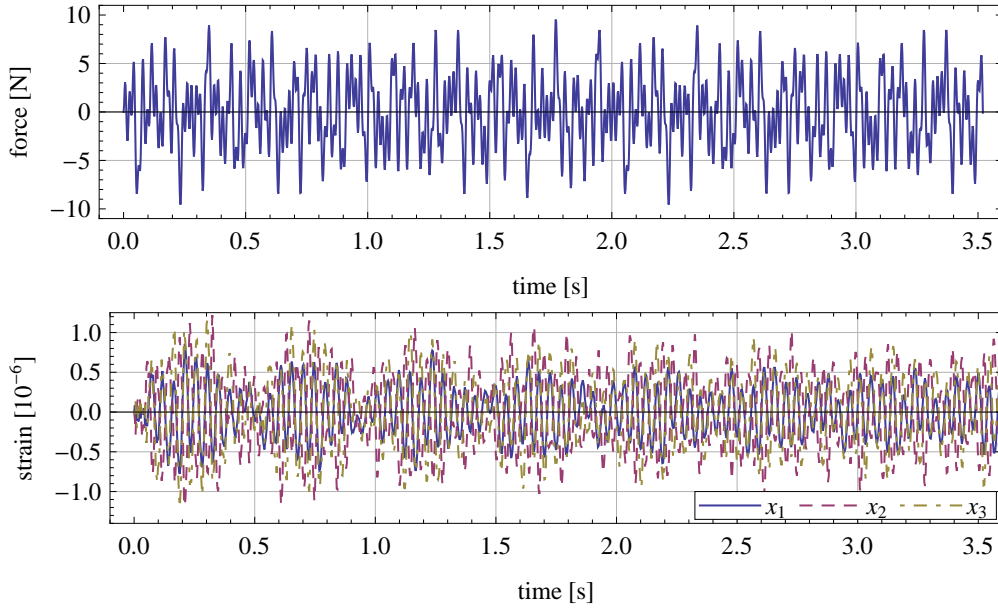


Figure 6.9. The excitation applied to the actuator clamps (top) and the corresponding structural responses (bottom).

The identification is performed using a moving time window. Each window has 400 time steps; each two successive windows have an overlapping section of 200 steps. A total of 8800 time steps is analyzed within the total time interval of 3.52 s, which is divided into 43 time sections. In each of them, the unknown excitation and virtual distortion are identified using an approximation based on forty two load shape functions. Two or three sensors are used separately; the identified excitations are shown in Fig. 6.10 and compared to the actual (measured) excitation.

Figure 6.11 plots the (scaled, see (6.3)) stress-strain relationship of the damaged element, as recovered using sensors x_1 and x_3 . The relationship resembles a linear function, which suggests that the damage can be represented by a constant reduction of stiffness, see (6.5b), which is indeed true. The extent of the damage of such a type is estimated separately in each time section, and the results are shown in Fig. 6.12. In this way, the damage can be monitored online, that is time section by time section. The average damage extent of all the time windows and the value identified in a single off-line identification are listed in Table 6.4.

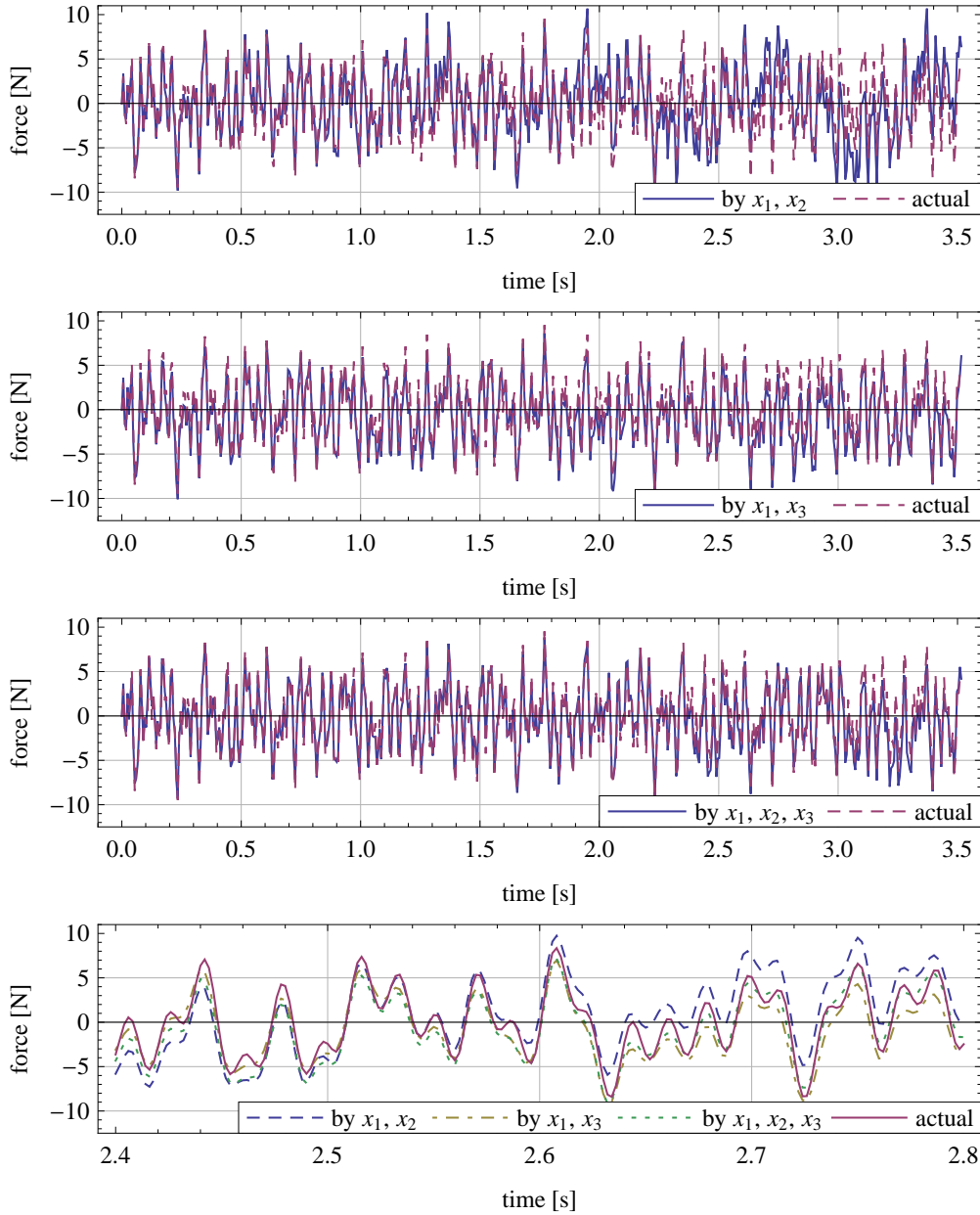


Figure 6.10. Excitation applied to the actuator clamps: actual and identified using different combinations of available sensors.

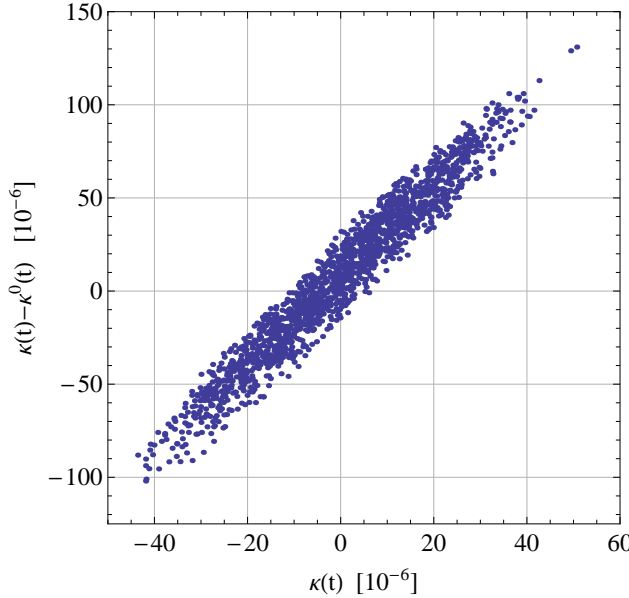


Figure 6.11. Identified (scaled, see (6.3)) stress-strain relationship of the damaged element recovered using sensors x_1 and x_3 .

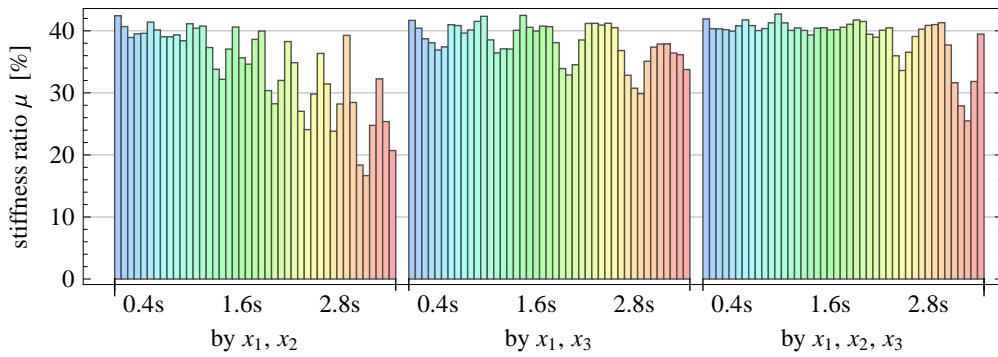


Figure 6.12. Damage extents identified online in each time section and with different combinations of sensors.

Table 6.4. Damage extent (in per cent) of the damaged segment: actual, identified off-line and online using different combinations of available sensors. The results of online identifications are computed as the average values of the results obtained in all time sections.

Actual	$\bar{\mu}_{1,2}^{\text{online}}$	$\mu_{1,2}^{\text{off-line}}$	$\bar{\mu}_{1,3}^{\text{online}}$	$\mu_{1,3}^{\text{off-line}}$	$\bar{\mu}_{1,2,3}^{\text{online}}$	$\mu_{1,2,3}^{\text{off-line}}$
42.0	34.0	32.7	38.8	38.1	39.1	38.8

As expected, the accuracy of identification is better if three sensors are used, although the results obtained with sensors x_1 and x_3 are also satisfactory. The results obtained with sensors x_1 and x_2 are not as accurate, which might be related to the fact that x_2 is much closer to x_1 , to the damaged element and to the actuator than x_3 .

6.3 Parametrization of loads

In the preceding section, the damages are represented in the form of equivalent pseudo loads (or virtual distortions) and identified using standard load identification procedures. This section describes the opposite solution, see [39, 40, 55]: the excitations are parametrized, so that damages and excitations are represented together by a single set of parameters that can be simultaneously updated in each iteration of the optimization procedure. All the unknowns are thus treated in a unified manner: no two-step identification procedures are required, and all standard optimization algorithms can be directly employed.

This section considers moving vehicular loads. They are represented by moving masses, which are treated here as the optimization variables and identified together with the damage parameters. This is contrary to most other researches in identification of moving loads, where the interaction forces between the structure and the masses usually play the roles of the unknowns. In these approaches, the values of the forces are in general assumed to be independent in successive time steps, so that, in order to ensure a unique solution, the number of sensors must not be smaller than the number of the moving masses. Such an identification is usually highly ill-conditioned and a numerical regularization is required. The regularization makes use of a priori assumptions about force time-histories, which usually concern their magnitude or smoothness (Tikhonov regularization). Such assumptions are often more numerical than physical in nature, and it is not always obvious how to design them, so that they can provide relevant information instead of the missing sensors (see the discussion of the unreconstructible component of the actual excitation in Chapter 2). By contrast, if the masses are treated as the optimization variables, the force time-histories in all time steps are coupled to the structural response and so they cease to be independent. This kind of an assumption is of a physical nature and allows the number of the necessary sensors to be decreased. This is illustrated in the numerical example of a three-span beam in Subsection 6.3.4, where a single strain sensor is used for accurate identification of three moving masses, and as many as seven unknowns (three masses and four stiffness reduction ratios) can be ac-

curately identified using two sensors only, even despite the three concurrently used types of modeling errors and the simulated 10% measurement error.

Therefore, compared to the approaches based on identification of the interaction forces, parametrization of the loads

- yields a far smaller number of optimization variables,
- significantly improves the conditioning of the identification process and
- decreases the number of sensors that are required for a unique solution.

However, these advantages come at the following cost:

- The identification problem becomes nonlinear, which is typical for parametric optimization problems.
- Moreover, the damages are parametrized, which means that their type must be known or assumed in advance, unlike in Section 6.2. Here, the damage is modeled in terms of stiffness reduction of the involved finite elements, (3.24), which seems to be typical for global SHM methods.

The VDM is employed via the concept of the moving dynamic influence matrix, which is defined here as a collection of the structural impulse response functions with respect to the time-dependent positions of the moving masses. For given values of the variables, the moving dynamic influence matrix allows the response of the system to be computed quickly without a full numerical simulation and without a repetitive assembly of the time-variant mass matrix anew in each time step.

From the practical point of view, it must be also stressed that before any practical application in bridge traffic monitoring, more research has to be performed, for example to test multi-DOF vehicle models [55], more advanced bridge models and to confirm the locality of the effects of the mesh-related model errors.

6.3.1 Modeling of moving masses

Moving masses in a bridge–vehicle system not only excite the supporting structure via their gravities but they also modify its inertial properties. Here, similar as in the case of structural damages, moving masses are modeled via the corresponding moving pseudo loads that are time-dependent and include the gravities of the masses as well as model all their inertial effects. Thanks to the approach of the VDM, the structural response can be quickly computed via the convolution of the pseudo loads with the pre-computed structural impulse response functions, so that a repeated numerical integration of the equation of motion as well as updating the mass matrix in each time step are avoided.

6.3.1.1 Pseudo loads

Consider N_m masses m_1, \dots, m_{N_m} that move with respective constant velocities over a flat supporting structure of a finite length (the undamaged bridge). Figure 6.13 illustrates the considered setup using a simply supported beam in the role of the bridge. Each mass is assumed to attach to the bridge at its current position.

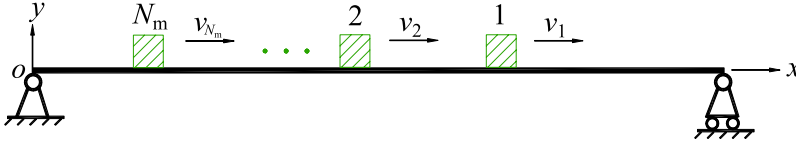


Figure 6.13. A sample supporting system and the moving masses.

In the standard approach, the bridge is modeled as a discrete finite element structure. The moving masses and the bridge collectively constitute a single system, which is excited by the moving gravities of the masses; the global excitation vector is computed in each time step using the shape functions of the finite elements that are currently carrying the masses. The system mass matrix is continuously re-assembled with respect to the current positions of the masses. The equation of motion of the undamaged system can be thus written in the following form:

$$(\mathbf{M} + \Delta\mathbf{M}(t)) \ddot{\mathbf{u}}^L(t) + \mathbf{C}\dot{\mathbf{u}}^L(t) + \mathbf{K}\mathbf{u}^L(t) = \sum_{i=1}^{N_m} m_i g \mathbf{b}_i(t), \quad (6.18)$$

where \mathbf{M} , \mathbf{C} and \mathbf{K} are respectively the mass, damping and stiffness matrices of the undamaged bridge. The matrix $\Delta\mathbf{M}(t)$ models the effects of the attached masses,

$$\Delta\mathbf{M}(t) = \sum_{i=1}^{N_m} m_i \mathbf{b}_i(t) \mathbf{b}_i^T(t), \quad (6.19)$$

and $\mathbf{b}_i(t)$ denotes the time-dependent global load allocation vector of the i th mass. If the mass is outside the bridge, the vector $\mathbf{b}_i(t)$ vanishes; otherwise, it is computed using the shape functions of the finite element that is currently carrying the mass. The dynamic response of the bridge can be obtained by a numerical integration of (6.18), provided the velocities of the masses are well below the critical speed, as discussed by Bajer and Dyniewicz in [278–280].

In accordance with the general idea of the virtual distortion method, the time-dependent matrix $\Delta\mathbf{M}(t)$ in (6.18) is moved to the right-hand side to obtain:

$$\mathbf{M}\ddot{\mathbf{u}}^L(t) + \mathbf{C}\dot{\mathbf{u}}^L(t) + \mathbf{K}\mathbf{u}^L(t) = \sum_{i=1}^{N_m} p_i^0(t)\mathbf{b}_i(t), \quad (6.20)$$

which is the equation of motion of the undamaged bridge alone subjected to the moving pseudo loads $p_i^0(t)$ that act at the positions of the moving masses and represent both their gravities and the inertial effects,

$$p_i^0(t) = m_i(g - a_i^L(t)), \quad (6.21)$$

where the vertical acceleration $a_i^L(t)$ of the i th mass couples the pseudo load $p_i^0(t)$ back to the structural response,

$$a_i^L(t) = \mathbf{b}_i^T(t)\ddot{\mathbf{u}}^L(t). \quad (6.22)$$

Notice that (6.21) is analogical to (3.28a).

6.3.1.2 Moving dynamic influence matrix

The dependence of the vertical accelerations of the moving masses on the pseudo loads $p_i^0(t)$ can be expressed explicitly by using in (6.22) the impulse response matrix $\ddot{\mathbf{H}}^{ap}(t)$ that contains the acceleration responses of all the DOFs of the undamaged bridge to unit impulse excitations in all its DOFs:

$$\begin{aligned} a_i^L(t) &= \mathbf{b}_i^T(t) \int_0^t \ddot{\mathbf{H}}^{ap}(t-\tau) \sum_{j=1}^{N_m} p_j^0(\tau) \mathbf{b}_j(\tau) d\tau \\ &= \sum_{j=1}^{N_m} \int_0^t \ddot{B}_{ij}^{ap}(t, \tau) p_j^0(\tau) d\tau, \end{aligned} \quad (6.23)$$

where the convolution kernel $\ddot{B}_{ij}^{ap}(t, \tau)$ represents the vertical acceleration of the i th mass at time t as a result of an impulsive excitation applied at time τ at the respective location of the j th mass,

$$\ddot{B}_{ij}^{ap}(t, \tau) = \mathbf{b}_i^T(t)\ddot{\mathbf{H}}^{ap}(t-\tau)\mathbf{b}_j(\tau). \quad (6.24)$$

Equation (6.23) is substituted into (6.21), which can be then stated in the form typical for the VDM:

$$m_i g = p_i^0(t) + m_i \sum_{j=1}^{N_m} \int_0^t \ddot{B}_{ij}^{ap}(t, \tau) p_j^0(\tau) d\tau. \quad (6.25)$$

Equation (6.25), if collected for all the considered moving masses, constitutes a system of linear integral equations with the pseudo loads $p_i^0(t)$ as the unknowns. The kernel of the respective matrix integral operator, $\tilde{B}_{ij}^{ap}(t, \tau)$, is expressed with respect to the positions of the moving masses that change in time, and thus it ceases to be a difference kernel; notice that an impulsive component can occur on its diagonal. The kernel, or its discretized version, is called the *moving dynamic influence matrix*. As it does not depend on the masses, it needs to be computed only once for a certain bridge and given velocities of the masses. Thereupon, in the coupled bridge–moving mass analysis, the pseudo loads $p_i^0(t)$ that model the masses can be quickly found by solving (a discretized version of) (6.25). In this way, thanks to the VDM, it is possible to avoid the repeated assembling of the system mass matrix in each time step, as required in any direct solution of (6.18).

6.3.1.3 Modeled structural response

Given the pseudo loads $p_i^0(t)$ and assumed zero initial conditions, the response $h_k^L(t)$ of the k th linear sensor placed in the structure is modeled in the following way:

$$h_k^L(t) = \sum_{i=1}^{N_m} \int_0^t B_{ki}^{hp}(t, \tau) p_i^0(\tau) d\tau, \quad (6.26)$$

where $B_{ki}^{hp}(t, \tau)$ denotes the respective impulse response function of the undamaged structure, that is the response of the k th sensor at time t to the unit impulsive excitation that is applied in time τ at the respective location of the i th mass.

6.3.2 Coupled modeling of moving masses and damages

6.3.2.1 Virtual distortions and pseudo loads

The VDM can be employed to simultaneously model stiffness-related damages and moving masses by using virtual distortions and pseudo loads respectively. As in (3.28), they are both coupled to the structural response, hence a coupled analysis is necessary. First, by an analogy to (3.29) and (6.9), the ac-

celeration $a_i(t)$ and distortion $\kappa_{ij}(t)$ responses of the damaged bridge structure are stated in the following form:

$$a_i(t) = \sum_{j=1}^{N_m} \int_0^t \ddot{B}_{ij}^{\text{ap}}(t, \tau) p_j^0(\tau) d\tau + \sum_{j,k} \int_0^t \ddot{B}_{ijk}^{\text{ak}}(t, \tau) \kappa_{jk}^0(\tau) d\tau, \quad (6.27\text{a})$$

$$\kappa_{ij}(t) = \sum_{k=1}^{N_m} \int_0^t B_{ijk}^{\text{kp}}(t, \tau) p_k^0(\tau) d\tau + \sum_{k,l} \int_0^t B_{ijkl}^{\text{kk}}(t - \tau) \kappa_{kl}^0(\tau) d\tau, \quad (6.27\text{b})$$

where $\ddot{B}_{ijk}^{\text{ak}}(t, \tau)$ and $B_{ijk}^{\text{kp}}(t, \tau)$ are the coupling matrices of the impulse response functions: $\ddot{B}_{ijk}^{\text{ak}}(t, \tau)$ contains the vertical acceleration of the i th mass at time t to an impulsive unit distortion φ_{jk} applied at time τ , and $B_{ijk}^{\text{kp}}(t, \tau)$ contains the response of the j th distortion of the i th element at time t as a result of an impulse excitation applied at time τ at the respective location of the k th mass.

Equations (6.27), when substituted into (3.28b) and (6.21), yield the following system of linear integral equations:

$$\begin{aligned} m_i g = & p_i^0(t) + m_i \sum_{j=1}^{N_m} \int_0^t \ddot{B}_{ij}^{\text{ap}}(t, \tau) p_j^0(\tau) d\tau \\ & + m_i \sum_{j,k} \int_0^t \ddot{B}_{ijk}^{\text{ak}}(t, \tau) \kappa_{jk}^0(\tau) d\tau, \end{aligned} \quad (6.28\text{a})$$

$$\begin{aligned} 0 = & (1 - \mu_i) \sum_{k=1}^{N_m} \int_0^t B_{ijk}^{\text{kp}}(t, \tau) p_k^0(\tau) d\tau \\ & - \kappa_{ij}^0(t) + (1 - \mu_i) \sum_{k,l} \int_0^t B_{ijkl}^{\text{kk}}(t - \tau) \kappa_{kl}^0(\tau) d\tau \end{aligned} \quad (6.28\text{b})$$

with the pseudo loads $p_i^0(t)$ and the virtual distortions $\kappa_{ij}^0(t)$ in the roles of the unknowns. Notice that the masses m_i and the damage extents μ_i , which are to be identified, occur in the kernels of the respective matrix integral operators only in the form of constant scaling factors; as a result, these kernel needs to be computed only once and does not have to be recomputed during the identification process.

6.3.2.2 Response of a damaged structure to moving masses

The pseudo loads and virtual distortions are obtained by solving (6.28). The response of the k th sensor can be then computed as follows,

$$h_k(t) = \sum_{i=1}^{N_m} \int_0^t B_{ki}^{\text{hp}}(t, \tau) p_i^0(\tau) d\tau + \sum_{i,j} \int_0^t B_{kij}^{\text{hk}}(t - \tau) \kappa_{ij}^0(\tau) d\tau. \quad (6.29)$$

6.3.2.3 Time discretization

In practice, only the discrete-time counterparts of (6.27) to (6.29) are used. The discrete response of the damaged structure subjected to moving loads is expressed in a similar form as in (6.10), that is by

$$\mathbf{h} = \mathbf{B}^{\text{hp}} \mathbf{p}^0 + \mathbf{B}^{\text{hk}} \boldsymbol{\kappa}^0, \quad (6.30)$$

where the vectors \mathbf{h} , $\boldsymbol{\kappa}^0$ and \mathbf{p}^0 respectively collect, for all time steps, the discrete responses of all considered sensors, the discrete virtual distortions of all potentially damaged elements and the pseudo loads that model all moving masses. The matrices \mathbf{B}^{hp} and \mathbf{B}^{hk} are the discretized counterparts of the corresponding integral operators in (6.29) and take the forms of block matrices of respective dimensions with lower-triangular blocks; the blocks in case of \mathbf{B}^{hk} are Toeplitz, since the corresponding operator has a difference kernel.

Similarly, the vectors of the discrete accelerations \mathbf{a} and distortions $\boldsymbol{\kappa}$ are linearly dependent on the discrete pseudo load \mathbf{p}^0 and the discrete virtual distortions $\boldsymbol{\kappa}^0$,

$$\begin{bmatrix} \mathbf{a} \\ \boldsymbol{\kappa} \end{bmatrix} = \begin{bmatrix} \mathbf{B}^{\text{ap}} & \mathbf{B}^{\text{ak}} \\ \mathbf{B}^{\text{kp}} & \mathbf{B}^{\text{kk}} \end{bmatrix} \begin{bmatrix} \mathbf{p}^0 \\ \boldsymbol{\kappa}^0 \end{bmatrix}, \quad (6.31)$$

which is an aggregated discrete-time version of (6.27).

Finally, the aggregated discrete-time counterparts of (3.28b) and (6.21) take the following forms:

$$\mathbf{p}^0 = \mathbf{m}(\mathbf{g} - \mathbf{a}), \quad (6.32a)$$

$$\boldsymbol{\kappa}^0 = (\mathbf{I} - \boldsymbol{\mu}) \boldsymbol{\kappa}, \quad (6.32b)$$

where \mathbf{m} and $\boldsymbol{\mu}$ are block diagonal matrices of respective dimensions with diagonal blocks, each of which has m_i or μ_i on the diagonal, and \mathbf{g} is the vector of appropriate length of Earth's gravities g . If (6.32) are substituted into (6.31), they yield the following linear system, which is a counterpart of (3.33c):

$$\begin{bmatrix} \mathbf{I} + \mathbf{m}\mathbf{B}^{\text{ap}} & \mathbf{m}\mathbf{B}^{\text{ak}} \\ (\mathbf{I} - \boldsymbol{\mu})\mathbf{B}^{\text{kp}} & (\mathbf{I} - \boldsymbol{\mu})\mathbf{B}^{\text{kk}} - \mathbf{I} \end{bmatrix} \begin{bmatrix} \mathbf{p}^0 \\ \boldsymbol{\kappa}^0 \end{bmatrix} = \begin{bmatrix} \mathbf{mg} \\ \mathbf{0} \end{bmatrix}. \quad (6.33)$$

The building blocks of (6.30) to (6.33) are the matrices $\mathbf{B}^{(\cdot)(\cdot)}$. These matrices store all the necessary information about the dynamics of the structure and are independent of the moving masses and the damage. Thus, given specific values of the masses m_i and the damage extents μ_i , the system (6.33) can be quickly assembled without any numerical structural simulations and then solved to obtain the pseudo loads and the virtual distortions, which are then substituted into (6.30) to compute the response of the damaged structure excited by the moving masses.

6.3.3 Identification

Assume that the discrete response \mathbf{h}^M of the damaged structure to unknown moving masses is measured and available. According to the approach presented in Section 6.2, the pseudo load \mathbf{p}^0 and the virtual distortions $\boldsymbol{\kappa}^0$ can be treated as independent unknowns and found by solving the following version of (6.30):

$$\mathbf{h}^M = \mathbf{B}^{hp}\mathbf{p}^0 + \mathbf{B}^{h\kappa}\boldsymbol{\kappa}^0 \quad (6.34)$$

with respect to the unknown vectors \mathbf{p}^0 and $\boldsymbol{\kappa}^0$, which are then used in (6.31) to compute the corresponding accelerations \mathbf{a} and distortions $\boldsymbol{\kappa}$. Finally, the unknown masses and damages are estimated via a least-square fitting of (6.32).

This section pursues another approach which is more parametric in nature and which treats the masses m_i and the damage extents μ_i as independent unknowns. These unknowns are used to determine the pseudo load \mathbf{p}^0 , the virtual distortions $\boldsymbol{\kappa}^0$ and finally the response \mathbf{h} . In this way, the number of unknowns is significantly reduced and thus fewer sensors are necessary and the results are numerically more stable; however, it is at the cost of assuming the damages to be of known types, such as the constant stiffness reduction considered here.

6.3.3.1 Optimization variables

Basically, the inverse problem of identification of unknown masses and damage parameters is formulated here as an optimization problem of minimization of the normalized mean-square distance between the measured structural response \mathbf{h}^M and the computed response \mathbf{h} with respect to the optimization variables m_i and μ_i . These variables have very different magnitudes, which can seriously impair the accuracy of many optimization procedures: the stiffness reduction ratios μ_i belong to the interval $[0, 1]$, while the masses m_i might be as large as several tens of thousands of kilograms. Moreover, while the damage extents

have a natural initial value of 1 (which corresponds to no damage), there is no such a straightforward initial value for the moving masses. Thus, an initial approximation m_i^{tr} (called the trial mass) of each mass m_i is first computed by using a temporary assumption that the bridge structure is undamaged and by approximating the pseudo loads with the moving gravities of the masses, that is by solving in the least-square sense the following overdetermined system:

$$\mathbf{h}^M = \mathbf{B}^{\text{hp}} \mathbf{m}^{\text{tr}} \mathbf{g}, \quad (6.35)$$

where \mathbf{m}^{tr} is the diagonal matrix of the same structure as \mathbf{m} in (6.32a), but includes the trial masses m_i^{tr} on the diagonal.

Given the trial masses, the optimization problem is stated in dimensionless variables μ_i^* , $i = 1, \dots, N_m + N_\mu$, where N_μ is the number of potentially damaged elements:

$$\mu_i^* := \begin{cases} \frac{m_i}{m_i^{\text{tr}}} & \text{for } i = 1, \dots, N_m, \\ \mu_{i-N_m} & \text{for } i = N_m + 1, \dots, N_m + N_\mu, \end{cases} \quad (6.36)$$

which all have the natural initial value of 1 and are all of a comparable magnitude.

6.3.3.2 Objective function

Defined the set of dimensionless optimization variables μ_i^* , the identification is stated in the form of the following optimization problem:

$$\begin{aligned} \text{minimize} \quad F(\mu_1^*, \dots, \mu_{N_m+N_\mu}^*) &:= \frac{1}{2} \frac{\|\mathbf{h}^M - \mathbf{h}\|^2}{\|\mathbf{h}^M\|^2}, \\ \text{subject to} \quad \mu_i^* &\geq 0, \quad i = 1, \dots, N_m + N_\mu, \end{aligned} \quad (6.37)$$

where \mathbf{h} is the response computed for the assumed values of the optimization variables via (6.36), (6.33) and (6.30).

6.3.3.3 Sensitivity analysis

The process of identification is equivalent to the minimization of the objective function defined in (6.37). It can be quickly performed using standard gradient-based optimization algorithms, provided the gradient can be computed at a reasonable numerical cost. The discrete-time formulation based on (6.33) and (6.30) allows the discrete adjoint method to be used [179, 180], which is quicker by one order of magnitude in comparison to the standard direct differentiation method [181].

For the purpose of notational simplicity, (6.30) and (6.33) and their first derivatives with respect to the variable μ_i^* are stated in the following simple aggregate forms:

$$\mathbf{P}(\boldsymbol{\mu}^*)\boldsymbol{\nu}^0 = \mathbf{b}, \quad (6.38a)$$

$$\mathbf{P}_i(\boldsymbol{\mu}^*)\boldsymbol{\nu}_i^0 = \mathbf{b}_i - \mathbf{P}_i(\boldsymbol{\mu}^*)\boldsymbol{\nu}^0, \quad (6.38b)$$

$$\mathbf{h} = \mathbf{B}^h \boldsymbol{\nu}^0, \quad (6.38c)$$

$$\mathbf{h}_i = \mathbf{B}^h \boldsymbol{\nu}_i^0, \quad (6.38d)$$

which are respectively the counterparts of (3.33c), (3.53), (3.33b) and (3.51), and where

$$\mathbf{P}(\boldsymbol{\mu}^*) = \begin{bmatrix} \mathbf{I} + \mathbf{m}\mathbf{B}^{ap} & \mathbf{m}\mathbf{B}^{a\kappa} \\ (\mathbf{I} - \boldsymbol{\mu})\mathbf{B}^{\kappa p} & (\mathbf{I} - \boldsymbol{\mu})\mathbf{B}^{\kappa\kappa} - \mathbf{I} \end{bmatrix}, \quad (6.39a)$$

$$\mathbf{b} = [\mathbf{mg} \quad \mathbf{0}]^T, \quad (6.39b)$$

$$\mathbf{B}^h = [\mathbf{B}^{hp} \quad \mathbf{B}^{h\kappa}], \quad (6.39c)$$

$$\boldsymbol{\nu}^0 = [\mathbf{p}^0 \quad \boldsymbol{\kappa}^0]^T, \quad (6.39d)$$

and the subscript i denotes the first derivative with respect to μ_i^* . The objective function is directly differentiated to obtain

$$F_i = -\frac{(\mathbf{h}^M - \mathbf{h})^T}{\|\mathbf{h}^M\|^2} \mathbf{B}^h \boldsymbol{\nu}_i^0, \quad (6.40)$$

which involves the first derivatives $\boldsymbol{\nu}_i^0$ of the virtual distortions and pseudo loads. The direct differentiation method computes $\boldsymbol{\nu}_i^0$ by solving (6.38b); for the full gradient, the solution has to be repeated $N_m + N_\mu$ times, that is once for each optimization variable μ_i^* . The discrete adjoint method adds to (6.40) the scalar product of an adjoint vector $\boldsymbol{\lambda}$ with (6.38b) and collects together all the terms that include $\boldsymbol{\nu}_i^0$ to obtain

$$F_i = \boldsymbol{\lambda}^T (\mathbf{P}_i(\boldsymbol{\mu}^*)\boldsymbol{\nu}^0 - \mathbf{b}_i) + \left(\boldsymbol{\lambda}^T \mathbf{P}(\boldsymbol{\mu}^*) - \frac{(\mathbf{h}^M - \mathbf{h})^T}{\|\mathbf{h}^M\|^2} \mathbf{B}^h \right) \boldsymbol{\nu}_i^0. \quad (6.41)$$

In this way, the first derivative of the objective function is stated as

$$F_i = \boldsymbol{\lambda}^T (\mathbf{P}_i(\boldsymbol{\mu}^*)\boldsymbol{\nu}^0 - \mathbf{b}_i), \quad (6.42)$$

where the adjoint vector $\boldsymbol{\lambda}$ is selected in such a way that the second term in (6.41) vanishes, that is at the cost of only a single solution of the adjoint equation

$$\mathbf{P}_i^T(\boldsymbol{\mu}^*)\boldsymbol{\lambda} = (\mathbf{B}^h)^T \frac{(\mathbf{h}^M - \mathbf{h})}{\|\mathbf{h}^M\|^2}. \quad (6.43)$$

The second order sensitivity analysis can be also based on the discrete direct-adjoint method, see Subsections 3.4.3.2 and 4.2.3.2.

6.3.3.4 Numerical procedures

In principle, if a small number of the time steps is used, the system matrix in (6.33) is of moderate dimensions and its inverse can be computed using direct methods. However, in off-line identification, in the case of a dense time discretization or a longer sampling time, the system can become prohibitively large and computationally hardly manageable in a direct way. In such cases, the system matrix, which is a structured block matrix composed of lower triangular matrices (of which not all are Toeplitz, unlike in previous chapters), can be rearranged into the lower triangular block form that can be exploited by a specialized linear solver (like block forward-substitution or dynamic programming [69, 73]) to reduce the numerical costs of the solution. Despite the inherent ill-conditioning of the system, application of such a solver is facilitated by the fact that both the matrix and the right-hand side vector are computed based on the FE model of the structure, and so they include only numerical errors, which are usually several orders of magnitude smaller than measurement errors. On the other hand, the left-hand side vector of (6.34) contains the measurement data and hence it can include significant measurements errors. Alternatively, an iterative solver might be considered, such as the CGLS method [128].

Furthermore, given the FE model of the undamaged structure, the proposed method can be used online by a repetitive application in a moving time window, that is basically in the same way as described in Subsection 6.2.3.

Notice also that, if the system parameters are known, the virtual distortions in (6.30) vanish, and the method can be employed also for identification of the moving masses only.

6.3.4 Numerical example

A multi-span frame structure is used to validate the proposed method for simultaneous identification of moving masses and damage. Measurement error and three types of model errors are taken into account in order to test the robustness of the method.

6.3.4.1 The structure and moving masses

Figure 6.14 shows a scheme of the considered three-span frame structure. It is made of steel with Young's modulus of 215 GPa and a density of $7.8 \times 10^3 \text{ kg/m}^3$. The mass is uniformly distributed at the rate of $15.3 \times 10^3 \text{ kg/m}$. The beam has a rectangular cross-section $b \times h = 0.89 \text{ m} \times 2.21 \text{ m}$, so that its second moment of area is 0.8 m^4 . The structure is 200 m long in total, while each of the two side spans is 50 m long. Each of the two piers is 20 m high and has the second moment of area of 0.16 m^4 .

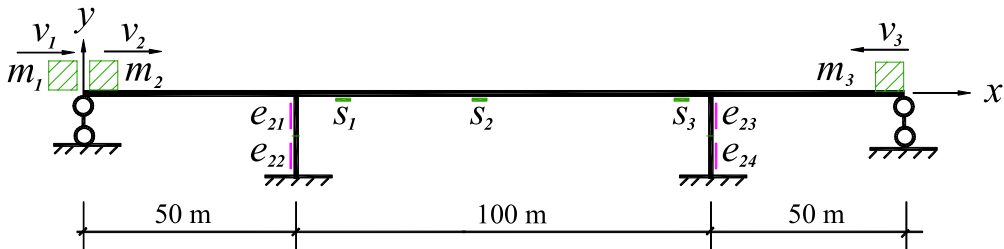


Figure 6.14. The damaged three-span frame structure and three moving masses.

It is assumed that three moving masses,

$$m_1 = 71.2 \times 10^3 \text{ kg}, \quad (6.44a)$$

$$m_2 = 60.0 \times 10^3 \text{ kg}, \quad (6.44b)$$

$$m_3 = 53.0 \times 10^3 \text{ kg}, \quad (6.44c)$$

pass over the structure with constant velocities of 34 m/s, 34 m/s and -30 m/s respectively. The initial positions of the masses are -3 m , 0 m and 200 m , respectively. Three strain sensors are employed for collecting the measurements: s_1 at the location of 65.2 m, s_2 at 95.2 m and s_3 at 145.2 m, see Fig. 6.14. The sensors are placed at the bottom surface of the beam, so that their distance to the neutral axis is $0.5h = 1.105 \text{ m}$.

6.3.4.2 Measurement errors and model errors

Measurement errors of the simulated measurement data \mathbf{h}^M are modeled by adding an uncorrelated Gaussian noise at k_n rms level, that is

$$\mathbf{h}^M \leftarrow \mathbf{h}^M + k_n \boldsymbol{\eta} \frac{\|\mathbf{h}^M\|}{\sqrt{N_r N_t}}, \quad (6.45)$$

where N_r and N_t are respectively the numbers of the sensors and of the time steps, and $\boldsymbol{\eta}$ is a column vector of the same length as \mathbf{h}^M (that is $N_r N_t$), whose elements are random numbers independently drawn from $N(0, 1)$. Altogether, three noise levels are used: $k_n \in \{0\%, 5\%, 10\%\}$.

Model errors are inevitable in practice. The influence of modeling errors is tested below by using two different FE models of the structure: one for identification purposes and a different one for the generation of the simulated measurements. For identification purposes, the beam is divided into 20 finite elements of 10 m each, and each of the two piers is divided into two elements of 10 m (the *original mesh*). These values are chosen based on Law *et al.* [105], where it is tested that a minimum of eight finite elements have to be used to model a typical single-span bridge deck for moving load identification. As described above, the moving masses are assumed to attach directly to the beam. This model is modified in order to generate the simulated measurements. The three following types of modifications are concurrently considered:

Type I Modification of the stiffness of all the elements. More precisely, uncorrelated Gaussian modifications with mean -2% and the standard deviation of 5% are used, as due to both aging and initial model inaccuracies.

Type II A damped mass–spring vehicle model (Kelvin–Voigt element) is used instead of the simple moving mass, see Fig. 6.15.

Type III A four times finer finite element mesh is used for simulation of the measurements, that is each of the 10 m elements is further divided into four equal elements of 2.5 m.

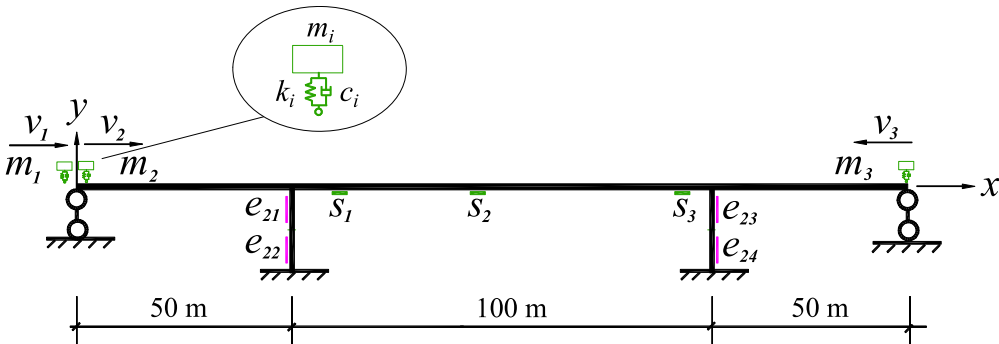


Figure 6.15. Type III model error: a mass–spring vehicle model is used instead of a simple moving mass.

For Type II model error, the parameters of the vehicle models are chosen as in [281, 282]: the stiffness $k_i = 286 \times 10^6$ N/m and the damping $c_i = 2.8 \times 10^6$ Ns/m, $i = 1, 2, 3$. Figure 6.16 compares the responses obtained using the original undamaged structure, as well as the same structure with Type III model error and with Type II+III model errors. For a flat beam considered here, the discrepancies between the responses obtained from the mass–spring vehicle model and those from the simple mass model are small. Similarly, noticeable effects of element mesh, like Type III model error, occur only at the times when the vehicles pass directly over the sensors: the finer mesh better reflects the local high-frequency components of the response. These local vibrations decay soon after the vehicle passes over the sensor. Therefore, in order to improve the accuracy and decrease the influence of Type III model error, the local vibrations can be removed from the measurements by modifying the original objective function in (6.37) as follows:

$$F(\mu_1^*, \dots, \mu_{n_m+n_e}^*) := \frac{1}{2} \frac{\|(\text{diag } \mathbf{w})(\mathbf{h}^M - \mathbf{h})\|^2}{\|(\text{diag } \mathbf{w})\mathbf{h}^M\|^2}, \quad (6.46)$$

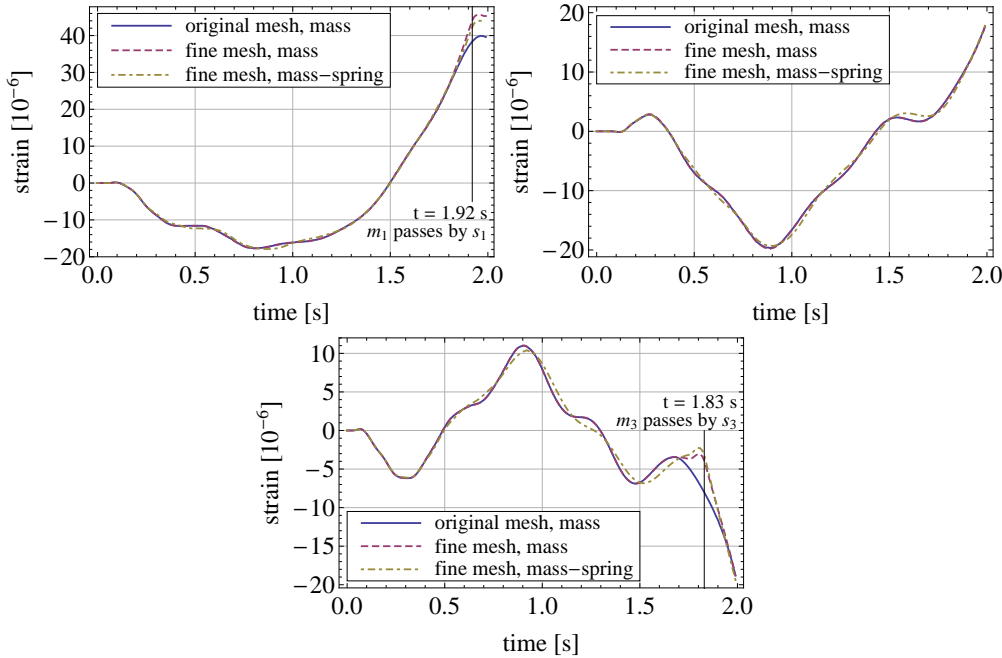


Figure 6.16. Responses of the undamaged system simulated using different meshes and vehicle models: (top left) sensor S1; (top right) sensor S2; (bottom) sensor S3.

where \mathbf{w} is a binary weighting vector, which contains only 1s with the exception of the time steps at which the vehicles are within a certain distance from any of the sensors (± 2.5 m is used here).

6.3.4.3 Identification cases

The following set of six cases is taken into account for a thorough test of the presented method:

Case 1 The structure is assumed to be undamaged. Only the three moving masses are identified. Measurement error of the undamaged structure is simulated at 0% and 5% rms level. No model error is assumed.

Case 2 Two pier elements (No. 21 and 23) are damaged with the damage extents

$$\mu_{21} = 0.4 \quad \mu_{23} = 0.7, \quad (6.47a)$$

while the other two pier elements remain undamaged,

$$\mu_{22} = 1.0 \quad \mu_{24} = 1.0. \quad (6.47b)$$

The moving masses and the damage extents are identified simultaneously. The damage location is limited to the four pier elements of the original mesh, so that four stiffness modification coefficients are used in optimization, besides the three variables related to the masses. In this way, the exact number of the damaged elements and their locations are treated as unknown and also identified. Measurement error is simulated at 5% rms level; no model error is used.

Case 3 As in Case 2, but Type I model error is additionally simulated, see Fig. 6.17a.

Case 4 As in Case 2, but model error Type II+III is used, that is the finer mesh and the mass-spring vehicle model are used to generate the simulated measurements, and no measurement error is considered. Identification of masses and damages is performed via (6.37), that is using all the responses without removing the local vibrations.

Case 5 As in Case 4, but local vibrations are removed from the responses via (6.46) and measurement error is simulated at 5% rms level.

Case 6 As in Case 5, but all model errors (Type I+II+III) are used concurrently, see Fig. 6.17b for the stiffness modifications, and measurement error is simulated at 10% rms level. Local vibrations are removed from the responses via (6.46).

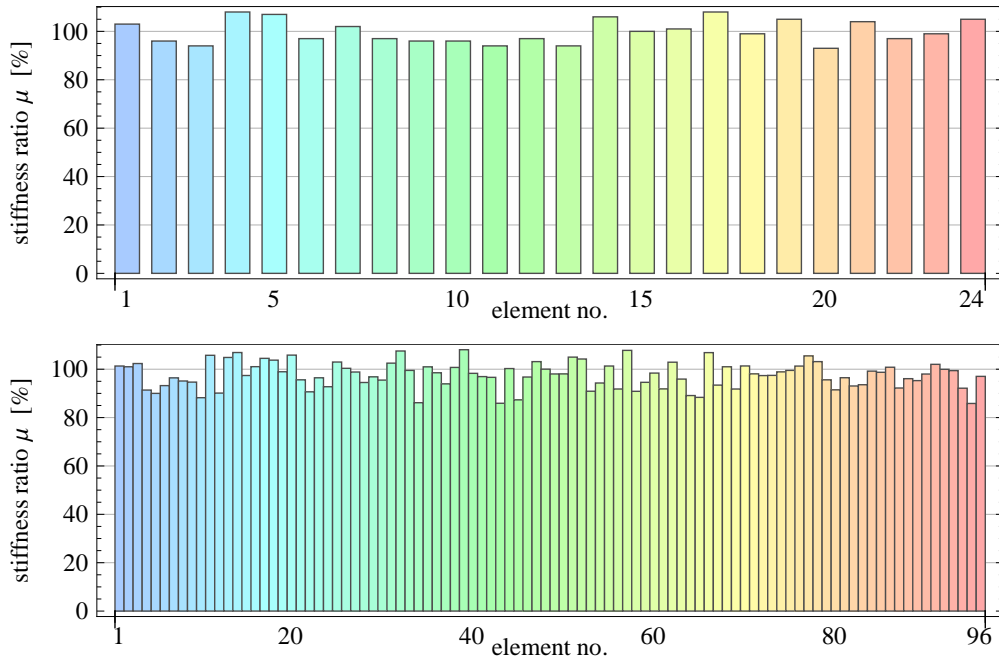


Figure 6.17. Stiffness reduction levels of the elements: (top) original mesh (Type I model error); (bottom) fine mesh (Type I+III model error).

Notice that in Cases 3 and 6 model error Type I is simulated. In these cases, the damage extents (6.47a) relate to the element stiffnesses in the modified model, and the actual (to-be-identified) damage extents in Cases 3 and 6 are slightly different, since they include also the model error besides the damage, see Tables 6.8 and 6.9.

In all cases, the structural response is calculated using the Newmark integration method with the parameters $\gamma = 1/4$ and $\beta = 1/2$ [145–148]. The integration time step equals 0.01 s (100 Hz sampling frequency). A total of 200 time steps is used; the sampling time interval is thus 2 s. The simulated noisy sensor responses in Case 1 and Case 2 are shown in Fig. 6.18.

6.3.4.4 Identification results

In the following, the results are discussed for the six mentioned cases. The results of mass identification are assessed by their relative accuracy, while the results of damage identification are more naturally assessed in terms of their absolute accuracy (percentage points).

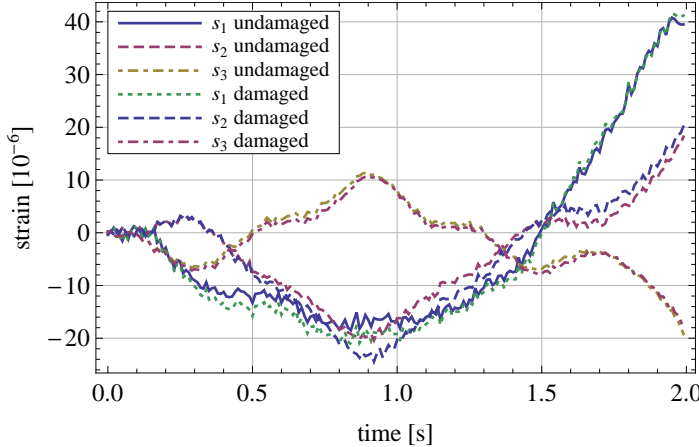


Figure 6.18. Simulated strain responses of the damaged and the intact systems in identification Case 1 and Case 2. Simulated measurement noise at 5% rms level.

Moving masses (Case 1). First, the three moving masses are identified using a direct solution of (6.34), where the virtual distortions κ^0 are assumed to vanish². For a unique solution, at least three sensors are required. The pseudo loads \mathbf{p}^0 are computed separately for the noise-free and the noise-contaminated measurements, see the left- and right-hand sides of Fig. 6.19. The truncated singular value decomposition is used for regularization; the corresponding regularization levels (the number k_{TSVD} of the truncated singular values) were determined using the L-curve technique [67, 135], that is by weighing in the log-log scale the residual of (6.34) vs. the norm of the first differences of the unknown pseudo load $\|\mathbf{L}\mathbf{p}^0\|$ and selecting the corner point. The L-curves are depicted in the top row of Fig. 6.19; they confirm that the equation (6.34) is seriously ill-conditioned. Moreover, consistently large values of the regularizing term $\|\mathbf{L}\mathbf{p}^0\|$ suggest that it is impossible to obtain accurate results even at the optimum regularization level. In the noise-free case, the optimum regularization level is $k_{\text{TSVD}} = 29$. The corresponding pseudo loads are computed and shown in Fig. 6.19 (bottom left); their end parts diverge from the actual mass-equivalent pseudo loads. With 5% noise contamination, the pseudo load is computed at the optimum value of $k_{\text{TSVD}} = 269$ and shown in Fig. 6.19 (bottom right); both the front and the end parts diverge very significantly from the actual values. Table 6.5 lists the

²This corresponds to the standard approach in which a nonparametrized moving force is identified directly.

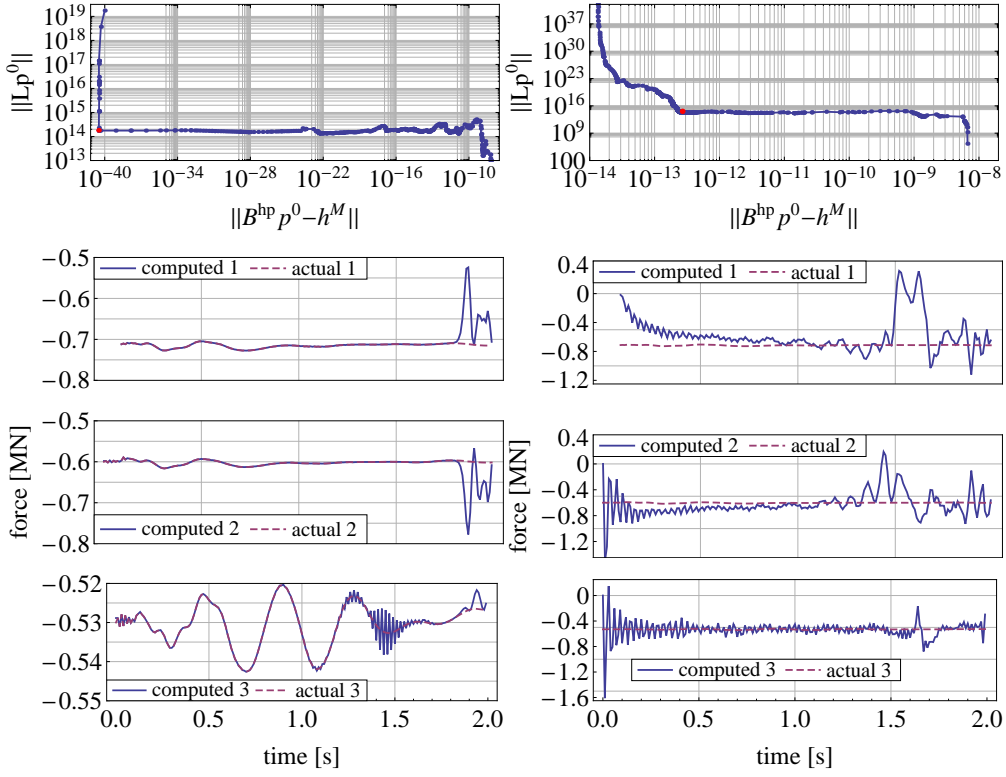


Figure 6.19. Case 1, three sensors. Moving load identification by a direct solution of (6.34): (*top left*) L-curve, noise-free measurements; (*top right*) L-curve, 5% rms measurement noise; (*bottom left*) computed pseudo loads, noise-free measurements; (*bottom right*) computed pseudo loads, 5% rms measurement noise. L is the matrix of the first differences. „computed *i*” and „actual *i*” denote the *i*th computed and actual pseudo load.

masses identified by least-square fitting of (6.21), where the accelerations are computed via (6.31). Given the large oscillations of the pseudo loads in the 5%-noise case, the identification errors are surprisingly small. However, the largest 20% error of the identified mass m_1 confirms that the results can be sensitive to the disturbances and noise in the measured response.

In comparison, the identification via (6.37) exploits the physical constraints imposed on the pseudo loads (which are required to be mass-equivalent) and hence turns out to be more robust to noise. Moreover, the masses are accurately identified using a single sensor only (s_1); the results are listed in Table 6.6. The initial trial values of the moving masses are computed by (6.35); in each

Table 6.5. Case 1. Identified masses and relative identification errors. Identification by (6.34) based on three sensors, (6.21) and (6.31).

	Actual [10 ³ kg]	Noise free		5% noise	
		identified [10 ³ kg]	error [%]	identified [10 ³ kg]	error [%]
m_1	71.2	70.56	0.90	56.62	20.48
m_2	60.0	60.23	0.38	62.08	3.47
m_3	53.0	52.72	0.53	53.16	0.30

Table 6.6. Case 1. Identified masses and relative identification errors. Identification by (6.37) and (6.35) based on a single sensor (s_1).

	Actual [10 ³ kg]	Noise free			5% noise		
		trial [10 ³ kg]	identified [10 ³ kg]	error [%]	trial [10 ³ kg]	identified [10 ³ kg]	error [%]
m_1	71.2	69.82	71.2013	0.0018	68.30	71.42	0.31
m_2	60.0	58.98	60.0003	0.0005	59.04	59.17	1.38
m_3	53.0	43.45	52.9995	0.0010	41.33	53.81	1.53

optimization step, the pseudo load \mathbf{p}^0 is calculated using the moving dynamic influence matrix \mathbf{B}^{ap} by (6.33), which reduces to

$$(\mathbf{I} + \mathbf{m}\mathbf{B}^{ap}) \mathbf{p}^0 = \mathbf{mg}. \quad (6.48)$$

Figure 6.20 compares the pseudo loads identified using the noise-contaminated measurements to the actual pseudo loads; the results are very satisfactory even though 5% rms noise is used, especially in comparison to Fig. 6.19 (bottom right).

Moving masses and damages (Cases 2–6). The damage is limited to the two piers, that is to the respective four finite elements of the original mesh. Together with the three moving masses (mass modification coefficients), seven variables have thus to be identified by minimizing the objective function (6.37) or (6.46). Responses of only two sensors are used for that purpose (s_1 and s_3); the initial trial mass values are estimated via (6.35).

The results of identification in Case 2 (5% measurement noise, no model error) are listed in Table 6.7. The three moving masses and four potential damages are identified accurately. As only two actual damages were simulated, the optimization allowed also their number and location to be identified as well,

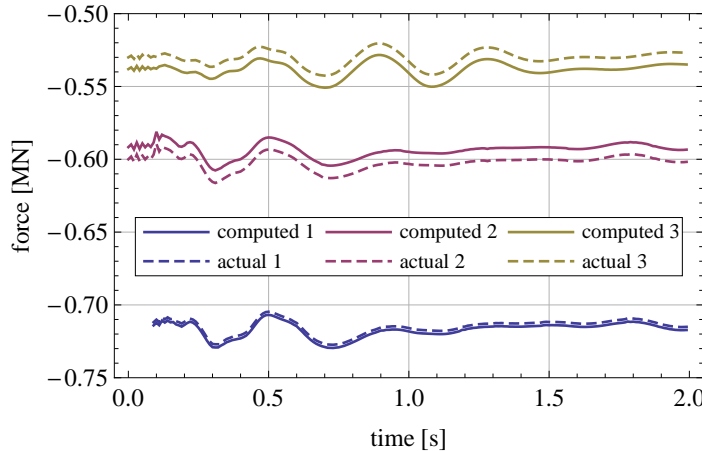


Figure 6.20. Case 1, single sensor s_1 , 5% measurement noise. Pseudo loads, actual and identified by (6.37); „computed i ” and „actual i ” denote the i th computed and actual pseudo load.

Table 6.7. Case 2. Masses and damage parameters identified via (6.37).

	Actual	Trial	Identified	Error [%]
m_1 [10^3 kg]	71.2	94.36	68.88	3.26
m_2 [10^3 kg]	60.0	46.27	60.63	1.05
m_3 [10^3 kg]	53.0	60.52	52.24	1.43
μ_{21}	0.40	—	0.38	2.23
μ_{22}	1.00	—	1.00	0.00
μ_{23}	0.70	—	0.68	2.27
μ_{24}	1.00	—	0.96	3.80

even if limited to the four considered pier elements. The results are relatively insensitive to the measurement error.

The results of identification in Cases 3 and 4 are listed in Table 6.8. They confirm that the model error of Type I (modified stiffness of finite elements) does influence the accuracy of damage identification (Case 3), but both the damage and the moving masses can still be identified with an acceptable accuracy even with the additional measurement error. For the model error of Type III (finer mesh), coupled with Type II error (mass–spring vehicle model), the direct use of the simulated measurements in (6.37) results in poor accuracy even without

Table 6.8. Cases 3–4. Masses and damage extents identified via (6.37).

	Case 3			Case 4		
	actual	identified	error [%]	actual	identified	error [%]
$m_1 [10^3 \text{ kg}]$	71.2	66.71	6.31	71.2	95.00	33.42
$m_2 [10^3 \text{ kg}]$	60.0	60.88	1.47	60.0	45.84	23.60
$m_3 [10^3 \text{ kg}]$	53.0	51.87	2.14	53.0	62.04	17.06
μ_{21}	0.398	0.343	5.52	0.40	0.529	12.86
μ_{22}	1.012	1.000	1.22	1.00	0.997	0.27
μ_{23}	0.666	0.635	3.06	0.70	0.997	29.73
μ_{24}	0.977	0.967	0.98	1.00	1.000	0.00

Table 6.9. Cases 5–6. Masses and damage extents identified via (6.46).

	Case 5			Case 6		
	actual	identified	error [%]	actual	identified	error [%]
$m_1[10^3 \text{ kg}]$	71.2	73.72	3.54	71.2	77.58	8.96
$m_2[10^3 \text{ kg}]$	60.0	56.45	5.91	60.0	56.34	6.11
$m_3[10^3 \text{ kg}]$	53.0	52.27	1.38	53.0	53.23	0.43
μ_{21}	0.40	0.356	4.36	0.382	0.379	0.29
μ_{22}	1.00	1.000	0.00	0.970	1.000	3.03
μ_{23}	0.70	0.637	6.33	0.692	0.647	4.47
μ_{24}	1.00	0.963	3.75	0.936	0.980	4.36

any measurement error (Case 4). However, simple filtering of the local vibrations via (6.46) significantly improves the accuracy to the level attained with Type I model error (Case 5, 5% measurement error included, see Table 6.9). These results suggest that in practice (6.46) should be always preferred over (6.37).

In the last test (Case 6), all three types of model errors are used together with the measurement error at 10% rms level. The identification is performed via (6.46). The results are listed in Table 6.9, where each actual damage extent is computed as an average of the damage extents of the four involved elements of the finer mesh. Given all the simulated errors, the results are of acceptable accuracy and not significantly worse than in the previous cases.

Load identification in elastoplastic structures

Chapter 2 discusses the problem of identification of dynamic excitations in linear structures. In particular, it offers a methodology of identification that is suited for the case of a limited number of sensors (fewer than required for a unique identification). That approach, as most of the others available in literature, see a review in Subsection 2.1.2, deals with linear structures and is based on a solution or an approximation of a solution to an ill-conditioned linear inverse problem. There is only a handful of reports on identification of dynamic loads in nonlinear structures [84, 89], including material [32] or geometric [90] nonlinearities.

The virtual distortion method is an effective tool for modeling of local structural modifications and damages, see Chapter 3. In a similar way, the VDM can be employed for fast modeling of material nonlinearities or inelasticities through the related distortions, such as plastic distortions, see, e.g., [28, 32, 161]. Basically, two general approaches are possible:

1. The distortions can be identified together with (and independently of) the unknown excitation in a standard linear identification procedure. Such an approach is used in Section 6.2 for simultaneous identification of excitation loads and unknown structural damages. An advantage is that the model of the nonlinearity can be unknown and might be identified together with the excitation; a disadvantage is that all the distortions have to be treated as independent and consequently an a priori precise information about the localization of damages is necessary in order to keep the necessary number of sensors reasonably small.
2. If the model of the nonlinearity and its parameters are known beforehand, its influence on the structural response can be modeled using the standard approach of the VDM. The excitations can be then treated as the only unknowns. An obvious advantage of such an approach is that, given the model, the distortions can be uniquely determined based on

the excitations; in this way, the number of sensors required for a unique identification is reasonably small and no prior information on the localization of nonlinearities is required. On the other hand, the model of the nonlinearity must correspond to the actual nonlinearities to ensure that meaningful results are obtained. Moreover, since the structure is no longer linear, the identification ceases to be equivalent to solving a linear inverse problem.

This chapter considers elastoplastic structures and the well-defined model of the bilinear isotropic hardening plasticity [283]. It is assumed that the model parameters (yield stress and hardening coefficient) are known, and the second from the above approaches is thus used. Plastic yield is modeled using plastic distortions, which are imposed on the linear structure and processed using the standard methodology of the VDM. Plastic distortions depend on the structural response in a nonlinear way, and thus they cannot be represented in the form of a solution to a linear integral equation such as (3.32). Instead, the formulation leads to a nonlinear integro-differential equation. Casting the problem in the discrete-time setting yields a relatively simple updating rule for plastic distortions, which is a version of the return-mapping algorithm [283] and which allows the solution to be advanced time step by time step and at a low cost without a typical iteration with respect to state variables.

Given the material model, the structural response depends uniquely on the assumed excitation and can be compared to the measured response for the purpose of identification of the unknown excitation. The direct differentiation method is applied to the discrete formulation to derive analytical formulas for the gradients of the response with respect to the unknown excitations, which allows any general-purpose gradient-based optimization approach to be used in a fast identification. The identification is essentially a least-squares problem, hence its Hessian can be approximated along the lines of the Gauss–Newton approach. As usual in the VDM, the structure, although materially nonlinear, is assumed to be geometrically linear.

For notational simplicity (and as in Section 6.2) only truss structures and strain sensors are considered here. With conceptually inessential modifications, the concept is applicable to other types of structures and linear sensors. Trusses are used here, since they are the simplest to describe: each element is associated with only one (axial) plastic distortion state, while already three states are necessary for a frame element (axial, pure bending and bending/shear) and even more for other elements, see Subsection 3.2.1. Nevertheless, the governing equations remain basically the same, although other structures can require more

variables and hence be notationally and computationally more demanding. The strain response is used for identification because of its straightforward relation to the plastic distortion of a truss element.

7.1 Bilinear isotropic hardening plasticity

Let $\varepsilon_i(t)$ denote the total strain of the i th truss element. It can be split into two parts: a purely elastic part and a plastic part, which is denoted by $\beta_i^0(t)$. The stress $\sigma_i(t)$ of the i th element is thus expressed as

$$\sigma_i(t) = E_i(\varepsilon_i(t) - \beta_i^0(t)). \quad (7.1)$$

In the following only *bilinear isotropic hardening plasticity* is considered as a relatively basic example, see Fig. 7.1, which requires for each element a single internal hardening variable $\Psi_i(t)$ called the *total plastic strain*. The evolution of $\Psi_i(t)$ in time is governed by the following simple strain hardening law:

$$\dot{\Psi}_i(t) := |\dot{\beta}_i(t)|. \quad (7.2)$$

The yield function $\Phi_i(\sigma_i, \Psi_i)$ is defined as

$$\Phi_i(\sigma_i, \Psi_i) := |\sigma_i| - \left(\sigma_i^* + \frac{\gamma_i E_i}{1 - \gamma_i} \Psi_i \right) \quad (7.3a)$$

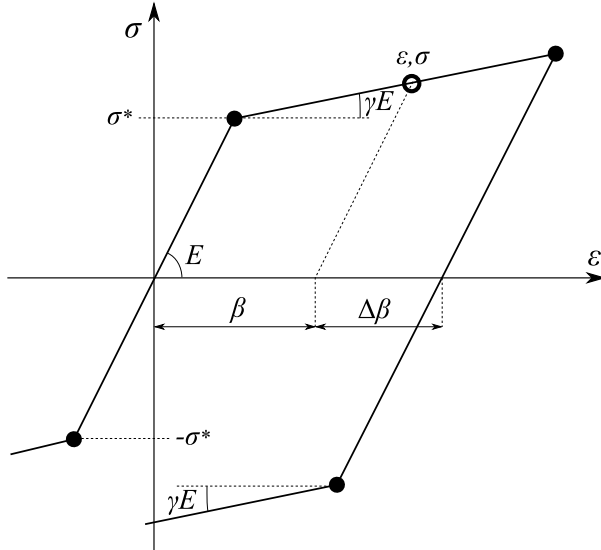


Figure 7.1. Constitutive relation for the bilinear isotropic hardening plasticity.

where σ_i^* , γ_i and E_i are respectively the initial plastic flow stress, the hardening coefficient and Young's modulus of the i th truss element, and the plastic modulus $\gamma_i E_i / (1 - \gamma_i)$ is determined based on a simple geometric analysis of Fig. 7.1. The range of admissible stresses is defined by the requirement that

$$\Phi_i(\sigma_i, \Psi_i) \leq 0. \quad (7.3b)$$

The plastic flow ($\dot{\beta}_i^0 \neq 0$) can take place only if the stress point is and persists on the yield surface defined by $\Phi_i = 0$. This is stated in the form of the following conditions of complementarity and persistency [283]:

$$\dot{\beta}_i^0(t)\Phi_i(t) = 0, \quad (7.4a)$$

$$\dot{\beta}_i^0(t)\dot{\Phi}_i(t) = 0, \quad (7.4b)$$

where

$$\Phi_i(t) := \Phi_i(\sigma_i(t), \Psi_i(t)). \quad (7.5)$$

The yield function is used to define the set Y_t of indices of truss elements that are instantaneously plastic at time t ,

$$(i \in Y_t) \equiv (\Phi_i(t) = 0 \quad \text{and} \quad \dot{\Phi}_i(t) = 0). \quad (7.6)$$

Other plasticity models can be relatively easily obtained by increasing the number of the internal variables [283].

7.2 The direct problem

7.2.1 Continuous formulation

According to the VDM, plastic strain $\beta_i^0(t)$ of the i th truss element is identified with its plastic distortion. The response of the structure depends on the external excitation loads as well as on the plastic distortions. Assuming zero initial conditions, similar as in (3.29) or (6.9), the strain response $\varepsilon_i(t)$ of the i th element of the elastoplastic truss is expressed as follows:

$$\varepsilon_i(t) = \varepsilon_i^L(t) + \sum_j \int_0^t B_{ij}^{\kappa\kappa}(t - \tau) \beta_j^0(\tau) d\tau, \quad (7.7a)$$

where

$$\varepsilon_i^L(t) = \sum_k \int_0^t B_{ik}^{\kappa f}(t - \tau) f_k^0(\tau) d\tau, \quad (7.7b)$$

and $\varepsilon_i^L(t)$ is the strain response of the i th element in the corresponding purely linear structure, $f_k^0(t)$ is the external excitation load applied in the k th DOF, and $B_{ik}^{\kappa f}(t)$ and $B_{ij}^{\kappa\kappa}(t)$ collect the respective impulse response functions of the linear system. Equation (7.15a) seems to be linear at first, but it is not, and the obvious reason is that the plastic distortions $\beta_j^0(t)$ are nonlinearly dependent on the excitations $f_k^0(t)$: only the excitations can be treated as independent input variables, while the plastic distortions have to be updated according to the assumed material model.

Equation (7.7a) is a version of the first basic equation of the VDM, (3.1). The counterpart to the second crucial equation of the VDM, (3.3), is obtained by comparing two following expressions for the stress rate $\dot{\sigma}_i(t)$ of instantaneously plastic elements, $i \in Y_t$:

1. The first expression is obtained by a differentiation of (7.1) with respect to time,

$$\dot{\sigma}_i(t) = E_i(\dot{\varepsilon}_i(t) - \dot{\beta}_i^0(t)), \quad (7.8)$$

and it is valid for all truss elements.

2. The second expression is obtained by noticing that the stresses of instantaneously plastic elements persist on the yield surface, which is expressed in (7.6) as

$$\frac{\partial}{\partial t} \Phi_i(t) = 0. \quad (7.9)$$

Substitution of the yield function (7.3a) and an explicit differentiation leads to

$$\begin{aligned} \dot{\sigma}_i(t) \operatorname{sign} \sigma_i(t) &= \frac{\gamma_i E_i}{1 - \gamma_i} \dot{\Psi}_i(t) \\ &= \frac{\gamma_i E_i}{1 - \gamma_i} |\dot{\beta}_i^0(t)|, \end{aligned} \quad (7.10)$$

where the second equality follows from the hardening law (7.2). It is noted that the stress direction must be the same as the direction of the plastic flow,

$$\operatorname{sign} \sigma_i(t) = \operatorname{sign} \dot{\beta}_i^0(t), \quad (7.11)$$

which is multiplied side by side with (7.10) to obtain

$$\dot{\sigma}_i(t) = \frac{\gamma_i E_i}{1 - \gamma_i} \dot{\beta}_i^0(t), \quad (7.12)$$

which is valid only if $i \in Y_t$, that is for elements instantaneously plastic at time t .

Comparison of (7.8) and (7.12) yields the following evolution rule for the plastic distortions of instantaneously plastic elements, $i \in Y_t$:

$$\dot{\beta}_i^0(t) = (1 - \gamma_i)\dot{\varepsilon}_i(t), \quad (7.13)$$

which is intuitively clear also from a purely geometric consideration of Fig. 7.1. Notice that the plastic distortions of instantaneously elastic elements remain constant due to (7.4), that is $\dot{\beta}_i^0(t) = 0$ if either $\Phi_i(t) = 0$ or $\dot{\Phi}_i(t) = 0$. Thus, by taking additionally into account the hardening law (7.2), the following rule can be formed to describe the evolution of the plastic distortions and total plastic strains:

$$\dot{\beta}_i^0(t) = (1 - \gamma_i)\dot{\varepsilon}_i(t)\mathbb{I}_{i \in Y_t}, \quad (7.14a)$$

$$\dot{\Psi}_i(t) = |\dot{\beta}_i^0(t)|, \quad (7.14b)$$

where $\mathbb{I}_{i \in Y_t}$ is the indicator function (2.64), the set Y_t of instantaneously plastic elements is determined based on the total plastic strain $\Psi_i(t)$ as defined in (7.6), and the strain rate $\dot{\varepsilon}_i(t)$ is obtained by differentiating (7.7a),

$$\begin{aligned} \dot{\varepsilon}_i(t) &= \dot{\varepsilon}^L(t) + \sum_j B_{ij}(0)\beta_j^0(t) + \sum_j \int_0^t \dot{B}_{ij}(t-\tau)\beta_j^0(\tau) d\tau \\ &= \dot{\varepsilon}^L(t) + \sum_j \int_0^t \dot{B}_{ij}(t-\tau)\beta_j^0(\tau) d\tau, \end{aligned} \quad (7.14c)$$

where the second equality follows from the fact that the strain does not change stepwise and thus $B_{ij}(0) = 0$, see (2.6). Equations (7.14a) express the current rate $\dot{\beta}_i^0(t)$ of plastic distortions in terms of their past values $\beta_i^0(\tau)$, $\tau \leq t$, and form thus an integro-differential equation, which is a specific form of the general equation of the VDM (3.4) and a counterpart to its other specific forms such as (3.28) or (5.6b). However, unlike them, (7.14a) is nonlinear due to the presence of the indicator function and the definition of Y_t . Theoretically, (7.14) could be integrated numerically to obtain the plastic distortions, which would be then substituted into (7.7a) to obtain the response.

7.2.2 Discrete-time setting

In practice, the response of the linear structure $\varepsilon_i^L(t)$ is known in discrete time steps every Δt , and the numerical solution for the elastoplastic structure has

to be advanced in the same discrete time steps. The procedure described below is a version of the classical return-mapping algorithm [283], whose standard implementation requires in each time step an iteration with respect to structural response. Here, application of the VDM in the form of (7.15a) allows such an iteration to be avoided.

Basically, a numerical integration scheme could be applied to (7.14) in order to obtain a set of stepping equations, which would explicitly describe the evolution of the plastic distortions in successive time steps. However, the indicator function in (7.14a) makes the plastic flow $\dot{\beta}_i^0(t)$ of the i th element discontinuous at the time instances, when the element enters or leaves the plastic regime. Such a discontinuity seriously undermines the approximation accuracy of numerical integration schemes. Thus, a derivative-free formulation is used here: the update rule for the plastic distortions in the discrete-time setting is obtained by an analysis of the stresses of the instantaneously plastic elements instead of their stress rates.

7.2.2.1 Response of the elastoplastic structure

The discrete strain response of the elastoplastic structure is expressed in the following discrete form of (7.7a):

$$\varepsilon_i(t) = \varepsilon_i^L(t) + \sum_j \sum_{\tau=0}^t D_{ij}^{\kappa\kappa}(t-\tau) \beta_j^0(\tau), \quad (7.15a)$$

where

$$\varepsilon_i^L(t) = \sum_k \sum_{\tau=0}^t D_{ik}^{\kappa f}(t-\tau) f_k^0(\tau), \quad (7.15b)$$

while $D_{ik}^{\kappa f}(t)$ and $D_{ij}^{\kappa\kappa}(t)$ are the discrete counterparts of the continuous impulse response functions $B_{ik}^{\kappa f}(t)$ and $B_{ij}^{\kappa\kappa}(t)$.

7.2.2.2 The update rule for plastic distortions

The backward Euler integration scheme is applied only to the hardening law (7.14b). This is unavoidable despite the discontinuity of $\dot{\beta}_i^0(t)$, because the hardening law is originally defined in (7.2) using a time derivative. The following discrete-time counterpart is obtained:

$$\Psi_i(t) := \Psi_i(t - \Delta t) + |\Delta \beta_i^0(t)|, \quad (7.16)$$

where $\Delta\beta_i(t)$ denotes the increment of the plastic strain,

$$\Delta\beta_i^0(t) := \beta_i^0(t) - \beta_i^0(t - \Delta t). \quad (7.17)$$

The update rule for these increments is obtained in the following analysis of the stresses of instantaneously plastic elements. The continuous evolution rule (7.14a) is not directly integrated for the reasons discussed above.

Trial elastic step. As in the classical return-mapping algorithm [283], the plastic distortion increments $\Delta\beta_i^0(t)$ are determined in each time step t by freezing temporarily the plastic flow and performing a purely elastic step, which yields the *trial strain* $\varepsilon_i^{\text{tr}}(t)$, *trial stress* $\sigma_i^{\text{tr}}(t)$ and *trial yield function* $\Phi_i^{\text{tr}}(t)$.

The trial step is performed by assuming that

$$\begin{aligned} \beta_i^{0\text{tr}}(t) &:= \beta_i^0(t - \Delta t), \\ \Psi_i^{\text{tr}}(t) &:= \Psi_i(t - \Delta t). \end{aligned} \quad (7.18)$$

Together with (7.15a), it yields the following formula for the trial strain:

$$\begin{aligned} \varepsilon_i^{\text{tr}}(t) &:= \varepsilon_i^L(t) + \sum_j \sum_{\tau=0}^{t-\Delta t} D_{ij}^{\kappa\kappa}(t-\tau) \beta_j^0(\tau) + \sum_j D_{ij}^{\kappa\kappa}(0) \beta_j^{0\text{tr}}(t) \\ &= \varepsilon_i^L(t) + \sum_j \sum_{\tau=0}^{t-\Delta t} D_{ij}^{\kappa\kappa}(t-\tau) \beta_j^0(\tau) + \sum_j D_{ij}^{\kappa\kappa}(0) \beta_j^0(t - \Delta t). \end{aligned} \quad (7.19)$$

By analogy to (7.1), the trial stress is obtained as

$$\begin{aligned} \sigma_i^{\text{tr}}(t) &:= E_i (\varepsilon_i^{\text{tr}}(t) - \beta_i^{0\text{tr}}(t)) \\ &= E_i (\varepsilon_i^{\text{tr}}(t) - \beta_i^0(t - \Delta t)). \end{aligned} \quad (7.20)$$

The corresponding trial yield function is given by

$$\begin{aligned} \Phi_i^{\text{tr}}(t) &:= \Phi_i(\sigma_i^{\text{tr}}(t), \Psi_i^{\text{tr}}(t)) \\ &= |\sigma_i^{\text{tr}}(t)| - \left(\sigma_i^* + \frac{\gamma_i E_i}{1 - \gamma_i} \Psi_i(t - \Delta t) \right). \end{aligned} \quad (7.21)$$

Notice that all trial values are fictitious and do not coincide with the actual values, unless the actual step is indeed purely elastic for all elements.

Actual strain, yield function and stress. According to (7.15a) and (7.19), the actual strain can be expressed in terms of the trial strain and plastic distortion increments as

$$\varepsilon_i(t) = \varepsilon_i^{\text{tr}}(t) + \sum_j D_{ij}^{\kappa\kappa}(0) \Delta\beta_j^0(t). \quad (7.22)$$

Similarly, (7.21) and (7.16) can be used to express the actual yield function in terms of the trial yield function and plastic distortion increment,

$$\Phi_i(t) = \Phi_i^{\text{tr}}(t) + |\sigma_i(t)| - |\sigma_i^{\text{tr}}(t)| - \frac{\gamma_i E_i}{1 - \gamma_i} |\Delta\beta_i^0(t)|. \quad (7.23)$$

In Subsection 7.2.1, the continuous evolution rule (7.14a) for plastic distortions is obtained by comparing two formulas for stress rates of instantaneously plastic elements. Here, a similar analysis is followed, but the stresses are analyzed instead of the stress rates. Given the trial stress, the actual stress $\sigma_i(t)$ of the i th instantaneously plastic element at time t can be expressed in two different ways:

1. Equation (7.1) yields,

$$\begin{aligned} \sigma_i(t) &= E_i \left(\varepsilon_i^{\text{tr}}(t) + \sum_j D_{ij}^{\kappa\kappa}(0) \Delta\beta_j^0(t) - \beta_i^0(t) \right) \\ &= E_i \left(\varepsilon_i^{\text{tr}}(t) + \sum_j D_{ij}^{\kappa\kappa}(0) \Delta\beta_j^0(t) - \beta_i^0(t - \Delta t) - \Delta\beta_i^0(t) \right) \quad (7.24) \\ &= \sigma_i^{\text{tr}}(t) + E_i \sum_j (D_{ij}^{\kappa\kappa}(0) - \delta_{ij}) \Delta\beta_j^0(t), \end{aligned}$$

where the three equalities follow respectively from (7.22), (7.17) and (7.20), and δ_{ij} is the Kronecker delta.

2. The stress of an instantaneously plastic element, $i \in Y_t$, must reside on the yield surface, $\Phi_i(t) = 0$, which is substituted in the left-hand side of (7.23) to obtain the following formula:

$$|\sigma_i(t)| = -\Phi_i^{\text{tr}}(t) + |\sigma_i^{\text{tr}}(t)| + \frac{\gamma_i E_i}{1 - \gamma_i} |\Delta\beta_i^0(t)|. \quad (7.25)$$

The actual stress, the trial stress and the plastic flow of an instantaneously plastic element are all of the same sign [283],

$$\text{sign } \sigma_i(t) = \text{sign } \sigma_i^{\text{tr}}(t) = \text{sign } \Delta\beta_i^0(t). \quad (7.26)$$

Equation (7.25) is multiplied by sign $\sigma_i(t)$, which due to (7.26) leads to

$$\sigma_i(t) = -\Phi_i^{\text{tr}}(t) \text{sign } \sigma_i^{\text{tr}}(t) + \sigma_i^{\text{tr}}(t) + \frac{\gamma_i E_i}{1 - \gamma_i} \Delta\beta_i^0(t) \quad (7.27)$$

Actual increments of plastic distortions. Equations (7.24) and (7.27) are combined together to yield the following equation:

$$E_i \sum_{j \in Y_t} \left(D_{ij}^{\kappa\kappa}(0) - \frac{\delta_{ij}}{1 - \gamma_i} \right) \Delta\beta_j^0(t) = -\Phi_i^{\text{tr}}(t) \text{sign } \sigma_i^{\text{tr}}(t), \quad (7.28)$$

which is valid only for instantaneously plastic elements, that is for $i \in Y_t$. Collected for all such elements, (7.28) constitutes a system of linear equations with the increments $\Delta\beta_i(t)$ of the plastic distortions in the role of the unknowns. Notice that the elements of the system matrix in (7.28) are constant and independent of the current state of the structure; they can be thus precomputed for all elements to obtain the full matrix and facilitate the simulation. In each time step, the rows and columns can be then simply selected according to the set Y_t of the instantaneously plastic elements. If in each time step only a limited number of elements are instantaneously plastic, the system (7.28) is small in dimensions and computationally inexpensive. The set Y_t is updated in each time step by verifying the yield condition (7.3b) and the stress compliance condition (7.26).

7.2.2.3 Scheme of computations

In the discrete-time setting, the direct problem is solved time step by time step, that is for $t = 0, \Delta t, \dots, T$. The initial conditions are usually assumed to be zero,

$$\varepsilon_i(0) = 0, \quad \beta_i^0(0) = 0, \quad \Psi_i(0) = 0, \quad Y_0 = \emptyset. \quad (7.29)$$

In each successive time step $t = \Delta t, \dots, T$, the following computations are necessary:

1. Trial strains, stresses and yield functions by (7.19), (7.20) and (7.21).
2. Temporary assumption of $Y_t := Y_{t-\Delta t}$.
3. Plastic distortion increments $\Delta\beta_i^0(t)$ by (7.28).
4. The corresponding strains and stresses by (7.15a) and (7.1).
5. For all elements, verification of the yield condition (7.3b) and its compliance with the assumed set Y_t of instantaneously plastic elements. Verification for $i \in Y_t$ of the stress compliance condition (7.26). If required,

the set Y_t is accordingly updated and the computations are repeated back from point 3 above.

6. Plastic strain increments and total plastic strains by (7.17) and (7.16).

Notice that no iteration with respect to the state variables is required, which is a characteristic feature of the presented approach. Points 3–5 are repeated only if the set Y_t needs to be updated in the current time step, which happens only when an elastic element enters the plastic regime or an instantaneously plastic element is unloaded; the proper set is then usually found after just a single update.

7.3 The inverse problem

Depending on the availability of the material model and on the number of the available sensors, the three following general cases are possible:

Strongly overdetermined problem. The number of sensors is not smaller than the total number of the potentially excited DOFs and yielding elements. In practice, this is possible only in the case of a very limited number of excited DOFs and a very localized plastic flow zone; an a priori information about the location of excitations and damages is thus required. The approach described in Section 6.2, or in Chapter 2 for overdetermined linear systems, is applicable with the external excitation loads $\mathbf{f}^0(t)$ and the plastic distortions $\beta^0(t)$ treated together as independent unknowns. Knowledge of the material model is not required.

Overdetermined problem. The number of sensors is not smaller than the number of potentially excited DOFs. The unique time-history of the excitation can be identified using a dedicated approach, such as the one presented below. The approach from Chapter 2 is not applicable, since the system is not linear.

Underdetermined problem. Fewer sensors than potentially excited DOFs. In general, the gradient-based optimization approach presented below identifies a nonunique excitation, which is observationally indistinguishable from the actual excitation. Tikhonov regularization or other problem-specific conditions such as the nonnegativity requirement can be used to additionally constrain the solution space.

Notice that the problem can happen to be singular and effectively underdetermined even with sufficiently many sensors, which is then due to specific topology of the structure and placement of the excitations and sensors.

The first approach amounts to an inverse linear problem that has been discussed in Chapter 2 and in Section 6.2. In the following, it is thus assumed that the model of the elastoplasticity is known in advance, so that only excitations $\mathbf{f}^0(t)$ are treated as independent unknowns. In such a case, both the direct and the inverse problems are nonlinear and require dedicated approaches. The discrete-time setting is used as more accurate due to reasons discussed in the previous section.

7.3.1 Objective function

The inverse problem of identification of unknown excitations is formulated here in the form of the problem of minimization of the mean square discrepancy between the measured response $\boldsymbol{\varepsilon}^M(t)$ and the modeled response $\boldsymbol{\varepsilon}(t)$. The following objective function is thus minimized:

$$F(\mathbf{f}^0) := \frac{1}{2} \sum_{t=0}^T \|\boldsymbol{\varepsilon}^M(t) - \boldsymbol{\varepsilon}(t)\|^2 + \frac{1}{2}\delta \|\mathbf{T}\mathbf{f}^0\|^2, \quad (7.30)$$

which is similar to (2.69), but allows the response $\boldsymbol{\varepsilon}(t)$ to be nonlinearly dependent on the excitation $\mathbf{f}^0(t)$ via (7.15a). The vector \mathbf{f} (without the time argument t) collects together the excitation loads for all time steps and in all potentially excited DOFs. The summation extends over all the time steps t in the considered time interval $[0, T]$.

The second term in (7.30) implements the Tikhonov regularization. The regularization parameter $\delta \geq 0$ may be assigned a specific numerical value for example by means of the L-curve technique [130, 135]. Notice that other techniques might be also used to constrain the solution space, such as the commonly used assumption of nonnegativity of the excitation loads, $\mathbf{f}(t) \geq \mathbf{0}$.

7.3.2 First order sensitivity analysis

The direct differentiation method can be used for first order sensitivity analysis of (7.30) and (7.28). Computed the gradient, the objective function can be minimized with any general-purpose gradient-based optimization algorithm. The derivatives of the objective function take the following form:

$$\frac{\partial F(\mathbf{f}^0)}{\partial f_i^0(t)} = \frac{1}{2}\delta \frac{\partial \|\mathbf{T}\mathbf{f}^0\|^2}{\partial f_i^0(t)} - \sum_j \sum_{\tau=t}^T (\varepsilon_j^M(\tau) - \varepsilon_j(\tau)) \frac{\partial \varepsilon_j(\tau)}{\partial f_i^0(t)}. \quad (7.31)$$

The first term in (7.31) can be computed in a straightforward way. The derivative of the response in the second term is nonvanishing for $t \leq \tau$ and can be then expressed by differentiating (7.15a) as

$$\frac{\partial \varepsilon_j(\tau)}{\partial f_i^0(t)} = D_{ji}^{\kappa f}(\tau - t) + \sum_{\zeta=t}^{\tau} \sum_k D_{jk}^{\kappa\kappa}(\tau - \zeta) \frac{\partial \beta_k^0(\zeta)}{\partial f_i^0(t)}, \quad (7.32)$$

which involves derivatives of the plastic distortions that can be expressed using their increments, see (7.17),

$$\frac{\partial \beta_k^0(\tau)}{\partial f_i^0(t)} = \sum_{\zeta=t}^{\tau} \frac{\partial \Delta \beta_k^0(\zeta)}{\partial f_i^0(t)}. \quad (7.33)$$

Derivatives of the increments can be computed (for ζ from t to τ) by solving the differentiated (7.28):

$$E_j \sum_{k \in Y_t} \left(D_{jk}^{\kappa\kappa}(0) - \frac{\delta_{jk}}{1 - \gamma_j} \right) \frac{\partial \Delta \beta_k^0(\zeta)}{\partial f_i^0(t)} = -\frac{\partial \Phi_j^{\text{tr}}(\zeta)}{\partial f_i^0(t)} \text{sign } \sigma_j^{\text{tr}}(\zeta), \quad (7.34)$$

where the right-hand side is given by

$$\frac{\partial \Phi_j^{\text{tr}}(\zeta)}{\partial f_i^0(t)} \text{sign } \sigma_j^{\text{tr}}(\zeta) = \frac{\partial \sigma_j^{\text{tr}}(\zeta)}{\partial f_i^0(t)} - \frac{\gamma_j E_j}{1 - \gamma_j} \mathbb{I}_{\zeta=t} \frac{\partial \Psi_j(\zeta - \Delta t)}{\partial f_i^0(t)} \text{sign } \sigma_j^{\text{tr}}(\zeta). \quad (7.35)$$

To use (7.35), the derivatives of the total plastic strain and of the trial stress are necessary. The latter are computed by (7.16) as

$$\frac{\partial \Psi_j(\tau - \Delta t)}{\partial f_i^0(t)} = \sum_{\zeta=t}^{\tau - \Delta t} \frac{\partial \Delta \beta_j^0(\zeta)}{\partial f_i^0(t)} \text{sign } \Delta \beta_j^0(\zeta), \quad (7.36)$$

while the former, by (7.19), (7.20) and (7.15b), are

$$\begin{aligned} \frac{\partial \sigma_j^{\text{tr}}(\tau)}{\partial f_i^0(t)} &= E_j D_{ji}^{\kappa f}(\tau - t) + E_j \sum_k \sum_{\zeta=t}^{\tau - \Delta t} D_{jk}^{\kappa\kappa}(\tau - \zeta) \frac{\partial \beta_k^0(\zeta)}{\partial f_i^0(t)} \\ &\quad + E_j \sum_k (D_{jk}^{\kappa\kappa}(0) - \delta_{jk}) \frac{\partial \beta_k^0(\tau - \Delta t)}{\partial f_i^0(t)}, \end{aligned} \quad (7.37)$$

where δ_{jk} denotes the Kronecker delta.

7.3.3 Approximate second order sensitivity analysis

The direct differentiation method is used in the previous section to obtain the gradient of the objective function. As a by-product, the Jacobian (7.32) of the response is computed. Since the optimization problem is basically a least-squares minimization problem, the Jacobian can be used for an approximate second order sensitivity analysis in a Gauss–Newton or Levenberg–Marquardt type optimization [137].

The second derivative of the objective function (7.30), as obtained via a direct differentiation,

$$\begin{aligned} \frac{\partial^2 F(\mathbf{f}^0)}{\partial f_i^0(t_1) \partial f_j^0(t_2)} &= \frac{1}{2} \delta \frac{\partial^2 \|\mathbf{T}\mathbf{f}^0\|^2}{\partial f_i^0(t_1) \partial f_j^0(t_2)} \\ &- \sum_k \sum_{\substack{\tau= \\ \max(t_1, t_2)}}^T (\varepsilon_k^M(\tau) - \varepsilon_k(\tau)) \frac{\partial^2 \varepsilon_k(\tau)}{\partial f_i^0(t_1) \partial f_j^0(t_2)} \\ &+ \sum_k \sum_{\substack{\tau= \\ \max(t_1, t_2)}}^T \frac{\partial \varepsilon_k(\tau)}{\partial f_i^0(t_1)} \frac{\partial \varepsilon_k(\tau)}{\partial f_j^0(t_2)}, \end{aligned} \quad (7.38)$$

involves the second derivatives of the response $\varepsilon_k(\tau)$, which are computationally costly to obtain. The crucial idea behind the Gauss–Newton optimization algorithm relies on the observation that the second derivatives are multiplied by response residuals and on an assumption that near the minimum the residuals are small enough to be approximated by zero,

$$\varepsilon_k^M(\tau) - \varepsilon_k(\tau) \approx 0. \quad (7.39)$$

As a result, the following approximation to the second derivative of the objective function is obtained:

$$\frac{\partial^2 F(\mathbf{f}^0)}{\partial f_i^0(t_1) \partial f_j^0(t_2)} \approx \frac{1}{2} \delta \frac{\partial^2 \|\mathbf{T}\mathbf{f}^0\|^2}{\partial f_i^0(t_1) \partial f_j^0(t_2)} + \sum_k \sum_{\substack{\tau= \\ \max(t_1, t_2)}}^T \frac{\partial \varepsilon_k(\tau)}{\partial f_i^0(t_1)} \frac{\partial \varepsilon_k(\tau)}{\partial f_j^0(t_2)}, \quad (7.40)$$

which involves only the first derivatives of the response, that is the Jacobi matrix of the response vector.

The Gauss–Newton optimization algorithm uses (7.40) to compute an approximation to the Hessian of the objective function, while the Levenberg–

Marquardt algorithm additionally modifies the approximated Hessian by adding a scaled identity matrix,

$$\frac{\partial^2 F(\mathbf{f}^0)}{\partial f_i^0(t_1) \partial f_j^0(t_2)} + \lambda \delta_{ij} \delta_{t_1 t_2}, \quad (7.41)$$

where $\delta_{..}$ is the Kronecker delta. In both cases, the approximated Hessian is used with the standard Newton update rule. Thus, the scaling coefficient $\lambda > 0$ in (7.41) is in fact a weighing factor that allows a smooth transition between the steepest descent and quasi-Newton character of the optimization steps.

7.4 Numerical example

7.4.1 The structure

The same modeled 3D truss structure is used as in Section 2.6, see Fig. 2.2. All of the material parameters are the same; however, the bilinear isotropic hardening plasticity is considered for all elements. The yield stress $\sigma^* = 250$ MPa, which is typical for steel, and the hardening coefficient $\gamma = 0.01$.

As in Chapter 2, unknown excitation loads can occur only vertically in each of the twelve upper nodes of the structure. Up to eleven strain sensors can be placed in between these nodes for identification purposes.

7.4.2 Actual excitation and the response

The to-be-identified excitation models a constant moving load of 1000 N, distributed in the form of two vertical loads, each of 500 N and 0.5 m apart from each other, which move from right to left along the whole modeled structure, see the top left plots in Figs. 7.4 and 7.5. The same load is used in Section 2.6; however, here the structure is assumed to have elastoplastic characteristics.

As a result of the modeled excitation, the yield stress level is exceeded in six structural elements, which are the upper horizontal elements no. 2, 3, 4, 5, 6 and 7. Their simulated exact responses are plotted in Fig. 7.2 using the solid lines; the dashed lines mark the responses of the other five upper horizontal elements that respond within the linear range. A comparison with the corresponding responses computed in the linear case (Fig. 2.8) reveals a significant effect of the elastoplastic material model: plastic distortions of the yielding elements are approximately an order of magnitude larger than their linear elastic strains. The effect of the bilinear material model, including properly modeled

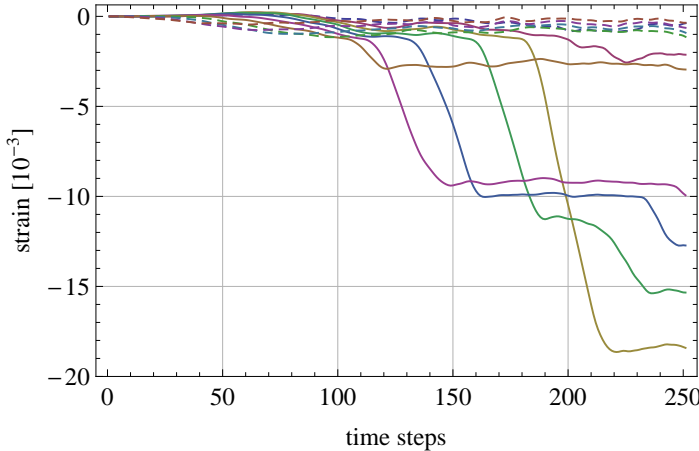


Figure 7.2. Simulated exact responses of the eleven strain sensors to the assumed actual excitation. Solid lines mark the responses of the elements that exceed the plastic yield level (elements no. 2 to 7); dashed lines mark the responses that occur within the linear range of the instrumented elements (elements no. 1, 8, 9, 10 and 11). The plot can be compared with the purely linear response shown in Fig. 2.8.

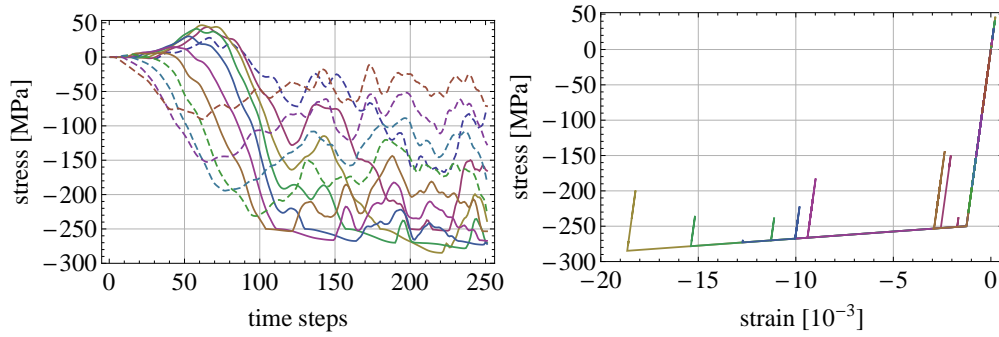


Figure 7.3. The eleven upper horizontal elements are equipped with strain sensors: (left) simulated stresses (solid lines mark the responses of the elements that exceed the yield stress level); (right) stress-strain curves. The unloading effect is clearly visible.

unloading, is also clearly visible in Fig. 7.3, which plots the stresses in the eleven considered elements (left) as well as their stress-strain curves (right).

For identification purposes, in order to simulate the measurement error, all the responses plotted in Fig. 7.2 are contaminated with a numerically generated independent Gaussian noise at the same level as in Section 2.6.

7.4.3 Sensor placement

Section 2.5 formulates three quantitative optimality criteria to assess and compare sensor placements. However, their formulation relies on the linearity of the identification procedure; they are not useful in the case of a structure featuring significant elastoplastic effects, because in such a structure plastic distortions can be significantly larger than linear elastic strains. The problem of optimum sensor placement for the purpose of load identification seems in this case to be open and unexplored. Here, three cases are tested:

1. First, full instrumentation is considered, that is all the eleven upper horizontal elements are equipped with strain sensors, $\pi_1 := \{1, 2, \dots, 11\}$.
2. Then, strain sensors are placed only in the elements that respond within their linear range, $\pi_2 := \{1, 8, 9, 10, 11\}$.
3. Finally, only plastically yielding elements are equipped with strain sensors, $\pi_3 := \{2, 3, 4, 5, 6, 7\}$.

The respective numbers of sensors (eleven, five and six) should be compared with the total number of the unknown loads (twelve). The identification problem is in all the cases nonunique, and the solution space is additionally constrained by the requirement of nonnegativity of the excitation, which is implemented using a quadratic penalty function. This is the same approach as used in the linear case in Section 2.6.

7.4.4 Identification results

The actual excitation is depicted in top left plots in Figs. 7.4 and 7.5 in the form of a density plot and a 3D plot respectively. The other three plots in these figures show the results of identification with the three considered sensor placements, π_1 , π_2 and π_3 .

Similarly as in the linear case considered in Section 2.6, the qualitative features of the actual excitation are identified properly, including its location and characteristic movement. In quantitative terms, the magnitude is identified only approximately, which should not be surprising, taking into account the simulated measurement noise and the insufficient number of sensors for a unique identification. The result for the placement π_1 is significantly more accurate, as compared to the other two tested placements. The obvious reason is the larger number of sensors used in this case. Notice also that even though the placement π_2 uses fewer sensors than π_3 , it provides more accurate results, which emphasizes the need for quantitative sensor placement criteria.

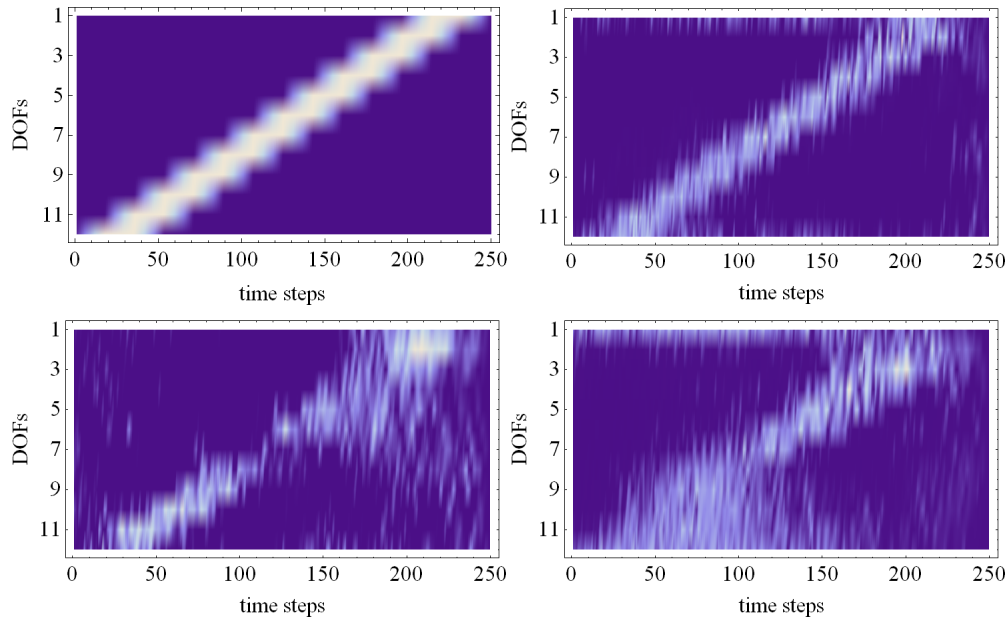


Figure 7.4. Identification results, density plots: (top left) actual excitation; (top right) sensor placement π_1 (all the sensors 1 to 11); (bottom left) sensor placement π_2 (linearly responding elements, no. 1, 8, 9, 10, 11); (bottom right) sensor placement π_3 (plastically yielding elements, no. 2 to 7).

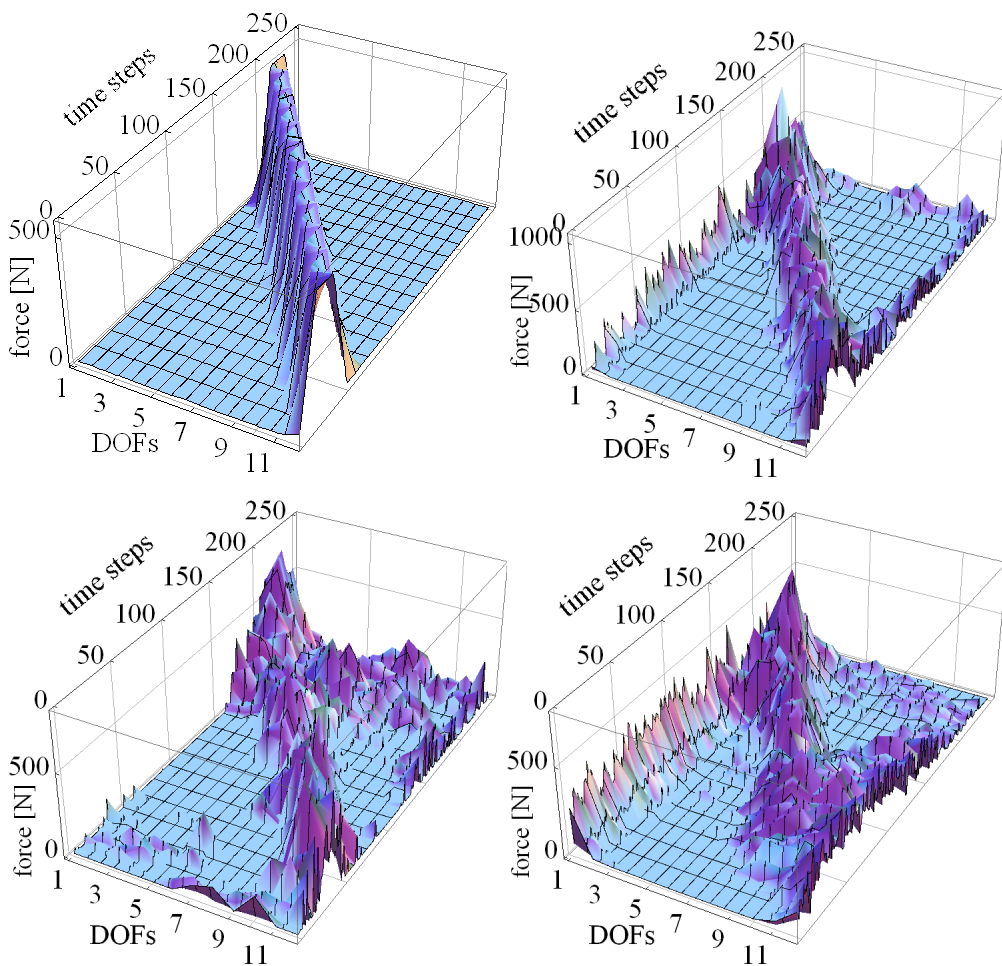


Figure 7.5. Identification results, 3D plots: (top left) actual excitation; (top right) sensor placement π_1 (all the sensors 1 to 11); (bottom left) sensor placement π_2 (linearly responding elements, no. 1, 8, 9, 10, 11); (bottom right) sensor placement π_3 (plastically yielding elements, no. 2 to 7).

8

Conclusions

This book is devoted to the inverse problem of identification of dynamic loads and its applications in global structural health monitoring. Load identification is a type II inverse problem (input identification), while most of the problems in global SHM are either of type I (system identification) and thus intrinsically different, or of a mixed type I+II and thus nonstandard. Besides developing new methods for load identification itself (in Chapters 2 and 7), this book demonstrates that, thanks to the general framework of the virtual distortion method (Chapter 3), many of the problems in SHM can be represented in the form of load identification problems and solved using the respective procedures (Chapters 4 to 6).

Some of the developed methods are new and constitute a new contribution to the field; Section 8.1 summarizes these that in author's opinion are most important. The research area is large and seems to be relatively unexplored. There are thus many challenging problems that are still open and currently under investigation; some of the most important or interesting are listed in Section 8.2.

8.1 Original results

Certain results reported in this book are original and constitute a new contribution to the field. The most important of them can be summarized as follows:

- Chapter 2 focuses the discussion of the inverse problem of dynamic load identification on the practically important, but apparently neglected in literature, case of a limited instrumentation (insufficient for a unique solution). In particular, the chapter (a) introduces the notions of the reconstructible and unreconstructible excitation spaces and (b) discusses various techniques for augmenting the missing information (unreconstructible space). In this context, the chapter (c) proposes three complementary quantitative measures for assessing different sensor placements.

- Chapter 3 reformulates the virtual distortion method using a continuous-time notation, which (a) emphasizes the mathematical structure of the reanalysis problem and its nonparametric character, as well as (b) reinterprets it in the form of the inverse problem of load identification.
- In Chapters 4 to 6, various nonstandard SHM problems are represented and solved in terms of a load identification problem using the unifying continuous-time setting of the VDM formulated in Chapter 3. This includes:
 - A nonparametric identification methodology proposed and experimentally verified in Chapter 4. Even though it allows parametrized modifications, damages or inelastic impacts to be identified, parametric numerical modeling of the involved structure is avoided by using purely experimental impulse response data.
 - The substructure isolation method described in Chapter 5, which allows crucial substructures to be virtually isolated from all the external influences. As a result, any global SHM method can be directly applied at the substructural level for the purpose of local monitoring. This is unlike all other substructuring approaches, as they are based on simultaneous identification of local damages and interface forces, which is a nonstandard problem that has to be solved using specifically tailored, dedicated SHM methods.
 - Two approaches to the problem of simultaneous identification of excitation loads and structural damages developed in Chapter 6. The considered problem is essentially an inverse problem of a mixed type I+II that is typically solved in cumbersome two-stage alternating optimization procedures. The proposed approaches reduce the problem to a pure inverse problem of either type I or type II, which allows it to be solved using typical approaches and avoid the alternation. Moreover, reduction to type II inverse problem (load identification) allows damages of unknown types to be identified via the recovered stress-strain relationships, so that damage type does not need to be assumed a priori.
- Chapter 7 develops a method for load identification in elastoplastic structures (with bilinear isotropic hardening), including a sensitivity analysis of the response. This is one of a very few researches devoted to indirect dynamic load identification in nonlinear structures.

8.2 Further research

The presented research on load identification and its application in SHM has generated a number of interesting methods and promising results. Many challenging problems and research directions seem to be still open and are currently under investigation. In particular

- The load identification methodology presented in Chapter 2 is based on the singular value decomposition, which is conceptually clear and appealing, but computationally a time-demanding procedure (time complexity is larger than linear with respect to the number of time steps). More effective versions of the approach and of the proposed optimality measures for sensor placement should be developed.
- Chapter 2 proposes three optimality measures for sensor placement with respect to the problem of load identification. Their relation to other sensor placement measures that have different aims (damage identification, characterization of structural response, control, etc.) and that are more widely researched in literature should be investigated.
- Resolution of nonparametric identification methods presented in Chapter 4 depends on measurement error level and structural topology, which are both reflected in the collected experimental impulse responses. Development of methods for assessing the ultimate resolution based on the experimental data seems to be an interesting research problem. In this context, other objective functions should be tested, especially those based on modal characteristics such as natural frequencies, damping ratios, etc.
- The substructure isolation methodology presented in Chapter 5 should be streamlined for applications in online isolation and local monitoring¹. Experimental verification in field tests are a natural further step towards practical applications.
- Section 6.2 reduces the mixed-type problem of simultaneous identification of excitations and damages to a pure type II inverse problem (load identification), which requires a relatively large number of sensors to ensure a unique solution. The methodology should be further developed to be applicable in the case of a limited instrumentation, which requires investigation and testing of various methods for augmenting the missing information, including those discussed in Chapter 2.

¹This task has been accomplished during the review process of this book, see [284].

- The direct differentiation method of sensitivity analysis in Chapter 7 requires a double loop with respect to time steps and is thus computationally extensive. Faster methods should be developed that attain a linear time complexity with respect to the number of time steps.
- The sensor placement criteria proposed in Section 2.5 rely on the linearity of the involved structure. Quantitative criteria for sensor placement for load identification in elastoplastic structures should be developed.

A

Linear inverse problem

Most identification problems analyzed in this book are either inverse linear problems or, thanks to the virtual distortion method, can be reduced to or represented in the form of such problems. Therefore, this appendix reviews the basics of the linear inverse problem with the focus on the often neglected aspects that turn out to be important in load identification: posedness, conditioning and regularization. No new results are introduced here. The appendix is partly based on two insightful introductions by Hansen [110, 111] and a very elegant functional analytic framework for linear integral equations by Kress [112, 285]. Basic notions from functional analysis are used here; for the background and proofs, see [112] or any other textbook on functional analysis, for example the classic texts of Rudin [286] or Kolmogorov and Fomin [287].

Load identification is originally a continuous-time problem. Hence, after a brief discussion of the fundamental general notions of a linear operator, posedness, conditioning and regularization, the appendix reviews integral linear inverse problems and then proceeds to their numerically treatable discretized counterparts, which in practice arise naturally due to the discrete nature of the measurement process. Such an outline allows also a clear exposition of the important notions of posedness, conditioning and compactness, which become relatively obfuscated in the process of discretization.

A.1 Linear operators

This section recalls briefly the definition of a linear operator and the few most basic related theorems and definitions.

Definition A.1 (linear operator). *An operator $\mathcal{A}: \mathbf{X} \rightarrow \mathbf{Y}$ from a linear space \mathbf{X} into a linear space \mathbf{Y} is called linear if and only if*

$$\mathcal{A}(\alpha x + \beta y) = \alpha \mathcal{A}x + \beta \mathcal{A}y \quad (\text{A.1})$$

for all $\alpha, \beta \in \mathbb{C}$ and all $x, y \in \mathbf{X}$.

A.1.1 Boundedness, continuity and compactness

One of the most important notions is the notion of a bounded operator and of the norm of an operator:

Definition A.2 (bounded operator, norm of an operator). *A linear operator $\mathcal{A}: \mathbf{X} \rightarrow \mathbf{Y}$ from a normed space \mathbf{X} into a normed space \mathbf{Y} is called bounded, if and only if there exists a positive number γ such that*

$$\|\mathcal{A}x\| \leq \gamma \|x\| \quad (\text{A.2})$$

for all $x \in \mathbf{X}$. Each such number γ is called a bound for \mathcal{A} . The smallest bound is called the norm of the operator \mathcal{A} ,

$$\|\mathcal{A}\| := \sup_{x \neq 0} \frac{\|\mathcal{A}x\|}{\|x\|}. \quad (\text{A.3})$$

In finite dimensional spaces, each linear operator is bounded and continuous. This is not true for linear operators defined on infinite dimensional spaces: such a linear operator can be noncontinuous and unbounded. The following theorem states the equivalence between continuity and boundedness of a linear operator:

Theorem A.3 (Kress [112]). *A linear operator is continuous if and only if it is bounded.*

A linear operator is thus either continuous and bounded, or noncontinuous and unbounded. A typical example of a noncontinuous linear operator is the operator of differentiation.

Example A.4 (a noncontinuous linear operator). *Let \mathcal{A} be the integration operator. The inverse operator \mathcal{A}^{-1} is the differentiation,*

$$(\mathcal{A}x)(t) := \int_0^t x(\tau) d\tau, \quad (\mathcal{A}^{-1}x)(t) = \frac{d}{dt}x(t), \quad (\text{A.4})$$

where $t \in [0, T]$. Both operators are linear, and \mathcal{A} is continuous and bounded. However, the inverse \mathcal{A}^{-1} is neither continuous nor bounded, as illustrated by the following example. Let

$$x_n(t) = \frac{\sin nt}{\sqrt{n}}, \quad \mathcal{A}^{-1}x_n(t) = \sqrt{n} \cos nt. \quad (\text{A.5})$$

In the maximum norm (A.9), as well as in the mean square norm (A.11), there is $\|x_n\| \rightarrow 0$ and thus $x_n \rightarrow 0$. On the other hand, $\|\mathcal{A}^{-1}x_n\| \sim \sqrt{n} \rightarrow \infty$. Consequently, \mathcal{A}^{-1} is noncontinuous and unbounded in both norms.

Of central importance in the theory of linear inverse problems, and so also in load identification, is the notion of a compact operator. Many equivalent definitions exist; a simple one can be stated as follows:

Definition A.5. *A linear operator $\mathcal{A}: \mathbf{X} \rightarrow \mathbf{Y}$ is called compact if and only if the image $(\mathcal{A}x_n)$ of each bounded sequence (x_n) in \mathbf{X} contains a convergent subsequence in \mathbf{Y} .*

Compact operators are important, because many of their properties are similar to that of finite dimensional linear operators. For example,

Theorem A.6 (Kress [112]). *Compact linear operators are bounded and continuous.*

It can be shown that the identity operator $\mathcal{I}: \mathbf{X} \rightarrow \mathbf{X}$ is compact if and only if \mathbf{X} is finite dimensional [112]. By considering the composition of a compact operator and its inverse, $\mathcal{A} \circ \mathcal{A}^{-1} = \mathcal{I}$, the following theorem can be proved, which justifies the classification of linear integral equations into first and second order, see Section A.2:

Theorem A.7 (Kress [112]). *A compact operator cannot have a bounded inverse unless its range is of a finite dimension.*

A.1.2 Ill-posedness, ill-conditioning and regularization

In 1902, Hadamard [288] has postulated three common sense properties that problems in mathematical physics should possess:

1. *Existence* of a solution.
2. *Uniqueness* of the solution.
3. *Continuity* of the solution with respect to the input.

Problems that did not possess all three properties had initially not been considered to be physically meaningful and consequently called *ill-posed* or *improperly posed*. Nevertheless, soon thereafter it has turned out that many important physical problems are ill-posed, such as the inverse heat transfer problem [289]. The most insightful of Hadamard's properties seems to be the third, which is meant to ensure stability of the solution in case the input data to the problem contains measurement or numerical errors. Nonexistence or nonuniqueness of solution can be often dealt with by imposing or removing physically nonsignificant restrictions on the input and output spaces. However, continuity of the solution depends also on the related norms, which are usually physically motivated and cannot be modified.

Ill-posedness is exemplified by the well-known Riemann–Lebesgue lemma, which basically states that Fourier coefficients of an absolutely integrable function f tend to zero,

$$\int_0^{2\pi} f(t) e^{-int} dt \xrightarrow{n \rightarrow \infty} 0. \quad (\text{A.6})$$

The Riemann–Lebesgue lemma implies that any integral transform of the form

$$(\mathcal{A}x)(t) := \int_0^{2\pi} A(t, \tau) x(\tau) d\tau, \quad t \in [0, 2\pi], \quad (\text{A.7})$$

where A is continuous, tends to damp high frequency components in $x(t)$: the higher the frequency, the more damped it is. In other words, an arbitrarily large perturbation of $x(t)$, if it is of frequency high enough, corresponds to an arbitrarily small perturbation of the transform $(\mathcal{A}x)(t)$. Consequently, the problem of finding a function given its transform (A.7) is noncontinuous and unbounded, and thus ill-posed. In particular, if $A(t, \tau) := \mathbb{I}_{\tau < t}$, here \mathbb{I} is the indicator function (2.64), then (A.7) corresponds to integration and the noncontinuity of the inverse problem is demonstrated in Example A.4. Note that continuity can be achieved by restricting the originally infinite dimensional input space to a finite dimensional space of functions with a limited frequency range, and even then the function can remain extremely sensitive to perturbations of its transform, if the considered frequency range is large enough.

The above example shows that, even for well-posed problems, an additional measure of sensitivity of the output with respect to the input data is necessary. Such a measure is called *conditioning*. The *condition number* of a linear problem $x \mapsto \mathcal{A}x$ is defined in terms of the relative sensitivity as, see (A.3),

$$\kappa_{\mathcal{A}} := \sup_{x, \Delta x \neq 0} \frac{\frac{\|\mathcal{A}(x + \Delta x) - \mathcal{A}x\|}{\|\mathcal{A}x\|}}{\frac{\|\Delta x\|}{\|x\|}} = \frac{\sup_{x \neq 0} \frac{\|\mathcal{A}x\|}{\|x\|}}{\inf_{x \neq 0} \frac{\|\mathcal{A}x\|}{\|x\|}} = \frac{\|\mathcal{A}\|}{\|\mathcal{A}^{-1}\|}. \quad (\text{A.8})$$

For nonlinear problems the condition number has to be computed locally. For a noncontinuous (and thus ill-posed) problem, the condition number is infinite.

Significantly ill-conditioned problems are usually difficult to solve directly, as even small measurement or numerical errors in the input data can significantly perturb the computed output. Though, such problems can be solved approximately by employing one of the numerous *regularization* techniques. These techniques effectively reduce the sensitivity by using additional information about

the expected output, such as smoothness, nonnegativity, etc. Regularization techniques for finite-dimensional linear systems are briefly reviewed in Subsection A.3.2.

A.2 Infinite dimensional integral problems

All the functions considered in this book are implicitly assumed to belong to one of the two following typical function spaces:

1. The Banach space $C[a, b]$ of continuous real-valued functions x defined on the interval $[a, b]$ and furnished with the *maximum norm*

$$\|x\|_\infty := \max_{t \in [a, b]} |x(t)|. \quad (\text{A.9})$$

2. The Hilbert space $L^2[a, b]$ (of the equivalence classes) of measurable and Lebesgue square-integrable real-valued functions x defined on the interval $[a, b]$ and furnished with the scalar product

$$\langle x, y \rangle := \int_a^b x(t)y(t) dt \quad (\text{A.10})$$

and the related *mean square norm*

$$\|x\|_2 := \sqrt{\langle x, x \rangle} = \left(\int_a^b x^2(t) dt \right)^{1/2}. \quad (\text{A.11})$$

Note that the space $L^2[a, b]$ is the complement of the space $C[a, b]$ with respect to the mean square norm.

These functional spaces, when required for load identification with more than just a single sensor or actuator, can be straightforwardly extended to the corresponding spaces of finite dimensional vectors of functions, $(C[a, b])^n$ or $(L^2[a, b])^n$, $n \in \mathbb{N}$. For example, the scalar product and the norm are defined in the latter space as

$$\langle \mathbf{x}, \mathbf{y} \rangle := \sum_{i=1}^n \langle x_i, y_i \rangle, \quad \|\mathbf{x}\|_2 := \sqrt{\langle \mathbf{x}, \mathbf{x} \rangle}. \quad (\text{A.12})$$

A.2.1 Linear integral operator

Linear integral operator is a special case of linear operator.

Definition A.8 (linear integral operator). *An operator $\mathcal{A}: \mathbf{X} \rightarrow \mathbf{Y}$ from a normed function space \mathbf{X} into a normed function space \mathbf{Y} , defined as*

$$(\mathcal{A}x)(t) := \int_a^b A(t, \tau)x(\tau) d\tau, \quad (\text{A.13})$$

where $A: \mathbb{R} \times \mathbb{R} \rightarrow \mathbb{R}$, is called a linear integral operator with the kernel $A(t, \tau)$.

Definition A.9 (Volterra operator). *A linear integral operator \mathcal{A} with a variable upper limit of integration,*

$$(\mathcal{A}x)(t) := \int_a^t A(t, \tau)x(\tau) d\tau, \quad (\text{A.14})$$

is called a Volterra integral operator.

Properties of an integral operator depend on its kernel. In load identification, the impulse response functions are either continuous or have a single discontinuity at time $t = 0$. If the system is time-invariant¹, the related kernels usually depend on the difference of the arguments, $A(t, \tau) = A(t - \tau)$, and are called difference kernels. According to the following definition, they can be classified as weakly singular:

Definition A.10 (weakly singular kernel, Kress [112]). *A kernel A , which for all $t, \tau \in [a, b]$, $t \neq \tau$, is continuous and, for certain positive constants M and $\alpha \in (-1, 0]$, satisfies*

$$|A(t, \tau)| \leq M|t - \tau|^\alpha, \quad (\text{A.15})$$

is called a weakly singular kernel.

Linear integral operators with continuous or weakly singular kernels are often called *smoothing* operators, as they tend to damp higher frequency components of their arguments. This is exemplified by the Riemann–Lebesgue lemma, see the example in Subsection A.1.2. Due to the following result, it is also in perfect agreement with Theorem A.7:

Theorem A.11 (Kress [112]). *An integral operator (A.13) with a continuous or weakly singular kernel is compact.*

¹A linear system is time-invariant, if actuators and sensors do not move.

An $m \times n$ matrix of integral operators $\mathcal{A}_{ij} : \mathbf{X} \rightarrow \mathbf{Y}$ is called a *matrix integral operator* $\mathbf{A} : \mathbf{X}^n \rightarrow \mathbf{Y}^m$. It is used to deal with the spaces of vectors of functions, like $(C[a, b])^n$ or $(L^2[a, b])^n$, and systems of linear integral equations. A matrix operator is obviously compact if and only if its component operators are all compact.

A.2.2 Linear integral equations

Linear operator equations of the following forms:

$$y = \mathcal{A}x, \quad y = (\mathcal{I} - \mathcal{A})x, \quad (\text{A.16})$$

where \mathcal{I} is the identity operator, are called to be respectively of the first and second kind. If \mathcal{A} is an integral operator, the equations, depending on the form of the integration limits, are called Fredholm or Volterra integral equations.

Definition A.12 (Fredholm integral equations). *Integral equations of the form*

$$y(t) = \int_a^b A(t, \tau)x(\tau) d\tau, \quad (\text{A.17a})$$

$$y(t) = x(t) - \int_a^b A(t, \tau)x(\tau) d\tau, \quad (\text{A.17b})$$

and called Fredholm integral equations of the first and second kind, respectively.

Fredholm equations in which $A(t, \tau) = 0$ for $t > \tau$ are called Volterra equations and expressed using variable upper integration limits. Such equations have special properties, see, e.g., Theorem A.16, and are thus usually treated separately from Fredholm equations.

Definition A.13 (Volterra integral equations). *Integral equations of the form*

$$y(t) = \int_a^t A(t, \tau)x(\tau) d\tau, \quad (\text{A.18a})$$

$$y(t) = x(t) - \int_a^t A(t, \tau)x(\tau) d\tau, \quad (\text{A.18b})$$

are called Volterra integral equations of the first and second kind, respectively.

The most common problem in load identification is the deconvolution problem of the structural response with respect to the impulse response function. In case of a displacement or velocity response, it is formulated in the form of the following integral equation:

$$y(t) = \int_a^t A(t-\tau)x(\tau) d\tau, \quad (\text{A.19})$$

which is a special case of Volterra integral equation of the first kind with a *difference kernel*. In view of Theorems A.7 and A.11, such a problem is ill-posed.

Note that systems of linear integral equations of the first and second kind can be conveniently stated using matrix integral operators as

$$\mathbf{y} = \mathcal{A}\mathbf{x}, \quad \mathbf{y} = (\mathcal{I} - \mathcal{A})\mathbf{x}. \quad (\text{A.20})$$

A.2.2.1 Equations of the first kind

Due to Theorems A.7 and A.11, the inverse of an integral operator with a continuous or weakly singular kernel cannot be bounded and, due to Theorem A.3, continuous. Therefore, the problem of solving a linear integral equation of the first kind does not have the third property postulated by Hadamard and is thus ill-posed, see the example in Subsection A.1.2. This can be illustrated using the singular value expansion of the related operator. A general formulation for a compact operator in a normed space can be found in [112]. Here, the expansion is defined in terms of the kernel of an integral operator.

Definition A.14 (singular value expansion [111, 112, 285]). *For any weakly singular kernel $A(t, \tau)$ defined on $[a, b]^2$, its singular value expansion (SVE) is defined in terms of the singular values μ_i and the corresponding left and right singular functions $u_i(t)$ and $v_i(\tau)$ as follows:*

$$A(t, \tau) = \sum_{i=1}^{\infty} \mu_i u_i(t) v_i(\tau), \quad (\text{A.21})$$

where the singular values are positive and ordered nonincreasing, $\mu_1 \geq \mu_2 \geq \dots > 0$, with no point of accumulation except possibly 0, and the singular functions form two orthonormal sequences (u_i) and (v_i) , that is

$$\langle u_i, u_j \rangle = \langle v_i, v_j \rangle = \delta_{ij}, \quad (\text{A.22})$$

where δ_{ij} denotes the Kronecker delta.

Since the left and right singular vectors are respectively orthonormal, the following relation holds:

$$(\mathcal{A}v_i)(t) = \mu_i u_i(t), \quad (\text{A.23})$$

where the integral operator \mathcal{A} is defined as in (A.13).

It is possible that there are only finitely many singular values. The series in (A.21) degenerates then into a finite sum and $A(t, \tau)$ is called a *degenerate kernel*. A nondegenerate weakly singular kernel has infinitely many singular values, which decay to zero. It can be proved that the more smooth is the kernel, the quicker the decay rate [111, 112]: if the kernel is n times continuously differentiable, then $\mu_i = O(i^{-n-1/2})$, and if it is infinitely many times differentiable, the decay rate is even exponential, $\mu_i = O(r^{-i})$ for a certain constant $r > 1$.

The right singular functions $v_i(t)$ form an orthonormal basis of the orthogonal complement of the null space of \mathcal{A} in the space $L^2[a, b]$, while $u_i(t)$ form an orthonormal basis of the range of \mathcal{A} . These bases resemble spectral bases, because the smaller the singular value, the more high-frequency components (oscillations or zero-crossings) have the corresponding singular functions [111, 126]. As a result, Equation (A.25) can be interpreted to be a generalization of the Riemann–Lebesgue lemma (A.6): the larger i , the more oscillatory $v_i(t)$ and the smaller its image $\mu_i u_i(t)$.

Consider an integral equation of the first kind (A.17a). A substitution of the SVE (A.21) yields

$$y(t) = \sum_{i=1}^{\infty} \mu_i \langle y, v_i \rangle u_i(t) \quad (\text{A.24})$$

with the scalar product defined as in (A.10). From (A.24) it can be deduced that the equation of the first kind (A.17a) has a particular solution

$$x(t) = \sum_{i=1}^{\infty} \frac{\langle y, u_i \rangle}{\mu_i} v_i(t) \quad (\text{A.25})$$

if and only if $y(t)$ belongs to the range of \mathcal{A} , which is spanned by the left singular functions $u_i(t)$, and

$$\|x\|^2 = \sum_{i=1}^{\infty} \frac{|\langle y, u_i \rangle|^2}{\mu_i^2} < \infty, \quad (\text{A.26})$$

which is called the *Picard condition* and means that $|\langle y, u_i \rangle|$ must decay to zero faster than the singular values μ_i .

The ill-posed nature of (A.17a) is clearly demonstrated in (A.25). If the input data (function $y(t)$) is perturbed within the range of \mathcal{A} to become

$$y_{\epsilon,i}(t) := y(t) + \epsilon u_i(t), \quad (\text{A.27})$$

then the perturbation propagates to the solution, which is then given by

$$x_{\epsilon,i}(t) = x(t) + \frac{\epsilon}{\mu_i} v_i(t). \quad (\text{A.28})$$

Consequently, even for an arbitrarily small perturbation factor ϵ , the amplification ratio of the perturbation,

$$\frac{\|x - x_{\epsilon,i}\|}{\|y - y_{\epsilon,i}\|} = \frac{1}{\mu_i}, \quad (\text{A.29})$$

can be made arbitrarily large, because the singular values tend to zero. The successive singular functions are increasingly more oscillatory [111, 126] and thus the higher is the frequency of the perturbation, the larger its amplification ratio. As a result, low-frequency components of the solution $x(t)$ are usually relatively easy to compute, while high-frequency components are more likely to be masked by measurement or numerical errors in the input data y and harder to extract.

A.2.2.2 Equations of the second kind

A systematic approach to integral equations of the second kind is offered by the Riesz [290] and Fredholm theories [291]. Originally, they have been formulated for integral equations in the space $C[a, b]$, but generalizations to other linear spaces and general operator equations are straightforward. This subsection, based on Kress [112, 285], reviews only the most important result of the Riesz theory. It emphasizes the main difference between Fredholm integral equations of the second and of the first kinds: if a solution $x(t)$ to (A.17b) exists, then it depends continuously on the input $y(t)$. Thus, if the first two of Hadamard's properties are satisfied for such an equation, then also the third property is satisfied.

The Riesz theory yields the following result:

Theorem A.15 (Kress [112]). *Let \mathbf{X} be a normed space and $\mathcal{A}: \mathbf{X} \rightarrow \mathbf{X}$ a compact linear operator. Consider the homogenous equation*

$$0 = x - \mathcal{A}x \quad (\text{A.30a})$$

and the inhomogeneous equation

$$y = x - \mathcal{A}x, \quad (\text{A.30b})$$

where $y \in \mathbf{X}$. Then either²

The homogeneous equation (A.30a) has only the trivial solution $x = 0$, and the inhomogeneous (A.30b) has a unique solution $x \in \mathbf{X}$ that depends continuously on y .

or

The homogeneous (A.30a) has a finite number m of linearly independent solutions x_1, \dots, x_m , and the inhomogeneous (A.30b) is either unsolvable or its general solution is a sum of a particular solution \tilde{x} and an arbitrary linear combination of x_1, \dots, x_m .

Thanks to the Riesz theory, the existence and uniqueness of the solution to an inhomogeneous equation of the second kind, (A.30b), can be verified via an examination of the stationary points of the related compact operator or, in other words, the Riesz theory states the equivalence between the surjectivity and injectivity of the related operator $\mathcal{I} - \mathcal{A}$.

Theorem A.15 is used in [112] to prove the fact that each Volterra integral equation of the second kind with a continuous kernel has a unique solution in $C[a, b]$. By using a compact matrix integral operator in place of \mathcal{A} , the same result can be applied to systems of integral equations and to prove the following theorem, which is formulated in terms of systems of Volterra integral equations:

Theorem A.16. *The system of Volterra integral equations of the second kind*

$$\mathbf{y} = \mathbf{x} - \mathcal{A}\mathbf{x}, \quad (\text{A.31})$$

where \mathcal{A} is an $n \times n$ matrix integral operator whose all component operators \mathcal{A}_{ij} are continuous, has for each $\mathbf{y} \in (C[a, b])^n$ a unique solution $\mathbf{x} \in (C[a, b])^n$.

Theorem A.16 ascertains the existence and uniqueness of the solution to several load identification problems analyzed throughout this book.

If the homogeneous equation (A.30a) has nontrivial solutions, Theorem A.15 offers no clues as to whether the inhomogeneous equation (A.30b) for a given inhomogeneity $y(t)$ is solvable or not. The answer is provided by the Fredholm theory, whose main result (the Fredholm alternative) basically states that in

²In functional analytic terms: the operator $\mathcal{I} - \mathcal{A}$ either is injective and surjective and has a bounded and thus continuous inverse or its null space has nonzero finite dimension and its range is a proper subspace of \mathbf{X} .

such a case the inhomogeneous equation is solvable if and only if the inhomogeneity is orthogonal to all solutions of the adjoint homogeneous equation [112].

The Fredholm alternative uses the notion of an adjoint operator. In case of an integral operator \mathcal{A} with a continuous or weakly singular kernel or a matrix integral operator composed of such operators, the adjoint operator is denoted by \mathcal{A}^* and it is also a (matrix) integral operator that is defined as

$$(\mathcal{A}x)(t) = \int_a^b A(t, \tau)x(\tau) d\tau, \quad (\mathcal{A}^*x)(t) = \int_a^b A(\tau, t)x(\tau) d\tau, \quad (\text{A.32})$$

for an integral operator \mathcal{A} or

$$(\mathbf{Ax})(t) = \int_a^b \mathbf{A}(t, \tau)\mathbf{x}(\tau) d\tau, \quad (\mathbf{A}^*\mathbf{x})(t) = \int_a^b \mathbf{A}^T(\tau, t)\mathbf{x}(\tau) d\tau. \quad (\text{A.33})$$

for a matrix integral operator \mathbf{A} .

A.2.3 Discretization

In practice, it rarely happens that an analytical solution to an integral equation can be found. The reason is twofold: first, unless the equation is extremely simplistic, an analytical solution rarely exists at all, and second, in applications the data is often given in an already discretized numerical form (sequences of measured or simulated values), which enforces discretization of the solution.

A properly discretized version of an integral equation can be expected to inherit some of the conditioning and posedness properties of the original problem. Equations of the first kind are ill-posed, and physical problems expressed in the form of such equations have thus a seemingly contradictory property: the finer the discretization, the worse is the conditioning of the resulting finite dimensional problem and so the less accurate is the computed solution. As a result, numerical regularization is a must. In load identification problems, regularization usually has to be also applied to the discretized versions of equations of the second kind: even if well-posed, they are often significantly ill-conditioned and hence a subject to a similar numerical treatment as the ill-posed equations of the first kind.

A comprehensive discussion of the numerical methods for discretization and numerical solution of linear integral equations can be found in Delves and Mohamed [292]. Kress [112, Chapters 11–14, 17] offers a more theoretical treatment,

while Hansen [111, Chapter 3] provides a short practical overview. These references discuss a great variety of approaches, which however come usually in two general flavors: quadrature (or Nyström) methods and projection methods. Formulas based on kernel expansions, such as (A.25), are appealing and theoretically important, but usually impractical, because the SVE is rarely known in advance and it is rather the finite dimensional version of the equation that is used to approximate the SVE than the opposite [293].

A.2.3.1 Quadrature/Nyström methods

These methods are based on the following standard formula for numerical integration:

$$\int_a^b h(t) dt \approx \sum_{j=1}^N \alpha_j h(t_j), \quad (\text{A.34})$$

where $t_j \in [a, b]$ are the quadrature points and α_j are the quadrature weights. Different quadrature rules give rise to different versions of the method. If applied to the integrations in (A.17), it yields

$$y(t) = \sum_{j=1}^N \alpha_j A(t, t_j) \tilde{x}(t_j), \quad (\text{A.35a})$$

$$y(t) = \tilde{x}(t) - \sum_{j=1}^N \alpha_j A(t, t_j) \tilde{x}(t_j), \quad (\text{A.35b})$$

where the tilde is used to mark explicitly the fact that the computed solution $\tilde{x}(t)$ is only an approximation to the exact solution $x(t)$. Now, the *collocation* requirement is enforced and (A.35) are required to be exactly satisfied at the collocation points. If the same quadrature points are used for this purpose, the following equations are obtained:

$$y(t_i) \approx \sum_{j=1}^N \alpha_j A(t_i, t_j) \tilde{x}(t_j), \quad (\text{A.36a})$$

$$y(t_i) \approx \sum_{j=1}^N (\delta_{ij} - \alpha_j A(t_i, t_j)) \tilde{x}(t_j), \quad (\text{A.36b})$$

which can be collected for all $i = 1, 2, \dots, N$ to form the respective finite dimensional linear systems with the unknowns $\tilde{x}(t_i)$. The equation of the first kind

can be collocated at points different from the quadrature points, provided they are not fewer in number.

Notice that the quadrature method is very natural in case the kernel $A(t, \tau)$ and the response $y(t)$ are provided right from the beginning in the discretized form of a sequence of measured or simulated values sampled at points t_i . The approximate solution is given then in exactly the same discrete form, and a continuous version can be obtained by interpolation. Otherwise, if the kernel and the response are continuous and an equation of the second kind is considered, the continuous version can be computed by a rearranged (A.35b):

$$\tilde{x}(t) = y(t) + \sum_{j=1}^N \alpha_j A(t, t_j) \tilde{x}(t_j). \quad (\text{A.37})$$

A.2.3.2 Projection methods

The result of a quadrature method is an approximation of the exact solution sampled at the quadrature points, which has been computed by collocating the equation at the collocation points. In projection methods, the approximate solution is sought in a certain finite dimensional space,

$$x(t) \approx \tilde{x}(t) := \sum_{j=1}^N \alpha_j x_j(t), \quad (\text{A.38})$$

where $x_j(t)$ are its basis functions. The combination coefficients α_j are computed by projecting (A.17) onto another finite dimensional space spanned by the basis functions $y_i(t)$, $i = 1, 2, \dots, N$,

$$\langle y_i, y \rangle = \langle y_i, \int_a^b A(\cdot, \tau) x(\tau) d\tau \rangle, \quad (\text{A.39a})$$

$$\langle y_i, y \rangle = \langle y_i, x - \int_a^b A(\cdot, \tau) x(\tau) d\tau \rangle, \quad (\text{A.39b})$$

and substituting (A.38). It yields

$$\int_a^b y_i(t)y(t) dt = \sum_{j=1}^N \alpha_j \int_a^b \int_a^b y_i(t) A(t, \tau) x_j(\tau) d\tau dt, \quad (\text{A.40a})$$

$$\int_a^b y_i(t)y(t) dt = \sum_{j=1}^N \alpha_j \int_a^b y_i(t) \left(x_j(t) - \int_a^b y_i(t) A(t, \tau) x_j(\tau) d\tau \right) dt, \quad (\text{A.40b})$$

which for both kinds of equations is a linear finite dimensional system of N equations and N unknowns α_j . As in the case of quadrature methods, a larger number of basis functions $y_i(t)$ can be used, which will provide an overdetermined finite dimensional system.

Notice that there is an essential difference between the projection approach and the quadrature approach, unless the Dirac delta functions are used at the quadrature points in the role of the basis functions $x_j(t)$ and $y_i(t)$.

A.3 Finite dimensional discretized problems

Whatever discretization method is used, its ultimate result is always equivalent to a finite dimensional system of linear equations

$$\mathbf{Ax} = \mathbf{y}, \quad (\text{A.41})$$

where $\mathbf{x} \in \mathbb{R}^{N_2}$ and $\mathbf{y} \in \mathbb{R}^{N_1}$ are the vectors of coefficients that define the approximations to the exact solution $x(t)$ and the exact response $y(t)$, and $\mathbf{A} \in \mathbb{R}^{N_1 \times N_2}$ is the respective finite dimensional counterpart of the operator \mathcal{A} in the original integral equation. Notice that the explicit notational distinction between the equations of the first and the second kind is lost in the discretization process, even if certain characteristic features of the original equation are reflected in (A.41).

A.3.1 Solvability and conditioning

If the linear system (A.41) is not significantly ill-conditioned, existence and uniqueness of its solution can be discussed in the terms of its dimensions and rank or, in other words, in the terms of surjectivity and injectivity of the linear operator corresponding to the matrix \mathbf{A} . In general, four cases are possible:

1. *Bijection* ($N_1 = N_2 = \text{rank } \mathbf{A}$, that is full-rank square \mathbf{A}). The equation has a unique solution.
2. *Surjection, but not injection* ($N_1 = \text{rank } \mathbf{A} < N_2$). For each \mathbf{y} there exist infinitely many solutions, which can be expressed in the form of a sum of a particular solution and the null space of \mathbf{A} .

3. *Injection, but not surjection* ($N_2 = \text{rank } \mathbf{A} < N_1$). Depending on \mathbf{y} , there is either a unique solution (if \mathbf{y} is in the range of \mathbf{A}) or no solution at all.
4. *Neither injection, nor surjection* ($\text{rank } \mathbf{A} < \min(N_1, N_2)$). Depending on \mathbf{y} , there are either infinitely many solutions (if \mathbf{y} is in the range of \mathbf{A}) or no solutions at all.

In problems of load identification, the equation is almost always extremely ill-conditioned. As a result, the null space of \mathbf{A} can be understood as becoming fuzzy: there exist subspaces of \mathbb{R}^{N_2} , which belong to the null space effectively, even if not formally. Effective membership of the null space is thus gradual and depends on the decay rate of the singular values and on the assumed accuracy level of \mathbf{y} , which is limited by the floating point arithmetic used in computations and often also by the measurement noise³. It can be explained in terms of the singular value decomposition, which is the discrete counterpart of the singular value expansion used in Subsection A.2.2.1:

Definition A.17 (singular value decomposition [111, 128]). *Each matrix $\mathbf{A} \in \mathbb{R}^{N_1 \times N_2}$ can be essentially uniquely⁴ represented in the form of the following product:*

$$\mathbf{A} = \mathbf{U}\Sigma\mathbf{V}^T, \quad (\text{A.42})$$

where \mathbf{U} and \mathbf{V} are square unitary matrices of appropriate dimensions, $\mathbf{U}^T\mathbf{U} = \mathbf{I}_{N_1}$ and $\mathbf{V}^T\mathbf{V} = \mathbf{I}_{N_2}$, and Σ is a diagonal matrix with nonnegative elements on the diagonal. Columns of \mathbf{U} and \mathbf{V} are called the left and right singular vectors. The positive diagonal elements σ_i of Σ are called the singular values of \mathbf{A} and are ordered nonincreasingly, $\sigma_1 \geq \sigma_2 \geq \dots$

Equation (A.42) can be expanded in terms of its singular values as

$$\mathbf{A} = \sum_{i=1}^N \sigma_i \mathbf{u}_i \mathbf{v}_i^T, \quad (\text{A.43})$$

where $N \leq \min(N_1, N_2)$ is the total number of the singular values and \mathbf{u}_i and \mathbf{v}_i denote the i th left and right singular vector of \mathbf{A} . Notice the direct correspondence between (A.43) and (A.21); the only important difference is that the singular values σ_i are always finite in number, while μ_i can form an infinite sequence that decays to zero. The relation between the SVE and the SVD of the discretized problem is discussed in [293].

³This concept is used in Chapter 2 to introduce the notion of the space of loads that are unreconstructible under given noise level.

⁴That is uniquely up to factors ± 1 and permutation of the singular vectors.

The decay rate of the singular values conveys full information about conditioning of the equation. A substitution of (A.43) into (A.41) yields the following expansion of \mathbf{Ax} in terms of the left singular vectors \mathbf{u}_i ,

$$\sum_{i=1}^N \sigma_i (\mathbf{v}_i^T \mathbf{x}) \mathbf{u}_i = \mathbf{y}. \quad (\text{A.44})$$

If the actual vector \mathbf{y} belongs to the range of \mathbf{A} , which is spanned by all the \mathbf{u}_i 's, then (A.41) has the following particular solution:

$$\mathbf{x} = \sum_{i=1}^N \frac{\mathbf{u}_i^T \mathbf{y}}{\sigma_i} \mathbf{v}_i. \quad (\text{A.45})$$

Equation (A.45) clearly demonstrates that conditioning of (A.41) depends on the decay rate of the singular values σ_i . A similar analysis as in Subsection A.2.2.1 yields the perturbed solution

$$\mathbf{x}_{\epsilon,i} = \mathbf{x} + \frac{\epsilon}{\sigma_i} \mathbf{v}_i \quad (\text{A.46})$$

to the equation, in which the vector \mathbf{y} is perturbed within the range of \mathbf{A} ,

$$\mathbf{y}_{\epsilon,i} := \mathbf{y} + \epsilon \mathbf{u}_i. \quad (\text{A.47})$$

The perturbation propagates thus with the amplification factor of σ_i^{-1} . Consequently, the condition number defined in (A.8) equals the ratio of the maximum to the minimum singular value,

$$\kappa_{\mathbf{A}} = \frac{\sigma_1}{\sigma_N}, \quad (\text{A.48})$$

and in general, conditioning of the subspace spanned by the i th singular vector equals σ_1/σ_i . As a result, if the SVD of a highly ill-conditioned problem is computed using floating point arithmetic, small singular values tend to level off due to the finite machine precision. The subspaces spanned by the corresponding singular vectors belong effectively to the null space of \mathbf{A} (its “numerical null space”) and should be disregarded in the solution process, as they do not convey any meaningful information. This observation yields the following discrete version of the Picard condition (A.26), which is cited here from [111, 294]: *Let κ denote the level at which the computed singular values σ_i level off due to rounding errors. The discrete Picard condition is satisfied if, for all singular values*

larger than κ , the corresponding coefficients $|\mathbf{u}_i^T \mathbf{y}|$ decay on average faster than the σ_i . Notice that the discrete Picard condition is not meant to guarantee the finiteness of the norm of the solution, but rather to verify if the original Picard condition (A.26) seems to be satisfied for the continuous problem that has given rise to (A.41).

A.3.2 Numerical regularization

Load identification problems are typically expressed in the form of Volterra integral equations, and as such, they are significantly ill-conditioned unless the considered setup is extremely simplistic. Thus, even if the response vector \mathbf{y} used for identification of the load vector \mathbf{x} contains no measurement noise, the presence of rounding errors in the floating point arithmetic can destroy the accuracy of a naively computed result. To be meaningful, the solution has to be numerically regularized using a proper value of the regularization parameter.

A.3.2.1 Regularization methods

If (A.41) is significantly ill-conditioned, any solution computed in a naive way using standard solution techniques would be dominated by numerical noise and useless. Ill-conditioning of the problem must be then taken into account in the solution process, and this is done by a numerical regularization of the solution.

In general terms, regularization can be understood as a process of discarding or attenuating these components of the solution \mathbf{x} that are too strongly affected by the errors present in \mathbf{y} . In the terms of the SVD-based solution (A.45), regularization is equivalent to using a filtering function $\psi(\sigma)$,

$$\mathbf{x} = \sum_{i=1}^N \psi(\sigma_i) \frac{\mathbf{u}_i^T \mathbf{y}}{\sigma_i} \mathbf{v}_i, \quad (\text{A.49})$$

in order to attenuate the components of the sum that correspond to small singular values and are prone to errors due to excessive amplification by the unattenuated factor σ_i^{-1} .

A comprehensive overview of regularization methods for Toeplitz matrices that are discretized versions of integral convolution operators can be found in Hansen [109], see also [110, 111].

Direct regularization. The direct regularization methods are analogous to the standard direct solution methods in that they compute the regularized solution at once, in a noniterative way. The two most popular methods of direct

regularization are the truncated singular value decomposition and the Tikhonov regularization.

The TSVD is sometimes called also the spectral cutoff method, because it simply neglects all the components of the full SVD-based solution that correspond to the singular values below certain cutoff level α , that is

$$\psi_{\text{TSVD}}(\sigma) = \begin{cases} 1 & \text{if } \sigma \geq \alpha, \\ 0 & \text{otherwise.} \end{cases} \quad (\text{A.50})$$

Computation of the TSVD-regularized solution requires the SVD of the matrix \mathbf{A} to be already computed. This is a numerically costly operation, but needs to be performed only once: given the SVD, (A.49) can be computed at a low cost for different vectors \mathbf{y} .

The Tikhonov regularization method originates from the work of Tikhonov on ill-posed integral problems, see [130]. In terms of (A.49), it is defined by the following filtering function:

$$\psi_{\text{Tikhonov}}(\sigma) = \frac{\sigma^2}{\sigma^2 + \alpha^2}, \quad (\text{A.51})$$

where α is the regularization parameter. In comparison to the TSVD, (A.51) results in a smooth transition between undamped and damped components of the solution. A direct application of the formula requires performing the SVD; however, it might be shown that the solution regularized using (A.51) can be also found by minimization of the following objective function:

$$F(\mathbf{x}) := \|\mathbf{y} - \mathbf{Ax}\|^2 + \alpha^2 \|\mathbf{x}\|^2, \quad (\text{A.52a})$$

which is a weighted sum of the residual of the underlying problem (A.41) and the regularization term. Usually, the following more general form is used:

$$F(\mathbf{x}) := \|\mathbf{y} - \mathbf{Ax}\|^2 + \alpha^2 \|\mathbf{Tx}\|^2, \quad (\text{A.52b})$$

where the matrix \mathbf{T} expresses the desired regularity conditions. Besides the identity matrix, often the matrices of the first or second differences are used or their weighted sums. The solution satisfies the regularized counterpart of the normal equation,

$$(\mathbf{A}^T \mathbf{A} + \alpha^2 \mathbf{T}^T \mathbf{T}) \mathbf{x} = \mathbf{A}^T \mathbf{y}, \quad (\text{A.53})$$

which corresponds to the least-squares problem of minimizing the residuum to the augmented system

$$\begin{bmatrix} \mathbf{A} \\ \alpha \mathbf{T} \end{bmatrix} \mathbf{x} = \begin{bmatrix} \mathbf{y} \\ \mathbf{0} \end{bmatrix}. \quad (\text{A.54})$$

Iterative regularization. Formulation of the Tikhonov regularization in the form of a minimization problem of the objective function (A.52b) suggests an iterative approach to regularization, in which the regularized solution is retrieved step by step, in a series of computationally inexpensive iterations. Minimization of the quadratic objective function (A.52b) can be performed in such a way, but it has a disadvantage that if the regularization parameter α is changed, the full optimization process needs to be repeated from the beginning.

The conjugate gradient least squares [111, 128] method is probably the most commonly used iterative regularization scheme. In general, the CGLS is the conjugate gradient algorithm applied to solve the normal equation

$$\mathbf{A}^T \mathbf{A} \mathbf{x} = \mathbf{A}^T \mathbf{y}. \quad (\text{A.55})$$

The CGLS is based on the conjugate gradient iterations, hence it is quickly convergent and instead of a factorization of the matrix \mathbf{A} , it requires only two black-box procedures that compute matrix–vector products $\mathbf{A}\mathbf{x}$ and $\mathbf{A}^T\mathbf{x}$. It might be shown that in each successive iteration the method recovers components of the solution that are related with increasingly smaller singular values. The number of iterations plays thus the role of the regularization parameter, which is a very useful property: to obtain a less regularized solution, it is enough just to perform a few more inexpensive iteration steps. In terms of the filtering function, the transition between undamped and damped components is not abrupt (as in the TSVD) but rather gradual, see [109, 110],

$$\psi_{\text{CGLS}}(\sigma) \approx \begin{cases} 1 & \text{for large singular values,} \\ O(\sigma^2) & \text{for small singular values.} \end{cases} \quad (\text{A.56})$$

In the transition range ψ_{CGLS} can slightly exceed one.

A.3.2.2 Regularization parameter

In all regularization methods, the amount of regularization is governed by the regularization parameter α (cutoff level of singular values in the TSVD, Tikhonov weighing parameter, number of CGLS iterations, etc.). Proper choice of this parameter is crucial, so that the computed solution is neither underregularized nor overregularized. A large number of different methods can be used to select the parameter; two comprehensive reviews with numerical tests can be found in [131, 132], see also [111, Chapter 5].

The most popular method is probably the L-curve approach, see, e.g., [135]. It is a log-log scale plot of the norm of the regularization term $\|\mathbf{T}\mathbf{x}\|$ vs. the

norm of the residuum $\|\mathbf{y} - \mathbf{Ax}\|$ parametrized by the regularization parameter α , see an example in Fig. 6.4 (left). The L-curve has usually an L-shaped form and consists of two branches: the horizontal branch that corresponds to overregularized solutions (small regularization term, increasingly larger residuum) and the vertical branch that corresponds to underregularized solutions (small residuum, increasingly larger regularization term). The optimum value of the regularization parameter is assumed to correspond to the corner of the curve. Notice that this criterion requires the solution to be computed several times for a range of regularization parameters. This can be time-consuming, if direct regularization methods are used, but straightforward with most of the iterative methods including the CGLS, as each its iteration is computationally inexpensive and retrieves an increasingly less regularized solution.

Bibliography

1. L. Ambrozinski, T. Stepinski, P. Packo, and T. Uhl. Self-focusing lamb waves based on the decomposition of the time-reversal operator using time-frequency representation. *Mechanical Systems and Signal Processing*, 27:337–349, 2012.
2. P. C. Chang and S. C. Liu. Recent research in nondestructive evaluation of civil infrastructures. *Journal of Materials in Civil Engineering*, 15(3):298–304, 2003.
3. W. Ostachowicz, P. Kudela, P. Malinowski, and T. Wandowski. Damage localisation in plate-like structures based on pzt sensors. *Mechanical Systems and Signal Processing*, 23(6):1805–1829, 2009.
4. W. J. Staszewski. Structural health monitoring using guided ultrasonic waves. In J. Holnicki-Szulc and C. A. Mota Soares, editors, *Advances in Smart Technologies in Structural Engineering*, pages 117–162. Springer, 2003.
5. T. Wandowski, P. Kudela, P. Malinowski, and W. Ostachowicz. Lamb waves for damage localisation in panels. *Strain*, 47(5):449–457, 2011.
6. A. Źak, M. Radzieński, M. Krawczuk, and W. Ostachowicz. Damage detection strategies based on propagation of guided elastic waves. *Smart Materials and Structures*, 21(3):035024, 2012.
7. K. K. Nair, A. S. Kiremidjian, and K. H. Law. Time series-based damage detection and localization algorithm with application to the ASCE benchmark structure. *Journal of Sound and Vibration*, 291(1–2):349–368, March 2006.
8. S. Silva, M. Dias Júnior, and V. Lopes Jr. Structural health monitoring in smart structures through time series analysis. *Structural Health Monitoring*, 7(3):231–244, 2008.
9. M. I. Friswell. Damage identification using inverse methods. *Philosophical Transactions of the Royal Society A*, 365(1851):393–410, 2007.

10. G. Yan. *Structural damage identification methods based on generalized flexibility matrix and wavelet analysis*. PhD thesis, School of Civil Engineering, Harbin Institute of Technology, China, 2006.
11. E. P. Carden and P. Fanning. Vibration based condition monitoring: A review. *Structural Health Monitoring*, 3(4):355–377, 2004.
12. P. C. Chang, A. Flatau, and S. C. Liu. Review paper: Health monitoring of civil infrastructure. *Structural Health Monitoring*, 2(3):257–267, 2003.
13. K. Worden and J. M. Dulieu-Barton. An overview of intelligent fault detection in systems and structures. *Structural Health Monitoring*, 3(1):85–98, 2004.
14. P. Kołakowski. Structural health monitoring – a review with the emphasis on low-frequency methods. *Engineering Transactions*, 55(3):239–275, 2007.
15. S. W. Doebling, C. R. Farrar, and M. B. Prime. A summary review of vibration-based damage identification methods. *The Shock and Vibration Digest*, 30(2):91–105, March 1998.
16. S. W. Doebling, C. R. Farrar, M. B. Prime, and D. W. Shevitz. Damage identification and health monitoring of structural and mechanical systems from changes in their vibration characteristics: A literature review. Technical Report LA-13070-MS, Los Alamos National Laboratory, Los Alamos, N.M., 1996.
17. T. Uhl and K. Mendrok. Overview of modal model based damage detection methods. In *Proc. of the Int'l Conf. on Noise and Vibration Engineering (ISMA2004)*, pages 561–575, Leuven, Belgium, 20–22 September 2004.
18. Z. Wei, L. H. Yam, and L. Cheng. NARMAX model representation and its application to damage detection for multi-layer composites. *Composite Structures*, 68(1):109–117, April 2005.
19. M. I. Friswell and J. E. Mottershead. *Finite element model updating in structural dynamics*. Kluwer Academic Publishers, 1995.
20. J. E. Mottershead and M. I. Friswell. Model updating in structural dynamics: A survey. *Journal of Sound and Vibration*, 167(2):347–375, 1993.
21. A. Garstecki, A. Knitter-Piątkowska, Z. Pozorski, and K. Ziopaja. Damage detection using parameter dependent dynamic experiments and wavelet transformation. *Journal of Civil Engineering and Management*, 10(3):191–197, 2004.
22. H. Kim and H. Melhem. Damage detection of structures by wavelet analysis. *Engineering Structures*, 26(3):347–362, 2004.

23. Z. K. Peng and F. L. Chu. Application of the wavelet transform in machine condition monitoring and fault diagnostics: a review with bibliography. *Mechanical Systems and Signal Processing*, 18(2):199–221, 2004.
24. M. Rucka and K. Wilde. Application of continuous wavelet transform in vibration based damage detection method for beams and plates. *Journal of Sound and Vibration*, 297(3–5):536–550, 2006.
25. M. M. Reda Taha, A. Noureldin, J. L. Lucero, and T. J. Baca. Wavelet transform for structural health monitoring: A compendium of uses and features. *Structural Health Monitoring*, 5(3):267–295, 2006.
26. L. E. Mujica, J. Vehí, W. Staszewski, and K. Worden. Impact damage detection in aircraft composites using knowledge-based reasoning. *Structural Health Monitoring*, 7(3):215–230, 2008.
27. P. Kołakowski, M. Wikło, and J. Holnicki-Szulc. The virtual distortion method – a versatile reanalysis tool for structures and systems. *Structural and Multidisciplinary Optimization*, 36(3):217–234, 2008.
28. J. Holnicki-Szulc and J. Gierliński. *Structural Analysis, Design and Control by the Virtual Distortion Method*. John Wiley & Sons Ltd, Chichester, 1995.
29. G. Suwała and Ł. Jankowski. A model-free method for identification of mass modifications. *Structural Control and Health Monitoring*, 19(2):216–230, 2012.
30. G. Suwała and Ł. Jankowski. Model-free damage identification of skeletal structures. In *Proc. of the 5th European Workshop on Structural Health Monitoring (EWSHM 2010)*, pages 925–930, Sorrento, Italy, June 29 – July 2 2010.
31. MeroForm System USA. M12 system, component catalogue. <http://www.meroform.us/pdf/m12.pdf>, 2006. online, retrieved April 2011.
32. Ł. Jankowski. Off-line identification of dynamic loads. *Structural and Multidisciplinary Optimization*, 37(6):609–623, 2009.
33. Ł. Jankowski, K. Sekuła, B. Błachowski, M. Wikło, and J. Holnicki-Szulc. Dynamic load monitoring. In J. Holnicki-Szulc, editor, *Smart Technologies for Safety Engineering*, chapter 4, pages 105–151. John Wiley & Sons, Chichester, 2008.
34. Ł. Jankowski, M. Wikło, G. Suwała, and J. Holnicki-Szulc. Reconstruction of impact load on a roadway arch support [Identyfikacja obciążenia

- udarowego obudowy górniczej]. In *Innovative and safe mechanisation systems for mineral exploitation (KOMTECH 2006)*, Zakopane, Poland, 14–16 November 2006 (in Polish).
- 35. Ł. Jankowski, M. Wikło, and J. Holnicki-Szulc. Robust post-accident reconstruction of loading forces. *Key Engineering Materials*, 347:659–664, 2007.
 - 36. M. Wikło and Ł. Jankowski. A posteriori impact identification. In *Proc. of the 3rd European Workshop on Structural Health Monitoring (EWSHM 2006)*, pages 675–682, Granada, Spain, 5–6 July 2006.
 - 37. M. Wikło, Ł. Jankowski, and J. Holnicki. Impact load identification – forensic engineering. In *Proc. of the 2nd Int'l Conf. on Nonsmooth Non-convex Mechanics (NNMAE 2006)*, Thessaloniki, Greece, 7–8 July 2006.
 - 38. G. Suwała and Ł. Jankowski. Model-free identification of added mass. In *Proc. of the 8th World Congress on Structural and Multidisciplinary Optimization (WCSMO-8)*, Lisbon, Portugal, June 1–5 2009.
 - 39. Q. Zhang, Ł. Jankowski, and Z. Duan. Simultaneous identification of moving mass and structural damage. In *Proceedings of the 8th World Congress on Structural and Multidisciplinary Optimization (WCSMO-8)*, Lisbon, Portugal, July 2009.
 - 40. Q. Zhang, Ł. Jankowski, and Z. Duan. Simultaneous identification of moving masses and structural damage. *Structural and Multidisciplinary Optimization*, 42(6):907–922, 2010.
 - 41. G. Suwała and Ł. Jankowski. A model-less method impact mass identification. In *Proc. of the 4th European Workshop on Structural Health Monitoring (EWSHM 2008)*, pages 365–373, Kraków, Poland, July 2–4 2008.
 - 42. G. Suwała and Ł. Jankowski. A model-less method for added mass identification. *Solid State Phenomena*, 147–149:570–575, 2009.
 - 43. G. Suwała and Ł. Jankowski. A benchmark for identification of structural modifications and inelastic impacts: the structure, test data and an example solution. In *Proceedings of the 5th ECCOMAS Thematic Conference on Smart Structures and Materials (SMART 2011)*, Saarbrücken, Germany, July 2011.
 - 44. G. Suwała and Ł. Jankowski. Experimental study of a model-free method for identification of stiffness-related structural damages. In *Proc. of the 6th European Workshop on Structural Health Monitoring (EWSHM 2012)*, Dresden, Germany, 3–6 July 2012.

45. G. Suwała and Ł. Jankowski. Model-free monitoring of structures. In *Proc. of the ECCOMAS Thematic Conference: Int. Symposium on Inverse Problems in Mechanics of Structures and Materials (IPM 2013)*, Rzeszów–Baranów Sandomierski, Poland, 24–27 April 2013.
46. J. Hou, Ł. Jankowski, and J. Ou. A substructure isolation method for local structural health monitoring. *Structural Control & Health Monitoring*, 18(6):601–618, 2011.
47. J. Hou, Ł. Jankowski, and J. Ou. Experimental study of the substructure isolation method for local health monitoring. *Structural Control & Health Monitoring*, 19(4):491–510, 2012.
48. J. Hou, Ł. Jankowski, and J. Ou. Substructural damage identification using local primary frequency. In *Proc. of the 11th International Symposium on Structural Engineering (ISSE 11th)*, Guangzhou, China, 18–20 December 2010.
49. J. Hou, Ł. Jankowski, and J. Ou. Substructural damage identification using time series of local measured response. In *Proc. of the 5th World Conference on Structural Control and Monitoring (5WCSCM 2010)*, Tokyo, Japan, 12–14 July 2010.
50. J. Hou, Ł. Jankowski, and J. Ou. Substructure isolation and identification using fft of measured local responses. In *Proc. of the 5th European Workshop on Structural Health Monitoring (EWSHM 2010)*, pages 913–918, Sorrento, Italy, 29 June – 2 July 2010.
51. J. Hou, Ł. Jankowski, and J. Ou. Local damage identification in frequency domain based on substructure isolation method. In *Proc. of the 6th Int'l Workshop on Advanced Smart Materials and Smart Structures Technology (ANCRiSST 2011)*, Dalian, China, 25–26 July 2011.
52. J. Hou, Ł. Jankowski, and J. Ou. Large substructure identification using substructure isolation method. In *Proc. SPIE 8345*, page 83453V, 2012.
53. J. Hou, Ł. Jankowski, and J. Ou. Substructure isolation method for online local damage identification using time series. In *Proc. of the 6th European Workshop on Structural Health Monitoring (EWSHM 2012)*, Dresden, Germany, 3–6 July 2012.
54. Q. Zhang, Z. Duan, and Ł. Jankowski. Moving mass identification based on virtual distortion method. *Journal of Vibration Engineering*, 23(5):494–501, 2010 (in Chinese).
55. Q. Zhang, Z. Duan, and Ł. Jankowski. Moving mass identification of vehicle-bridge coupled system based on virtual distortion method. *Chi-*

- nese *Journal of Theoretical and Applied Mechanics*, 43(3):598–610, 2011 (in Chinese).
- 56. Q. Zhang, Z. Duan, Ł. Jankowski, and F. Wang. Experimental validation of a fast dynamic load identification method based on load shape function. *Journal of Vibration and Shock*, 30(9):98–102, 154, 2011 (in Chinese).
 - 57. Q. Zhang, Ł. Jankowski, and Z. Duan. Identification of coexistent load and damage. *Structural and Multidisciplinary Optimization*, 41(2):243–253, 2010.
 - 58. Q. Zhang, Ł. Jankowski, and Z. Duan. Damage identification using substructural virtual distortion method. In *Proc. SPIE 8345*, page 83453X, 2012.
 - 59. Q. Zhang, Ł. Jankowski, and Z. Duan. Identification of excitation time histories and parametrized structural damages. *Mechanical Systems and Signal Processing*, 33:56–68, 2012.
 - 60. Q. Zhang, Ł. Jankowski, and Z. Duan. Identification of coexistent load and damage based on virtual distortion method. In *Proceedings of the 4th European Workshop on Structural Health Monitoring*, pages 1121–1128, Kraków, Poland, July 2–4, 2008 2008.
 - 61. Q. Zhang, Ł. Jankowski, and Z. Duan. Fast identification of loads and damages using a limited number of sensors. In *Proceedings of the 5th European Workshop on Structural Health Monitoring (EWSHM 2010)*, pages 1039–1044, Sorrento, Italy, 29 June – 2 July 2010.
 - 62. Q. Zhang, Ł. Jankowski, and Z. Duan. Experimental verification of a methodology for simultaneous identification of coexistent loads and damages. In *Proceedings of the 8th International Conference on Condition Monitoring and Machinery Failure Prevention Technologies (CM/MFPT 2011)*, Cardiff, UK, June 20–22 2011.
 - 63. Z. Mróz and A. Garstecki. Optimal loading conditions in the design and identification of structures. Part 1: Discrete formulation. *Structural and Multidisciplinary Optimization*, 29(1):1–18, 2005.
 - 64. P. Czop, K. Mendrok, and T. Uhl. Application of inverse linear parametric models in the identification of rail track irregularities. *Archive of Applied Mechanics*, 81(11):1541–1554, 2011.
 - 65. B. J. Dobson and E. Rider. A review of the indirect calculation of excitation forces from measured structural response data. *Proceedings of the Institution of Mechanical Engineers, Part C: Journal of Mechanical Engineering Science*, 204(2):69–75, 1990.

66. H. Inoue, J. J. Harrigan, and S. R. Reid. Review of inverse analysis for indirect measurement of impact force. *Applied Mechanics Reviews*, 54(6):503–524, 2001.
67. E. Jacquelin, A. Bennani, and P. Hamelin. Force reconstruction: analysis and regularization of a deconvolution problem. *Journal of Sound and Vibration*, 265(1):81–107, July 2003.
68. M. Klinkov and C.-P. Fritzen. An updated comparison of the force reconstruction methods. *Key Engineering Materials*, 347:461–466, 2007.
69. T. Uhl. The inverse identification problem and its technical application. *Archive of Applied Mechanics*, 77(5):325–337, May 2007.
70. T. Uhl and K. Mendrok. *Application of the inverse identification problem to the determination of loading forces in mechanical structures [Zastosowanie odwrotnego zadania identyfikacji do wyznaczania sił obciążających konstrukcje mechaniczne]*. Wydawnictwo Naukowe Instytutu Technologii Eksploatacji (PIB), Kraków, 2005 (in Polish).
71. L. Yu and T. H. T. Chan. Recent research on identification of moving loads on bridges. *Journal of Sound and Vibration*, 305(1–2):3–21, 2007.
72. K. Mendrok. *Inverse problem in structural health monitoring*. Wydawnictwo Naukowe Instytutu Technologii Eksploatacji (PIB), Radom, 2010.
73. R. Adams and J. F. Doyle. Multiple force identification for complex structures. *Experimental Mechanics*, 42(1):25–36, 2002.
74. J. F. Doyle. *Modern experimental stress analysis – completing the solution of partially specified problems*. John Wiley & Sons Ltd, Chichester, 2004.
75. P. E. Hollandsworth and H. R. Busby. Impact force identification using the general inverse technique. *International Journal of Impact Engineering*, 8(4):315–322, 1989.
76. Z. R. Lu and S. S. Law. Force identification based on sensitivity in time domain. *Journal of Engineering Mechanics (ASCE)*, 132(1):1050–1056, 2006.
77. H. Inoue, H. Ishida, K. Kishimoto, and T. Shibuya. Measurement of impact load by using an inverse analysis technique: Comparison of methods for estimating the transfer function and its application to the instrumented charpy impact test. *Japan Society of Mechanical Engineers International Journal*, 34(4):453–458, 1991.
78. K. Mendrok and T. Uhl. Load identification using a modified modal filter technique. *Journal of Vibration and Control*, 16(1):89–105, 2010.

79. S. Ödeen and B. Lundberg. Prediction of impact force by impulse responses method. *International Journal of Impact Engineering*, 11(2):149–158, 1991.
80. E. Parloo, P. Verboven, P. Guillaume, and M. Van Overmeire. Force identification by means of in-operation modal models. *Journal of Sound and Vibration*, 262(1):161–173, 2003.
81. E. Parloo. *Application of Frequency Domain System Identification Techniques in the Field of Operational Modal Analysis*. PhD thesis, Vrije Universiteit Brussel, May 2003.
82. J. F. Doyle. A wavelet deconvolution method for impact force identification. *Experimental mechanics*, 37(4):403–408, 1997.
83. J.-J. Liu, C.-K. Ma, I-C. Kung, and D.-C. Lin. Input force estimation of a cantilever plate by using a system identification technique. *Computer Methods in Applied Mechanics and Engineering*, 190:1309–1322, 2000.
84. Q. P. Ha and H. Trinh. State and input simultaneous estimation for a class of nonlinear systems. *Automatica*, 40(10):1779–1785, 2004.
85. M. Klinkov and C.-P. Fritzen. Online estimation of external loads from dynamic measurements. In *Proceedings of the International Conference on Noise and Vibration Engineering (ISMA)*, pages 3957–3968, Leuven, Belgium, 2006.
86. M. S. Allen and T. G. Carne. Comparison of inverse structural filter (ISF) and sum of weighted accelerations technique (SWAT) time domain force identification methods. In *47th AIAA/ASME/ASCE/AHS/ASC Structures, Structural Dynamics, and Materials Conference*, May 2006.
87. M. S. Allen and T. G. Carne. Delayed, multi-step inverse structural filter for robust force identification. *Mechanical Systems and Signal Processing*, 22(5):1036–1054, 2008.
88. D. C. Kammer. Input force reconstruction using a time domain technique. *Journal of Vibration and Acoustics*, 120(4):868–874, 1998.
89. C.-K. Ma and C.-C. Ho. An inverse method for the estimation of input forces acting on non-linear structural systems. *Journal of Sound and Vibration*, 275:953–971, 2004.
90. N. Davendralingam and J. F. Doyle. Nonlinear identification problems under large deflections. *Experimental Mechanics*, 48(4):529–538, 2008.
91. L. E. Mujica. *A hybrid approach of knowledge-based reasoning for structural assessment*. PhD thesis, University of Girona, June 2006.

92. J. C. Briggs and M.-K. Tse. Impact force identification using extracted modal parameters and pattern matching. *International Journal of Impact Engineering*, 12(3):361–372, 1992.
93. X. Cao, Y. Sugiyamac, and Y. Mitsui. Application of artificial neural networks to load identification. *Computers and Structures*, 69:63–78, 1998.
94. E. Wu, C.-Z. Tsai, and L.-H. Tseng. A deconvolution method for force reconstruction in rods under axial impact. *Journal of Acoustical Society of America*, 104(3):1418–1426, 1998.
95. N. Hu and H. Fukunaga. A new approach for health monitoring of composite structures through identification of impact force. *Journal of Advanced Science*, 17(1–2):82–89, 2005.
96. H. Fukunaga and N. Hu. Experimental impact force identification of composite structures. In *Proc. of the 3rd European Workshop on Structural Health Monitoring (EWSHM 2006)*, pages 840–847, July 2006.
97. L. Gaul and S. Hurlebaus. Identification of the impact location on a plate using wavelets. *Mechanical Systems and System Processing*, 12(6):783–795, 1997.
98. M. T. Martin and J. F. Doyle. Impact force location in frame structures. *International Journal of Impact Engineering*, 18(1):79–97, 1996.
99. S. S. Law and X. Q. Zhu. Bridge dynamic responses due to road surface roughness and braking of vehicle. *Journal of Sound and Vibration*, 282(3–5):805–830, 2005.
100. X. Q. Zhu and S. S. Law. Identification of moving interaction forces with incomplete velocity information. *Mechanical Systems and Signal Processing*, 17(6):1349–1366, 2003.
101. S. S. Law, T. H. T. Chan, and Q. H. Zeng. Moving force identification: a time domain method. *Journal of Sound and vibration*, 201(1):1–22, 1997.
102. S. S. Law, T. H. T. Chan, and Q. H. Zeng. Moving force identification – A frequency and time domain analysis. *Journal of Dynamic System, Measurement and Control*, 121(3):394–401, 1999.
103. T. H. T. Chan, S. S. Law, T. H. Yung, and X. R. Yuan. An interpretive method for moving force identification. *Journal of Sound and Vibration*, 219:503–524, 1999.
104. T. H. T. Chan and C. O'Connor. Wheel loads from highway bridge strains: field studies. *Journal of Structural Engineering*, 116(7):1751–1771, 1990.

105. S. S. Law, J. Q. Bu, X. Q. Zhu, and S. L. Chan. Vehicle axle loads identification using finite element method. *Engineering Structures*, 26(8):1143–1153, 2004.
106. T. H. T. Chan, L. Yu, and S. S. Law. Moving force identification studies, I: Theory. *Journal of Sound and Vibration*, 247(1):59–76, 2001.
107. T. H. T. Chan, L. Yu, S. S. Law, and T. H. Yung. Moving force identification studies, II: Comparative studies. *Journal of Sound and Vibration*, 247(1):77–95, 2001.
108. X. Q. Zhu and S. S. Law. Practical aspects in moving load identification. *Journal of Sound and Vibration*, 258(1):123–146, 2002.
109. P. C. Hansen. Deconvolution and regularization with Toeplitz matrices. *Numerical Algorithms*, 29:323–378, 2002.
110. P. C. Hansen. *Rank-deficient and discrete ill-posed problems. Numerical aspects of linear inversion*. SIAM, Philadelphia, 1998.
111. P. C. Hansen. *Discrete inverse problems: insight and algorithms*. SIAM, Philadelphia, 2010.
112. R. Kress. *Linear integral equations*. Springer, New York, 2nd edition, 1999.
113. L. Yu and T. H. T. Chan. Moving force identification based on the frequency-time domain method. *Journal of Sound and Vibration*, 261(2):329–349, 2003.
114. S. S. Law, T. H. T. Chan, X. Q. Zhu, and Q. H. Zeng. Regularization in moving force identification. *Journal of Engineering Mechanics (ASCE)*, 127(2):136–148, 2001.
115. X. Q. Zhu and S. S. Law. Moving load identification on multi-span continuous bridges with elastic bearings. *Mechanical Systems and Signal Processing*, 20(7):1759–1782, 2006.
116. A. González, C. Rowley, and E. J. O'Brien. A general solution to the identification of moving vehicle forces on a bridge. *International Journal for Numerical Methods in Engineering*, 75(3):335–354, 2008.
117. S. S. Law and Y. L. Fang. Moving force identification: optimal state estimation approach. *Journal of Sound and Vibration*, 239(2):233–254, 2001.
118. T. Pinkaew. Identification of vehicle axle loads from bridge responses using updated static component technique. *Engineering Structures*, 28(11):1599–1608, 2006.

119. T. Pinkaew and P. Asnachinda. Experimental study on the identification of dynamic axle loads of moving vehicles from the bending moments of bridges. *Engineering Structures*, 29(9):2282–2293, 2007.
120. A. Mackiewicz, J. Holnicki-Szulc, and F. Lopez-Almansa. Optimal sensor location in active control of flexible structures. *AIAA Journal*, 34(4):857–859, 1996.
121. C. Papadimitriou, Y. Haralampidis, and K. Sobczyk. Optimal experimental design in stochastic structural dynamics. *Probabilistic Engineering Mechanics*, 20(1):67–78, 2005.
122. W. K. Gawronski. *Advanced structural dynamics and active control of structures*. Mechanical Engineering Series. Springer, 2004.
123. M. van de Wal and B. de Jager. A review of methods for input/output selection. *Automatica*, 37(4):487–510, 2001.
124. E. Jacquelin, A. Bennani, and M. Massenzio. Analysis of a force reconstruction problem. *Structural Engineering and Mechanics*, 21(3):237–254, 2005.
125. W. M. Said and W. J. Staszewski. Optimal sensor location for damage detection using mutual information. In *Proc. of the 11th Int'l Conf. on Adaptive Structures and Technologies*, pages 428–435, Nagoya, Japan, 23–26 October 2000.
126. P. C. Hansen, M. E. Kilmer, and R. H. Kjeldsen. Exploiting residual information in the parameter choice for discrete ill-posed problems. *BIT Numerical Mathematics*, 46(1):41–59, 2006.
127. J. M. Starkey and G. L. Merrill. On the ill-conditioned nature of indirect force-measurement techniques. *International Journal of Analytical and Experimental Modal Analysis*, 4(3):103–108, July 1989.
128. Å. Björck. *Numerical Methods in Scientific Computing*, volume 2. SIAM, Philadelphia, in press.
129. A. Neumaier. Solving ill-conditioned and singular linear systems: A tutorial on regularization. *SIAM Review*, 40(3):636–666, September 1998.
130. A. N. Tikhonov and V. Y. Arsenin. *Solutions of ill-posed problems*. V. H. Winston and Sons (distributed by Wiley, New York), 1977.
131. F. Bauer and M. A. Lukas. Comparing parameter choice methods for regularization of ill-posed problems. *Mathematics and Computers in Simulation*, 81(9):1795–1841, 2011.

132. R. Palm. *Numerical Comparison of Regularization Algorithms for Solving Ill-Posed Problems*. PhD thesis, University of Tartu, January 2010.
133. G. H. Golub and C. F. Van Loan. *Matrix computations*. The John Hopkins University Press, 3rd edition, 1996.
134. R. H.-F. Chan and X.-Q. Jin. *An introduction to iterative Toeplitz solvers*. SIAM, Philadelphia, 2007.
135. P. C. Hansen. The L-curve and its use in the numerical treatment of inverse problems. In P. R. Johnston, editor, *Computational Inverse Problems in Electrocardiology*, chapter 4, pages 119–142. WIT Press, Southampton, 2001.
136. Å. Björck. *Numerical Methods for Least Squares Problems*. SIAM, Philadelphia, 1996.
137. J. Nocedal and S. J. Wright. *Numerical Optimization*. Springer, New York, 2nd ed. edition, 2006.
138. Z. Bai, J. Demmel, J. Dongarra, A. Ruhe, and H. van der Vorst. *Templates for the Solution of Algebraic Eigenvalue Problems: A Practical Guide*. SIAM, Philadelphia, 1987.
139. G. Dahlquist and Å. Björck. *Numerical Methods in Scientific Computing*, volume 1. SIAM, Philadelphia, 2008.
140. M. Fornasier and H. Rauhut. Compressive sensing. In O. Scherzer, editor, *Handbook of Mathematical Methods in Imaging*, chapter 2, pages 187–228. Springer, 2011.
141. J. E. T. Penny, M. I. Friswell, and S. D. Garvey. Automatic choice of measurement locations for dynamic testing. *AIAA Journal*, 32(2):407–414, 1994.
142. W. J. Staszewski and K. Worden. An overview of optimal sensor location methods for damage detection. In *Proc. of SPIE*, volume 4326, pages 179–187, 2001.
143. K. Worden and A. P. Burrows. Optimal sensor placement for fault detection. *Engineering Structures*, 23(8):885–901, 2001.
144. E. Majchrzak and J. Mendakiewicz. Sensitivity analysis as a tool of optimal sensors location for solidification parameters estimation. *Materials Science Forum*, 638–642:2640–2645, 2010.
145. C. I. Bajer. Time integration methods – still questions. In W. Szczęśniak, editor, *Theoretical Foundations of Civil Engineering*, volume 1, pages 45–54, Warsaw, Poland, 2002.

146. K.-J. Bathe. *Finite Element Procedures*. Prentice Hall, 1995.
147. N. M. Newmark. A method of computation in structural dynamics. *Transactions, ASCE*, 127:1406–1435, 1962.
148. W. H. Press, S. A. Teukolsky, W. T. Vetterling, and B. P. Flannery. *Numerical Recipes: The Art of Scientific Computing*. Cambridge University Press, 3rd edition, 2007.
149. W. Nowacki. *Theory of elasticity [Teoria sprężystości]*. PWN, Warsaw, 1970 (in Polish).
150. J. D. Eshelby. The determination of the elastic field of an ellipsoidal inclusion, and related problems. *Proceedings of the Royal Society of London. Series A: Mathematical and Physical Sciences*, 241(1226):376–396, 1957.
151. E. Kröner. *Continuum theory of dislocations and internal stresses [Kontinuumstheorie der Versetzungen und Eigenspannungen]*, volume 5 of *Ergebnisse der Angewandten Mathematik*. Springer, Berlin, 1958 (in German).
152. E. Kröner. General continuum theory of dislocations and internal stresses [Allgemeine Kontinuumstheorie der Versetzungen und Eigenspannungen]. *Archive for Rational Mechanics and Analysis*, 4(1):273–334, 1959 (in German).
153. J. H. Argyris. Elasto-plastic matrix displacement analysis of three-dimensional continua. *Journal of the Royal Aeronautical Society*, 69:633–636, 1965.
154. G. Maier. A matrix structural theory of piecewiselinear plasticity with interacting yield planes. *Meccanica*, 7(1):54–66, 1970.
155. K. I. Majid and T. Celik. The elastic-plastic analysis of frames by the theorems of structural variation. *International Journal for Numerical Methods in Engineering*, 21(4):671–681, 1985.
156. J. Holnicki-Szulc and J. Gierliński. Structural modifications simulated by virtual distortions. *International Journal for Numerical Methods in Engineering*, 28(3):645–666, 1989.
157. J. Holnicki-Szulc. Prestress of truss and frame structures. *Journal of the Structural Division*, 105(3):601–616, 1979.
158. J. Holnicki-Szulc and R. T. Haftka. Vibration mode shape control by prestressing. *AIAA Journal*, 30(7):1924–1927, 1992.
159. J. Holnicki-Szulc. *Virtual Distortion Method*. Lecture Notes in Engineering. Springer-Verlag, 1991.

160. P. V. Makode, M. R. Ramirez, and R. B. Corotis. Reanalysis of rigid frame structures by the virtual distortion method. *Structural and Multidisciplinary Optimization*, 11(1–2):71–79, 1996.
161. J. T. Putresza and P. Kołakowski. Sensitivity analysis of frame structures (virtual distortion method approach). *International Journal for Numerical Methods in Engineering*, 50(6):1307–1329, 2001.
162. J. Holnicki-Szulc, editor. *Smart Technologies for Safety Engineering*. John Wiley & Sons Ltd, Chichester, 2008.
163. M. Wikło and J. Holnicki-Szulc. Optimal design of adaptive structures. Part II. Adaptation to impact loads. *Structural and Multidisciplinary Optimization*, 37(4):351–366, 2009.
164. M. Di Paola. Probabilistic analysis of truss structures with uncertain parameters (virtual distortion method approach). *Probabilistic Engineering Mechanics*, 19(4):321–329, 2004.
165. M. Di Paola, A. Pirrotta, and M. Zingales. Stochastic dynamics of linear elastic trusses in presence of structural uncertainties (virtual distortion approach). *Probabilistic Engineering Mechanics*, 19(1–2):41–51, 2004.
166. U. Kirsch. Reanalysis and sensitivity reanalysis by combined approximations. *Structural and Multidisciplinary Optimization*, 40(1–6):1–15, 2010.
167. U. Kirsch, M. Kocvara, and J. Zowe. Accurate reanalysis of structures by a preconditioned conjugate gradient method. *International Journal for Numerical Methods in Engineering*, 55(2):233–251, 2002.
168. M. A. Akgün, J. H. Garcelon, and R. T. Haftka. Fast exact linear and non-linear structural reanalysis and the Sherman-Morrison-Woodbury formulas. *International Journal for Numerical Methods in Engineering*, 50(7):1587–1606, March 2001.
169. W. W. Hager. Updating the inverse of a matrix. *SIAM Review*, 31(2):221–239, 1989.
170. J. S. Arora. Survey of structural reanalysis techniques. *Journal of the Structural Division*, 4(4):783–802, 1976.
171. J.-F. M. Barthelemy and R. T. Haftka. Approximation concepts for optimum design – a review. *Structural Optimization*, 5(3):129–144, 1993.
172. A. M. Abu Kassim and B. H. V. Topping. Static reanalysis: A review. *Journal of Structural Engineering*, 113(5):1029–1045, 1987.
173. M. Mróz, Ł. Jankowski, and J. Holnicki-Szulc. A VDM-based method for fast reanalysis and identification of structural damping. In *Proc. of*

- the 8th World Congress on Structural and Multidisciplinary Optimization (WCSMO-8)*, Lisbon, Portugal, June 1–5 2009.
- 174. M. Mróz, Ł. Jankowski, and J. Holnicki-Szulc. VDM-based identification of localized, damage induced damping. In *Proc. of the 5th European Workshop on Structural Health Monitoring (EWSHM 2010)*, pages 988–993, Sorrento, Italy, June 29 – July 2 2010.
 - 175. M. Wikło. *Design of adaptive systems exposed to impact loads [Projektowanie ustrojów adaptacyjnych poddawanych obciążeniom udarowym]*. PhD thesis, Institute of Fundamental Technological Research of the Polish Academy of Sciences (IPPT PAN), Warsaw, 2007 (in Polish).
 - 176. K. Dems and Z. Mróz. Identification of damage in beam and plate structures using parameter-dependent frequency changes. *Engineering Computations*, 18(1–2):96–120, 2001.
 - 177. K. Dems and Z. Mróz. Damage identification using modal, static and thermographic analysis with additional control parameters. *Computers and Structures*, 88(21–22):1254–1264, 2010.
 - 178. K. Dems and J. Turant. Structural damage identification using frequency and modal changes. *Bulletin of the Polish Academy of Sciences*, 59(1):27–32, 2011.
 - 179. R. T. Haftka and Z. Gürdal. *Elements of structural optimization*. Kluwer Publishers, 3rd edition, 1992.
 - 180. M. Kleiber, H. Antunez, and P. Kowalczyk. *Parameter Sensitivity in Non-linear Mechanics: Theory and Finite Element Computations*. John Wiley & Sons, 1997.
 - 181. D. I. Papadimitriou and K. C. Giannakoglou. Aerodynamic shape optimization using first and second order adjoint and direct approaches. *Archives of Computational Methods in Engineering*, 15(4):447–488, 2008.
 - 182. P. Tazowski and M. Kleiber. Parameter and shape sensitivity of thermo-viscoelastic response. *Computers and Structures*, 84(5–6):385–399, 2006.
 - 183. J. D. Achenbach. Structural health monitoring – What is the prescription? *Mechanics Research Communications*, 36(2):137–142, 2009.
 - 184. W. Fan and P. Qiao. Vibration-based damage identification methods: A review and comparative study. *Structural Health Monitoring*, 10(1):83–111, 2011.
 - 185. C.-P. Fritzen and P. Kraemer. Self-diagnosis of smart structures based on dynamical properties. *Mechanical Systems and Signal Processing*, 23(6):1830–1845, 2009.

186. P. Kołakowski, L. E. Mujica, and J. Vehí. Two approaches to structural damage identification: Model updating vs. soft computing. *Journal of Intelligent Material Systems and Structures*, 17(1):63–79, 2006.
187. K. Mendrok and T. Uhl. The application of modal filters for damage detection. *Smart structures and systems*, 6(2):115–133, 2010.
188. K. Mendrok and T. Uhl. Experimental verification of the damage localization procedure based on modal filtering. *Structural Health Monitoring: An International Journal*, 10(2):157–171, 2011.
189. O. Bareille, M. Kharrat, W. Zhou, and M. N. Ichchou. Distributed piezoelectric guided-T-wave generator, design and analysis. *Mechatronics*, 5(5):544–551, 2012.
190. P. J. Fanning and E. P. Carden. Experimentally validated added mass identification algorithm based on frequency response functions. *Journal of Engineering Mechanics*, 130(9):1045–1051, 2004.
191. M. Ge and E. M. Lui. Structural damage identification using system dynamic properties. *Computers and Structures*, 83(27):2185–2196, 2005.
192. W. Ostachowicz, M. Krawczuk, M. Cartmell, and M. Gilchrist. Wave propagation in delaminated beam. *Computers and Structures*, 82(6):475–483, 2004.
193. W. Ostachowicz. Damage detection of structures using spectral finite element method. *Computers and Structures*, 86(3–5):454–462, 2008.
194. W. Ostachowicz, M. Krawczuk, and M. Cartmell. The location of a concentrated mass on rectangular plates from measurements of natural vibrations. *Computers and Structures*, 80(16–17):1419–1428, 2002.
195. A. Świercz, P. Kołakowski, and J. Holnicki-Szulc. Damage identification in skeletal structures using the virtual distortion method in frequency domain. *Mechanical Systems and Signal Processing*, 22(8):1826–1839, 2008.
196. T. Burczyński, W. Kuś, A. Długosz, and P. Orantek. Optimization and defect identification using distributed evolutionary algorithms. *Engineering Applications of Artificial Intelligence*, 17(4):337–344, 2004.
197. B. Kouchmeshky, W. Aquino, and A. E. Billek. Structural damage identification using co-evolution and frequency response functions. *Structural Control & Health Monitoring*, 15(2):162–182, 2008.
198. G. S. Wang. Application of hybrid genetic algorithm to system identification. *Structural Control and Health Monitoring*, 16(2):125–153, 2009.

199. R. Schaefer. Global optimization problems. *Studies in Computational Intelligence*, 74:7–30, 2007.
200. L. E. Mujica Delgado. *A hybrid approach of knowledge-based reasoning for structural assessment*. PhD thesis, University of Girona, 2006.
201. L. E. Mujica Delgado, J. Vehí, W. Staszewski, and K. Worden. Impact damage detection in aircraft composites using knowledge-based reasoning. *Structural Health Monitoring: An International Journal*, 7(3):215–230, 2008.
202. R. Le Riche, D. Gualandris, J. J. Thomas, and F. Hemez. Neural identification of non-linear dynamic structures. *Journal of Sound and Vibration*, 248(2):247–265, 2001.
203. W. J. Staszewski. Intelligent signal processing for damage detection in composite materials. *Composites Science and Technology*, 62(7–8):941–950, 2002.
204. T. Szolc, P. Tauzowski, R. Stocki, and J. Knabel. Damage identification in vibrating rotor-shaft systems by efficient sampling approach. *Mechanical Systems and Signal Processing*, 23(5):1615–1633, 2009.
205. M. Liefvendahl and R. Stocki. A study on algorithms for optimization of latin hypercubes. *Journal of Statistical Planning and Inference*, 136(9):3231–3247, 2006.
206. Ch. Efstathiades, C. C. Baniotopoulos, P. Nazarko, L. Ziemiański, and G. E. Stavroulakis. Application of neural networks for the structural health monitoring in curtain-wall systems. *Engineering Structures*, 29(12):3475–3484, 2007.
207. P. Nazarko and L. Ziemiański. Towards application of soft computing in structural health monitoring. In L. Rutkowski, R. Scherer, R. Tadeusiewicz, L. Zadeh, and J. Zurada, editors, *Artifical Intelligence and Soft Computing*, volume 6114 of *Lecture Notes in Computer Science*, pages 56–63. Springer Berlin–Heidelberg, 2010.
208. Z. Waszczyzyn and L. Ziemiański. Neural networks in mechanics of structures and materials – new results and prospects of applications. *Computers and Structures*, 79(22–25):2261–2276, 2001.
209. Z. Waszczyzyn and L. Ziemiański. Neural networks in the identification analysis of structural mechanics problems. In Z. Mróz and G. E. Stavroulakis, editors, *Parameter Identification of Materials and Structures*, volume 469 of *CISM*, chapter 7, pages 265–340. Springer, Wien–New York, 2005.

210. Z. Waszczyszyn and L. Ziemiański. Neurocomputing in the analysis of selected inverse problems of mechanics of structures and materials. *Computer Assisted Mechanics and Engineering Sciences (CAMES)*, 13(1):125–159, 2006.
211. M. Link, S. Stöhr, and M. Weiland. Identification of structural property degradations by computational model updating. *Key Engineering Materials*, 347:19–34, 2007.
212. M. Link and M. Weiland. Damage identification by multi-model updating in the modal and in the time domain. *Mechanical Systems and Signal Processing*, 23(6):1734–1746, 2009.
213. M. Link, M. Weiland, and Th. Seckert. Computational model updating for damage identification in the time domain. In *Proceedings of the International Conference on Noise and Vibration Engineering (ISMA)*, Leuven, Belgium, September 2008.
214. W. Moczulski. Problems of declarative and procedural knowledge acquisition for machinery diagnostics. *Computer Assisted Mechanics and Engineering Sciences (CAMES)*, 9(1):71–86, 2002.
215. O. R. de Lautour and P. Omenzetter. Nearest neighbor and learning vector quantization classification for damage detection using time series analysis. *Structural Control and Health Monitoring*, 17(6):614–631, 2010.
216. M. Krommer and Y. Vetyukov. A novel damage detection method based on spatial compatibility filtering. In R. Scheidl and B. Jacoby, editors, *Proc. of 13th Mechatronics Forum International Conference (Mechatronics 2012)*, volume 3, pages 732–739, Linz, Austria, September 17–19th 2012.
217. M. Krommer and H. Irschik. Design of piezoelectric sensors for structural and health monitoring based on the principle of virtual work. *Advanced Materials Research*, 745:73–87, 2013.
218. F. Casciati and S. Casciati. Structural health monitoring by Lyapunov exponents of non-linear time series. *Structural Control and Health Monitoring*, 13(1):132–146, 2006.
219. J. Iwaniec, T. Uhl, W. J. Staszewski, and A. Klepka. Detection of changes in cracked aluminium plate determinism by recurrence analysis. *Nonlinear Dynamics*, 70(1):125–140, 2012.
220. J. Kiciński. Model based diagnostics – today and tomorrow. *Diagnostyka*, 30(1):241–247, 2004.

221. L. Faravelli and S. Casciati. Structural damage detection and localization by response change diagnosis. *Progress in Structural Engineering and Materials*, 6(2):104–115, 2004.
222. M. Kleiber, J. Knabel, and J. Rojek. Response surface method for probabilistic assessment of metal forming failures. *International Journal for Numerical Methods in Engineering*, 60(1):51–67, 2004.
223. J.-N. Juang and R. S. Pappa. An eigensystem realization algorithm for modal parameter identification and model reduction. *Journal of Guidance, Control, and Dynamics*, 8(5):620–627, 1985.
224. W. Heylen, S. Lammens, and P. Sas. *Modal analysis theory and testing*. Katholieke Universiteit Leuven, Faculty of Engineering, Department of Mechanical Engineering, 1998.
225. P. Vanhonacker. Differential and difference sensitivities of natural frequencies and mode shapes of mechanical structures. *AIAA Journal*, 18(12):1511–1514, 1980.
226. P. Vanhonacker. *The Use of Modal Parameters of Mechanical Structures in Sensitivity Analysis-, System Synthesis- and System Identification Methods*. PhD thesis, Department of Mechanical Engineering, Katholieke Universiteit Leuven, Belgium, 1980.
227. K. C. Park, G. W. Reich, and K. F. Alvin. Structural damage detection using localized flexibilities. *Journal of Intelligent Material Systems and Structures*, 9(11):911–919, 1998.
228. K. C. Park and G. W. Reich. Use of substructural transmission zeros for structural health monitoring. *AIAA Journal*, 38(6):1040–1046, 2000.
229. D. Bernal. Flexibility-based damage localization from stochastic realization results. *Journal of Engineering Mechanics*, 132(6):651–658, 2006.
230. Z. Duan, G. Yan, J. Ou, and B. F. Spencer. Damage detection in ambient vibration using proportional flexibility matrix with incomplete measured DOFs. *Structural Control and Health Monitoring*, 14(2):186–196, 2007.
231. C.-B. Yun and E. Y. Bahng. Substructural identification using neural networks. *Computers and structures*, 77(1):41–52, 2000.
232. Y. Bao, H. Li, Y. An, and J. Ou. Dempster–Shafer evidence theory approach to structural damage detection. *Structural Health Monitoring*, 11(1):13–26, 2012.
233. Y. An and J. Ou. Experimental and numerical studies on model updating method of damage severity identification utilizing four cost functions. *Structural Control and Health Monitoring*, 20(1):107–120, 2013.

234. C. G. Koh, L. M. See, and T. Balendra. Estimation of structural parameters in time domain: A substructure approach. *Earthquake Engineering and Structural Dynamics*, 20(8):787–801, 1991.
235. C. G. Koh, B. Hong, and C. Y. Liaw. Substructural and progressive structural identification methods. *Engineering Structures*, 25(12):1551–1563, 2003.
236. A. W. C. Oreta and T. Tanabe. Element identification of member properties of framed structures. *Journal of Structural Engineering*, 120(7):1961–1976, 1994.
237. D. Zhang and E. A. Johnson. Substructure identification for shear structures: cross-power spectral density method. *Smart Materials and Structures*, 21:055006, 2012.
238. C.-B. Yun and H.-J. Lee. Substructural identification for damage estimation of structures. *Structural Safety*, 19(1):121–140, 1997.
239. K. F. Tee, C. G. Koh, and S. T. Quek. Substructural first- and second-order model identification for structural damage assessment. *Earthquake Engineering and Structural Dynamics*, 34(15):1755–1775, 2005.
240. K. F. Tee, C. G. Koh, and S. T. Quek. Numerical and experimental studies of a substructural identification strategy. *Structural Health Monitoring*, 8(5):397–410, 2009.
241. C. G. Koh and K. Shankar. Substructural identification method without interface measurement. *Journal of Engineering Mechanics (ASCE)*, 129(7):769–776, 2003.
242. J. N. Yang and H. W. Huang. Substructure damage identification using sequential nonlinear LSE method. In *Proceedings of the 4th International Conference on Earthquake Engineering*, Taipei, Taiwan, October 2006.
243. J. N. Yang and H. W. Huang. Substructure damage identification using damage tracking technique. In *Proc. SPIE 6529*, page 65292R, 2007.
244. Y. Lei, Y. Wu, and T. Li. Identification of non-linear structural parameters under limited input and output measurements. *International Journal of Non-Linear Mechanics*, 47(10):1141–1146, 2012.
245. K. V. Yuen and L. S. Katafygiotis. Substructure identification and health monitoring using noisy response measurements only. *Computer-Aided Civil and Infrastructure Engineering*, 21(4):280–291, 2006.
246. D. Zhang, C. DeVore, and E. A. Johnson. Experimental verification of controlled substructure identification for shear structures. In *Proceedings*

- of the 5th World Conference on Structural Control and Monitoring (5WC-SCM), Tokyo, Japan, July 2010.
- 247. T. N. Trinh and C. G. Koh. An improved substructural identification strategy for large structural systems. *Structural Control and Health Monitoring*, 19(8):686–700, 2012.
 - 248. Z. Xing and A. Mita. A substructure approach to local damage detection of shear structure. *Structural Control and Health Monitoring*, 19(2):309–318, 2012.
 - 249. X. J. Wang, C. G. Koh, and Z. Zhang. Damage identification based on strain and translational measurements with substructure approach. In *Proceedings of the 1st Middle East Conference on Smart Monitoring, Assessment and Rehabilitation of Civil Structure*, Dubai, UAE, February 2011.
 - 250. J. Hou, Ł. Jankowski, and J. Ou. Structural damage identification by adding virtual masses using the virtual distortion method. *Structural and Multidisciplinary Optimization*, 48(1):59–72, 2013.
 - 251. N. G. Nalitolela, J. E. T. Penny, and M. I. Friswell. Updating model parameters by adding an imagined stiffness to the structure. *Mechanical Systems and Signal Processing*, 7(2):161–172, 1993.
 - 252. D. Bojczuk and Z. Mróz. Determination of optimal actuator forces and positions in smart structures using adjoint method. *Structural and Multidisciplinary Optimization*, 30(4):308–319, 2005.
 - 253. R. J. Allemang. The modal assurance criterion – twenty years of use and abuse. *Sound and Vibration*, (August):14–21, 2003.
 - 254. F. Claeysen, N. Lhermet, R. Le Letty, F. Barillot, M. Debarnot, M. F. Six, G. Thomin and M. Privat, and P. Bouchilloux. Piezoelectric actuators and motors based on shell structures. In *Proceedings of SPIE*, volume 3991, pages 202–209, 2000.
 - 255. J. Chen and J. Li. Simultaneous identification of structural parameters and input time history from output-only measurements. *Computational Mechanics*, 33(5):365–374, 2004.
 - 256. Z. R. Lu and S. S. Law. Identification of system parameters and input force from output only. *Mechanical Systems and Signal Processing*, 21(5):2099–2111, 2007.
 - 257. K. Zhang, H. Li, Z. Duan, and S. S. Law. A probabilistic damage identification approach for structures with uncertainties under unknown input. *Mechanical Systems and Signal Processing*, 25(4):1126–1145, 2011.

258. C.-Y. Kim, D.-S. Jung, N.-S. Kim, S.-D. Kwon, and M. Q. Feng. Effect of vehicle weight on natural frequencies of bridges measured from traffic-induced vibration. *Earthquake Engineering and Engineering Vibration*, 2(1):109–115, 2003.
259. S. S. Law, S. Q. Wu, and Z. Y. Shi. Moving load and prestress identification using wavelet-based method. *Journal of Applied Mechanics*, 75(2):021014, 2008.
260. X. Q. Zhu and S. S. Law. Damage detection in simply supported concrete bridge structure under moving vehicular loads. *Journal of Vibration and Acoustics*, 129(1):58–65, 2007.
261. Z. R. Lu and J. K. Liu. Identification of both structural damages in bridge deck and vehicular parameters using measured dynamic responses. *Computers and Structures*, 89(13–14):1397–1405, 2011.
262. Z. R. Lu and J. K. Liu. Parameters identification for a coupled bridge-vehicle system with spring-mass attachments. *Applied Mathematics and Computation*, 219(17):9174–9186, 2013.
263. M. Hoshiya and O. Maruyama. Identification of running load and beam system. *Journal of Engineering Mechanics ASCE*, 113(6):813–824, 1987.
264. L. Majumder and C. S. Manohar. A time-domain approach for damage detection in beam structures using vibration data with a moving oscillator as an excitation source. *Journal of Sound and Vibration*, 268(4):699–716, 2003.
265. L. Majumder and C. S. Manohar. Nonlinear reduced models for beam damage detection using data on moving oscillator-beam interactions. *Computers and Structures*, 82(2–3):301–314, 2004.
266. H. A. Nasrellah and C. S. Manohar. A particle filtering approach for structural system identification in vehicle-structure interaction problems. *Journal of Sound and Vibration*, 329(9):1289–1309, 2010.
267. R. Sieniawska, P. Śniady, and S. Żukowski. Identification of the structure parameters applying a moving load. *Journal of Sound and Vibration*, 319(1–2):355–365, 2009.
268. V. Pakrashi, A. O'Connor, and B. Basu. A bridge-vehicle interaction based experimental investigation of damage evolution. *Structural Health Monitoring*, 9(4):285–296, 2010.
269. C. Bilello and L. A. Bergman. Vibration of damaged beams under a moving mass: theory and experimental validation. *Journal of Sound and Vibration*, 274(3–5):567–582, 2004.

270. C. Bilello, L. A. Bergman, and D. Kuchma. Experimental investigation of a small scale bridge model under a moving mass. *Journal of Structural Engineering*, 130(5):799–804, 2004.
271. J. Q. Bu, S. S. Law, and X. Q. Zhu. Innovative bridge condition assessment from dynamic response of a passing vehicle. *Journal of Engineering Mechanics*, 132(12):1372–1379, 2006.
272. S. S. Law and X. Q. Zhu. Dynamic behaviour of damaged concrete bridge structures under moving vehicular loads. *Engineering Structures*, 26(9):1279–1293, 2004.
273. J. W. Lee, J. D. Kim, C. B. Yun, J. H. Yi, and J. M. Shim. Health monitoring method for bridges under ordinary traffic loadings. *Journal of Sound and Vibration*, 257(2):247–264, 2002.
274. M. Kokot and J. Holnicki-Szulc. Defect identification in electrical circuits via the virtual distortion method. Part 1: Steady-state case. *Journal of Intelligent Material Systems and Structures*, 20(12):1465–1473, 2009.
275. A. Orłowska, P. Kołakowski, and J. Holnicki-Szulc. Detecting delamination zones in composites by embedded electrical grid and thermographic methods. *Smart Materials and Structures*, 20(10):105009, 2011.
276. M. I. Friswell and J. E. T. Penny. Crack modeling for structural health monitoring. *Structural Health Monitoring*, 1(2):139–148, 2002.
277. W. Ostachowicz and M. Krawczuk. On modelling of structural stiffness loss due to damage. *Key Engineering Materials*, 204–205:185–200, 2001.
278. C. I. Bajer and B. Dyniewicz. Numerical modelling of structure vibrations under inertial moving load. *Archive of Applied Mechanics*, 79(6–7):499–508, 2009.
279. B. Dyniewicz and C. I. Bajer. New feature of the solution of a Timoshenko beam carrying the moving mass particle. *Archive of Applied Mechanics*, 62(5):327–341, 2010.
280. C. I. Bajer and B. Dyniewicz. *Numerical Analysis of Vibrations of Structures under Moving Inertial Load*, volume 65 of *Lecture Notes in Applied and Computational Mechanics*. Springer, 2012.
281. F. T. K. Au, R. J. Jiang, and Y. K. Cheung. Parameter identification of vehicles moving on continuous bridges. *Journal of Sound and Vibration*, 269(1–2):91–111, 2004.
282. G. Sheng, C. Li, and B. Zhao. Dynamic analysis of a simply-supported beam subjected to moving vehicles. *Engineering Mechanics*, 23(12):154–158, 2006 (in Chinese).

283. J. C. Simo and T. J. R. Hughes. *Computational inelasticity*, volume 7 of *Interdisciplinary Applied Mathematics*. Springer, 1989.
284. J. Hou, L. Jankowski, and J. Ou. An online substructure identification method for local structural health monitoring. *Smart Materials and Structures*, 22(9):095017, 2013.
285. R. Kress. Integral equations. In N. Higham, editor, *The Princeton Companion to Applied Mathematics*. Princeton University Press, Princeton, in press.
286. W. Rudin. *Functional analysis*. Mc-Graw Hill, 2nd edition, 1991.
287. A. N. Kolmogorov and S. W. Fomin. *Elements of the Theory of Functions and Functional Analysis* [*Èlementy teorii funkciij i funkcional'nogo analiza*]. Nauka, Moskva, 4th edition, 1976 (in Russian).
288. J. Hadamard. On partial differential problems and their physical significance [in French: Sur les problèmes aux dérivées partielles et leur signification physique]. *Princeton University Bulletin*, 13:49–52, 1902.
289. J. Hadamard. *Lectures on Cauchy's problem in linear partial differential equations*. Yale University Press, New Haven, 1923.
290. F. Riesz. On linear functional equations [Über lineare Funktionalgleichungen]. *Acta Mathematica*, 41:71–98, 1916 (in German).
291. I. Fredholm. On a class of functional equations [Sur une classe d'équations fonctionnelles]. *Acta Mathematica*, 27:365–390, 1903 (in French).
292. L. M. Delves and J. L. Mohamed. *Computational methods for integral equations*. Cambridge University Press, 1988.
293. P. C. Hansen. Computation of the singular value expansion. *Computing*, 40(3):185–199, 1988.
294. P. C. Hansen. The discrete picard condition for discrete ill-posed problems. *BIT Numerical Mathematics*, 30(4):658–672, 1990.